Computational Design of Two-Dimensional Phosphorus on Gas Sensing and Catalysis

by

Pengfei Ou

Department of Mining and Materials Engineering

McGill University, Montréal

December 2019

A thesis submitted to McGill University in partial fulfillment of the requirements for the degree of Doctor of Philosophy

Abstract

The rediscovery of black phosphorus (black P) and the prediction of blue P as new, non-metallic, and single-element two-dimensional (2D) nanomaterials have ignited the interest of researchers in these materials for a variety of fields. Originating from the field-effect transistors, multilayer black P has demonstrated great promise in numerous applications, such as photodetectors, photovoltaics, and imaging devices. Recently, 2D black P has also been proven to be a promising candidate for chemical sensing of various common gases using field-effect transistors, due to its large molecular adsorption energy, inherently large surface/volume ratio, and anisotropic electronic properties. However, the candidacy of its structural derivatives including black P nanotubes and nanowires, as well as chemical or gas sensing of other chemical compounds (e.g., volatile organic compounds) remain unexplored. In addition, more recently, 2D black/blue P has been extensively studied to construct efficient photocatalysts for catalyzing hydrogen evolution reaction (HER) and nitrogen reduction reaction (NRR) under ambient conditions. Unfortunately, the large-area basal plane of 2D black/blue P exhibits inertness with only exposed edge sites being active towards these photocatalytic applications. Besides, the catalytic activity of these photocatalysts varied significantly depending on defects, dopants, metal contacts, and a multitude of additional factors.

With the express goal of shedding light on the physical and chemical properties of 2D black/blue P and its derivatives toward the enhanced performance of 2D black/blue P-based electronic devices and photocatalysts, the present thesis systematically studied their potential applications, particularly focusing on the sensitivity of gas sensors using field-effect transistors and catalytic activity of photocatalysts. This thesis employed both the first-principles calculations to reveal the fundamental chemical and electronic properties associated with these applications, the non-equilibrium Green's function formalism to predict the electronic transport properties, as well as the nudged elastic band method and computational hydrogen electrode

model to determine the kinetic energy barrier and reaction energetics, thus, to provide theoretical guidance on the design of 2D black/blue P.

This thesis is constructed from four interconnected manuscripts, two of them are already published in peer-reviewed journals, with the other two to be submitted. The scope of this thesis includes, in a broader context, gas sensors built from single-walled black P nanotubes (Chapter 4), 2D black P using as gas sensor for volatile organic compounds (Chapter 5), single-atom catalysts supported on nitrogen-doped 2D black P for electrochemical NRR (Chapter 6), and HER electrocatalysts based on transition metal/blue P heterojunctions (Chapter 7). These studies provide mechanistic insights into the defect, strain, and substrate engineering of 2D black/blue P, and more generally, a rational paradigm for exploiting the potential applications of 2D nanomaterials through systematic first-principles calculations.

Résumé

La redécouverte du phosphore noir (P noir) et la prédiction du P bleu en tant que nanomatériaux bidimensionnels (2D) non métalliques à élément unique ont suscité l'intérêt des chercheurs pour ces matériaux dans une variété de domaines. Issu des transistors à effet de champ, le P noir à couches multiples s'est révélé très prometteur dans de nombreuses applications, telles que les photodétecteurs, le photovoltaïque et les dispositifs d'imagerie. Récemment, le P noir 2D s'est également révélé être un candidat prometteur pour la détection chimique de divers gaz communs à l'aide de transistors à effet de champ, en raison de sa grande énergie d'adsorption moléculaire, de son rapport surface/volume intrinsèquement important et de ses propriétés électroniques anisotropes. Cependant, les candidatures de ses dérivés structurels, y compris les nanotubes et les nanofils de P noir, ainsi que la détection chimique ou gazeuse d'autres composés chimiques (par exemple, les composés organiques volatils), restent inexplorées. De plus, plus récemment, le P noir/bleu 2D a été largement étudié pour construire des photocatalyseurs efficaces pour catalyser la réaction de dégagement d'hydrogène (HER) et la réaction de réduction d'azote (NRR) dans les conditions ambiantes. Malheureusement, la grande surface de la couche basale du P noir/bleu 2D présente une inertie, seuls les bords exposés étant actifs pour ces applications photocatalytiques. En outre, l'activité catalytique de ces photocatalyseurs varie considérablement en fonction des défauts, des dopants, des contacts métalliques et d'une multitude de facteurs supplémentaires.

Dans le but de faire la lumière sur les propriétés physiques et chimiques du P noir/bleu 2D et de ses dérivés vers l'amélioration des performances des appareils électroniques et des photocatalyseurs basées sur le P noir/bleu 2D, la présente thèse a systématiquement étudié ses applications potentielles, en se concentrant particulièrement sur la sensibilité des capteurs de gaz utilisant des transistors à effet de champ et l'activité catalytique des photocatalyseurs. Cette thèse fait usage à la fois les calculs des premiers principes pour révéler les propriétés chimiques

et électroniques fondamentales associées à ces applications, le formalisme de la fonction de Green hors équilibre pour prédire les propriétés de transport électronique, ainsi que la méthode des bandes élastiques et le modèle numérique d'électrode à hydrogène pour déterminer la barrière d'énergie cinétique et l'énergie de réaction, ainsi, pour fournir des conseils théoriques sur la conception de P noir/bleu 2D.

Cette thèse est construite à partir de quatre manuscrits interconnectés, deux d'entre eux sont déjà publiés dans des revues à comité de lecture, les deux autres devant encore être soumis. La portée de cette thèse comprend, dans un contexte plus large, des capteurs de gaz construits à partir de nanotubes de P noir à paroi unique (Chapitre 4), du P noir 2D utilisant comme capteur de gaz pour les composés organiques volatils (Chapitre 5), des catalyseurs à un atome supportés sur l'azote P noir 2D dopé pour NRR électrochimique (Chapitre 6) et les électrocatalyseurs HER basés sur des hétérojonctions métal de transition/P bleu (Chapitre 7). Ces études fournissent des informations mécanistiques sur l'ingénierie des défauts, des déformations et des substrats du P noir/bleu 2D, et plus généralement, un paradigme rationnel pour exploiter les applications potentielles des nanomatériaux 2D grâce à des calculs systématiques de premiers principes.

Acknowledgements

First, I would like to express my sincere appreciation to my parents for teaching me perseverance and diligence in my life and being supportive of pursuing my Ph.D. degree. Besides, if anyone has been more inspiring and helpful than my parents, that would be my advisor: Professor Jun Song. His passion for scientific research and insights on fundamental knowledge have kept me constantly searching the enjoyment along the pathway of my Ph.D. study. He has not only guided me on how to conduct research in the right direction and improve the quality of my manuscripts, but also his easy-going personality alleviates my pressure from the research.

In addition to my advisor, I would like to extend my gratitude to the members of the Multiscale Modeling of Materials Group, particularly Dr. Fanchao Meng, Dr. Cheng Chen, Dr. Xiao Zhou, and Dr. Guoqiang Lan, for always being available for fruitful discussion and technical assistance. I would like to acknowledge the McGill Engineering Doctoral Award (MEDA) for the financial support and Supercomputer CLUMEQ (Consortium Laval-UQAM-McGill and Eastern Quebec) Supercomputer for providing the computational resources. Last but not the least, I would also like to thank all the friends that I met, and I feel lucky to have them during this journey. Without them, life could be much more tedious and difficult for me.

Preface and Contributions of Authors

This thesis is manuscript-based and consists of two articles that published on peer-reviewed journals and two unpublished manuscripts of the original studies of the authors. The authorship and contributions of authors are described below (* denotes the corresponding author):

1. **Single-walled black phosphorus nanotube as a superior gas sensor: Compared with monolayer black phosphorus**, to be submitted.

By: Pengfei Ou, Xiao Zhou, Yiqing Chen, Cheng Chen, Fanchao Meng, and Jun Song*

2. **Superior sensing properties of black phosphorus as gas sensors: A case study on the volatile organic compounds**, *Advanced Theory and Simulations*, **2019**, *2*, 1800103.

By: Pengfei Ou, Pengfei Song, Xinyu Liu, and Jun Song*

3. **Single molybdenum center supported on N-doped black phosphorus as an efficient electrocatalyst for nitrogen fixation**, *Nanoscale*, **2019**, *11*, 13600-13611.

By: Pengfei Ou, Xiao Zhou, Fanchao Meng, Cheng Chen, Yiqing Chen, and Jun Song*

4. **Electrical metal contacts to monolayer blue phosphorus: electronic and chemical properties**, to be submitted.

By: Pengfei Ou, Guoqiang Lan, Yiqing Chen, Xiao Zhou, Cheng Chen, Fanchao Meng, and Jun Song*

Author contributions: For the above four manuscripts, PO and JS conceived the ideas; PO performed all the first-principles calculations under the direction of JS; PO wrote the manuscripts and JS revised the texts. For paper 2, PS and XL assisted in conceiving the idea and analyzing the data from experimental perspective. For other papers, CC, YC, GL, FM and XZ offered technical assistance and fruitful discussion on the calculation results.

Table of Contents

List of Figures

List of Tables

Chapter 1 : Introduction

The fascinating properties of two-dimensional (2D) nanomaterials have stimulated the rapid expansion of the family of 2D nanomaterials. Starting from the wonder material graphene from mechanical exfoliation in 2004,[1] a wide variety of 2D nanomaterials have been reported, followed by the discovery of the most prominent hexagonal boron nitride (h-BN),[2] transition metal dichalcogenides (TMDs),[3] MXenes,[4] and black phosphorus (black P),[5] among others. Black P garnered extensive attention after its nanosheet was first fabricated[6] and it has been demonstrated to exhibit various appealing characteristics, including the thickness-dependent direct band gap changing from 0.91 eV for monolayer to 0.28 eV for five-layer,[7] mobility as high as ~1,000 $cm^2 V^{-1} s^{-1}$,[5] thickness-dependent on/off ratio of up to 10^4,[6] and strong in-plane anisotropy.[8] Closely related to black P, another P allotrope, blue P was predicted by first-principles calculations and suggested to share similar thermodynamic stability with black P.[9-10] Unlike black P, blue P has a layered buckled structure with an indirect band gap varying from ~3 eV[9, 11] for monolayer to ~2 eV for its bulk form.[10] The fascinating properties of 2D blue P are mostly from theoretical predictions, including mobility of up to ~3×10^5 $cm^2 V^{-1} s^{-1}$,[11] an anisotropic thermal conductivity along the zigzag direction,[12] as well as superconductivity above 20 K by metal intercalations.[13]

Collectively, the available fabrication techniques of 2D black/blue P can be categorized into top-down (e.g., mechanical exfoliation,[6, 14] liquid-phase exfoliation,[15-20] etc.) isolation and bottom-up (e.g., chemical vapor deposition (CVD),[21-23] molecular beam epitaxy (MBE),[23] etc.) synthesis, within which the mechanical exfoliation and CVD are two major techniques that favored by the researchers. Moreover, the enormous interests on 2D nanomaterials have driven significant and continuous development in those fabrication techniques.[21-23] The advancement of growth techniques has further facilitated and motivated great efforts from researchers to study the physical and chemical properties of 2D black/blue P

experimentally and theoretically. To date, 2D black/blue P has been reported to cover a board range of applications in various fields, such as field-effect transistors,[5, 24-25] spintronics,[26-27] optoelectronics,[8, 28] photodetectors,[29-30] batteries,[31-32] and solar cells.[33] Among these applications, 2D black/blue P are particularly promising in various sensing applications due to their strong in-plane anisotropy, along with their higher surface-to-volume ratio and larger molecular adsorption energy compared to other 2D nanomaterials,[34-35] stemmed from their puckered or buckled structure. Their chemical sensing capabilities range from gas,[17, 34, 36-41] humidity,[42-45] metal ions,[46] H_2O_2,[47] immunoglobulin G (IgG),[48-49] to myoglobin (Mb),[50] etc. On the other hand, 2D black/blue P is considered as one of the most promising candidates to solve the worldwide energy crisis by using them as photocatalysts under ambient conditions,[51] including hydrogen evolution and water splitting,[52-55] carbon dioxide reduction,[56] and nitrogen fixation,[57-58] etc.

The goal of this thesis is to computational exploit and understand the unique properties of black/blue P and further explore their potential applications, with particular focus on gas sensing and electrocatalysis. Through our studies, we elucidated the roles of structural derivatives, growth substrates, defects, and dopants, therefore, accordingly provided theoretical predictions and mechanistic insights toward synthesizing and designing black/blue P for resolving challenges that existed for their target applications. The objectives of the thesis are specified as follows:

1. Examine the structural derivative and the curvature effect of single-walled black P nanotubes on the sensing performance towards common toxic gases;
2. Theoretical explore the capability of chemical sensing the volatile organic compounds by using monolayer black P;
3. Activate the large-area basal plane of 2D black/blue P for electrochemical NRR by creating the single-atom center near the defects;

4. Explore the metal substate induced effects on the physical and chemical properties of 2D black/blue P;
5. Tune 2D black/blue P into an optimal HER photocatalyst by metal substrate coupling.

The calculation results achieved from the above objectives are included in Chapters 4-7 of the thesis. To be more specific:

1. Chapter 4 compared the adsorption capability of single-walled black P nanotube and monolayer black P towards sensing the common toxic gases through first-principles calculations. The curvature effect in controlling the adsorption sensitivity was clarified by varying the nanotubes with a series of diameters.
2. Chapter 5 examined the potential application of 2D black P on the chemical sensing of volatile organic compounds using first-principles calculations and non-equilibrium Green's function formalism. The key characteristics of a VOC sensor, including the voltage-current characteristics, response, and recovery time were analyzed.
3. Chapter 6 studied single molybdenum centers supported on 2D black P doped by nitrogen, serving as an efficient electrocatalyst for the nitrogen reduction reaction. The ultrahigh catalytic activity was confirmed by analyzing the free energy diagram, and the competing hydrogen evolution reaction was also demonstrated to be suppressed on these single molybdenum centers.
4. Chapter 7 explored the contact nature (Schottky or ohmic contact, n- or p-type) of heterojunctions between the transition metal and 2D blue P. The intrinsic reasons for different contact types were clarified by quantitatively comparing various interfacial properties. The metal substrates were also found to significantly enhance the binding strength of hydrogen and render 2D blue P a more optimal HER electrocatalyst.

1.1 References

(1) Novoselov, K. S.; Geim, A. K.; Morozov, S. V.; Jiang, D.; Zhang, Y.; Dubonos, S. V.; Grigorieva, I. V.; Firsov, A. A., Electric Field Effect in Atomically Thin Carbon Films. *Science* **2004**, *306*, 666-669.

(2) Li, L. H.; Chen, Y., Atomically Thin Boron Nitride: Unique Properties and Applications. *Adv. Funct. Mater.* **2016**, *26*, 2594-2608.

(3) Splendiani, A.; Sun, L.; Zhang, Y.; Li, T.; Kim, J.; Chim, C.-Y.; Galli, G.; Wang, F., Emerging Photoluminescence in Monolayer MoS_2. *Nano Lett.* **2010**, *10*, 1271-1275.

(4) Naguib, M.; Mochalin, V. N.; Barsoum, M. W.; Gogotsi, Y., 25th Anniversary Article: Mxenes: A New Family of Two-Dimensional Materials. *Adv. Mater.* **2014**, *26*, 992-1005.

(5) Li, L.; Yu, Y.; Ye, G. J.; Ge, Q.; Ou, X.; Wu, H.; Feng, D.; Chen, X. H.; Zhang, Y., Black Phosphorus Field-Effect Transistors. *Nat. Nanotechnol.* **2014**, *9*, 372-377.

(6) Liu, H.; Neal, A. T.; Zhu, Z.; Luo, Z.; Xu, X.; Tománek, D.; Ye, P. D., Phosphorene: An Unexplored 2D Semiconductor with a High Hole Mobility. *ACS Nano* **2014**, *8*, 4033-4041.

(7) Qiao, J.; Kong, X.; Hu, Z.-X.; Yang, F.; Ji, W., High-Mobility Transport Anisotropy and Linear Dichroism in Few-Layer Black Phosphorus. *Nat. Commun.* **2014**, *5*, 4475.

(8) Xia, F.; Wang, H.; Jia, Y., Rediscovering Black Phosphorus as an Anisotropic Layered Material for Optoelectronics and Electronics. *Nat. Commun.* **2014**, *5*, 4458.

(9) Zhu, Z.; Tománek, D., Semiconducting Layered Blue Phosphorus: A Computational Study. *Phys. Rev. Lett.* **2014**, *112*, 176802.

(10) Guan, J.; Zhu, Z.; Tománek, D., Phase Coexistence and Metal-Insulator Transition in Few-Layer Phosphorene: A Computational Study. *Phys. Rev. Lett.* **2014**, *113*, 046804.

(11) Xiao, J.; Long, M.; Zhang, X.; Ouyang, J.; Xu, H.; Gao, Y., Theoretical Predictions on the Electronic Structure and Charge Carrier Mobility in 2D Phosphorus Sheets. *Sci. Rep.* **2015**, *5*, 9961.

(12) Jain, A.; McGaughey, A. J., Strongly Anisotropic in-Plane Thermal Transport in Single-Layer Black Phosphorene. *Sci. Rep.* **2015**, *5*, 8501.

(13) Zhang, J.-J.; Dong, S., Prediction of above 20 K Superconductivity of Blue Phosphorus Bilayer with Metal Intercalations. *2D Mater.* **2016**, *3*, 035006.

(14) Castellanos-Gomez, A.; Vicarelli, L.; Prada, E.; Island, J. O.; Narasimha-Acharya, K.; Blanter, S. I.; Groenendijk, D. J.; Buscema, M.; Steele, G. A.; Alvarez, J., Isolation and Characterization of Few-Layer Black Phosphorus. *2D Mater.* **2014**, *1*, 025001.

(15) Brent, J. R.; Savjani, N.; Lewis, E. A.; Haigh, S. J.; Lewis, D. J.; O'Brien, P., Production of Few-Layer Phosphorene by Liquid Exfoliation of Black Phosphorus. *Chem. Commun.* **2014**, *50*, 13338-13341.

(16) Yasaei, P.; Kumar, B.; Foroozan, T.; Wang, C.; Asadi, M.; Tuschel, D.; Indacochea, J. E.; Klie, R. F.; Salehi-Khojin, A., High-Quality Black Phosphorus Atomic Layers by Liquid-Phase Exfoliation. *Adv. Mater.* **2015**, *27*, 1887-1892.

(17) Hanlon, D.; Backes, C.; Doherty, E.; Cucinotta, C. S.; Berner, N. C.; Boland, C.; Lee, K.; Harvey, A.; Lynch, P.; Gholamvand, Z., Liquid Exfoliation of Solvent-Stabilized Few-Layer Black Phosphorus for Applications Beyond Electronics. *Nat. Commun.* **2015**, *6*, 8563.

(18) Kang, J.; Wood, J. D.; Wells, S. A.; Lee, J.-H.; Liu, X.; Chen, K.-S.; Hersam, M. C., Solvent Exfoliation of Electronic-Grade, Two-Dimensional Black Phosphorus. *ACS Nano* **2015**, *9*, 3596-3604.

(19) Zhao, W.; Xue, Z.; Wang, J.; Jiang, J.; Zhao, X.; Mu, T., Large-Scale, Highly Efficient, and Green Liquid-Exfoliation of Black Phosphorus in Ionic Liquids. *ACS Appl. Mater. Interfaces* **2015**, *7*, 27608-27612.

(20) Guo, Z.; Zhang, H.; Lu, S.; Wang, Z.; Tang, S.; Shao, J.; Sun, Z.; Xie, H.; Wang, H.; Yu, X. F., From Black Phosphorus to Phosphorene: Basic Solvent Exfoliation, Evolution of

Raman Scattering, and Applications to Ultrafast Photonics. *Adv. Funct. Mater.* **2015**, *25*, 6996-7002.
(21) Li, X.; Deng, B.; Wang, X.; Chen, S.; Vaisman, M.; Karato, S.-i.; Pan, G.; Lee, M. L.; Cha, J.; Wang, H., Synthesis of Thin-Film Black Phosphorus on a Flexible Substrate. *2D Mater.* **2015**, *2*, 031002.
(22) Smith, J. B.; Hagaman, D.; Ji, H.-F., Growth of 2D Black Phosphorus Film from Chemical Vapor Deposition. *Nanotechnology* **2016**, *27*, 215602.
(23) Zhang, J. L.; Zhao, S.; Han, C.; Wang, Z.; Zhong, S.; Sun, S.; Guo, R.; Zhou, X.; Gu, C. D.; Yuan, K. D., Epitaxial Growth of Single Layer Blue Phosphorus: A New Phase of Two-Dimensional Phosphorus. *Nano Lett.* **2016**, *16*, 4903-4908.
(24) Buscema, M.; Groenendijk, D. J.; Blanter, S. I.; Steele, G. A.; Van Der Zant, H. S.; Castellanos-Gomez, A., Fast and Broadband Photoresponse of Few-Layer Black Phosphorus Field-Effect Transistors. *Nano Lett.* **2014**, *14*, 3347-3352.
(25) Banerjee, L.; Mukhopadhyay, A.; Sengupta, A.; Rahaman, H., Performance Analysis of Uniaxially Strained Monolayer Black Phosphorus and Blue Phosphorus *n*-MOSFET and *p*-MOSFET. *J. Comput. Electron.* **2016**, *15*, 919-930.
(26) Avsar, A.; Tan, J. Y.; Kurpas, M.; Gmitra, M.; Watanabe, K.; Taniguchi, T.; Fabian, J.; Özyilmaz, B., Gate-Tunable Black Phosphorus Spin Valve with Nanosecond Spin Lifetimes. *Nat. Phys.* **2017**, *13*, 888.
(27) Sun, M.; Tang, W.; Ren, Q.; Wang, S.-k.; Yu, J.; Du, Y., A First-Principles Study of Light Non-Metallic Atom Substituted Blue Phosphorene. *Appl. Surf. Sci.* **2015**, *356*, 110-114.
(28) Xie, J.; Si, M.; Yang, D.; Zhang, Z.; Xue, D., A Theoretical Study of Blue Phosphorene Nanoribbons Based on First-Principles Calculations. *J. Appl. Phys.* **2014**, *116*, 073704.
(29) Engel, M.; Steiner, M.; Avouris, P., Black Phosphorus Photodetector for Multispectral, High-Resolution Imaging. *Nano Lett.* **2014**, *14*, 6414-6417.
(30) Chen, X.; Lu, X.; Deng, B.; Sinai, O.; Shao, Y.; Li, C.; Yuan, S.; Tran, V.; Watanabe, K.; Taniguchi, T., Widely Tunable Black Phosphorus Mid-Infrared Photodetector. *Nat. Commun.* **2017**, *8*, 1672.
(31) Li, Q.-F.; Duan, C.-G.; Wan, X.; Kuo, J.-L., Theoretical Prediction of Anode Materials in Li-Ion Batteries on Layered Black and Blue Phosphorus. *J. Phys. Chem. C* **2015**, *119*, 8662-8670.
(32) Xiao, X.; Wang, M.; Tu, J.; Jiao, S., The Potential Application of Black and Blue Phosphorene as Cathode Materials in Rechargeable Aluminum Batteries: A First-Principles Study. *Phys. Chem. Chem. Phys.* **2019**, *21*, 7021-7028.
(33) Yang, Y.; Gao, J.; Zhang, Z.; Xiao, S.; Xie, H. H.; Sun, Z. B.; Wang, J. H.; Zhou, C. H.; Wang, Y. W.; Guo, X. Y., Black Phosphorus Based Photocathodes in Wideband Bifacial Dye-Sensitized Solar Cells. *Adv. Mater.* **2016**, *28*, 8937-8944.
(34) Kou, L.; Frauenheim, T.; Chen, C., Phosphorene as a Superior Gas Sensor: Selective Adsorption and Distinct *I–V* Response. *J. Phys. Chem. Lett.* **2014**, *5*, 2675-2681.
(35) Montes, E.; Schwingenschlögl, U., Superior Selectivity and Sensitivity of Blue Phosphorus Nanotubes in Gas Sensing Applications. *J. Mater. Chem. C* **2017**, *5*, 5365-5371.
(36) Abbas, A. N.; Liu, B.; Chen, L.; Ma, Y.; Cong, S.; Aroonyadet, N.; Köpf, M.; Nilges, T.; Zhou, C., Black Phosphorus Gas Sensors. *ACS Nano* **2015**, *9*, 5618-5624.
(37) Cui, S.; Pu, H.; Wells, S. A.; Wen, Z.; Mao, S.; Chang, J.; Hersam, M. C.; Chen, J., Ultrahigh Sensitivity and Layer-Dependent Sensing Performance of Phosphorene-Based Gas Sensors. *Nat. Commun.* **2015**, *6*, 8632.
(38) Cho, S. Y.; Lee, Y.; Koh, H. J.; Jung, H.; Kim, J. S.; Yoo, H. W.; Kim, J.; Jung, H. T., Superior Chemical Sensing Performance of Black Phosphorus: Comparison with MoS_2 and Graphene. *Advanced Materials* **2016**, *28*, 7020-7028.

(39) Cho, S.-Y.; Koh, H.-J.; Yoo, H.-W.; Jung, H.-T., Tunable Chemical Sensing Performance of Black Phosphorus by Controlled Functionalization with Noble Metals. *Chem. Mater.* **2017**, *29*, 7197-7205.
(40) Mayorga‐Martinez, C. C.; Sofer, Z.; Pumera, M., Layered Black Phosphorus as a Selective Vapor Sensor. *Angew. Chem. Int. Ed.* **2015**, *54*, 14317-14320.
(41) Sofer, Z.; Bouša, D.; Luxa, J.; Mazanek, V.; Pumera, M., Few-Layer Black Phosphorus Nanoparticles. *Chem. Commun.* **2016**, *52*, 1563-1566.
(42) Yasaei, P.; Behranginia, A.; Foroozan, T.; Asadi, M.; Kim, K.; Khalili-Araghi, F.; Salehi-Khojin, A., Stable and Selective Humidity Sensing Using Stacked Black Phosphorus Flakes. *ACS Nano* **2015**, *9*, 9898-9905.
(43) Erande, M. B.; Pawar, M. S.; Late, D. J., Humidity Sensing and Photodetection Behavior of Electrochemically Exfoliated Atomically Thin-Layered Black Phosphorus Nanosheets. *ACS Appl. Mater. Interfaces* **2016**, *8*, 11548-11556.
(44) Zhu, C.; Xu, F.; Zhang, L.; Li, M.; Chen, J.; Xu, S.; Huang, G.; Chen, W.; Sun, L., Ultrafast Preparation of Black Phosphorus Quantum Dots for Efficient Humidity Sensing. *Chem.: Eur. J* **2016**, *22*, 7357-7362.
(45) Late, D. J., Liquid Exfoliation of Black Phosphorus Nanosheets and Its Application as Humidity Sensor. *Microporous Mesoporous Mater.* **2016**, *225*, 494-503.
(46) Li, P.; Zhang, D.; Liu, J.; Chang, H.; Sun, Y. e.; Yin, N., Air-Stable Black Phosphorus Devices for Ion Sensing. *ACS Appl. Mater. Interfaces* **2015**, *7*, 24396-24402.
(47) Yan, S.; Wang, B.; Wang, Z.; Hu, D.; Xu, X.; Wang, J.; Shi, Y., Supercritical Carbon Dioxide-Assisted Rapid Synthesis of Few-Layer Black Phosphorus for Hydrogen Peroxide Sensing. *Biosens. Bioelectron.* **2016**, *80*, 34-38.
(48) Mayorga-Martinez, C. C.; Mohamad Latiff, N.; Eng, A. Y. S.; Sofer, Z. k.; Pumera, M., Black Phosphorus Nanoparticle Labels for Immunoassays via Hydrogen Evolution Reaction Mediation. *Anal. Chem.* **2016**, *88*, 10074-10079.
(49) Chen, Y.; Ren, R.; Pu, H.; Chang, J.; Mao, S.; Chen, J., Field-Effect Transistor Biosensors with Two-Dimensional Black Phosphorus Nanosheets. *Biosens. Bioelectron.* **2017**, *89*, 505-510.
(50) Kumar, V.; Brent, J. R.; Shorie, M.; Kaur, H.; Chadha, G.; Thomas, A. G.; Lewis, E. A.; Rooney, A. P.; Nguyen, L.; Zhong, X. L., Nanostructured Aptamer-Functionalized Black Phosphorus Sensing Platform for Label-Free Detection of Myoglobin, a Cardiovascular Disease Biomarker. *ACS Appl. Mater. Interfaces* **2016**, *8*, 22860-22868.
(51) Li, B.; Lai, C.; Zeng, G.; Huang, D.; Qin, L.; Zhang, M.; Cheng, M.; Liu, X.; Yi, H.; Zhou, C., Black Phosphorus, a Rising Star 2D Nanomaterial in the Post-Graphene Era: Synthesis, Properties, Modifications, and Photocatalysis Applications. *Small* **2019**, *15*, 1804565.
(52) Lei, W.; Mi, Y.; Feng, R.; Liu, P.; Hu, S.; Yu, J.; Liu, X.; Rodriguez, J. A.; Wang, J.-o.; Zheng, L., Hybrid 0D–2D Black Phosphorus Quantum Dots–Graphitic Carbon Nitride Nanosheets for Efficient Hydrogen Evolution. *Nano Energy* **2018**, *50*, 552-561.
(53) Zhu, M.; Sun, Z.; Fujitsuka, M.; Majima, T., Z‐Scheme Photocatalytic Water Splitting on a 2D Heterostructure of Black Phosphorus/Bismuth Vanadate Using Visible Light. *Angew. Chem. Int. Ed.* **2018**, *57*, 2160-2164.
(54) Gao, X.; Shen, Y.; Ma, Y.; Wu, S.; Zhou, Z., A Water Splitting Photocatalysis: Blue Phosphorus/g-GeC Van Der Waals Heterostructure. *Appl. Phys. Lett.* **2019**, *114*, 093902.
(55) Ren, K.; Wang, S.; Luo, Y.; Xu, Y.; Sun, M.; Yu, J.; Tang, W., Strain-Enhanced Properties of Van Der Waals Heterostructure Based on Blue Phosphorus and g-GaN as a Visible-Light-Driven Photocatalyst for Water Splitting. *RSC Adv.* **2019**, *9*, 4816-4823.

(56) Han, C.; Li, J.; Ma, Z.; Xie, H.; Waterhouse, G. I.; Ye, L.; Zhang, T., Black Phosphorus Quantum Dot/gC_3N_4 Composites for Enhanced CO_2 Photoreduction to Co. *Sci. China Mater.* **2018**, *61*, 1159-1166.
(57) Zhang, L.; Ding, L. X.; Chen, G. F.; Yang, X.; Wang, H., Ammonia Synthesis under Ambient Conditions: Selective Electroreduction of Dinitrogen to Ammonia on Black Phosphorus Nanosheets. *Angew. Chem.* **2019**, *131*, 2638-2642.
(58) Qiu, P.; Xu, C.; Zhou, N.; Chen, H.; Jiang, F., Metal-Free Black Phosphorus Nanosheets-Decorated Graphitic Carbon Nitride Nanosheets with C–P Bonds for Excellent Photocatalytic Nitrogen Fixation. *Appl. Catal. B* **2018**, *221*, 27-35.

Chapter 2 : Literature Review

Chapter 2 summarizes the recent research progress in two-dimensional (2D) black phosphorus (black P)/blue P relevant to the studies presented in this thesis. Particularly it is worth noting that here the literature review concentrates on the fundamental properties, fabrication techniques, and potential applications of 2D black/blue P, in accordance with the focus of the thesis. The following sections are organized as the follows: first, the fundamental structures and properties of 2D black/blue P are summarized, followed by reviewing of the state-of-the-art preparation (i.e., the top-down and bottom-up synthesis) of 2D black/blue P, together with relevant recent theoretical studies of growth mechanisms. Finally, studies on the multifarious applications based on monolayer and multilayer black/blue P will be surveyed, including electronic and optoelectronic devices, solar to energy conversion, and more importantly sensors and photocatalysis applications.

2.1 Structure and properties

2.1.1 Phosphorus allotropes

Phosphorus is a non-metallic element and prominent for its diversity in the allotropes, e.g., white phosphorus (white P), red phosphorus (red P), and black phosphorus (black P).[1] White P, the most reactive form of phosphorus with a metastable tetrahedral P_4 molecular structure (the bond angle is 60º rather than 109.28º), was found in 1669 by Henning Brand.[2] Nowadays, three different structures are known for white P (i.e., α-, β-, and γ-P_4),[3-4] they are toxic, highly reactive, and can be applied as the starting material to synthesize other phosphorus allotropes. After the discovery of white P, a more stable amorphous polymer of red P was first prepared in 1848, where white P was treated at about 300 ºC.[5] The structure of the synthesized red P is constructed from a polymeric network of various amorphous phosphorus building units (see Figure 2.1), and five different types of crystalline forms that exhibit a reddish color (types

I-V) have been found to be existed for red P.[3], [6-11] In 2005, 1D red P nanowires were fabricated by Ruck et al. by heating the amorphous red P in an evacuated capsule at approximate 570 ºC for a couple of days.[8] It was also confirmed that the crystal structure of crystalline red P is fibrous type (type IV) and closely related to that of Hittorf's phosphorus, and therefore they denoted its structure as P_8 and P_9, since it consists double tubes formed from eight or nine P atoms (Figure 2.1c). In addition, Hittorf first synthesized violet phosphorus (violet P) in 1865, which also belongs to the category of red P.[12] Similar to fibrous red P (type IV), violet P (type V) is also a tubular structure that linked together by a phosphorus chain of P_8 and P_9 cages.[13-14] These tubes are perpendicularly oriented to one another between different layers in violet P, however, in fibrous red P, the tubes are arranged as paralleled double tubes that link to each other between layers (Figure 2.1d).[13] Besides, Böcker and Häser predicted a variety of P nanorods by *ab-initio* techniques and named them by the repeating units, i.e., [P8]P4(4)[, [P10]P2[, and [P12(4)]P2[(Figure 2.1e).[15]

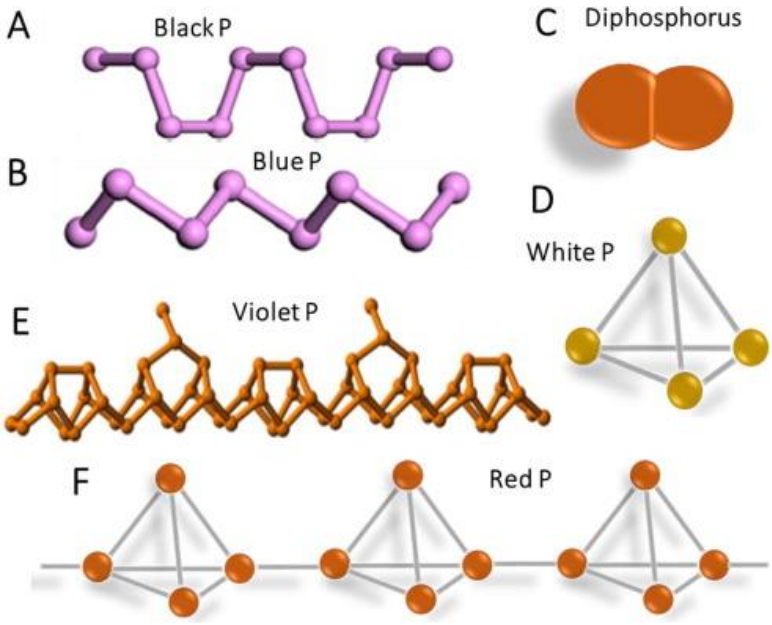

Figure 2.1 Atomic structures of selected polytypes for layered and tubular phosphorus allotropes: (a) orthorhombic black P, (b) blue P, (c) fibrous red P, (d) violet P, and (e) P nanorods.[16] [Figures adapted with permissions]

Among all allotropes, black P is thermodynamically most stable. The bulk form of black P is stacked by multiple monolayer, each composed of orthorhombic puckered structure, interacting via weak van der Waals (vdW) interactions with an interlayer distance of 5.5 Å in the perpendicular direction with each of the layers built of P_6 rings with sp^3 hybridization (Figure 2.1a).[17] The non-planar puckered structure with two unidentical bond angles of 96.3º and 102.1º also results in two inequivalent bond lengths of 2.22 and 2.24 Å for the in-plane and out-plane bonds, respectively.[18] The in-plane bond connects the neighboring P atoms in the same plane, whereas the out-plane bond links the P atoms in the upper or lower layer of P atoms. Similar to graphene, two featured directions are also recognized in black P, i.e., armchair and zigzag directions, with the lattice constants being 4.58 and 3.32 Å along each of the directions, respectively.[19]

In addition to those allotropes mentioned above, another particular allotrope, blue phosphorus (blue P), was predicted recently to share the layered structure and exhibit equally thermodynamic stability with the black P allotrope with only 2 meV $atom^{-1}$ higher in cohesive energy by using density functional theory (DFT) calculations.[20-21] Unlike black P, P atoms in blue P are covalently bonded in a graphene-like honeycomb structure in the sp^2 hybridization, with the in-plane lattice constants being both 3.33 Å along with the armchair and zigzag directions.[20] Despite these differences, the layers in blue P are also held by weak vdW interactions with an interlayer distance of 5.63 Å. Therefore, the layered structure of black and blue P promises the accessibility of applying “top-down” procedures, such as mechanical or liquid-phase exfoliation, to fabricate the monolayer from their bulk forms.

Black P and blue P are the main subjects of research focus in this thesis. Consequently, hereafter the literature reviews will mainly concentration on them.

2.1.2 Electronic properties

Understanding the electronic structure and band gap of 2D black/blue P is essential for their design of high-performance sensors and photocatalysts. Unlike MoS_2, which displays an indirect-direct band gap transition from its bulk form to monolayer, black P exhibits an invariably direct band gap in both multilayer and monolayer according to the study by Wu et al. (Figure 2.2a).[22] The theoretically predicted values were between 1.51 and 2.00 eV for monolayer black P, in reasonable agreement with those from the experimental measurements, ranging from 1.00 to 1.75 eV (summarized in Table 2.1).[19, 23-30] The discrepancy between theoretical calculations and experimental measurements is ascribed to the fact that the thickness of samples is difficult to be measured precisely. Despite the discrepancy, same trend is observed both theoretically and experimentally, i.e., the band gap monotonically decreasing with the increasing number of layers for black P (Table 2.1). The increasing layer leads to the band splitting at Γ point near the band gap, which in turn results in a decrease in the band gap.[23] Additionally, the conduction band (CB) and valence band (VB) for monolayer black P are dominantly contributed by the p_z states rather than p_y, which is the exact opposite to the case of graphene as p_y states providing the largest contribution in the CB and VB (Figure 2.2b).

Table 2.1 Band gap of multilayer black P obtained from various methods, including band gap from DFT and optical absorption spectra, and the optical band gap from photoluminescence.

Number of layers	1	2	3	4	5	Bulk
DFT (band gap, eV)[19]	1.51	0.98	0.80	0.66	0.59	0.36
DFT (band gap, eV)[23]	1.60	1.01	0.68	0.46	/	0.10
DFT (band gap, eV)[24]	2.00	1.32	1.06	/	/	0.29
Optical absorption spectra (band gap, eV)[25]	/	1.88	1.43	1.19	1.04	0.33
Optical absorption spectra (band gap, eV)[26]	1.38	1.23	1.05	0.85	0.72	/
Optical absorption spectra (band gap, eV)[27]	1.73	1.15	0.83	/	/	0.35
Photoluminescence (optical band gap, eV)[28]	1.00	0.68	0.53	0.48	/	0.30
Photoluminescence (optical band gap, eV)[29]	/	1.29	0.98	0.88	0.80	/
Photoluminescence (optical band gap, eV)[30]	1.75	1.29	0.97	0.84	0.80	/

However, blue P is an indirect band gap semiconductor with a wide band gap of approximate 2 eV[20], [31] and 2.73,[31] or 2.62 eV[32] that predicted by the hybrid functional of HSE06,[33] with the CBM located between the Γ–M direction and VBM between K–Γ direction. Similar to black P, the band gap of blue P is also inversely correlated to the thickness, and the band gap may vary by up to a factor of 2 if the thickness is altered.[20] The dependence between the band gap and thickness of multilayer blue P is a result of interlayer band dispersion near the Fermi level.

Aside from thickness variation, molecular doping,[34] strain engineering (compressive or tensile strains),[35-36] chemical functionalization,[37] and external electric field[31], [38] are also effective methods to modulate their band gaps, which promise to further expand the applications of 2D black/blue P.

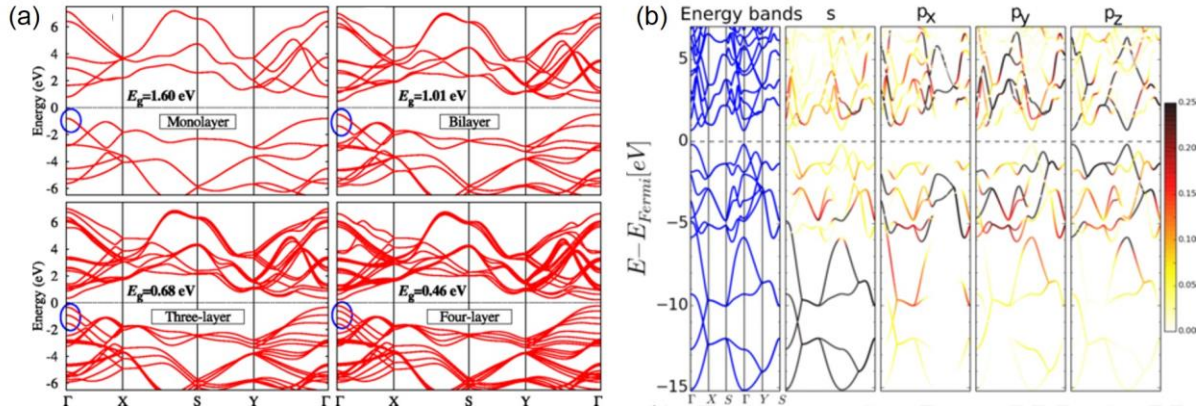

Figure 2.2 (a) Calculated band structure for one- to four-layer black P by using *GW* approximation. Blue circles indicate the band splitting at Γ point close to the band gap.[23] (b) Energy band diagram and orbital decomposed ones along the high-symmetry path with the color bar indicates the contribution of each *s* and *p* orbital.[39] [Figures adapted with permissions]

2.1.3 Optical adsorption properties

Multilayer black P exhibits a tunable band gap and therefore a wide range of light absorption from ultraviolent to infrared (Figure 2.3a),[40] bridging the gap between semi-metallic graphene and semiconducting transition metal dichalcogenides (TMDs) with a comparatively large band gap. Enormous efforts, both theoretical and experimental, have been

carried out to examine the optical absorption properties of single- and few-layer black P, which have been demonstrated to be direction-dependent (e.g., armchair and zigzag) due to intrinsic anisotropy of monolayer black P.22, 24, 41The symmetry-forbidden selection rule, i.e., an inversion symmetry and mirror reflection symmetry (M_y) for the crystal structure of monolayer black P only along the zigzag direction, which renders the high anisotropy of optical absorption properties.42-43 The optical adsorption spectra of few-layer and bulk black P was predicted by Qiao et al., when linearly polarized light is incident along the armchair and zigzag directions.19 Strong linear dichroism was observed from the results, namely, the band edge for the first peak falls quickly with the thickness for armchair direction (from 1.55 eV for monolayer to 0.46 eV for bulk black P). On the contrary, it only slightly falls along the zigzag direction with its peak found at 3.14 eV for 1-layer and remains at 2.76 eV for bulk black P (Figure 2.3b). The authors have proposed an experimental setup to measure the orientation of black P samples by using optical absorption spectroscopy (Figure 2.3b). When the light is incident along the perpendicular direction and linearly polarized in different directions, the orientation can be identified by rotating the sample and monitoring the optical absorption signals. Ling et al. also demonstrated that the armchair direction absorbs more polarized light than the zigzag by computing the absorption coefficient and measuring the absorbance spectra.44

On the other hand, Mogulkoc et al. examined the optical absorption properties of few-layer blue P theoretically by extracting the hopping parameters of tight-binding Hamiltonian.45 Monolayer and bilayer blue P are almost transparent when light is polarized perpendicularly to the surface and between 0 to 2 eV. Similar to black P, an anisotropic behavior of optical absorption properties was also suggested in blue P, which originated from the decreasing low energy photons in its bilayer and 2D nature of its atomic structure.

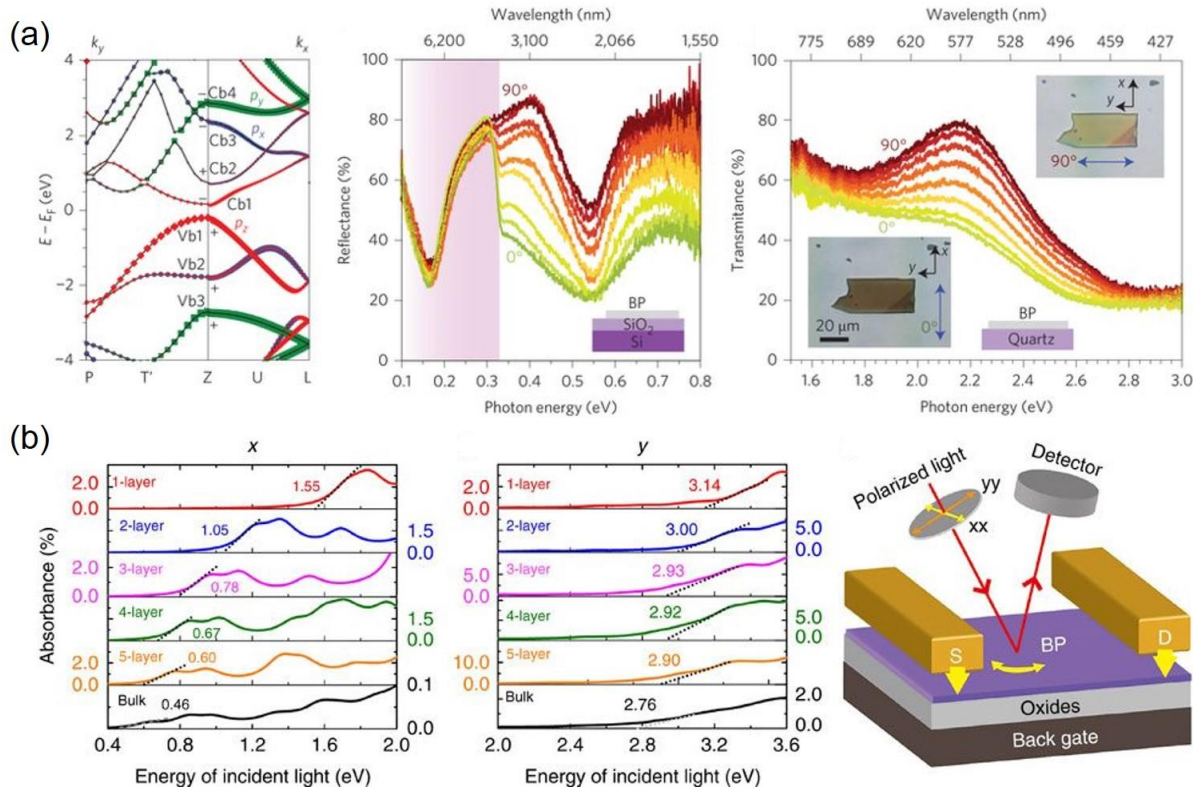

Figure 2.3 (a) Left: Orbital decomposed band dispersion of bulk black P. The parity of the bands is indicated by '+' and '−'. Blue, red, and green lines denote band dispersion from the p_x, p_y, and p_z orbitals. Middle and right: Evolution of reflection and polarization-dependent absorption in the infrared (middle) and visible light (right) spectral regime with the linearly polarized incident light along different directions (0º and 90º indicate armchair and zigzag directions, respectively). The purple shaded area indicates the energies above the band gap.[40] (b) Left and middle: Optical absorbance of one- to five-layer and bulk black P when light is incident along the perpendicular direction and polarized along armchair (x) (left) and zigzag directions (y) (middle), respectively. Right: Schematic of the experimental setup to detect the orientation of as-synthesized samples by using the optical absorption spectroscopy, to facilitate the utilization of highest-mobility direction of a multilayer black P in the FETs.[19] [Figures adapted with permissions]

2.1.4 Charge mobility

High charge mobility of black/blue P is one of the excellent intrinsic properties which attract enormous attention, and giant efforts have been devoted to implementing them into practical applications. Aside from the anisotropic electronic and optical absorption properties, black/blue P also exhibit anisotropic behavior in charge mobility owing to their anisotropic effective mass.[46-47] For black P, the effective masses of electrons and holes along the zigzag direction (0.14 and 0.13 m_e) is an order of magnitude smaller than those of armchair direction

(1.23 and 13.09 m_e), which suggests that the charge carrier transport is much more favorable along the armchair direction (Figure 2.4a).[48] However, blue P shows the opposite scenario, the carrier transport would preferentially happen along the zigzag direction due to its three times larger effective masses, compared to those of armchair direction.[47] Based on *ab-initio* calculations, the electron mobility of black P is 1,100-1,140 $cm^2\ V^{-1}\ s^{-1}$ along the armchair direction, which is significantly higher than that of zigzag direction (~80 $cm^2\ V^{-1}\ s^{-1}$).[27] In contrast, the hole mobility is 640-700 $cm^2\ V^{-1}\ s^{-1}$ in armchair direction, being 40 times smaller than that in another direction (10,000-26,000 $cm^2\ V^{-1}\ s^{-1}$). It is noteworthy that the experimentally measured hole mobilities are 600 and 400 $cm^2\ V^{-1}\ s^{-1}$ along the armchair and zigzag directions for black P respectivley, which are extraordinarily smaller than theoretical results, which reveals a significant space for improvement (Figure 2.4b).[49] Based on previous studies, various methods have been applied to modulate the charge mobility of black/blue P, such as layer adjustment and strain engineering. For example, Liu et al. found that the charge mobility is dependent on the varying thickness, that is, the charge mobility increases with the increasing thickness except for the monolayer black P (Figure 2.4c).[28] Peng et al. found that the effective masses also rely on the applied compressive stress. The characteristics of effective masses differ with the strains applied in varying degrees and along different directions, and therefore exerting a notable effect on the carrier mobility.[50] Strain engineering also has been confirmed to be an effective method to regulate the charge mobilities of blue P nanoribbons and nanotubes by Xiao et al. (Figure 2.4d).[51]

Overall, black/blue P potentially overcome the limitations of TMDs and graphene, which intrinsically possess not only tunable band gap and high carrier mobility, but also intriguing optical absorption properties. Therefore, 2D black/blue P has been considered as the promising materials that can be employed in various applications, such as channel material in

a gas sensor, and photocatalysts to catalyze hydrogen evolution reaction (HER) and nitrogen reduction reaction (NRR), which will be explicitly discussed in Section 2.3.

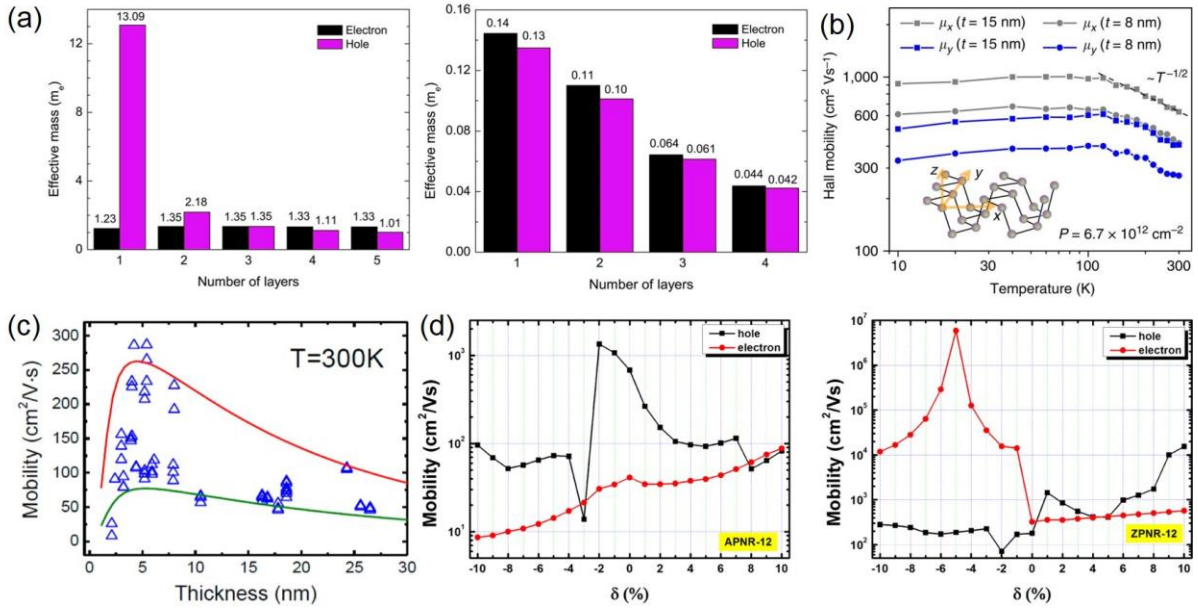

Figure 2.4 (a) Calculated effective masses of electron (black) and hole (purple) along zigzag (left) and armchair (right) directions with respect to the thickness of multilayer black P.[48] (b) Hall mobilities measured for black P with a thickness of 8 and 15 nm along the armchair (*x*) and zigzag (*y*) directions, respectively (the hole doping concentration is 6.7×10^{12} cm^{-2}).[49] (c) Field-effect mobilities in multilayers black P with varying thickness.[28] (d) Charge mobilities summary as a function of applied strains for blue P nanoribbons.[51] [Figures adapted with permissions]

2.2 Synthesis of 2D black/blue P

Effective and controlled fabrication methods have always been key in the exploration and application of 2D nanomaterials. Therefore, the discovery of oversimplified, facile, and environment-friendly synthetic process for 2D nanomaterials is developed to be a vital task, which is significant for the study of their electronic, optical, physical, and chemical properties. To date, the fabrication methods of 2D black/blue P can be classified mainly into two categories: the top-down and bottom-up synthesis.

2.2.1 Top-down techniques

The nature of layered structure and weak interlayer interaction of 2D nanomaterials renders them possible to be exfoliated by the top-down synthesis.[52] With its weak vdW

interactions between adjacent layers which was shown to be only 151 meV from multilevel quantum chemical calculations[53], which indicates that 2D black P can also be exfoliated by this strategy from bulk black P. In 2014, mono- or few-layer black P was first produced by a scotch-tape-based microcleavage method,[28] in which scotch tapes were repeatedly used many times to detach the nanoflakes off the bulk crystal and subsequently transferred onto the Si/SiO_2 substrate. This results in high-quality monolayer black P but yields a small quantity of the material, only limited for laboratory use. Additionally, the adhesive residue will cause the contamination of as-prepared black P thin films, which is another shortcoming. Therefore, to optimize this conventional route, a modified mechanical exfoliation method of the adhesive tape coupled with viscoelastic polydimethylsiloxane (PDMS) was developed by Castellanos-Gomez et al, which substantially enhance the yield and reduces the contamination of the synthesized nanoflakes.[54] Nonetheless, the multistep operation of adhesion and peeling in the mechanical exfoliation method renders uncontrollable thickness and size of samples, which requires other experimental techniques for a quantitative estimation, for instance, Raman spectroscopy[55] or optical microscopy.[27] Besides, this method can be only applied to a chunk of layered material with fairly low throughput and results in micrometer-sized black P fragments, which limits its practical application of large-scale devices.

Another top-down synthesis method, liquid-phase exfoliation, has been extensively applied to peel off the monolayer from the layered bulk crystals for various 2D nanomaterials, including graphene,[56] hexagonal boron nitride (h-BN),[57] g-C_3N_4,[58] and TMDs.[59] In this technique, ultrasonic energy is used to break down the vdW interactions between the stacking layers. The organic solvents that possess suitable surface energy are selected to broaden the interlayer distance and facilitate the delamination process.[43, 60] Liquid-phase exfoliation is a good technique for large-scale production of black P nanoflakes, however, the selection of organic solvents needs to be carefully taken due to the chemical reactivity of black P. The ideal

organic solvents should be anhydrous and oxygen-free that isolates the black P from oxygen and water, since the lone-pairs of P atoms in black P tend to react with the oxygen and water, leading to the surface degradation. In 2014, three- to five-layer high-purity black P nanosheets with a dimension of 200 × 200 nm^2 were successfully obtained in the solvent of N-methyl-2-pyrrolidone (NMP) via liquid-phase exfoliation, and 20 × 20 nm^2 monolayer and bilayer black P can also be gathered if exfoliation time is extended to 48 hours.[61] Ever since, considerable studies have been concentrated on the advancement of liquid-phase exfoliation for mass production of black P with controllable thickness and size, as well as high quality and good stability. Yasaei et al. found that the inert and polarized solvents (e.g., dimethylformamide (DMF) and dimethyl sulf-oxide (DMSO)) are suitable to synthesize atomically thin black P. The prepared nanoflakes are in the form of stable and uniform dispersions and exhibit excellent electrical properties compared to those from mechanical exfoliation.[26] Hanon et al. adopted liquid-phase exfoliation to produce large quantities of high-quality, multilayer black P nanosheets by choosing N-cyclohexyl-2-pyrrolidone (CHP) as the solvent, with controllable size and noticeable photoluminescence (PL).[62] Sresht et al. investigated the solvent-black P interactions between monolayer black P and a variety of organic solvents by using theoretical simulations, they found that highly crystalline black P can also be prepared in the solvent of isopropyl alcohol (IPA).[63] To substantially enhance the yield of liquid-phase exfoliation, stable and electronic-grade black P dispersions with high concentration (~0.4 mg mL^{-1}) were produced in the solvent of NMP by Kang et al. (Figure 2.5a).[64] As shown in Figure 2.5b, Zhao et al. manufactured highly stable and concentrated (up to 0.095 mg mL^{-1}) monolayer black P dispersions using ionic liquids rather than organic solvents. No obvious sedimentation and aggregation were observed on the prepared suspensions for one month in the ambient condition.[65] Additionally, Guo et al. designed a basic-NMP liquid-phase exfoliation method to prepare black P with high yield, controllable size and thickness, as well as remarkable water

stability in a mixed NaOH/NMP solvent (Figure 2.5c).[66] Therefore, a controllable and large-scale production of dispersions for multilayer black P can be realized by the facile and eco-friendly liquid-phase exfoliation, which consolidates the basis of in-situ studies and practical applications of black P.

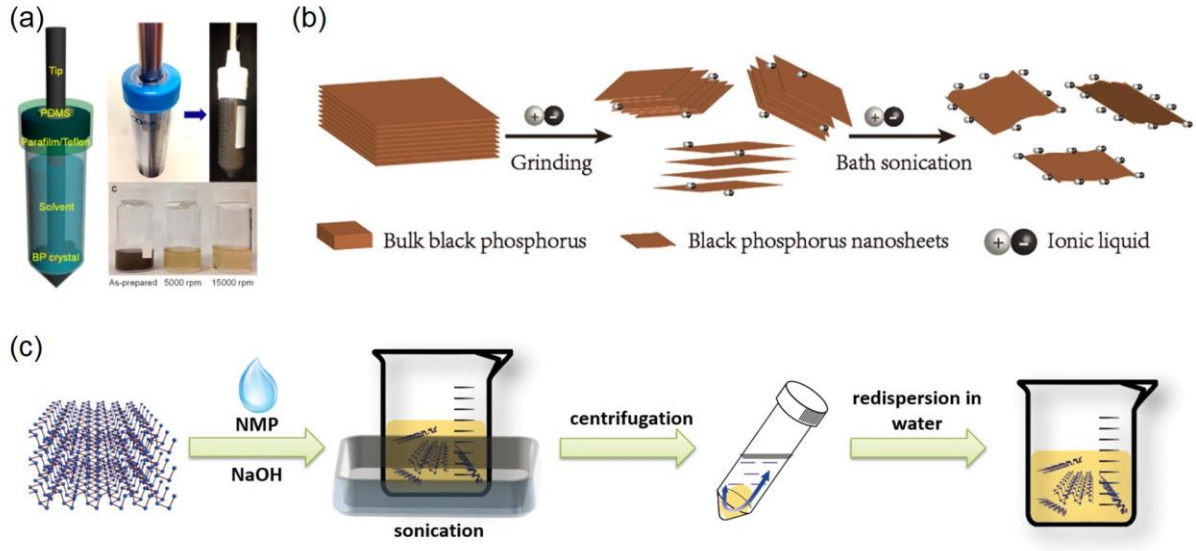

Figure 2.5 (a) Solvent exfoliation of black P by a sealed-tip ultrasonication system in organic solvents.[64] (b) Schematic of ionic liquid exfoliation of monolayer black P from the bulk black P.[65] (c) Schematic of a basic-NMP liquid-phase exfoliation method to fabricate monolayer black P (NMP = N-methyl-2-pyrrolidone).[66] [Figures adapted with permissions]

2.2.2 Bottom-up techniques

Bottom-up synthesis is another route of fabricating the 2D nanomaterials, which directly synthesize 2D nanoflakes at the atomic scale via chemical reactions that are dependent on the experimental conditions and precursors. The bottom-up synthetic methods include chemical vapor deposition (CVD) and molecular beam epitaxy (MBE), etc.

One particular bottom-up method that has seen extensive usage is the CVD.[67-68] During the past decade, CVD has been successfully employed to fabricate the stable and large-scale graphene with high yield, which also promises a great potential in synthesizing other kinds of 2D nanomaterials, such as h-BN and TMDs. Inspired by this, Li et al. in 2015 developed a scalable method to synthesize large-scale black P.[69] First, they deposited a thin red P film onto the polymer substrate by thermal deposition, followed by a subsequent

conversion from red P to black P at ambient temperature but with a high pressure (> 8 GPa), as shown in Figure 2.6a. The produced large-area (4 mm^2) black P thin film holds a thickness of approximately 40 nm, where the area of black P film can be controlled by scaling up the chamber size, meanwhile, the thickness is also tunable by varying the scale of holding time at 400 °C. Besides, large-area multilayers black P was successfully synthesized by in-situ CVD growth by first heating red P at 600 °C, and then heating the substrate that contains Sn/SnI_4 mineralizer and red P thin films to 900 °C under high pressure of 27.2 atm (Figure 2.6b).[70] The as-synthesized black P with a variable thickness of 3.4–600 nm and a large area of 0.35–100 μm^2 can be beneficial to the study of its intrinsic properties. More recently, monolayer blue P was successfully synthesized with the aid of MBE technique by Zhang et al. (Figure 2.6c).[71] Monolayer blue P was epitaxially synthesized on clean Au(111) surface by using black P as the precursor, P atoms were deposited on a substrate by evaporation below 260 °C to make sure that P_4 molecules were condensed from their gas phase in the initial growth stage, rather than P_2 molecules. The average interlayer modulation in the optimized system is much smaller than the typical value of free-standing one, which suggests that monolayer blue P strongly interacts with Au(111) substrate.

To shed light on the mechanism for the bottom-up synthesis of black/blue P, DFT calculations were performed to elucidate the interactions between the black/blue P and the growth substrates. Zeng et al. suggested that the epitaxial growth of monolayer blue P can be realized on GaN(001) substrate via a half-layer-by-half-layer mechanism, in which the GaN(001) substrate is first deposited by half layer of P atoms and then covered by the other half (Figure 2.7a).[72] The thermodynamic stability of as-synthesized monolayer blue P is further confirmed by the *ab-initio* molecular dynamics simulations. Motivated by the experimental synthesis of monolayer blue P on Au(111) substrate,[71] Han et al. theoretically examined the growth behavior and nucleation mechanism of P clusters on the surface of

Au(111).[73] The energy regarding the formation of blue P clusters monotonically reduces with an increasing number of P atoms (Figure 2.7b), which indicates an energetically preference on the formation of monolayer blue P. In contrast, the P cluster that represents the formation of black P showed less energetically preference, as evidenced by much higher formation energy than those of blue P clusters.

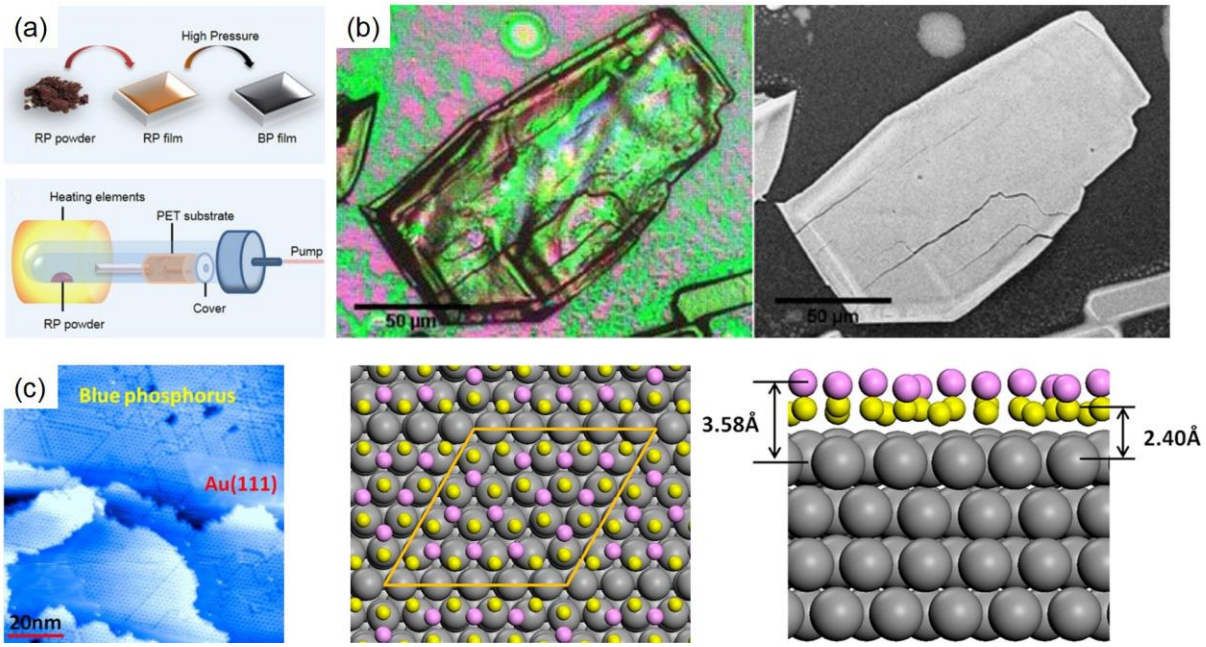

Figure 2.6 (a) Schematic illustrations of fabrication process (up) and apparatus (down) for the large-scale synthesis of black P thin films.[69] (b) A bright field image (left) and a SEM image (right) for a 600 nm-thick black P.[70] (c) Left: High-resolution scanning tunneling microscopy (STM) image for monolayer blue P epitaxially synthesized on Au(111) surface along with the top (middle) and side views (right) of the atomic geometries.[71] [Figures adapted with permissions]

To further discover the appropriate substrate for the selective CVD growth of black/blue P, Qiu et al. investigated the 2D black/blue P on various metal substrates. Tin (Sn) was revealed to be a catalyst for the synthesis of black P, meanwhile, the majority of metal substrates can be also used as the substrates to synthesize the blue P.[74] Besides, Gao et al. also studied the interaction of P_{27} nanoflakes on pristine and modified h-BN as well as Cu(111) surfaces.[75] The black P nanoflake is broken down due to the strong interaction with Cu(111), whereas cannot be stabilized by the weak interaction with h-BN. An intermediate interaction

can be modulated by modifying the h-BN substrate, and thus the P_{27} nanoflake can preserve a stable structure of black P due to an increased edge reconstruction barrier. In this regard, the selective growth of black/blue P and other allotropes can be realized by choosing an appropriate growth substrate.

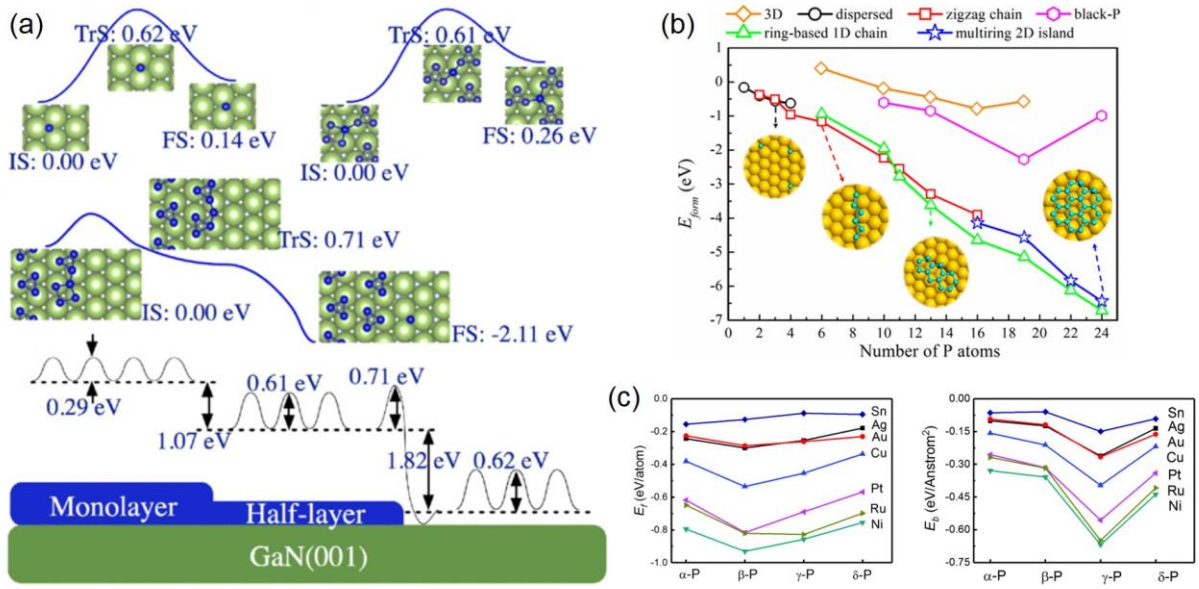

Figure 2.7 (a) Top: Diffusion barriers when one P atom adsorbed on the surface of a pristine GaN(001) (top left) and a GaN(001) that covered by half-layer P atoms (top right). Middle: Ehrlich-Schwoebel barrier when one P atom climb down the step of a pristine GaN(001) and GaN(001) that covered by half-layer P atoms. Bottom: Overview of the calculated diffusion barriers.[72] (b) Formation energy of P clusters with respect to the number of P atoms. Insets illustrate the corresponding atomic structures. (c) Calculated energies of formation (left) and binding (right) of monolayer black/blue P on different metal surfaces.[74] [Figures adapted with permissions]

2.3 Applications

2.3.1 Sensors

Black P layered nanomaterials have been reported in various sensing applications, such as gas,[62, 76-82] humidity,[83-86] and metal-ion sensing,[87] etc. Unlike most other 2D nanomaterials which show a flat surface morphology, the black P exhibits a puckered structure, offering higher surface-to-volume ratio. Thus, the adsorption strength between the molecule and host layer is maximized by a larger surface area, which has been demonstrated to be advantageous for the gas sensors for toxic NO_2,[76-79] H_2,[80] and CH_3OH.[81-82] In 2004, Kou

et al. first predicted that the monolayer black P can sense N-based gas molecules, where NH_3/NO_2 donate/accept the electrons to the host layer and reflect a reduced/increased current in the signal.[76] Besides, the current-voltage characteristics that determined from the non-equilibrium Green's function formalism turns out to be direction-dependent, corresponding to the anisotropic electronic structure of monolayer black P. Later on, Abbas et al. reported the first experimental realization of NO_2 gas sensor based on multilayer black P with excellent detection sensitivity down to 5 ppb.[77] More recently, Cho et al. performed a comparative study of chemical sensing performances of NO_2 between black P, MoS_2, and graphene by precisely controlling the size of these nanoflakes (approximate 400 nm^2).[79] The sensitivity and response time of black P are about 20 times higher and 40 times faster than the those of other 2D nanomaterials, when operating at the concentration level of 0.1-100 ppm (Figure 2.8a). In addition to NO_2, surface modifications of black P enabled it to be capable of detecting the low concentration of non-paramagnetic H_2 with high response amplitude by incorporating Pt into the surface.[80] Besides, the Au-incorporated black P exhibited high ambient stability and low noise baseline when applied as the channel material. Another type of black P-based gas sensor has also been developed by using the electrochemical impedance spectroscopy in the detection of CH_3OH.[81] The measured impedance phase suggests a linear dependence on the concentration of CH_3OH in the range between 390 and 1800 ppm. The relative standard deviation (RSD) of 18% from the experiments on various sensor devices indicated a good reproducibility, and the limit of detection (LOD) can be down to 28 ppm, much smaller the occupational exposure limit of 200 ppm. The device is also well selective to methanol sensing and can distinguish methanol from other interference vapor, such as water and ethanol. Even more significant, the black P sensor showed no evident degradation and maintained more than 90% of the original response for a 20-day period when exposed to 1140 ppm methanol.

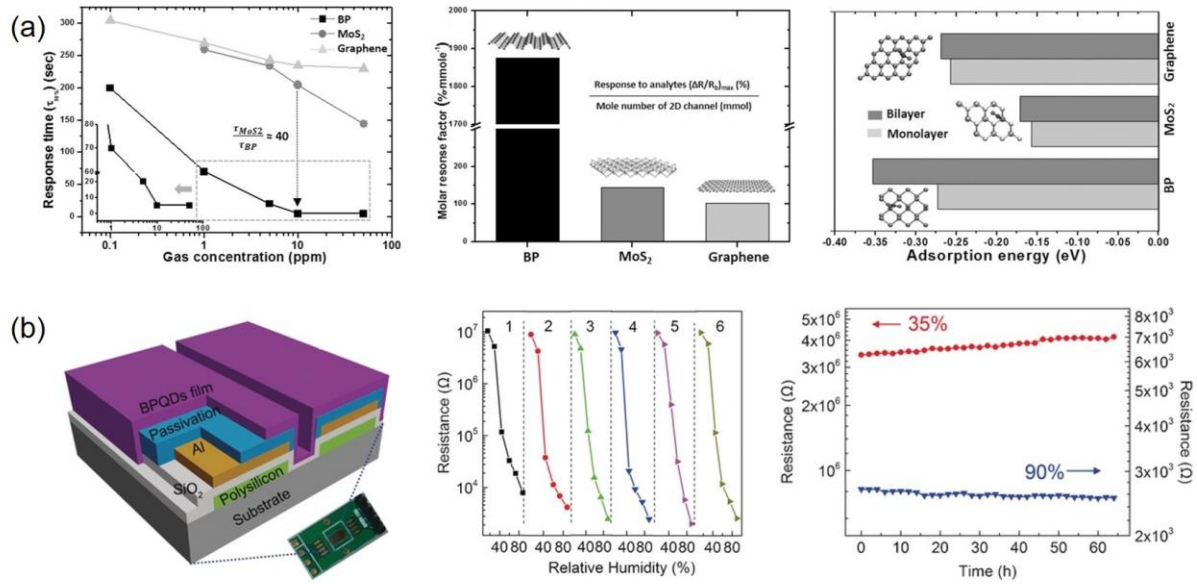

Figure 2.8 (a) Left: Measured response time ($\tau_{90\%}$) of black P, MoS_2, and graphene sensors to NO_2 concentration varying from 0.1 to 100 ppm. Middle: Calculated molecular response (% $mmol^{-1}$) of black P, MoS_2, and graphene sensors. Right: DFT calculated adsorption energy of NO_2 onto the surfaces of monolayer and bilayer for black P, MoS_2, and graphene.[79] (b) Left: Illustration of resistive humidity sensor based on the black P QDs. Middle: The relationship between resistance and relative humidity for 6 consecutive tests. Right: Stable response at relative humidity of 35% and 90% for over 66 h.[85] [Figures adapted with permissions]

On the other hand, the recognized reasons for the degradation of black P in ambient conditions can be manipulated to be beneficial for its application in humidity sensors,[83-86] which have extensive usage in industrial process controlling and environmental monitoring. Manisha et al. reported a humidity sensor based on electrochemical exfoliated black P that can achieve a sensitivity of up to ~521% when the relative humidity is in the range of 11-97%.[84] Another ultrasensitive humidity sensor based on black P films has also been reported to be stable after exposure to ambient conditions up to 3 months and offer fairly stable responses at relative humidity of 35% and 83% for over 72 h.[83] Besides, Zhu et al. demonstrated that the quantum dots (QDs) of black P outperformed the nanosheets in terms of humidity sensor, which showed excellent stability with slight change in the response characteristics after 66 h exposure (Figure 2.8b).[85]

In addition to the gas sensors, few-layer black P also has been reported in the biosensor applications for H_2O_2,[88] immunoglobulin G (IgG),[89-90] as well as myoglobin (Mb).[91] Wang et al. have investigated the inherent electrochemical properties of black P and suggested it can be beneficial for the biosensing schemes.[92] Yan et al. constructed the first non-enzymatic H_2O_2 sensor by using multilayer black P with a height of ~4.5 nm and yielded a LOD of 10^{-7} M. The synthesis of black P was manipulated in a stainless-steel reactor charged by supercritical CO_2 to the desired pressure, thus prevent the products from oxidation.[88] Electrochemical detection of the rabbit IgG protein has been realized in an immunoassay with hydrogen evolution mediation based on black P nanoparticles (NPs) (Figure 2.9a).[89] This novel immunoassay was based on the NPs with varying sizes from 40 to 200 nm that were fabricated by electrochemical exfoliation. Good selectivity and reproducibility were shown in the proposed scheme with gold NPs, evidenced by a low LOD of 0.98 ng mL^{-1} and an RSD of 18%. Low cytotoxicity of black P is one of the characteristics that highly desirable in the utilization of biosensors, especially for biomolecular labeling.[93-95] The cell-toxicity effect of black P for A549, HeLa, COS-7, and CHO-K1 cells was observed to be comparable to that of TMDs, and even lower than graphene oxides.[93-95] However, the cytotoxicity of black P has also been reported to efficiently kill the cancer cell lines, which suggests that black P possess the therapeutic potential as a photodynamic treatment agent.[96-98] Finally, a cardiac biomarker sensor based on liquid-phase exfoliation black P has been reported for labeling Mb, which has achieved a low LOD (~0.137 pg mL^{-1}) and an excellent sensitivity (ca. 51 μA pg^{-1} mL cm^{-2}) with concentrations varying from 1 pg mL^{-1} to 16 μg mL^{-1} (Figure 2.9b).[91] The poly-l-lysine (PLL) functionalized black P was used to achieve the electrochemical detection of cardiac biomarker Mb by specifically monitoring the charge transfer from Mb to PLL-modified aptasensor (Figure 2.9b).

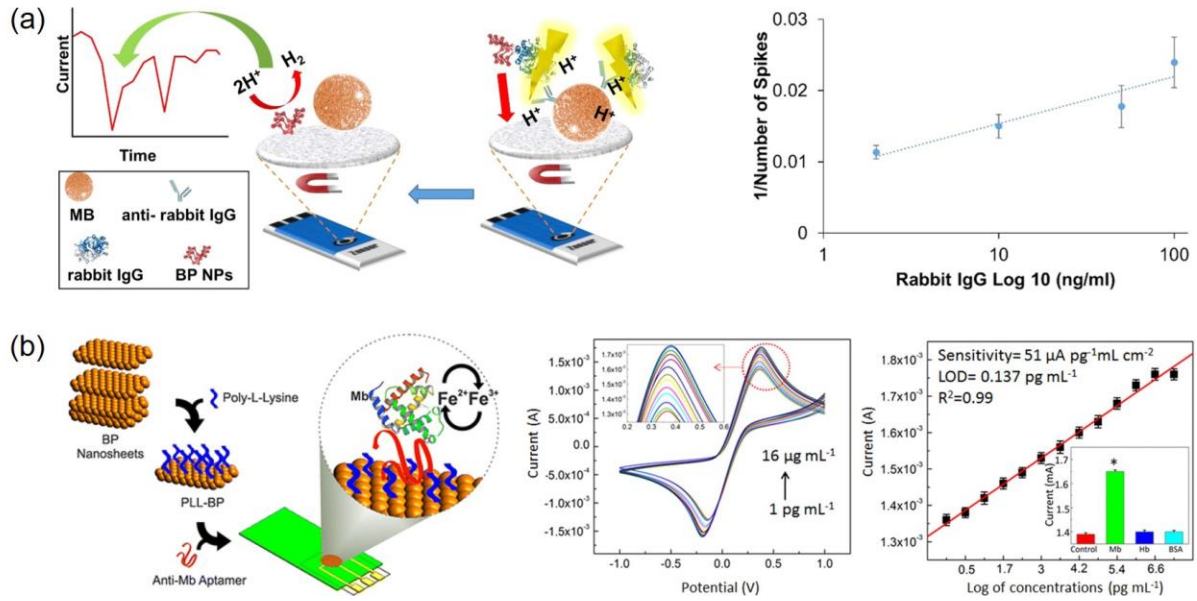

Figure 2.9 (a) Left: Schematic of immunoassay for protein IgG using black P nanoparticles (NPs) and HER electrocatalysts (proton reduction) by impact electrochemistry (spikes count) as a detection method (MB = Magnetic beads). Right: Linear relationship between the rabbit IgG concentrations as a function of the inverse of spikes counts.89 (b) Left: Schematic illustration of procedures of surface modification by using poly-L-lysine (PLL) on the liquid-phase exfoliated black P nanosheets for label-free detection of myoglobin (Mb). Middle: Current-potential characteristics at concentrations vary from 1 pg mL^{-1} to 16 pg mL^{-1} measured on PLL-functionalized aptasensor. Inset contains enlarged area of redox peak of analyte Mb. Right: Calibration plot for Mb at various concentrations. Inset indicates a comparison of current response between the developed sensor and those with a structurally related protein (hemoglobin, Hb) and a nonrelated protein (bovine serum albumin, BSA).91 [Figures adapted with permissions]

2.3.2 Photocatalytic hydrogen evolution reaction

Ever since Fujishima et al. first discovered the hydrogen (H_2) production from the electrochemical photocatalysis of water by using n-type TiO_2 electrode in 1972, visible-light-driven H_2 generation was considered as a promising strategy for the direct capture and storage of solar energy and further conversion into solar fuels.99-100 Black P holds substantial promise in the application of efficient photocatalytic HER catalyst in the post-graphene era owing to its large surface-volume ratio, tunable direct band gap, and high carrier mobility.101 Besides, HSE06 hybrid functional calculations on the positions of band edges suggested that the VBM of monolayer black P is less positive than the redox potential of O_2/H_2O (1.23 V), indicating O_2 might not be generated by oxygen evolution reaction (OER). However, the CBM

resides more negative than the redox potential of H^+/H_2 (0 V), which confirmed that the HER can be catalyzed by monolayer black P (Figure 2.10a).[48] Recently, Zhu et al. first designed a novel Z-scheme photocatalytic system by using black P/bismuth vanadate ($BiVO_4$) heterostructure to generate H_2 and O_2 from spontaneously solar-driven water splitting.[102] The band structures of black P and $BiVO_4$ construct a Z-scheme photocatalysis system, where electrons in the CB of black P and holes in the VB of $BiVO_4$ that generated by visible light irradiation participate in the reduction and oxidation reactions, respectively (Figure 2.10b). Benefited from the Z-scheme, the production rates of H_2 and O_2 can achieve 160 and 102 μmol g^{-1} h^{-1} when the wavelength of incident light is larger than 420 nm, without applying the sacrificial agents and external bias. Aside from the above-mentioned photocatalysts, many other black P-based systems also have been reported in the applications of efficient H_2 production from photocatalytic water splitting that driven by solar energy.[101, 103-107]

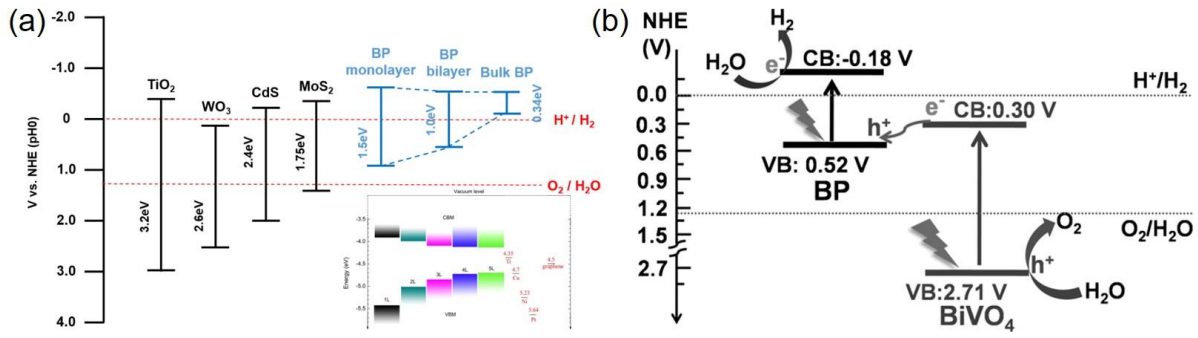

Figure 2.10 (a) CBM and VBM positions for few-layer black P as well as the redox potentials of H^+/H_2 (0 V) and O_2/H_2O (1.23 V) versus the normal hydrogen electrode (vs. NHE).[108] Inset shows DFT calculated CBM and VBM positions for few-layer black P by using HSE06 hybrid functional.[48] (b) The proposed Z-scheme in the black P/$BiVO_4$ heterostructure for overall photocatalytic water splitting.[102] [Figures adapted with permissions]

2.3.3 Nitrogen reduction reaction

Ammonia (NH_3) production is considered as one of the most significant reactions in modern agriculture and industry, as being the raw material for various synthetic chemicals, including, fertilizers, medicaments, dyes, explosives, and resins.[109-112] Haber-Bosch process is the main synthetic route for the mass production of NH_3 in the industry, which requires harsh

reaction conditions, accounting for more than 1% of worldwide energy consumption annually.[113] Therefore, alternative processes with good environmental sustainability and low energy consumption are highly imperative to develop.[113-114] Electrocatalysis and photocatalysis occur at ambient conditions, have great potential in solving the energy crisis and simplifying the reactor design, which represents green and economical strategies for sustainable NH_3 production.[115-116]

First, it is a vital task to search for an electrocatalyst with optimal catalytic performance and good selectivity. Recently, the well-exfoliated multilayer black P was reported by Zhang et al. to be a promising material for NRR with a faradaic efficiency of 5.07% and a yield of 31.37 μg h^{-1} mg^{-1}_{cat}.[117] Few-layer black P has a general good structural stability, whereas it did suffer from partial oxidation during the electrochemical measurements, evidenced by blue-shift of the Raman peaks, and enhanced oxidation peak in the XPS spectra (Figure 2.11a). Nonetheless, only a slight decrease was observed in the Faradaic efficiency and yield rate after five consecutive cycles which indicated good durability of the catalyst.

On the other hand, inspired by the successful applications of semiconducting NRR photocatalysts under visible light irradiation, including Ga_2O_3,[118] g-C_3N_4,[119] and TiO_2,[120] etc., various efforts have been devoted to construct the heterojunction between black P and these materials, to obtain NRR photocatalysts with superior stability and efficiency. Recently, Qiu et al. reported a metal-free black P/g-C_3N_4 heterojunction with excellent catalytic activity for NRR.[121] The photocatalytic NRR rate under visible light illumination of 0.05black P/g-C_3N_4 (347.5 μmol L^{-1} h^{-1}) is significantly better than g-C_3N_4 (40.5 μmol L^{-1} h^{-1}), and surprisingly, even surpasses Pt loaded g-C_3N_4. The C–P covalent bonds that formed between black P and g-C_3N_4 exerts a significant effect in enhancing the photocatalytic activity and contributes to two aspects (Figure 2.11b): the C–P bonds alter the π-conjugate scheme of g-C_3N_4 and increase the excited electrons in the heterojunction; the photogenerated electrons can

efficient transfer via the C–P bonds and therefore enhance the separation efficiency. Furthermore, the lone-pairs of P atoms in black P are occupied owing to the formation of C–P bonds and inhibits the degradation of black P by resulting in the reduced oxygen reactive sites. The environmental stability was attested by exposing to ambient conditions for 30 days, and no significant changes in the chemical structure were observed. Besides, the durability of 0.05black P/g-C_3N_4 as a photocatalyst was also further confirmed by cycle experiment, no remarkable deterioration was observed after five cycles under visible light irradiation. Overall, these studies revealed that the expedition in designing a highly stable and efficient catalyst for NRR with low energy consumption and better environmental sustainability by reducing the usage of metal elements.

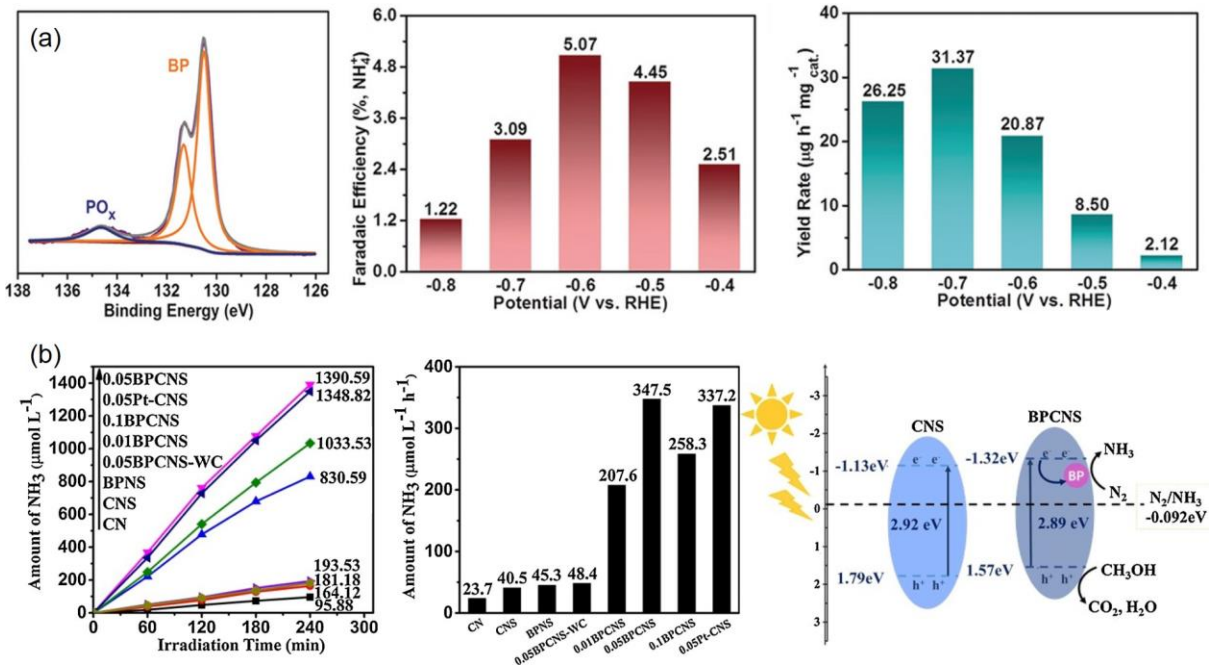

Figure 2.11 (a) Left: XPS spectra of few-layer black P nanosheets. A major doublet peak represents the successfully preparation of the samples, and a weak oxidized PO_x peak indicates the partially oxidation of black P. Middle: Faradaic efficiency and right: NH_3 yield rate with respect to the potentials.[117] (b) Left: Time course and middle: average reaction rate of photocatalytic NRR on various compositions. Right: Proposed photocatalytic NRR mechanism over 0.05black P/g-C_3N_4.[121] [Figures adapted with permissions]

2.4 References

(1) Gusmão, R.; Sofer, Z.; Pumera, M., Black Phosphorus Rediscovered: From Bulk Material to Monolayers. *Angew. Chem. Int. Ed.* **2017**, *56*, 8052-8072.

(2) Wiberg, E.; Holleman, A. F., *Holleman-Wiberg's Inorganic Chemistry (Ed.: N. Wiberg)*; Academic Press, San Diego, CA, USA, **2001**, p 677-740.

(3) Bachhuber, F.; von Appen, J.; Dronskowski, R.; Schmidt, P.; Nilges, T.; Pfitzner, A.; Weihrich, R., Van Der Waals Interactions in Selected Allotropes of Phosphorus. *Z. Kristallogr. Cryst. Mater.* **2015**, *230*, 107-115.

(4) Okudera, H.; Dinnebier, R. E.; Simon, A., The Crystal Structure of Γ-P_4, a Low Temperature Modification of White Phosphorus. *Z. Kristallogr. Cryst. Mater.* **2005**, *220*, 259-264.

(5) DeWitt, T.; Skolnik, S., Conversion of Liquid White Phosphorus to Red Phosphorus. I. Kinetics of the Reaction[1]. *J. Am. Chem. Soc.* **1946**, *68*, 2305-2309.

(6) Thurn, H.; Krebs, H., Über Struktur Und Eigenschaften Der Halbmetalle. XXII. Die Kristallstruktur Des Hittorfschen Phosphors. *Acta Cryst. B* **1969**, *25*, 125-135.

(7) Pfitzner, A.; Bräu, M. F.; Zweck, J.; Brunklaus, G.; Eckert, H., Phosphorus Nanorods—Two Allotropic Modifications of a Long-Known Element. *Angew. Chem. Int. Ed.* **2004**, *43*, 4228-4231.

(8) Ruck, M.; Hoppe, D.; Wahl, B.; Simon, P.; Wang, Y.; Seifert, G., Fibrous Red Phosphorus. *Angew. Chem. Int. Ed.* **2005**, *44*, 7616-7619.

(9) Bachhuber, F.; von Appen, J.; Dronskowski, R.; Schmidt, P.; Nilges, T.; Pfitzner, A.; Weihrich, R., The Extended Stability Range of Phosphorus Allotropes. *Angew. Chem. Int. Ed.* **2014**, *53*, 11629-11633.

(10) Eckstein, N.; Hohmann, A.; Weihrich, R.; Nilges, T.; Schmidt, P., Synthesis and Phase Relations of Single-Phase Fibrous Phosphorus. *Z. Anorg. Allg. Chem.* **2013**, *639*, 2741-2743.

(11) Pfitzner, A., Phosphorus Remains Exciting! *Angew. Chem. Int. Ed.* **2006**, *45*, 699-700.

(12) Hittorf, W., Zur Kenntniss Des Phosphors. *Ann. Phys. (Berlin)* **1865**, *202*, 193-228.

(13) Thurn, H.; Kerbs, H., Crystal Structure of Violet Phosphorus. *Angew. Chem. Int. Ed.* **1966**, *5*, 1047-1048.

(14) Smith, J. B.; Hagaman, D.; DiGuiseppi, D.; Schweitzer-Stenner, R.; Ji, H. F., Ultra-Long Crystalline Red Phosphorus Nanowires from Amorphous Red Phosphorus Thin Films. *Angew. Chem. Int. Ed.* **2016**, *55*, 11829-11833.

(15) Böcker, S.; Häser, M., Covalent Structures of Phosphorus: A Comprehensive Theoretical Study. *Z. Anorg. Allg. Chem.* **1995**, *621*, 258-286.

(16) Lin, S.; Chui, Y.; Li, Y.; Lau, S. P., Liquid-Phase Exfoliation of Black Phosphorus and Its Applications. *FlatChem* **2017**, *2*, 15-37.

(17) Du, Y.; Ouyang, C.; Shi, S.; Lei, M., *Ab Initio* Studies on Atomic and Electronic Structures of Black Phosphorus. *J. Appl. Phys.* **2010**, *107*, 093718.

(18) Carvalho, A.; Wang, M.; Zhu, X.; Rodin, A. S.; Su, H.; Neto, A. H. C., Phosphorene: From Theory to Applications. *Nat. Rev. Mater.* **2016**, *1*, 16061.

(19) Qiao, J.; Kong, X.; Hu, Z.-X.; Yang, F.; Ji, W., High-Mobility Transport Anisotropy and Linear Dichroism in Few-Layer Black Phosphorus. *Nat. Commun.* **2014**, *5*, 4475.

(20) Zhu, Z.; Tománek, D., Semiconducting Layered Blue Phosphorus: A Computational Study. *Phys. Rev. Lett.* **2014**, *112*, 176802.

(21) Guan, J.; Zhu, Z.; Tománek, D., Phase Coexistence and Metal-Insulator Transition in Few-Layer Phosphorene: A Computational Study. *Phys. Rev. Lett.* **2014**, *113*, 046804.

(22) Wu, J.; Mao, N.; Xie, L.; Xu, H.; Zhang, J., Identifying the Crystalline Orientation of Black Phosphorus Using Angle‐Resolved Polarized Raman Spectroscopy. *Angew. Chem. Int. Ed.* **2015**, *54*, 2366-2369.
(23) Rudenko, A. N.; Katsnelson, M. I., Quasiparticle Band Structure and Tight-Binding Model for Single-and Bilayer Black Phosphorus. *Phys. Rev. B* **2014**, *89*, 201408.
(24) Tran, V.; Soklaski, R.; Liang, Y.; Yang, L., Layer-Controlled Band Gap and Anisotropic Excitons in Few-Layer Black Phosphorus. *Phys. Rev. B* **2014**, *89*, 235319.
(25) Woomer, A. H.; Farnsworth, T. W.; Hu, J.; Wells, R. A.; Donley, C. L.; Warren, S. C., Phosphorene: Synthesis, Scale-up, and Quantitative Optical Spectroscopy. *ACS Nano* **2015**, *9*, 8869-8884.
(26) Yasaei, P.; Kumar, B.; Foroozan, T.; Wang, C.; Asadi, M.; Tuschel, D.; Indacochea, J. E.; Klie, R. F.; Salehi-Khojin, A., High-Quality Black Phosphorus Atomic Layers by Liquid-Phase Exfoliation. *Adv. Mater.* **2015**, *27*, 1887-1892.
(27) Li, L.; Kim, J.; Jin, C.; Ye, G. J.; Qiu, D. Y.; Felipe, H.; Shi, Z.; Chen, L.; Zhang, Z.; Yang, F., Direct Observation of the Layer-Dependent Electronic Structure in Phosphorene. *Nat. Nanotechnol.* **2017**, *12*, 21.
(28) Liu, H.; Neal, A. T.; Zhu, Z.; Luo, Z.; Xu, X.; Tománek, D.; Ye, P. D., Phosphorene: An Unexplored 2D Semiconductor with a High Hole Mobility. *ACS Nano* **2014**, *8*, 4033-4041.
(29) Zhang, S.; Yang, J.; Xu, R.; Wang, F.; Li, W.; Ghufran, M.; Zhang, Y.-W.; Yu, Z.; Zhang, G.; Qin, Q., Extraordinary Photoluminescence and Strong Temperature/Angle-Dependent Raman Responses in Few-Layer Phosphorene. *ACS Nano* **2014**, *8*, 9590-9596.
(30) Yang, J.; Xu, R.; Pei, J.; Myint, Y. W.; Wang, F.; Wang, Z.; Zhang, S.; Yu, Z.; Lu, Y., Optical Tuning of Exciton and Trion Emissions in Monolayer Phosphorene. *Light Sci. Appl* **2015**, *4*, e312.
(31) Ghosh, B.; Nahas, S.; Bhowmick, S.; Agarwal, A., Electric Field Induced Gap Modification in Ultrathin Blue Phosphorus. *Phys. Rev. B* **2015**, *91*, 115433.
(32) Zhang, S.; Xie, M.; Li, F.; Yan, Z.; Li, Y.; Kan, E.; Liu, W.; Chen, Z.; Zeng, H., Semiconducting Group 15 Monolayers: A Broad Range of Band Gaps and High Carrier Mobilities. *Angew. Chem. Int. Ed.* **2016**, *55*, 1666-1669.
(33) Heyd, J.; Scuseria, G. E.; Ernzerhof, M., Hybrid Functionals Based on a Screened Coulomb Potential. *J. Chem. Phys.* **2003**, *118*, 8207-8215.
(34) Jing, Y.; Tang, Q.; He, P.; Zhou, Z.; Shen, P., Small Molecules Make Big Differences: Molecular Doping Effects on Electronic and Optical Properties of Phosphorene. *Nanotechnology* **2015**, *26*, 095201.
(35) Fei, R.; Yang, L., Strain-Engineering the Anisotropic Electrical Conductance of Few-Layer Black Phosphorus. *Nano Lett.* **2014**, *14*, 2884-2889.
(36) Liu, L.; Wu, X.; Liu, X.; Chu, P. K., Strain-Induced Band Structure and Mobility Modulation in Graphitic Blue Phosphorus. *Appl. Surf. Sci.* **2015**, *356*, 626-630.
(37) Hembram, K.; Jung, H.; Yeo, B. C.; Pai, S. J.; Kim, S.; Lee, K.-R.; Han, S. S., Unraveling the Atomistic Sodiation Mechanism of Black Phosphorus for Sodium Ion Batteries by First-Principles Calculations. *J. Phys. Chem. C* **2015**, *119*, 15041-15046.
(38) Zhang, C.; Yu, M.; Anderson, G.; Dharmasena, R. R.; Sumanasekera, G., The Prospects of Phosphorene as an Anode Material for High-Performance Lithium-Ion Batteries: A Fundamental Study. *Nanotechnology* **2017**, *28*, 075401.
(39) Lopez-Bezanilla, A., Effect of Atomic-Scale Defects and Dopants on Phosphorene Electronic Structure and Quantum Transport Properties. *Phys. Rev. B* **2016**, *93*, 035433.
(40) Yuan, H., et al., Polarization-Sensitive Broadband Photodetector Using a Black Phosphorus Vertical p–n Junction. *Nat. Nanotechnol.* **2015**, *10*, 707-713.
(41) Ramasubramaniam, A.; Muniz, A. R., *Ab Initio* Studies of Thermodynamic and Electronic Properties of Phosphorene Nanoribbons. *Phys. Rev. B* **2014**, *90*, 085424.

(42) Wang, X.; Jones, A. M.; Seyler, K. L.; Tran, V.; Jia, Y.; Zhao, H.; Wang, H.; Yang, L.; Xu, X.; Xia, F., Highly Anisotropic and Robust Excitons in Monolayer Black Phosphorus. *Nat. Nanotechnol.* **2015**, *10*, 517.
(43) Yi, Y.; Yu, X.-F.; Zhou, W.; Wang, J.; Chu, P. K., Two-Dimensional Black Phosphorus: Synthesis, Modification, Properties, and Applications. *Mater. Sci. Eng. R Rep* **2017**, *120*, 1-33.
(44) Ling, X.; Huang, S.; Hasdeo, E. H.; Liang, L.; Parkin, W. M.; Tatsumi, Y.; Nugraha, A. R.; Puretzky, A. A.; Das, P. M.; Sumpter, B. G., Anisotropic Electron-Photon and Electron-Phonon Interactions in Black Phosphorus. *Nano Lett.* **2016**, *16*, 2260-2267.
(45) Mogulkoc, Y.; Modarresi, M.; Mogulkoc, A.; Ciftci, Y., Electronic and Optical Properties of Bilayer Blue Phosphorus. *Comput. Mater. Sci.* **2016**, *124*, 23-29.
(46) Keyes, R. W., Correlation between Mobility and Effective Mass in Semiconductors. *J. Appl. Phys.* **1959**, *30*, 454-454.
(47) Xiao, J.; Long, M.; Zhang, X.; Ouyang, J.; Xu, H.; Gao, Y., Theoretical Predictions on the Electronic Structure and Charge Carrier Mobility in 2D Phosphorus Sheets. *Sci. Rep.* **2015**, *5*, 9961.
(48) Cai, Y.; Zhang, G.; Zhang, Y.-W., Layer-Dependent Band Alignment and Work Function of Few-Layer Phosphorene. *Sci. Rep.* **2014**, *4*, 6677.
(49) Xia, F.; Wang, H.; Jia, Y., Rediscovering Black Phosphorus as an Anisotropic Layered Material for Optoelectronics and Electronics. *Nat. Commun.* **2014**, *5*, 4458.
(50) Peng, X.; Wei, Q.; Copple, A., Strain-Engineered Direct-Indirect Band Gap Transition and Its Mechanism in Two-Dimensional Phosphorene. *Phys. Rev. B* **2014**, *90*, 085402.
(51) Xiao, J.; Long, M.; Deng, C.-S.; He, J.; Cui, L.-L.; Xu, H., Electronic Structures and Carrier Mobilities of Blue Phosphorus Nanoribbons and Nanotubes: A First-Principles Study. *J. Phys. Chem. C* **2016**, *120*, 4638-4646.
(52) Tan, C.; Cao, X.; Wu, X.-J.; He, Q.; Yang, J.; Zhang, X.; Chen, J.; Zhao, W.; Han, S.; Nam, G.-H., Recent Advances in Ultrathin Two-Dimensional Nanomaterials. *Chem. Rev.* **2017**, *117*, 6225-6331.
(53) Sansone, G.; Maschio, L.; Usvyat, D.; Schütz, M.; Karttunen, A., Toward an Accurate Estimate of the Exfoliation Energy of Black Phosphorus: A Periodic Quantum Chemical Approach. *J. Phys. Chem. Lett.* **2015**, *7*, 131-136.
(54) Castellanos-Gomez, A.; Vicarelli, L.; Prada, E.; Island, J. O.; Narasimha-Acharya, K.; Blanter, S. I.; Groenendijk, D. J.; Buscema, M.; Steele, G. A.; Alvarez, J., Isolation and Characterization of Few-Layer Black Phosphorus. *2D Mater.* **2014**, *1*, 025001.
(55) Favron, A.; Gaufrès, E.; Fossard, F.; Phaneuf-L'Heureux, A.-L.; Tang, N. Y.; Lévesque, P. L.; Loiseau, A.; Leonelli, R.; Francoeur, S.; Martel, R., Photooxidation and Quantum Confinement Effects in Exfoliated Black Phosphorus. *Nat. Mater.* **2015**, *14*, 826.
(56) Bourlinos, A. B.; Georgakilas, V.; Zboril, R.; Steriotis, T. A.; Stubos, A. K., Liquid-Phase Exfoliation of Graphite Towards Solubilized Graphenes. *Small* **2009**, *5*, 1841-1845.
(57) Zhou, K. G.; Mao, N. N.; Wang, H. X.; Peng, Y.; Zhang, H. L., A Mixed-Solvent Strategy for Efficient Exfoliation of Inorganic Graphene Analogues. *Angew. Chem. Int. Ed.* **2011**, *50*, 10839-10842.
(58) Yang, S.; Gong, Y.; Zhang, J.; Zhan, L.; Ma, L.; Fang, Z.; Vajtai, R.; Wang, X.; Ajayan, P. M., Exfoliated Graphitic Carbon Nitride Nanosheets as Efficient Catalysts for Hydrogen Evolution under Visible Light. *Adv. Mater.* **2013**, *25*, 2452-2456.
(59) Coleman, J. N.; Lotya, M.; O'Neill, A.; Bergin, S. D.; King, P. J.; Khan, U.; Young, K.; Gaucher, A.; De, S.; Smith, R. J., Two-Dimensional Nanosheets Produced by Liquid Exfoliation of Layered Materials. *Science* **2011**, *331*, 568-571.
(60) Niu, L.; Coleman, J. N.; Zhang, H.; Shin, H.; Chhowalla, M.; Zheng, Z., Production of Two-Dimensional Nanomaterials via Liquid-Based Direct Exfoliation. *Small* **2016**, *12*, 272-293.

(61) Brent, J. R.; Savjani, N.; Lewis, E. A.; Haigh, S. J.; Lewis, D. J.; O'Brien, P., Production of Few-Layer Phosphorene by Liquid Exfoliation of Black Phosphorus. *Chem. Commun.* **2014**, *50*, 13338-13341.
(62) Hanlon, D.; Backes, C.; Doherty, E.; Cucinotta, C. S.; Berner, N. C.; Boland, C.; Lee, K.; Harvey, A.; Lynch, P.; Gholamvand, Z., Liquid Exfoliation of Solvent-Stabilized Few-Layer Black Phosphorus for Applications Beyond Electronics. *Nat. Commun.* **2015**, *6*, 8563.
(63) Sresht, V.; Padua, A. A.; Blankschtein, D., Liquid-Phase Exfoliation of Phosphorene: Design Rules from Molecular Dynamics Simulations. *ACS Nano* **2015**, *9*, 8255-8268.
(64) Kang, J.; Wood, J. D.; Wells, S. A.; Lee, J.-H.; Liu, X.; Chen, K.-S.; Hersam, M. C., Solvent Exfoliation of Electronic-Grade, Two-Dimensional Black Phosphorus. *ACS Nano* **2015**, *9*, 3596-3604.
(65) Zhao, W.; Xue, Z.; Wang, J.; Jiang, J.; Zhao, X.; Mu, T., Large-Scale, Highly Efficient, and Green Liquid-Exfoliation of Black Phosphorus in Ionic Liquids. *ACS Appl. Mater. Interfaces* **2015**, *7*, 27608-27612.
(66) Guo, Z.; Zhang, H.; Lu, S.; Wang, Z.; Tang, S.; Shao, J.; Sun, Z.; Xie, H.; Wang, H.; Yu, X. F., From Black Phosphorus to Phosphorene: Basic Solvent Exfoliation, Evolution of Raman Scattering, and Applications to Ultrafast Photonics. *Adv. Funct. Mater.* **2015**, *25*, 6996-7002.
(67) Shi, Y.; Li, H.; Li, L.-J., Recent Advances in Controlled Synthesis of Two-Dimensional Transition Metal Dichalcogenides via Vapour Deposition Techniques. *Chem. Soc. Rev.* **2015**, *44*, 2744-2756.
(68) Xie, J.; Zhang, H.; Li, S.; Wang, R.; Sun, X.; Zhou, M.; Zhou, J.; Lou, X. W.; Xie, Y., Defect-Rich MoS_2 Ultrathin Nanosheets with Additional Active Edge Sites for Enhanced Electrocatalytic Hydrogen Evolution. *Adv. Mater.* **2013**, *25*, 5807-5813.
(69) Li, X.; Deng, B.; Wang, X.; Chen, S.; Vaisman, M.; Karato, S.-i.; Pan, G.; Lee, M. L.; Cha, J.; Wang, H., Synthesis of Thin-Film Black Phosphorus on a Flexible Substrate. *2D Mater.* **2015**, *2*, 031002.
(70) Smith, J. B.; Hagaman, D.; Ji, H.-F., Growth of 2D Black Phosphorus Film from Chemical Vapor Deposition. *Nanotechnology* **2016**, *27*, 215602.
(71) Zhang, J. L.; Zhao, S.; Han, C.; Wang, Z.; Zhong, S.; Sun, S.; Guo, R.; Zhou, X.; Gu, C. D.; Yuan, K. D., Epitaxial Growth of Single Layer Blue Phosphorus: A New Phase of Two-Dimensional Phosphorus. *Nano Lett.* **2016**, *16*, 4903-4908.
(72) Zeng, J.; Cui, P.; Zhang, Z., Half Layer by Half Layer Growth of a Blue Phosphorene Monolayer on a GaN(001) Substrate. *Phys. Rev. Lett.* **2017**, *118*, 046101.
(73) Han, N.; Gao, N.; Zhao, J., Initial Growth Mechanism of Blue Phosphorene on Au(111) Surface. *J. Phys. Chem. C* **2017**, *121*, 17893-17899.
(74) Qiu, L.; Dong, J.; Ding, F., Selective Growth of Two-Dimensional Phosphorene on Catalyst Surface. *Nanoscale* **2018**, *10*, 2255-2259.
(75) Gao, J.; Zhang, G.; Zhang, Y.-W., The Critical Role of Substrate in Stabilizing Phosphorene Nanoflake: A Theoretical Exploration. *J. Am. Chem. Soc.* **2016**, *138*, 4763-4771.
(76) Kou, L.; Frauenheim, T.; Chen, C., Phosphorene as a Superior Gas Sensor: Selective Adsorption and Distinct *I–V* Response. *J. Phys. Chem. Lett.* **2014**, *5*, 2675-2681.
(77) Abbas, A. N.; Liu, B.; Chen, L.; Ma, Y.; Cong, S.; Aroonyadet, N.; Köpf, M.; Nilges, T.; Zhou, C., Black Phosphorus Gas Sensors. *ACS nano* **2015**, *9*, 5618-5624.
(78) Cui, S.; Pu, H.; Wells, S. A.; Wen, Z.; Mao, S.; Chang, J.; Hersam, M. C.; Chen, J., Ultrahigh Sensitivity and Layer-Dependent Sensing Performance of Phosphorene-Based Gas Sensors. *Nat. Commun.* **2015**, *6*, 8632.
(79) Cho, S. Y.; Lee, Y.; Koh, H. J.; Jung, H.; Kim, J. S.; Yoo, H. W.; Kim, J.; Jung, H. T., Superior Chemical Sensing Performance of Black Phosphorus: Comparison with MoS_2 and Graphene. *Advanced Materials* **2016**, *28*, 7020-7028.

(80) Cho, S.-Y.; Koh, H.-J.; Yoo, H.-W.; Jung, H.-T., Tunable Chemical Sensing Performance of Black Phosphorus by Controlled Functionalization with Noble Metals. *Chem. Mater.* **2017**, *29*, 7197-7205.
(81) Mayorga-Martinez, C. C.; Sofer, Z.; Pumera, M., Layered Black Phosphorus as a Selective Vapor Sensor. *Angew. Chem. Int. Ed.* **2015**, *54*, 14317-14320.
(82) Sofer, Z.; Bouša, D.; Luxa, J.; Mazanek, V.; Pumera, M., Few-Layer Black Phosphorus Nanoparticles. *Chem. Commun.* **2016**, *52*, 1563-1566.
(83) Yasaei, P.; Behranginia, A.; Foroozan, T.; Asadi, M.; Kim, K.; Khalili-Araghi, F.; Salehi-Khojin, A., Stable and Selective Humidity Sensing Using Stacked Black Phosphorus Flakes. *ACS Nano* **2015**, *9*, 9898-9905.
(84) Erande, M. B.; Pawar, M. S.; Late, D. J., Humidity Sensing and Photodetection Behavior of Electrochemically Exfoliated Atomically Thin-Layered Black Phosphorus Nanosheets. *ACS Appl. Mater. Interfaces* **2016**, *8*, 11548-11556.
(85) Zhu, C.; Xu, F.; Zhang, L.; Li, M.; Chen, J.; Xu, S.; Huang, G.; Chen, W.; Sun, L., Ultrafast Preparation of Black Phosphorus Quantum Dots for Efficient Humidity Sensing. *Chem.: Eur. J* **2016**, *22*, 7357-7362.
(86) Late, D. J., Liquid Exfoliation of Black Phosphorus Nanosheets and Its Application as Humidity Sensor. *Microporous Mesoporous Mater.* **2016**, *225*, 494-503.
(87) Li, P.; Zhang, D.; Liu, J.; Chang, H.; Sun, Y. e.; Yin, N., Air-Stable Black Phosphorus Devices for Ion Sensing. *ACS Appl. Mater. Interfaces* **2015**, *7*, 24396-24402.
(88) Yan, S.; Wang, B.; Wang, Z.; Hu, D.; Xu, X.; Wang, J.; Shi, Y., Supercritical Carbon Dioxide-Assisted Rapid Synthesis of Few-Layer Black Phosphorus for Hydrogen Peroxide Sensing. *Biosens. Bioelectron.* **2016**, *80*, 34-38.
(89) Mayorga-Martinez, C. C.; Mohamad Latiff, N.; Eng, A. Y. S.; Sofer, Z. k.; Pumera, M., Black Phosphorus Nanoparticle Labels for Immunoassays Via Hydrogen Evolution Reaction Mediation. *Anal. Chem.* **2016**, *88*, 10074-10079.
(90) Chen, Y.; Ren, R.; Pu, H.; Chang, J.; Mao, S.; Chen, J., Field-Effect Transistor Biosensors with Two-Dimensional Black Phosphorus Nanosheets. *Biosens. Bioelectron.* **2017**, *89*, 505-510.
(91) Kumar, V.; Brent, J. R.; Shorie, M.; Kaur, H.; Chadha, G.; Thomas, A. G.; Lewis, E. A.; Rooney, A. P.; Nguyen, L.; Zhong, X. L., Nanostructured Aptamer-Functionalized Black Phosphorus Sensing Platform for Label-Free Detection of Myoglobin, a Cardiovascular Disease Biomarker. *ACS Appl. Mater. Interfaces* **2016**, *8*, 22860-22868.
(92) Wang, L.; Sofer, Z.; Pumera, M., Voltammetry of Layered Black Phosphorus: Electrochemistry of Multilayer Phosphorene. *ChemElectroChem* **2015**, *2*, 324-327.
(93) Sun, Z.; Xie, H.; Tang, S.; Yu, X. F.; Guo, Z.; Shao, J.; Zhang, H.; Huang, H.; Wang, H.; Chu, P. K., Ultrasmall Black Phosphorus Quantum Dots: Synthesis and Use as Photothermal Agents. *Angew. Chem. Int. Ed.* **2015**, *54*, 11526-11530.
(94) Latiff, N. M.; Teo, W. Z.; Sofer, Z.; Fisher, A. C.; Pumera, M., The Cytotoxicity of Layered Black Phosphorus. *Chem.: Eur. J* **2015**, *21*, 13991-13995.
(95) Lee, H. U.; Park, S. Y.; Lee, S. C.; Choi, S.; Seo, S.; Kim, H.; Won, J.; Choi, K.; Kang, K. S.; Park, H. G., Black Phosphorus (BP) Nanodots for Potential Biomedical Applications. *Small* **2016**, *12*, 214-219.
(96) Zhang, W.; Huynh, T.; Xiu, P.; Zhou, B.; Ye, C.; Luan, B.; Zhou, R., Revealing the Importance of Surface Morphology of Nanomaterials to Biological Responses: Adsorption of the Villin Headpiece onto Graphene and Phosphorene. *Carbon* **2015**, *94*, 895-902.
(97) Lv, R.; Yang, D.; Yang, P.; Xu, J.; He, F.; Gai, S.; Li, C.; Dai, Y.; Yang, G.; Lin, J., Integration of Upconversion Nanoparticles and Ultrathin Black Phosphorus for Efficient Photodynamic Theranostics under 808 nm near-Infrared Light Irradiation. *Chem. Mater.* **2016**, *28*, 4724-4734.

(98) Wang, H.; Yang, X.; Shao, W.; Chen, S.; Xie, J.; Zhang, X.; Wang, J.; Xie, Y., Ultrathin Black Phosphorus Nanosheets for Efficient Singlet Oxygen Generation. *J. Am. Chem. Soc.* **2015**, *137*, 11376-11382.
(99) Fujishima, A.; Honda, K., Electrochemical Photolysis of Water at a Semiconductor Electrode. *Nature* **1972**, *238*, 37-38.
(100) Yuan, J.; Liu, X.; Tang, Y.; Zeng, Y.; Wang, L.; Zhang, S.; Cai, T.; Liu, Y.; Luo, S.; Pei, Y., Positioning Cyanamide Defects in g-C_3N_4: Engineering Energy Levels and Active Sites for Superior Photocatalytic Hydrogen Evolution. *Appl. Catal. B* **2018**, *237*, 24-31.
(101) Lei, W.; Mi, Y.; Feng, R.; Liu, P.; Hu, S.; Yu, J.; Liu, X.; Rodriguez, J. A.; Wang, J.-o.; Zheng, L., Hybrid 0D–2D Black Phosphorus Quantum Dots–Graphitic Carbon Nitride Nanosheets for Efficient Hydrogen Evolution. *Nano Energy* **2018**, *50*, 552-561.
(102) Zhu, M.; Sun, Z.; Fujitsuka, M.; Majima, T., Z-Scheme Photocatalytic Water Splitting on a 2D Heterostructure of Black Phosphorus/Bismuth Vanadate Using Visible Light. *Angew. Chem. Int. Ed.* **2018**, *57*, 2160-2164.
(103) Tian, B.; Tian, B.; Smith, B.; Scott, M.; Hua, R.; Lei, Q.; Tian, Y., Supported Black Phosphorus Nanosheets as Hydrogen-Evolving Photocatalyst Achieving 5.4% Energy Conversion Efficiency at 353 K. *Nat. Commun.* **2018**, *9*, 1397.
(104) Zhao, G.; Wang, T.; Shao, Y.; Wu, Y.; Huang, B.; Hao, X., A Novel Mild Phase-Transition to Prepare Black Phosphorus Nanosheets with Excellent Energy Applications. *Small* **2017**, *13*, 1602243.
(105) Kong, L.; Ji, Y.; Dang, Z.; Yan, J.; Li, P.; Li, Y.; Liu, S., g-C_3N_4 Loading Black Phosphorus Quantum Dot for Efficient and Stable Photocatalytic H_2 Generation under Visible Light. *Adv. Funct. Mater.* **2018**, *28*, 1800668.
(106) Liang, Q.; Shi, F.; Xiao, X.; Wu, X.; Huang, K.; Feng, S., In Situ Growth of CoP Nanoparticles Anchored on Black Phosphorus Nanosheets for Enhanced Photocatalytic Hydrogen Production. *ChemCatChem* **2018**, *10*, 2179-2183.
(107) Lin, Y.; Pan, Y.; Zhang, J., In-Situ Grown of Ni_2P Nanoparticles on 2D Black Phosphorus as a Novel Hybrid Catalyst for Hydrogen Evolution. *Int. J. Hydrog. Energy* **2017**, *42*, 7951-7956.
(108) Lee, T. H.; Kim, S. Y.; Jang, H. W., Black Phosphorus: Critical Review and Potential for Water Splitting Photocatalyst. *Nanomaterials* **2016**, *6*, 194.
(109) Erisman, J. W.; Sutton, M. A.; Galloway, J.; Klimont, Z.; Winiwarter, W., How a Century of Ammonia Synthesis Changed the World. *Nat. Geosci* **2008**, *1*, 636.
(110) Schlögl, R., Catalytic Synthesis of Ammonia—a "Never-Ending Story"? *Angew. Chem. Int. Ed.* **2003**, *42*, 2004-2008.
(111) Galloway, J. N.; Townsend, A. R.; Erisman, J. W.; Bekunda, M.; Cai, Z.; Freney, J. R.; Martinelli, L. A.; Seitzinger, S. P.; Sutton, M. A., Transformation of the Nitrogen Cycle: Recent Trends, Questions, and Potential Solutions. *Science* **2008**, *320*, 889-892.
(112) Canfield, D. E.; Glazer, A. N.; Falkowski, P. G., The Evolution and Future of Earth's Nitrogen Cycle. *Science* **2010**, *330*, 192-196.
(113) Van der Ham, C. J.; Koper, M. T.; Hetterscheid, D. G., Challenges in Reduction of Dinitrogen by Proton and Electron Transfer. *Chem. Soc. Rev.* **2014**, *43*, 5183-5191.
(114) Shi, M. M.; Bao, D.; Wulan, B. R.; Li, Y. H.; Zhang, Y. F.; Yan, J. M.; Jiang, Q., Au Sub-Nanoclusters on TiO_2 toward Highly Efficient and Selective Electrocatalyst for N_2 Conversion to NH_3 at Ambient Conditions. *Adv. Mater.* **2017**, *29*, 1606550.
(115) Chen, Z.; Zhao, J.; Cabrera, C. R.; Chen, Z., Computational Screening of Efficient Single-Atom Catalysts Based on Graphitic Carbon Nitride (g-C_3N_4) for Nitrogen Electroreduction. *Small Methods* **2018**, 1800368.
(116) Nishibayashi, Y.; Saito, M.; Uemura, S.; Takekuma, S.-i.; Takekuma, H.; Yoshida, Z.-i., Buckminsterfullerenes: A Non-Metal System for Nitrogen Fixation. *Nature* **2004**, *428*, 279.

(117) Zhang, L.; Ding, L. X.; Chen, G. F.; Yang, X.; Wang, H., Ammonia Synthesis under Ambient Conditions: Selective Electroreduction of Dinitrogen to Ammonia on Black Phosphorus Nanosheets. *Angew. Chem. Int. Ed.* **2019**, *58*, 2612-2616.
(118) Cao, S.; Zhou, N.; Gao, F.; Chen, H.; Jiang, F., All-Solid-State Z-Scheme 3, 4-Dihydroxybenzaldehyde-Functionalized Ga_2O_3/Graphitic Carbon Nitride Photocatalyst with Aromatic Rings as Electron Mediators for Visible-Light Photocatalytic Nitrogen Fixation. *Appl. Catal. B* **2017**, *218*, 600-610.
(119) Cao, S.; Chen, H.; Jiang, F.; Wang, X., Nitrogen Photofixation by Ultrathin Amine-Functionalized Graphitic Carbon Nitride Nanosheets as a Gaseous Product from Thermal Polymerization of Urea. *Appl. Catal. B* **2018**, *224*, 222-229.
(120) Zhao, W.; Zhang, J.; Zhu, X.; Zhang, M.; Tang, J.; Tan, M.; Wang, Y., Enhanced Nitrogen Photofixation on Fe-Doped TiO_2 with Highly Exposed (1 0 1) Facets in the Presence of Ethanol as Scavenger. *Appl. Catal. B* **2014**, *144*, 468-477.
(121) Qiu, P.; Xu, C.; Zhou, N.; Chen, H.; Jiang, F., Metal-Free Black Phosphorus Nanosheets-Decorated Graphitic Carbon Nitride Nanosheets with C–P Bonds for Excellent Photocatalytic Nitrogen Fixation. *Appl. Catal. B* **2018**, *221*, 27-35.

Chapter 3 : Methodology

3.1 Introduction

In recent years, numerical simulations have enjoyed enormous progress in almost every field of interdisciplinary materials science and engineering. Numerical simulations have evolved into a thrilling and brand-new branch with the advances of high-performance computers, namely, “computational materials science”. It was developed to bring together different disciplines, including materials science, physics, chemistry, and engineering, etc.[1] Computational materials science mainly includes the following two aspects: i) materials-related calculations and simulations, starting from the experimental data to simulate the actual processes by mathematical models and numerical predictions; ii) computer-aided materials design, designing through theoretical models and calculations to predict the structure and properties of the target material. The former makes materials research not only stagnate in the qualitative discussion of experimental results but also turns the experimental results of specific materials systems into a general and quantitative theory; the latter renders the research and development of materials more directional and forward-looking. It contributes to original innovation and can significantly improve the efficiency of scientific research. Therefore, computational materials science has become a bridge that combines the theory and experiments in material science.

Figure 3.1 illustrates the commonly used calculation methods in the computational materials science targeting at materials at different length scales, including the first-principles calculations, molecular dynamics, Monte Carlo simulations, cellular automata, and finite element analysis, among others. Among various computational techniques, first-principles calculation is of particular importance for the research fields of condensed matter physics, quantum chemistry, nanocomponents, etc., and constructs an increasingly significant role in

the design of materials performance and composition as well as the exploration of novel materials. Density functional theory (DFT) consolidates the foundation of first-principles calculations. It can accurately predict the system energy and other required electronic, thermodynamic, and chemical properties, without the input of any empirical parameters. The disadvantage of this method is that the dependence on high-performance computers is relatively high, and the amount of calculation is relatively large. However, with the continuous developments of first-principles methods and modern computers, especially high-performance computers, and the unprecedented improvements of computing power, the empirical and semi-empirical methods have gradually replaced by first-principles calculations, and become the mainstream method in the computational materials science.

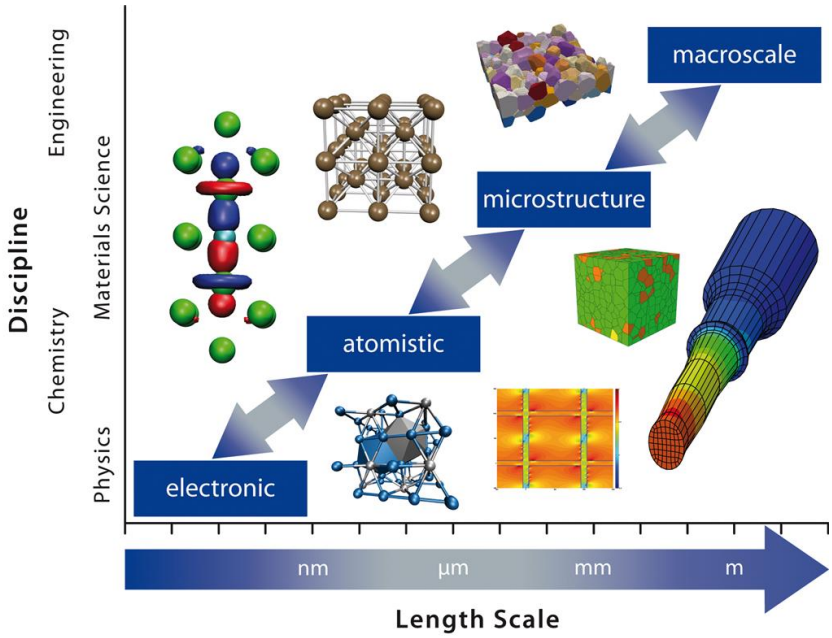

Figure 3.1 Schematic of the dependence of different disciplines (physics, chemistry, materials science, and engineering) on different length scales ranging from electronic, atomistic, microstructure, to macroscale.[2]

3.2 The first-principles rationale

In physics, the first-principles calculation, or *ab-initio* (*ab initio*) calculation, is referring to all calculations on the basis of quantum mechanics,[3] e.g., the calculation of molecular structure and energy according to the interactions between electrons and nuclei to

predict various properties of a certain material. In any situation, quantum mechanics makes it possible to capture the behaviors of electrons and atomic nuclei, and the behavior of electrons usually determines the majority properties of materials (except for nuclear reactions). However, the strong interaction between electrons results in an impossibility of accurately solving the Schrödinger equation. To practically solve the Schrödinger equation in condensed matter physics, it necessitates the introduction of approximations or assumptions, and include some empirical parameters,[4] therefore inevitably sacrifice the accuracy of the calculation results to some extent, which will be discussed in the following Sections 3.3-3.5.

3.3 Born-Oppenheimer approximation

Given that the properties of a material are seamlessly correlated with the behaviors of electrons, such that it is crucial to interpret the structure of the electrons for the study of the order of electrons in the solids. The starting point of the first-principles is to explore the electronic structure of a system by resolving the Schrödinger equation. A Schrödinger equation that governs the motion law in a many-particle system at the microscopic scale is expressed as:

$$H\psi(\vec{r},\vec{R}) = E\psi(\vec{r},\vec{R}) \tag{3.1}$$

where H refers to the Hamiltonian that includes the kinetic energy of nuclear and extranuclear electrons and their interaction energy, and E denote the total energy. $\psi(\vec{r},\vec{R})$ is the wave function, where $\vec{r}$ and $\vec{R}$ represent for the coordinates of electron and nucleus, respectively.

If external fields are not considered, the Hamiltonian should include the kinetic energy all electrons and nuclei as well as the interaction energy between them, thus it leads the form:

$$H = H_{\mathrm{e}} + H_{\mathrm{N}} + H_{\mathrm{e-N}} \tag{3.2}$$

here, H_{e} and H_{N} represent the Hamiltonians for electrons and nuclei, including kinetic energy and Coulomb interaction, respectively. $H_{\mathrm{e-N}}$ indicates the Coulomb interaction between these ions. The equations for each of the sub-items are listed below:

$$H_{\mathrm{e}}(\vec{r}) = T_{\mathrm{e}}(\vec{r}) + V_{\mathrm{e}}(\vec{r}) = -\sum_{i} \frac{\hbar^2}{2m_i} \nabla_i^2 + \frac{1}{8\pi\varepsilon_0} \sum_{i \neq i'} \frac{e^2}{\left|\vec{r}_i - \vec{r}_{i'}\right|} \tag{3.3}$$

$$H_{\mathrm{N}}(\vec{R}) = T_{\mathrm{N}}(\vec{R}) + V_{\mathrm{N}}(\vec{R}) = -\sum_{j} \frac{\hbar^2}{2M_j} \nabla_j^2 + \frac{1}{8\pi\varepsilon_0} \sum_{j \neq j'} \frac{Ze^2}{\left|\vec{R}_j - \vec{R}_{j'}\right|} \tag{3.4}$$

$$H_{\mathrm{e-N}}(\vec{r}, \vec{R}) = V_{\mathrm{e-N}}(\vec{r}, \vec{R}) = \sum_{ij} -\frac{Ze^2}{4\pi\varepsilon_0 \left|\vec{r}_i - \vec{R}_j\right|} \tag{3.5}$$

Therefore, the total Hamiltonian of a system can be expanded to:

$$H = -\sum_{i} \frac{\hbar^2}{2m_i} \nabla_i^2 + \frac{1}{8\pi\varepsilon_0} \sum_{i \neq i'} \frac{e^2}{\left|\vec{r}_i - \vec{r}_{i'}\right|} - \sum_{j} \frac{\hbar^2}{2M_j} \nabla_j^2 + \frac{1}{8\pi\varepsilon_0} \sum_{j \neq j'} \frac{Ze^2}{\left|\vec{R}_j - \vec{R}_{j'}\right|} - \sum_{ij} \frac{Ze^2}{4\pi\varepsilon_0 \left|\vec{r}_i - \vec{R}_j\right|} \tag{3.6}$$

where, m_i and r_i denote the mass and coordinates of the *i*-th electron, M_j and R_j represent the mass and coordinates of the *i*-th nucleus.

The Schrödinger equation in the condensed matter for a many-particle system becomes difficult to solve due to a great number of coupling nuclei and electrons. Besides, the mass of a nucleus is about 1,800 times to that of an electron, and thus, correspondingly the speed of the nucleus and electrons is significantly different. Therefore, the motion of the nuclei and electrons can be treated separately, that is, the spatial distribution of electrons is not considered when taking care of the motions of the nucleus; meanwhile, when considering the motion of electrons, the nucleus is regarded as a quasi-stationary particle, only considering their instantaneous positions at this particular time. This is the Born-Oppenheimer (BO) approximation that proposed by M. Born and J. R. Oppenheimer in 1927, also known as the "adiabatic approximation".[5]

Under the BO approximation, the total wavefunction of a system is approximately expressed as the product of an electronic wavefunction and a nuclear wavefunction, and this gives a solution to the Schrödinger equation for a many-particle system:

$$\psi(\vec{r},\vec{R}) = \chi(\vec{R})\varphi(\vec{r},\vec{R}) \tag{3.7}$$

where $\chi(\vec{R})$ and $\varphi(\vec{r},\vec{R})$ indicate the electronic and nuclear wavefunction, respectively, and the new Hamiltonian is introduced as:

$$H_{\mathrm{BO}} = H_{\mathrm{e}}(\vec{r}) + V_{\mathrm{N}}(\vec{R}) + H_{\mathrm{e-N}}(\vec{r},\vec{R}) \tag{3.8}$$

that is:

$$H_{\mathrm{BO}} = -\sum_i \frac{\hbar^2}{2m_i}\nabla_i^2 + \frac{1}{8\pi\varepsilon_0}\sum_{i\neq i'}\frac{e^2}{\left|\vec{r}_i - \vec{r}_{i'}\right|} + \frac{1}{8\pi\varepsilon_0}\sum_{j\neq j'}\frac{Ze^2}{\left|\vec{R}_j - \vec{R}_{j'}\right|} - \sum_{ij}\frac{Ze^2}{4\pi\varepsilon_0\left|\vec{r}_i - \vec{R}_j\right|} \tag{3.9}$$

The BO approximation treats the nuclei in a quasi-stationary state and separates the motions of electrons and nuclei, and therefore, simplifies the Schrödinger equation. However, for a system containing plenty of electrons, to describe their motions in the equilibrium potential field is still an extremely complicate many-body problem, and it requires further simplification to solve the many-body Schrödinger equation.

3.4 Hartree-Fock approximation

Even though BO approximation has greatly simplified the Schrödinger equation, it is still inaccessible to achieve an accurate solution since the Coulomb interaction between electrons makes the instantaneous position of all other electrons directly related to the potential of the electron. Therefore, one of the keys to practically solve the Schrödinger equations is to simplify the interaction between electrons. It would be approximated to solve a single-electron motion problem if the interaction between electrons is neglected in any given potential field. In 1928, D. R. Hartree assumed that an electron in the system is moving in a mean potential field that generated by an average Coulomb interaction between this electron and all the others.[6-7] Under this assumption, the potential field of each electron in the system is regarded as an equivalent potential field, and then the many-electron problem becomes a single-electron one.

Based on the Hartree's hypothesis, the wavefunction of a system is a product of the individual electron wavefunction, and each electron wavefunction is only related to its coordinates:

$$\psi(r) = \varphi_1(r_1)\varphi_2(r_2)\varphi_3(r_3)\cdots\varphi_N(r_{\mathrm{N}}) \tag{3.10}$$

This form of the wavefunction is called the Hartree product. However, J. C. Slater and J. A. Gaunt independently pointed out that the Hartree product could be turned into a one-electron equation by invoking the variational principle in 1928:[8-9]

$$\left[-\frac{\hbar^2}{2m}\nabla_i^2 + \sum_{i\neq i'}\int dr' \frac{\left|\psi_i(\vec{r}')\right|^2}{\left|\vec{r}_i - \vec{r}_{i'}\right|} + V_{\mathrm{e-N}}\right]\psi_i(\vec{r}) = E_i\psi_i(\vec{r}) \tag{3.11}$$

where its Hamiltonian (one-electron Hamiltonian) expressed as:

$$H_i = \left[-\frac{\hbar^2}{2m}\nabla_i^2 + \sum_{i\neq i'}\int dr' \frac{\left|\psi_i(\vec{r}')\right|^2}{\left|\vec{r}_i - \vec{r}_{i'}\right|} + V_{\mathrm{e-N}}\right]\psi_i(\vec{r}) \tag{3.12}$$

The motion of a single electron in the lattice potential of $V(\vec{r})$ and the mean potential field of other electrons at the coordinates of $\vec{r}$ is described in eqn. (3.12). The Lagrange multiplier E_i combines the energies of each individual electrons, and thus, gives the total energy E for such a system:

$$E = \langle\psi|H|\psi\rangle\sum_i E_i \tag{3.13}$$

The Hartree equation is of great significance: by introducing a mean potential field, it allows us to transform the many-electron Schrödinger equation into a single-electron equation, and each of them can be described by the same Schrödinger equation. However, these equations also cannot be solved by multiple iterations due to their non-linear characteristics.

Although the various quantum states of each electron in the Hartree product fulfill the Pauli exclusion principle, however, V. A. Fock and Slater independently pointed out in 1928 that the Hartree method neglects the principle of antisymmetry of the wavefunction. In

response to this issue, they improved the wavefunction on the basis of Hartree and introduced the Slater determinant into single-electron wavefunction to ensure the antisymmetry in 1930:[10-11]

$$\psi(r_1, r_2, \cdots, r_N) = \frac{1}{\sqrt{N!}} \begin{vmatrix} \varphi_1(r_1) & \varphi_2(r_1) & \cdots & \varphi_N(r_1) \\ \varphi_1(r_2) & \varphi_2(r_2) & \cdots & \varphi_N(r_2) \\ \vdots & \vdots & \ddots & \vdots \\ \varphi_1(r_N) & \varphi_2(r_N) & \cdots & \varphi_N(r_N) \end{vmatrix} \tag{3.14}$$

where, $\varphi_\lambda(r_i)$ indicates a single-electron wavefunction at the energy level of λ that contains the spin state and spatial position of the *i*-th electron, which satisfies the orthogonal normalization. The above Slater determinant ensures an antisymmetry: that is, exchanging any two electrons which is equivalent to exchanging two rows of the Slater determinant, and the determinant only changes in the positive/negative sign. If two electrons have the same coordinates, then $\psi(r_1, r_2, \cdots, r_N) = 0$. Substituting the above wavefunction into the Schrödinger equation by invoking the variational method, the single-electron equation can be derived:

$$\left[-\frac{\hbar^2}{2m}\nabla_i^2 + V_{e-N} + \sum_{i \neq i'} \int dr' \frac{\left|\psi_{i'}(\vec{r}')\right|^2}{\left|\vec{r} - \vec{r}'\right|} - \sum_{i \neq i'} \int dr' \frac{\psi_{i'}^*(r')\psi_i(r')}{\left|\vec{r} - \vec{r}'\right|} \right] \psi_i(\vec{r}) = E_i \psi_i(\vec{r}) \tag{3.15}$$

and this is the famous Hartree-Fock (HF) equation.

Compared to the Hartree equation, the HF equation gives rise to an exchange term due to the antisymmetry of wavefunction. As can be seen from eqn. (3.15), any electron in the system (such as the *i*-th electron) moves in the potential field generated by all ions and other surrounding electrons. The potential field that a certain electron subjected to is not only related to the motion of other electrons, but also correlated with its own movement. This is mainly because the motion of the electron will affect the movement of other electrons, which will affect the potential field.

The HF method considers the electronic exchange effect exactly, however, this method solves the non-relativistic Schrödinger equation instead of the relativistic Dirac equation, rendering the HF method remains inherently approximate as it neglects the relativistic effect. Moreover, since the HF method ignores the electronic correlation energy, it is not capable of accurately computing the electronic excitation and binding energy, as well as reflecting the transition state. To improve the accuracy, several other methods have been proposed, for instance, adding the excited state to form a non-iterative modified Møller-Plesset perturbation method.[12] However, this method is not suitable for a system that contains a huge number of particles due to an enormous computation workload. Later in 1927, shortly after the introduction of the Schrödinger equation, L. H. Thomas[13] and E. Fermi[14] independently proposed another method of dealing with the many-body problem, so-called the Thomas-Fermi (TF) model. In the TF model, a semiclassical approximation was made that the electrons are uniformly distributed in a small volume, whereas the electron density still varies from one small volume to the next. Although the TF model fails to accurately describe the many-body effects between the electrons, its establishment was treated as the precursor to the later developed DFT.

3.5 Density functional theory

In general, DFT is attempted to interpret the properties of a system by using functionals, i.e., the spatially dependent electron density. Even though the concept of DFT originated from the TF model and made use of the Hohenberg-Kohn (HK) theorems as the theoretical basis, the name of DFT was coming from by considering the integration of electron density into functionals in this method. Currently, DFT is considered as one of the most versatile and popular methodologies that being currently used in the computational chemistry and physics, and condensed matter physics, etc.

3.5.1 Thomas-Fermi model

L. H. Thomas[13] and E. Fermi[14] almost simultaneously realized that the charge distribution in an atom can be approximated by a statistical model, in the year of 1927. By assuming that the potential field generated by the nucleus and all the electrons in an atom is slowly and continuously changing, the motion of the electron in this potential field can be regarded as a degenerate electron gas that obeys the Fermi-Dirac distribution at absolute zero temperature. In the TF model, the potential energy of an atom is expressed by a functional of electron density, however, it neglects the effect of electron correlation and only considers the nuclear-electron and electron-electron interactions. Therefore, this model yields inaccurate quantitative predictions to some general features of realistic systems.

3.5.2 Hohenberg-Kohn theorems

Based on the BO approximation and TF model, P. Hohenberg and W. Kohn[15] proposed the so-called HK theorems in 1964. DFT has its root in the HK theorems, therefore the HK theorems can determine the energy functional of a give system at the ground state:

$$E[\rho,V]=T[\rho]+\int d\vec{r}V_{\text{ext}}(\vec{r})\rho(\vec{r})+\frac{1}{2}\int\int d\vec{r}d\vec{r}'\frac{\rho(\vec{r})\rho(\vec{r}')}{|\vec{r}-\vec{r}'|}+E_{\text{xc}}[\rho] \tag{3.16}$$

where, $T[\rho]$ represents for the kinetic energy of the electron, $\int d\vec{r}V_{\text{ext}}(\vec{r})\rho(\vec{r})$ considers the external field effect, $\frac{1}{2}\int\int d\vec{r}d\vec{r}'\frac{\rho(\vec{r})\rho(\vec{r}')}{|\vec{r}-\vec{r}'|}$ for the Coulomb exclusion between the electrons, and $E_{\text{xc}}[\rho]$ for the exchange-correlation (XC) effect, including all interactions that are not included in the non-interacting particle model. Although the HK theorems state that the $\rho(\vec{r})$ is a fundamental parameter to determine the potential, and therefore, physical properties of a many-particle system. However, the theorems does not explicitly explain how to obtain a solvable ground state density $\rho(\vec{r})$, kinetic energy functional $T[\rho]$ and XC energy $E_{\text{xc}}[\rho]$.

3.5.3 Kohn-Sham equations

Later on, the Kohn-Sham (KS) equations were proposed in which a different auxiliary system that is able to determine the values of $\rho(\vec{r})$ and $T[\rho]$ was introduced, which were named after W. Kohn and L. J. Sham16. The auxiliary system is composed of electrons possessing the same electron density similar to the above-described interacting system but not interacting with each other. Basically, in the KS equations, the kinetic energy $T[\rho]$ of interacting participles in any given system is replaced by $T_0[\rho]$ of non-interacting particles that maintains the same density. Therefore, all the differences between $T[\rho]$ and $T_0[\rho]$ can be incorporated into $E_{xc}[\rho]$. This allows the ground state density for an interacting system to be written as the contribution of *N* independent orbitals:

$$\rho(\vec{r}) = \sum_{i=1}^{N} \varphi_i^*(r)\varphi_i(\vec{r}) \tag{3.17}$$

where $\varphi_i(\vec{r})$ denote the corresponding KS orbital. For the electron density in a non-interacting system, we can always find a unique external potential that corresponds to it. The ground state wavefunction can be rewritten by using the Slater determinant when representing the *N* independent orbitals with the lowest energy for a non-interacting system. Therefore, even if the ground state wavefunction of the interacting electronic system is not strictly composed of the Slater determinant, the relationship of the interaction system is still valid. This leads to the ground state density for an *N*-particle system:

$$\rho_0(\vec{r}) = \sum_{i=1}^{N} \left|\varphi_i(\vec{r})\right|^2 \tag{3.18}$$

and the KS kinetic energy functional as:

$$T_0[\rho] = -\frac{\hbar^2}{2m}\sum_{i=1}^{N}\int d\vec{r}\,\varphi_i^*(\vec{r})\nabla^2\varphi_i(\vec{r}) \tag{3.19}$$

By incorporating all the complicate many-body terms into the XC term, eqn. (3.16) can be rewritten as:

$$E[\rho,V]=T_0[\rho]+\int d\vec{r}V_{\text{ext}}(\vec{r})\rho(\vec{r})+\frac{1}{2}\int\int d\vec{r}d\vec{r}\,'\frac{\rho(\vec{r})\rho(\vec{r}\,')}{|\vec{r}-\vec{r}\,'|}+E_{\text{xc}}[\rho] \tag{3.20}$$

where, $T_0[\rho]$ is the independent-particle kinetic energy, $\int d\vec{r}V_{\text{ext}}(\vec{r})\rho(\vec{r})$ represent for the external potential generated by the nuclei and any other external fields, $\frac{1}{2}\int\int d\vec{r}d\vec{r}\,'\frac{\rho(\vec{r})\rho(\vec{r}\,')}{|\vec{r}-\vec{r}\,'|}$ denote the energy of Coulomb interaction, and $E_{\text{xc}}[\rho]$ is the XC energy. If the total number is conserved for the particles:

$$\int d\vec{r}\rho(\vec{r})=N \tag{3.21}$$

and apply variational to eqn. (3.21),

$$\left\{-\frac{\hbar^2}{2m}\nabla^2+\int\frac{\rho(\vec{r}\,')}{|\vec{r}-\vec{r}\,'|}d\vec{r}\,'+\frac{\delta E_{\text{xc}}[\rho]}{\delta\rho(\vec{r})}+V_{\text{ext}}(\vec{r})\right\}\varphi_i(\vec{r})=\varepsilon_i\varphi_i(\vec{r}) \tag{3.22}$$

This is the typical representation of KS equation, and it can be rewritten as:

$$\left\{-\frac{\hbar^2}{2m}\nabla^2+V_{\text{eff}}(\vec{r})\right\}\varphi_i(\vec{r})=\varepsilon_i\varphi_i(\vec{r}) \tag{3.23}$$

where $V_{\text{eff}}(\vec{r})$ represent for an effective external potential that non-interacting electrons are locally subjected to,

$$V_{\text{eff}}(\vec{r})=\int\frac{\rho(\vec{r}\,')}{|\vec{r}-\vec{r}\,'|}d\vec{r}\,'+\frac{\delta E_{\text{xc}}[\rho]}{\delta\rho(\vec{r})}+V_{\text{ext}}(\vec{r}) \tag{3.24}$$

where $\int\frac{\rho(\vec{r}\,')}{|\vec{r}-\vec{r}\,'|}d\vec{r}\,'$ for the electronic Coulomb interactions, $\frac{\delta E_{\text{xc}}[\rho]}{\delta\rho(\vec{r})}$ for the XC potential that contains all the complicate many-body interactions, $V_{\text{ext}}(\vec{r})$ denotes the external potential.

The significance of the KS equations is resulted in transforming the interacting many-body problem into another form regarding the independent particles. In this sense, the ground

state problem of the interacting many-body system is then treated as a similar problem but for independent particles in an effective potential field, thus giving a strictly theoretical basis for the single-electron approximation. Compared with the HF method, the KS equation replaces the model of interacting particles with the non-interacting one and incorporates the complexity of the interactions into the XC functional that decomposes into the exchange and correlation terms. The exchange energy refers to the reduction in the energy caused by the antisymmetry of the wavefunction. The correlation energy corresponds to the differences between the actual total energy of various practical systems and the one only considers the exchange energy. Although the KS equation is strictly derived and superior to the HF approximation, still the XC term is unknown, one needs to find the appropriate expression of XC energy for a soluble KS equation.

3.5.4 Exchange-correlation functionals

The interpretation of the KS equation is simpler and more rigorous than the HF approximation, which conceptually replaces the ground state of many-electron problem by an auxiliary independent-particle problem. Indeed, the KS equation has led to significant approximations that are the basis of most calculations which aiming of making "first-principles" or "*ab-initio*" predictions for the condensed matter. Only by obtaining an accurate and easy-to-express XC term can the equation be practically soluble in the computational science, and presumably is a key to accurately solving the quantum many-body problems. Great effort has been made to explore the representation of XC energy, the local density approximation (LDA)[17-19] and generalized-gradient approximations (GGAs) are the most notably and remarkably accurate ones,[20-22] among a variety of different approximation methods that have been proposed.

3.5.4.1 Local density approximation

LDA was developed by W. Kohn and L. J. Sham in 1965, in which they replaced the interacting electrons in a non-homogeneous electronic system by non-interacting homogeneous electron gas (HEG). Specifically, the electron density in a small volume (*dr*) can be approximately treated by a constant and only relates to its location *r*, within which a HEG without interaction is uniformly distributed in each of these small volumes. Under this approximation, it yields the expression of XC energy of:

$$E_{\mathrm{xc}}[\rho] = \int \rho(\vec{r})\varepsilon_{\mathrm{xc}}(\rho)d^3r \tag{3.25}$$

where $\varepsilon_{\mathrm{xc}}(\rho)$ refers to the XC energy of each particle in a uniform, non-interacting HEG with the electron density of ρ, with the corresponding XC potential as

$$V_{\mathrm{xc}}(\vec{r}) = \frac{\delta E_{\mathrm{xc}}[\rho]}{\delta\rho(\vec{r})} = \varepsilon_{\mathrm{xc}}\left[\rho(\vec{r})\right] + \rho\left(\vec{r}\right)\frac{d\varepsilon_{\mathrm{xc}}\left[\rho(\vec{r})\right]}{d\rho(\vec{r})} \tag{3.26}$$

Here, one needs to figure out the exact form of $\varepsilon_{\mathrm{xc}}[\rho(\vec{r})]$ in order to determine the ground state energy. The commonly used XC energy is constructed by Dirac, which takes the form:

$$\varepsilon_{\mathrm{xc}}[\rho(\vec{r})] = -\frac{3}{4}\left(\frac{3\rho(\vec{r})}{\pi}\right)^{1/3} \tag{3.27}$$

The exchange potential $V_{\mathrm{x}}(\vec{r})$ can be computed once the exchange energy $\varepsilon_{\mathrm{xc}}[\rho(\vec{r})]$ and eqn. (3.26) are combined. The most commonly used correlation energy was computed by Ceperley and Alder using Monte Carlo method, that is, when $r_s \geq 1$ ($r_s = (3/4\pi\rho)^{1/3}$ where r_s denotes the dimensionless Wigner-Seitz parameter), the correlation energy is expressed as:

$$\varepsilon_{\mathrm{c}} = \frac{-0.2846}{1+1.0529\sqrt{r_{\mathrm{s}}}+0.3334r_{\mathrm{s}}} \tag{3.28}$$

However, $r_s < 1$ yields

$$\varepsilon_{\mathrm{c}} = -0.09604 + 0.0622\ln r_{\mathrm{s}} - 0.0232r_{\mathrm{s}} + 0.0040r_{\mathrm{s}}\ln r_{\mathrm{s}} \tag{3.29}$$

In this way, once the $V_c(\vec{r})$ is determined, we can calculate the ground state energy by combining with the KS equations.

However, regardless of the substantial success of LDA on the predictions of various properties (i.e., the lattice constant, binding energy, and mechanical properties), some limitations are also encountered in its actual applications. For instance, the electronic structure calculations of systems that contain 3*d* or 4*f* valence electrons are remarkably deviated from the experimental measurements; it overestimates the binding energy of the *s*-*d* system; it also underestimates the band gap of the semiconductor. LDA is limited in some extent but made itself functional in its own right, meanwhile, these limitations has stimulated researchers to devote into the development of other improved functionals (such as GGAs described below).[23]

3.5.4.2 Generalized-gradient approximations

The term GGAs denotes a variety of methods to consider the gradient of the electron density, for a better description of the true electron density in a non-homogenous electronic system, with a generalized form as:

$$E_{xc}[\rho] = \int f_{xc}\left(\rho(\vec{r}), \left|\nabla\rho(\vec{r})\right|\right) d\vec{r} \tag{3.30}$$

Within the numerous forms that have been proposed for the XC potential under GGAs, Perdew-Burke-Ernzerhof (PBE),[20] BLYP,[22] Perdew-Wang (PW91),[24] and Beeke (B88)[25] are the most commonly used forms, among others. LDA tends to accurately describe the structural and vibrational properties of weakly correlated systems but fails for strongly correlated ones. In contrast, GGAs substantially improve the calculations of exchange and correlation energies, and is potentially more accurate when dealing with molecular crystals and transition metals.

3.5.5 External potential

According to the KS equation, when the XC functional is determined, the next step is to explicitly deal with the problem of the external potential that the electron is subjected to.

The pseudopotential is developed to simplify the complex motion problem of core electrons and nucleus in an atom, such that the original term of Coulomb potential in the Schrödinger equation is eliminated and replaced by a term of modified effective potential. Various attempts have been fulfilled to deal with the pseudopotentials explicitly, such as empirical, semiempirical,[26] norm-conserving,[27] and ultrasoft pseudopotentials,[28] etc. Among them, ultrasoft is the most common form of pseudopotentials that firstly proposed by Vanderbilt et al. in 1900,[28] which has been widely incorporated in the current codes of plane-wave electronic structure calculations. The ultrasoft pseudopotential model can effectively treat the pseudo reference states within the cut-off radius, to reduce the necessity of required plane-wave functions and the workload of calculations, which has achieved remarkable successes in the calculations of transition metals and rare-earth elements.

3.5.6 The realization of DFT

The realization of the first-principles calculation mainly depends on the true internal potential of an ion is replaced by which kind of pseudopotential is chosen to describe the XC term, and what kind of basis vector is implemented to expand the wavefunction. DFT is supported by various solid-state physics and quantum chemistry packages, including ABINIT,[29] Vienna *ab-initio* simulation package (VASP),[30-31] Quantum ESPRESSO,[32] Siesta,[33] WIEN2K,[34] Gaussian,[35] and Crystal.[36]

Most of the theoretical calculations presented in this thesis were performed using VASP,[30-31] which uses the plane-wave basis set to self-consistently solve the KS equation, and describes the interaction between the ionic core-state and electronic valence-state by the ultra-soft pseudopotentials[30] or the projected-augmented wave method,[37] with the Monkhorst-Pack grids to treat the *k*-points in the reciprocal space.[38] The Brillouin zone can be integrated using the tetrahedron method with Blöchl corrections,[39] Fermi-smearing method,[30] Gaussian-smearing method,[40] or Methfessel-Paxton method.[41] Currently, VASP is the most

commonly used package in the computational materials science, due to the high computational efficiency, implementation of multiple computational methods, and a variety of accurate pseudopotentials. Figure 3.2 illustrates a flowchart of the self-consistent calculation process for solving the ground state of the KS equation within the VASP package. First, electron density $\rho(\vec{r})$ of a specific system is assumed for an initial value, and then, the effective potential V_{eff} corresponds to this density is calculated and substituted into the KS equation to solve the wavefunction. Next, the wavefunction is used to calculate a new electron density and compared with the initial guess. Only if the difference between the initial guess and newly computed electron density meets the convergence criterion, VASP package exits the calculation and outputs the results. Otherwise, the iterative procedure is continued with the last computed electron density instead of the initial guess.

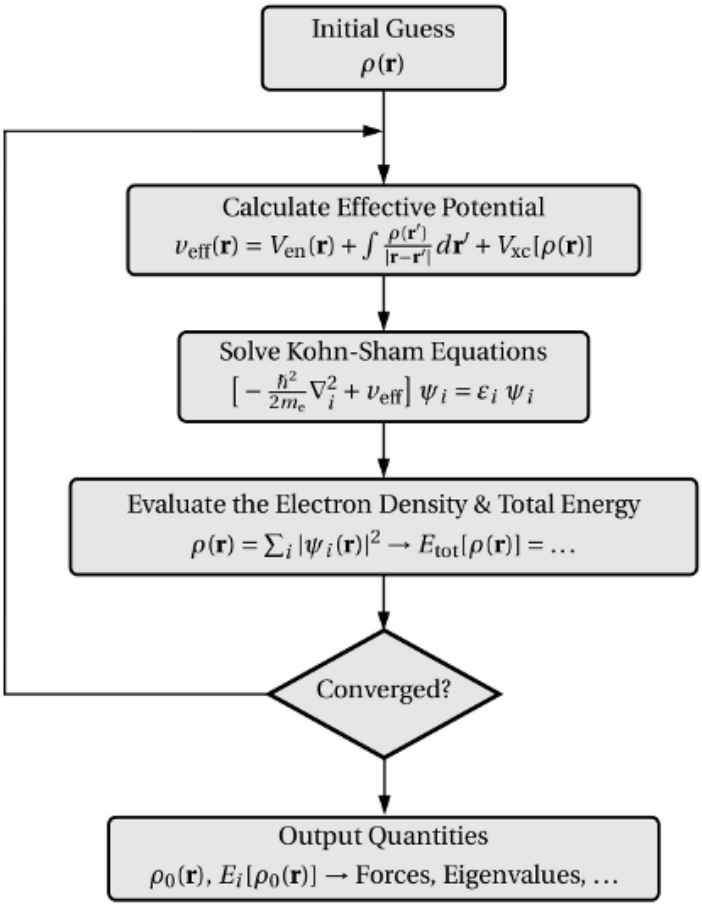

Figure 3.2 A flowchart of the self-consistent loop for solving the ground state of the Kohn-Sham equations within the VASP package.[42]

3.6 References

(1) Raabe, D., *Computational Materials Science-the Simulation of Materials Microstructures and Properties*; Wiley-VCH, **1998**.
(2) http://www.icams.de/content/research/.
(3) Segall, M.; Lindan, P. J.; Probert, M. a.; Pickard, C. J.; Hasnip, P. J.; Clark, S.; Payne, M., First-Principles Simulation: Ideas, Illustrations and the CASTEP Code. *J. Phys.: Condens. Matter* **2002**, *14*, 2717.
(4) Hafner, J., *Ab-Initio* Simulations of Materials Using VASP: Density-Functional Theory and Beyond. *J. Comput. Chem.* **2008**, *29*, 2044-2078.
(5) Born, M.; Oppenheimer, R., Zur Quantentheorie Der Molekeln. *Ann. Phys. (Berlin)* **1927**, *389*, 457-484.
(6) Hartree, D. R. In *The Wave Mechanics of an Atom with a Non-Coulomb Central Field. Part I. Theory and Methods*, Mathematical Proceedings of the Cambridge Philosophical Society, Cambridge University Press: 1928; pp 89-110.
(7) Hartree, D. R. In *The Wave Mechanics of an Atom with a Non-Coulomb Central Field. Part II. Some Results and Discussion*, Mathematical Proceedings of the Cambridge Philosophical Society, Cambridge University Press: 1928; pp 111-132.
(8) Slater, J. C., The Self Consistent Field and the Structure of Atoms. *Phys. Rev.* **1928**, *32*, 339.
(9) Gaunt, J. In *A Theory of Hartree's Atomic Fields*, Mathematical Proceedings of the Cambridge Philosophical Society, Cambridge University Press: 1928; pp 328-342.
(10) Fock, V., Näherungsmethode Zur Lösung Des Quantenmechanischen Mehrkörperproblems. *Z. Phys.* **1930**, *61*, 126-148.
(11) Slater, J. C., Note on Hartree's Method. *Phys. Rev.* **1930**, *35*, 210.
(12) Wang, J.; Wang, G.; Zhao, J., Structure and Electronic Properties of Ge_n (n = 2–25) Clusters from Density-Functional Theory. *Phys. Rev. B* **2001**, *64*, 205411.
(13) Thomas, L. H. In *The Calculation of Atomic Fields*, Mathematical Proceedings of the Cambridge Philosophical Society, Cambridge University Press: **1927**; pp 542-548.
(14) Fermı, E., A Statistical Method for the Determination of Some Properties of Atoms. II. Application to the Periodic System of the Elements. *Z. Phys.* **1928**, *48*, 7379.
(15) Hohenberg, P.; Kohn, W., Inhomogeneous Electron Gas. *Phys. Rev.* **1964**, *136*, B864-B871.
(16) Kohn, W.; Sham, L. J., Self-Consistent Equations Including Exchange and Correlation Effects. *Phys. Rev.* **1965**, *140*, A1133-A1138.
(17) Slater, J. C., A Simplification of the Hartree-Fock Method. *Phys. Rev.* **1951**, *81*, 385-390.
(18) Ceperley, D. M.; Alder, B. J., Ground State of the Electron Gas by a Stochastic Method. *Phys. Rev. Lett.* **1980**, *45*, 566-569.
(19) Perdew, J. P.; Zunger, A., Self-Interaction Correction to Density-Functional Approximations for Many-Electron Systems. *Phys. Rev. B* **1981**, *23*, 5048-5079.
(20) Perdew, J. P.; Burke, K.; Ernzerhof, M., Generalized Gradient Approximation Made Simple. *Phys. Rev. Lett.* **1996**, *77*, 3865-3868.
(21) Perdew, J. P.; Kurth, S.; Zupan, A.; Blaha, P., Accurate Density Functional with Correct Formal Properties: A Step Beyond the Generalized Gradient Approximation. *Phys. Rev. Lett.* **1999**, *82*, 2544-2547.
(22) Lee, C.; Yang, W.; Parr, R. G., Development of the Colle-Salvetti Correlation-Energy Formula into a Functional of the Electron Density. *Phys. Rev. B* **1988**, *37*, 785-789.
(23) Martin, R. M.; Martin, R. M., *Electronic Structure: Basic Theory and Practical Methods*; Cambridge University Press, **2004**.

(24) Perdew, J. P.; Wang, Y., Accurate and Simple Analytic Representation of the Electron-Gas Correlation Energy. *Phys. Rev. B* **1992**, *45*, 13244-13249.
(25) Becke, A. D., Density-Functional Exchange-Energy Approximation with Correct Asymptotic Behavior. *Phys. Rev. A* **1988**, *38*, 3098-3100.
(26) Cohen, M. L.; Chelikowsky, J. R., *Electronic Structure and Optical Properties of Semiconductors*; Springer Science & Business Media, **2012**; Vol. 75.
(27) Hamann, D.; Schlüter, M.; Chiang, C., Norm-Conserving Pseudopotentials. *Phys. Rev. Lett.* **1979**, *43*, 1494.
(28) Vanderbilt, D., Soft Self-Consistent Pseudopotentials in a Generalized Eigenvalue Formalism. *Phys. Rev. B* **1990**, *41*, 7892.
(29) http://www.abinit.org/.
(30) Kresse, G.; Furthmüller, J., Efficient Iterative Schemes for *Ab Initio* Total-Energy Calculations Using a Plane-Wave Basis Set. *Phys. Rev. B* **1996**, *54*, 11169-11186.
(31) Kresse, G.; Furthmüller, J., Efficiency of *Ab-Initio* Total Energy Calculations for Metals and Semiconductors Using a Plane-Wave Basis Set. *Comput. Mater. Sci.* **1996**, *6*, 15-50.
(32) http://www.pwscf.org/.
(33) Soler, J. M.; Artacho, E.; Gale, J. D.; García, A.; Junquera, J.; Ordejón, P.; Sánchez-Portal, D., The Siesta Method for *Ab Initio* Order-N Materials Simulation. *J. Phys: Conden Matter.* **2002**, *14*, 2745-79.
(34) http://www.wien2k.at/.
(35) http://www.gaussian.com/.
(36) http://www.crystal.irnito.it/.
(37) Blöchl, P. E., Projector Augmented-Wave Method. *Phys. Rev. B* **1994**, *50*, 17953-17979.
(38) Monkhorst, H. J.; Pack, J. D., Special Points for Brillouin-Zone Integrations. *Phys. Rev. B* **1976**, *13*, 5188-5192.
(39) Blöchl, P. E.; Jepsen, O.; Andersen, O. K., Improved Tetrahedron Method for Brillouin-Zone Integrations. *Phys. Rev. B* **1994**, *49*, 16223-16233.
(40) Fu, C. L.; Ho, K. M., First-Principles Calculation of the Equilibrium Ground-State Properties of Transition Metals: Applications to Nb and Mo. *Phys. Rev. B* **1983**, *28*, 5480-5486.
(41) Methfessel, M.; Paxton, A. T., High-Precision Sampling for Brillouin-Zone Integration in Metals. *Phys. Rev. B* **1989**, *40*, 3616-3621.
(42) Gös, W. Hole Trapping and the Negative Bias Temperature Instability. Technischen Universität Wien, http://www.iue.tuwien.ac.at/phd/goes/, 2011.

Chapter 4 : Single-Walled Black Phosphorus Nanotube as a Superior Gas Sensor: Compared with Monolayer Black Phosphorus

This chapter is related to the application of black phosphorus in gas sensing. Here the embedded manuscript studied the performance of single-walled black phosphorus nanotube as a superior gas sensor towards sensing the common toxic gases compared to the monolayer black phosphorus, through first-principles calculations. The most stable adsorption configurations and its related adsorption energies and charge transfer were quantified and the curvature effect in controlling the adsorption capability and sensitivity was clarified via modeling the nanotubes with various diameters.

- This chapter is to be submitted, appeared as: Pengfei Ou, Xiao Zhou, Yiqing Chen, Cheng Chen, Fanchao Meng, and Jun Song, **Single-walled black phosphorus nanotube as a superior gas sensor: Compared with monolayer black phosphorus**.

4.1 Abstract

The capability of single-walled black phosphorus nanotube (SW-PNT) of sensing the common toxic gas molecules (NH_3, CO, NO, NO_2, and SO_2) was examined by using first-principles calculations. Various adsorption characteristics, including the adsorption geometry and energy, and the transferred charge were determined. SW-PNTs exhibits the strongest interaction with NO_2 molecule, among others, reflected by the adsorption energy of 661.9 meV on SW-PNTs which is almost three time higher than that of 243.2 meV on monolayer. By analyzing the charge density differences, NH_3 is acting as electron donor when adsorbed on SW-PNTs, whereas the remaining acting as electron acceptors. In contrast to the results on monolayer black P, the SW-PNTs are generally more sensitive towards sensing these common toxic molecules particularly for NO_2, which is evidenced by larger adsorption energy, structural distortion of molecules, and transferred charge values. Furthermore, a comparative study on the curvature effect indicates that the adsorption capability of NO_2 on the outer surface is decreasing with the increasing radius of SW-PNTs. These results suggest that the sensitivity of a gas sensor by using field-effect transistor can be enhanced by applying the SW-PNT with a smaller diameter as the channel material.

4.2 Introduction

To date, monolayer black phosphorus (black P), i.e. phosphorene, has offered great opportunities in various applications ascribed to its unique physical and chemical properties, including a high hole mobility of up to 1 000 $cm^2 V^{-1} s^{-1}$ that exceeds the graphene or transition metal dichalcogenides (TMDCs),[1] an on/off ratio of up to 10^4,[2-3] and in-plane anisotropy resulted from its orthorhombic puckered structure. Monolayer black P is also anticipated to demonstrate other intriguing electronical, mechanical, and optical properties which can be tuned by strain engineering,[4-7] nanostructuring,[8-11] chemical modification,[12-14] and electric gating,[3, 15-18] due to its tunable band gap[19] and the sp^3 hybridization within the basal plane.

Chemical sensing is one of the most promising among various applications for black P due to the following reasons. First, the chemical sensing towards various chemicals on black P is suggested to be comparable or even higher than MoS_2 and graphene by using first-principles calculations, particularly for NO and NO_2.[12, 20] Second, black P exhibits larger surface-to-volume ration than MoS_2 and graphene that inherited from its orthorhombic puckered structure, this would maximize the adsorption effect and thus enhance the sensitivity of the channel material.[21] Third, the out-of-plane electrical conductance is much reduced in black P, which may render an enhanced response signal to the target analytes when adsorbed on surface.[22] Furthermore, black P is also predicted to be potential candidate for a superior gas sensor owing to its direction-selective current-voltage characteristics.[12]

In previous studies, single-walled black P nanotubes (SW-PNTs) have been predicted to be possible by theoretical calculations,[23-25] and also have initiated several studies on their unique and tunable properties. More recently, the monolayer black P was predicted to maintain its stability under a tensile strain of up to 30% by first-principles calculations[5] due to its small Young's modulus,[4] which renders PNTs worth exploring. Besides, the band gap of both zigzag and armchair PNTs are indirect, exhibiting highly anisotropic electronic behaviors. It was found that zigzag PNTs can achieve semiconducting to semi-metallic transitions, while armchair PNTs always behave as semiconductors.[10] The electronic properties of PNTs can also be tuned from semiconducting to metallic via applying strain and electric field.[8] Recently, based on the numerical simulations via molecular dynamics, Shi et al.[26] discovered that a wider black P nanoribbon can self-assemble into chiral nanotubes with different radii upon carbon nanotubes, which provides a possibility of potential fabrication for the PNTs. Therefore, to exploit the potential applications of black P, it is necessary to further explore the potential of PNTs as the channel material in a gas sensor.

In this study, a comparatives study of various adsorption characteristics when different toxic gas molecules adsorbed on the outer surface of SW-PNTs and monolayer black P was performed, including NH_3, CO, NO, NO_2, and SO_2. Firstly, we determined the preferential binding positions and corresponding adsorption energies. It is demonstrated that the binding strength is highly correlated with the amount of transferred charge between the P surface (i.e., SW-PNTs and monolayer black P) and gas molecules. The SW-PNTs are more stable and sensitive than monolayer black P regarding the sensing of gas molecules, particularly for NO_2. The adsorption on black P-based systems (i.e., SW-PNTs and monolayer black P in the present case) are generally stronger than MoS_2 and graphene, which inclines to generate an enhanced influence on the electronic properties of host layer, rendering them a more sensitive gas sensor. Particularly, the curvature effect on detecting gas molecules was also studied in a comparative manner, through modeling SW-PNTs with various diameters. To our knowledge, no previous studies have reported on these issues theoretically or experimentally.

4.3 Computational method

Density functional theory (DFT) calculations were performed by Vienna *ab-initio* simulation package (VASP)[27-28] to investigate the mechanisms of the common toxic gas molecules adsorbed on the SW-PNTs and monolayer black P. Spin-polarization effect was considered when calculating the adsorptions of paramagnetic gas molecules, i.e., NO and NO_2, but not included for other gas molecules. The generalized gradient approximation was adopted to treat the exchange-correlation functional as parametrized by Perdew-Burke-Ernzerhof.[29] The adsorption geometries were performed by using a conjugate gradient algorithm, and the structural relaxation was considered to be converged until the Hellmann-Feynman force on each of the atom fell under 0.01 eV $Å^{-1}$. The empirical correction of DFT-D2 method of Grimme was included for a better description of the weak van der Waals force.[30]

The lateral distance between each SW-PNT was set to 30 Å to make sure the supercell was not interacting with its periodic image. In comparison, the black P was modeled as a 4 × 3 × 1 monolayer which contains 48 P atoms with a distance of 20 Å in the vertical direction, to avoid the mirror interaction between multiple monolayer. The plane-wave energy cut-off was chosen as 500 eV and the *k*-point grids were set to gamma-only and 4 × 4 × 1 for SW-PNTs and monolayer black P, respectively. The gas molecules were isolated in a cubic box with a more than 20 Å length on each side and used gamma-only *k*-point of Brillouin zone to determine their total energies. The adsorption characteristics of gas molecule on the outer surface of SW-PNTs and monolayer black P was simplified by only considering one molecule. For simplicity, the configurations with only one gas molecule adsorbed onto the outer surface of the SW-PNTs or monolayer black P have been investigated. The volume and shape of unit cell were kept fixed with only the positions of atoms to relax when relaxing the adsorption geometries of these gas molecules on the SW-PNTs, whereas, the volume and shape along with all the atoms were allowed to relax in the structural relaxation of basal plane of monolayer black P.

4.4 Results and discussion

4.4.1 Atomic structures of monolayer black P and SW-PNT

Black P, the most thermodynamically stable P allotrope, which is layered material that constructed in a puckered honeycomb structure with orthorhombic crystal system (space group of *Cmca* (no. 64) and Pearson symbol of *oC*8), as shown in Figure 4.1a. Each P atom is bonding with other three P atoms, within which, three out of four are sitting in the same plane, with the fourth one located at the paralleled adjacent plane. The lattice constants of monolayer black P is optimized to be $a = 4.57$ Å and $b = 3.30$ Å respectively, and calculated puckered height (i.e., the interlayer distance between monolayer) is 2.11 Å. The optimized bonding lengths of P−P bonds are 2.22 Å and 2.25 Å for the bonds in horizontal and vertical directions,

respectively. The bond angles at each P atom in monolayer black P is added up to 303.78°, close to the idealized value of 328° for the sp^3 (tetrahedral) hybridization and much smaller than 360° for sp^2 (planar) hybridization.

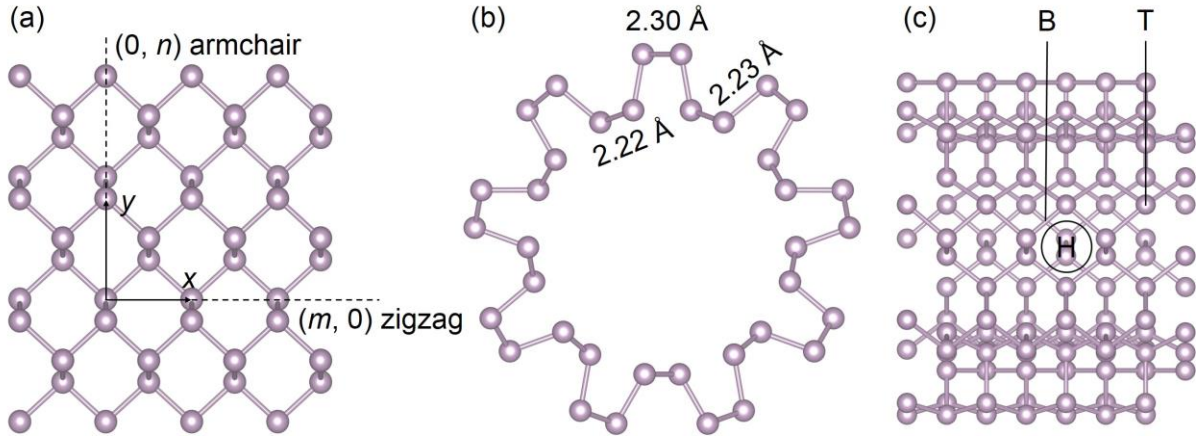

Figure 4.1 Schematic view of SW-PNT which is formed by rolling up a (a) monolayer black P with the roll-up vector of $\vec{R} = m\vec{x} + n\vec{y}$, where *x* and *y* denote the zigzag and armchair directions, respectively. Top (b) and side (c) views of the atomic structure of (0, 9)SW-PNT along the armchair direction. Three adsorption sites of the SW-PNT were chosen by considering their high symmetry, i.e., H site (a hexagon hollow), T site (top of a P atom), and B site (between the P−P bond that forms a certain angle).

The SW-PNTs are built by rolling up a monolayer black P along either armchair or zigzag directions (see Figure 4.1a). A pair of integer indexes (*m*, *n*) can be used to describe the formation of any specific SW-PNT, usually named as zigzag (*m*, 0) or armchair (0, *n*) nanotubes based on their diameters and chirality. Infinite 1D (0, 8), (0, 9), (0, 10), (0, 11), and (0, 12)SW-PNTs which includes 96, 108, 120, 132, and 144 atoms respectively, were chosen as the research objectives due to their higher symmetries and lower computing workloads. Periodic-boundary conditions and supercell approximations are used herein.

4.4.2 Adsorption geometry and energy

To quantitative compare the adsorption strength between the SW-PNTs or monolayer black P and studied gas molecules, the adsorption energy obtained from DFT calculations is defined as eqn. (4.1)

$$E_{\text{ad}} = E(\text{gas/substrate}) - E(\text{gas}) - E(\text{substrate}) \tag{4.1}$$

where E(gas/substrate), E(gas), and E(substrate) denotes the total energy of SW-PNT/monolayer black P with an adsorbed gas molecule, the energies of an isolated gas molecule and SW-PNT/monolayer black P, respectively. In this case, a negative E_{ad} implies an exothermic adsorption process which is energetically favored, in the contrary, a positive one refers to the opposite scenario.

To determine the most stable configurations, various orientations of NH_3, CO, NO, NO_2, and SO_2 molecules relating to the adsorption sites with high structural symmetry on SW-PNTs and monolayer black P are examined, respectively. Taking the NO adsorption as an illustrative example, initially, the adsorption geometries were modeled by placing one NO molecule horizontally or vertically on the outer surface of (0, 9)SW-PNT with a distance of ~2 Å. Besides, the vertical adsorption can be varied into two orientations, either the N or O atom interact with and pointing to the P atom in (0, 9)SW-PNT. Specifically, three different adsorption sites that exhibits high structural symmetry were considered, i.e., Hollow (H) site (a hexagon hollow), Top (T) site (top of a P atom), and Bridge (B) site (between a P−P bond that forms a certain angle) (as illustrated in Figure 4.1c). The high symmetric adsorption sites of monolayer black P were determined by adopting similar strategy as of (0, 9)SW-PNT.

The isolated gas molecules were first optimized to validate the method that applied in the present study, and the calculated bond lengths of NH_3, CO, NO, NO_2, and SO_2 are 1.02, 1.14, 1.17, 1.21, and 1.45 Å, respectively. The bond angles for the non-linear molecules (i.e., NH_3, NO_2, and SO_2) are 106.62°, 133.90°, and 119.25°. These optimized values agree reasonable with the reported experimental and theoretical values in the previous studies.[31-32] In addition to the structural parameters, the total magnetic moment when magnetic NO and NO_2 adsorbed on SW-PNTs and monolayer black P were calculated to be 1 μ_B, which is similar to the theoretical results that reported on the adsorption of monolayer MoS_2.[33]

Table 4.1 Various adsorption characteristics of different gas molecules before and after the adsorption onto (0, 9)SW-PNT and monolayer black P. The bond length of the free molecule (b, in Å), the change of bond length (Δb, in Å) and bond angle ($\Delta\theta$), the adsorption energy (E_{ad}, in meV), and the charge transfer from (0, 9)SW-PNT/monolayer black P to the gas molecule (ΔQ, in e). Negative ΔQ means the gas molecule acts as electron donor and gives electron away to the (0, 9)SW-PNT/monolayer black P.

	Isolated gas		(0, 9)SW-PNT				Monolayer black P			
	b	θ	Δb	$\Delta\theta$	ΔQ	E_{ad}	Δb	$\Delta\theta$	ΔQ	E_{ad}
NH_3	1.022	106.62	−0.001	0.97	−0.029	−416.36	−0.001	0.98	−0.017	−203.40
CO	1.143		0.001		0.026	−288.52	0.001		0.020	−77.28
NO	1.169		0.013		0.168	−456.02	0.018		0.221	−295.03
NO_2	1.212	133.90	0.047	−14.7	0.546	−661.92	0.014	−5.77	0.214	−243.18
SO_2	1.448	119.25	0.004	−0.67	0.098	−422.93	0.001	−0.30	0.031	−127.40

For (0, 9)SW-PNT, as shown in Figure 4.2, remarkable differences in the adsorption geometries were observed for different gas molecules, specifically, (a) NH_3 and NO_2 molecules favor the adsorption at the B site, with N−H and N−O bond length of 1.021 Å and 1.259 Å, respectively. The bond angle of NO_2 after adsorption is 118.41°, which is a large distortion compared to that of 133.90° for its isolate gas phase, indicating a relatively strong interaction between NO_2 and (0, 9)SW-PNT; (b) the O atoms in CO and NO adsorb close to the (0, 9)SW-PNT, and T site is the most energetically favored adsorption site with an adsorption energy of 288.5 and 456.0 meV, respectively. The adsorption energies decrease from NO_2 to CO and follow the sequence of NO_2 > NO > SO_2 > NH_3 > CO. Obviously, the E_{ad} values for NO and NO_2 on (0, 9)SW-PNT are totally different from those on MoS_2 nanotubes. For NO and NO_2, the E_{ad} values on (0, 9)SW-PNT are predicted to be 456.0 and 661.9 meV, which are much larger than that on MoS_2 nanotubes with 129.3 and 35.6 meV, respectively. Since higher adsorption energy results in a strong binding between the adsorbates and substrate, we expect that the interaction between NO or NO_2 and SW-PNTs are much stronger than that of MoS_2 nanotubes.

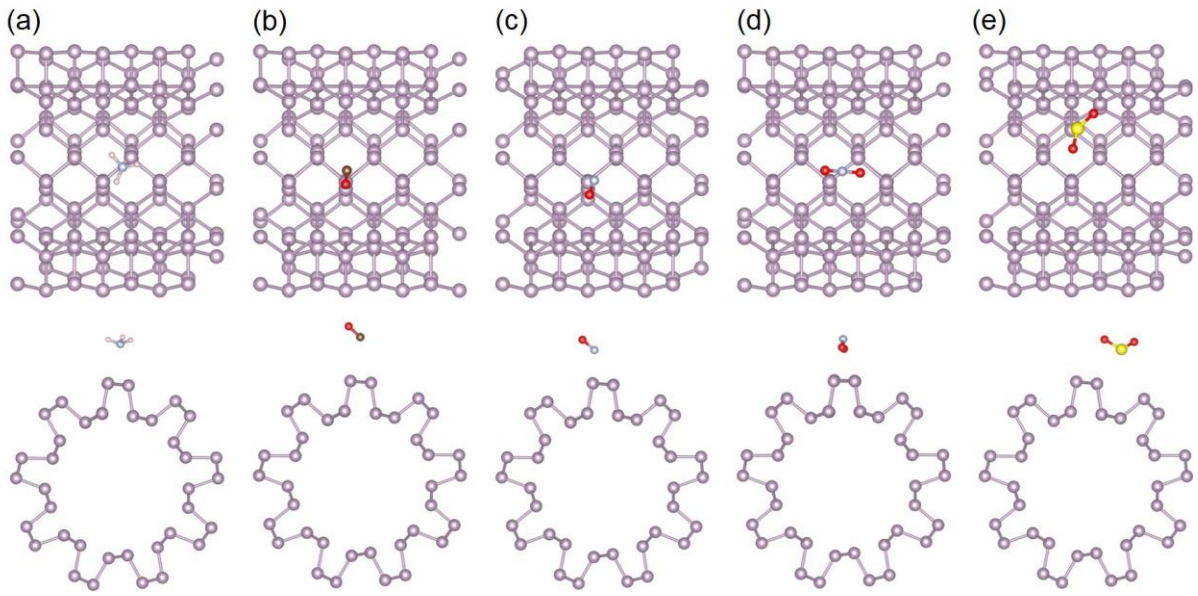

Figure 4.2 Top and side views of the most stable geometries of (a) NH_3, (b) CO, (c) NO, (d) NO_2, and (e) SO_2 adsorbed on the outer surface of (0, 9)SW-PNT are provided in the first and second row, respectively. The purple balls represent the P atoms, whereas the pink, black, white, red and yellow balls indicates the H, C, N, O, and S atoms, respectively.

The circumstances of these gas molecules absorbed on monolayer black P also have been examined compared to that of (0, 9)SW-PNT. All the possible adsorption sites were constructed to achieve the most stable adsorption geometries for each of the gas molecules. Unlike the (0, 9)SW-PNT, NO has the largest adsorption energy of 295.03 meV amongst them, which agrees well with the recent theoretical results[12] and also confirmed the fact that monolayer black P can be applied as the potential channel material in a NO gas sensor. The value of E_{ad} for NO_2 (243.2 meV) adsorbed onto the monolayer black P agrees well with the previous theoretical result based on the GGA functional (273 meV).[20] Additionally, the E_{ad} values for NH_3, CO, and SO_2 are 203.4, 77.3, and 127.4 meV, respectively. According to the calculation results, all gas molecules physically adsorb on monolayer black P since the E_{ad} is generally smaller than 500 meV. No notable variations of bond lengths (Δb) (less than 0.02 Å) in optimized geometries are observed for all gas molecules. For the non-linear gas molecules of NH_3 and SO_2, the bond angles remain unchanged before and after the adsorption, except for NO_2. CO, NO, and NO_2 preferentially adsorb at the T site, among others, however, the NH_3 is

found to be most stable with its center of mass locating at the H site. Meanwhile, SO_2 is almost parallel aligning with the P layer with the S atom sitting on top of the P−P bond. The top and side views of most stable geometries of adsorption of monolayer black P are illustrated in Figure 4.3.

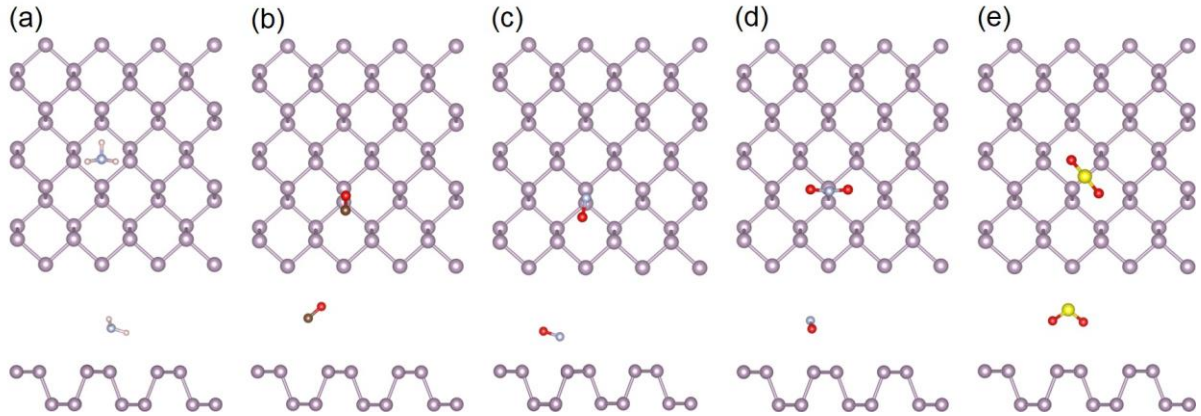

Figure 4.3 Top and side views of the most stable geometries of (a) NH_3, (b) CO, (c) NO, (d) NO_2, and (e) SO_2 adsorbed on the basal plane of monolayer black P are provided in the first and second row, respectively. The purple spheres indicate the P atoms, whereas the pink, black, white, red and yellow spheres represent for the H, C, N, O, and S atoms, respectively.

Next, it is significant to make a comparison between the key characteristics of CO, NH_3, NO, NO_2, and SO_2 adsorbed onto the (0, 9) SW-PNT and monolayer black P. For both systems, the adsorption energies are smaller than 1 eV, indicating the adsorption strength is between the strong physisorption and weak chemisorption. The adsorption energies are much enhanced when these gas molecules adsorbed on (0, 9) SW-PNT, with the maximum increase in E_{ad} of 418.7 meV for NO_2 adsorption, and the minimum of 161.0 meV for NO adsorption. The E_{ad} value of NO_2 adsorption on (0, 9)SW-PNT (661.9 meV) is almost three time higher than that of monolayer black P (243.2 meV), which reflects much stronger interaction between the NO_2 and (0, 9)SW-PNT. The adsorption energies are increased by 213.0, 211.2, and 295.5 meV for NH_3, CO, and SO_2, respectively. After analyzing the adsorption energy, we can conclude that the SW-PNT could enhance the adsorption capability and sensitivity in terms of sensing these molecules, particularly for NO_2, when compared with its monolayer. Black P has been

developed to achieve a highly selective response to paramagnetic NO_2 when operating under room temperature,[20], [34-35] along with an ultrafast response time and a high sensitivity that detects the analytes at ppb levels.[20] Previous theoretical calculations also suggest that the selective response of black P can also be realized owing to its larger molecular adsorption energy compared to other 2D nanomaterials, such as MoS_2 and graphene.[20] Therefore, it is predicted that the SW-PNTs could enhance the adsorption capability and sensitivity of FET gas sensors in detecting NO_2 gas.

Furthermore, the Bader charge analysis[36-39] was employed to analyze the charge distribution and elucidate the nature of interactions between SW-PNT/monolayer black P and adsorbed gas molecules, therefore, to explore the changes in molecules induced by the adsorption. The tendency of gaining or losing the electrons can be interpreted by the relative withdrawing or donating capabilities for electrons of these gas molecules. As shown in Table 4.1, a positive ΔQ means the charge is transferred from the adsorbed gas molecules to SW-PNT/monolayer black P. Specifically, CO, NO, NO_2, and SO_2 demonstrate the capability of electron-withdrawing, whereas NH_3 donates electrons to the host layers. This agrees well with the theoretical findings in the previous studies that, NO and NO_2 are withdrawing electrons, and NH_3 is donating electrons to either monolayer black P[12], [35] or monolayer MoS_2.[31-33] The trend of gaining or losing electrons for NH_3, CO, NO, NO_2, and SO_2 is similar for both SW-PNT and monolayer black P, and the calculation results are also in the same order of magnitude. Detailly, NO_2 acts as charge-acceptor and accepts 0.546 e from the (0, 9)SW-PNT, which is significantly larger than that on monolayer black P with a value of 0.214 e. This is also in line with the fact that the adsorption energy of NO_2 on (0, 9)SW-PNT (661.92 meV) is remarkably higher than that of on monolayer black P (243.18 meV).

The value of transferred charge between SW-PNT/monolayer black P and gas molecules is an essentially important factor determining the sensitivity a FET sensor.[35] The

higher value of transferred charge would result in greater variation in the conductivity of the channel material, and thus more sensitive the sensor. A great amount of charge is involved in the NO_2 adsorption on (0, 9)SW-PNT compared to that of monolayer black P, which indicates that the SW-PNT shows greater sensitivity than monolayer black P when assembled into a NO_2 gas sensor. To estimate the mechanism of charge transfer, we have performed the analysis on the charge density differences between the SW-PNT/monolayer black P and gas molecules in these adsorbed systems. The charge density differences were determined by the following eqn. (4.2)

$$\Delta\rho(z) = \rho(\text{gas/substrate}) - \rho(\text{gas}) - \rho(\text{substrate}) \quad (4.2)$$

where substate denotes the (0, 9)SW-PNT or monolayer black P, and gas represents for the gas molecules of NH_3, CO, NO, NO_2, and SO_2. The iso-surface images of charge density differences are depicted in Figure 4.4 for NH_3, CO, NO, NO_2, and SO_2 molecules adsorbed on (0, 9)SW-PNT, where the light yellow and blue regions indicate the charge accumulation and depletion, respectively. A noticeable charge depletion is observed when NO, NO_2, CO, and SO_2 adsorbed on outer surface of (0, 9)SW-PNT revealing that they are acting as charge acceptors and withdrawing the electrons from (0, 9)SW-PNT, except for NH_3 behaves oppositely by donating electrons to (0, 9)SW-PNT. Charge transfer between analytes and 2D nanomaterials can thus induce the variation in the conductance of black P FETs with varying concentrations. Given that the analytes traps electrons from black P in a gas sensor, it would reduce the concentration of electrons in the conduction band, and result in an increased resistivity of black P. On the contrary, the resistance of black P would increase if the analytes devote electrons to black P in a gas sensor. On the basis of theoretical results that obtained in the present study, we can conclude that different operations should be applied to detect various gas molecules which originated from different charge transfer behavior. Specifically, a more positive gate voltage is thus needed to operate the SW-PNT gas sensors by using FET in the

detection of gas molecules of CO, NO, NO_2, and SO_2; In contrast, a low gate voltage is required when detecting the NH_3.

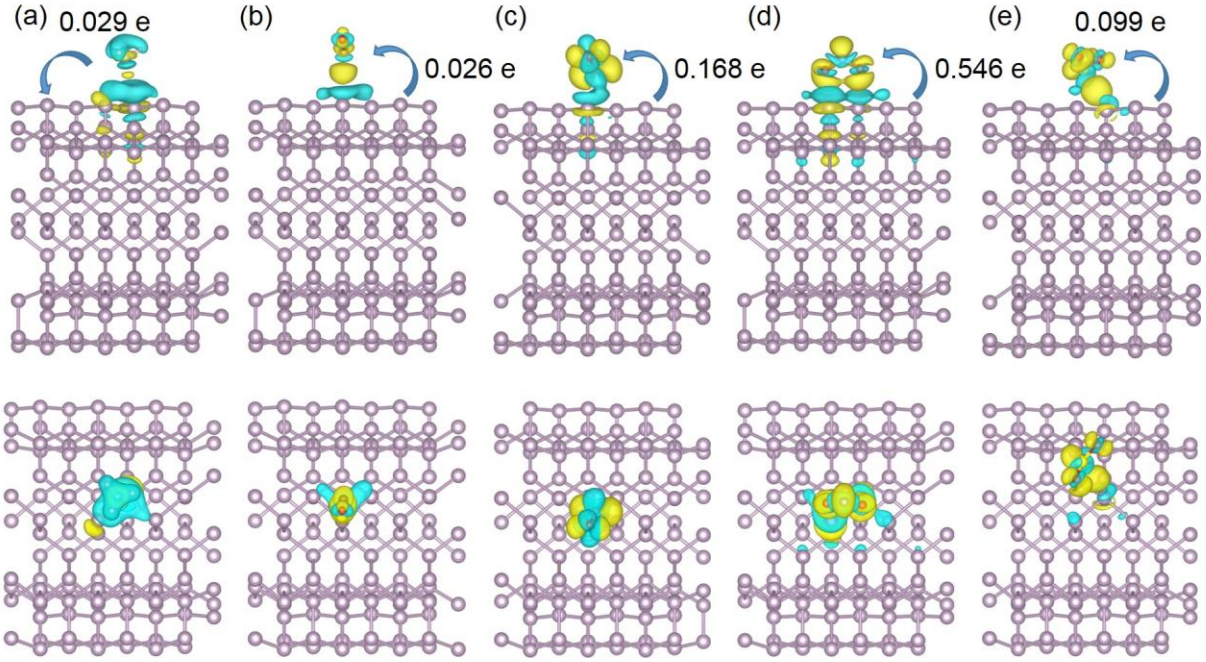

Figure 4.4 Top and side views of the iso-surface plots of charge density difference for (a) NH_3, (b) CO, (c) NO, (d) NO_2, and (e) SO_2 adsorbed on the outer surface of (0, 9)SW-PNT are provided in the first and second row, respectively. The light yellow and blue shaded regions correspond to the charge accumulation and depletion respectively, along with the direction and value of the charge transfer.

4.4.3 Curvature and strain engineering

To study the curvature effect on the adsorption capability of SW-PNTs towards adsorbates, we have further examined the adsorption characteristics of gas molecule adsorption on the SW-PNTs with different curvatures. To be more specific, we have selected multiple SW-PNTs with diameters varying from (0, 8), (0, 10), (0, 11), to (0, 12), and performed similar calculations by placing the studied gas molecules on the outer surface of these SW-PNTs in the same geometries as on (0, 9)SW-PNT. By comparing the results obtained for the (0, 8), (0, 9), (0, 10), (0, 11), and (0, 12)SW-PNTs and the 4 × 3 × 1 monolayer black P (can be treated as a SW-PNT with infinite diameter), it is concluded that the adsorption energy generally decreases with the increasing diameter of SW-PNT despite their zigzag shapes, as shown in

Figure 4.5a. Since the SW-PNT is constructed by rolling up a monolayer black P, the intrinsic strain in SW-PNT usually renders larger bond lengths of P−P bonds compared to its monolayer. To provide intuitive understanding of strain effect on the adsorption energy, the adsorption of NO_2 on a corrugated monolayer black P, which is equal to have an anisotropic compressive strain artificially applied, was also studied. As shown in Figure 4.5b, the NO_2 adsorption energy (604.4 meV) is significantly enhanced on the corrugated monolayer black P compared to that of the pristine one (243.2 meV), which is even comparable to the values of SW-PNTs. We also notice that the recent study by Jeong et al[40] reported that the response and sensitivity of a graphene sensor would be much enhanced by using the self-corrugated graphene, where the wrinkled surfaces of graphene are stemmed from the strain induced structure modifications. In general, compressive or tensile strain has dramatic effect on the NO_2 sensing ability of a black P gas sensor. Further efforts should be devoted to the studies regarding the strain engineering on the adsorption behavior.

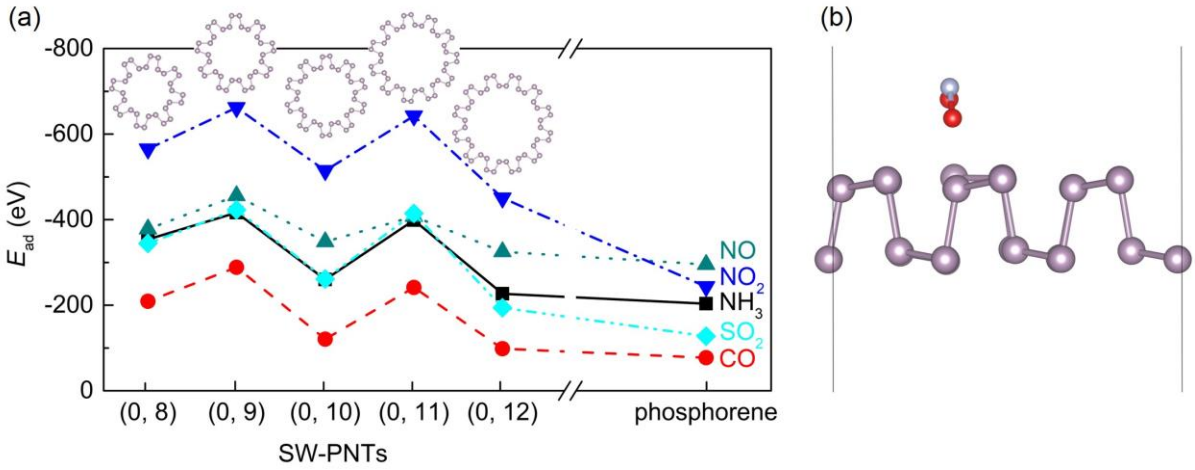

Figure 4.5 (a) The calculated adsorption energy (E_{ad} in meV) for gas molecules of NH_3, CO, NO, NO_2, and SO_2 adsorbed on (0, 8), (0, 9), (0, 10), (0, 11), and (0, 12)SW-PNTs (open geometric shapes), compared with monolayer black P (nanotube with an infinite diameter, the adsorption energies are represented as horizontal dashed lines). (b) Optimized geometry of NO_2 adsorption on the corrugated monolayer black P.

4.5 Conclusions

In conclusion, we have estimated the candidacy of SW-PNTs of chemical sensing the toxic gas molecules (i.e., NH_3, CO, NO, NO_2, and SO_2) by first-principles calculations. Different adsorption sites and orientations were systematically investigated to determine the most stable geometry. Our results demonstrate that all gas molecules are physiosorbed on the outer surface of (0, 9)SW-PNT and behaving as either charge donors or acceptors with a small amount of charge transfer. The largest adsorption energy is achieved when NO_2 adsorbed on (0, 9)SW-PNT, whereas, the adsorption energy is minimized by NH_3 adsorption. Compared with the monolayer black P, we can see that the binding strengths are significant enhanced when gas molecules interact with (0, 9)SW-PNT. In addition to the adsorption energy, we further studied mechanism of charge transfer between the substrate and gas molecules, and the results show that the charge transfer values for NH_3, CO, NO, NO_2, and SO_2 are in the same order of magnitude. Nevertheless, the transferred charge between (0, 9)SW-PNT and NO_2 (0.546 e) is much larger than that of monolayer black P (0.214 e). It is indicated by our theoretical results that the SW-PNTs would have higher capability and sensitivity than its monolayer in the detection of NO_2 gas. Furthermore, the curvature effect on the adsorption characteristics of SW-PNT have also been explored, we found that the enhanced adsorption energy can be obtained by either choosing a SW-PNT with smaller diameter or applying compressive strain. Overall, high adsorption capability turns out to be a remarkable feature of SW-PNT and suggests its promise in the gas sensing application.

4.6 Acknowledgements

The authors would like to acknowledge the support from the NSERC Discovery grant (grant # RGPIN-2017-05187), NSERC Strategic grant (grant # STPGP 494012-16), and McGill Engineering Doctoral Award (MEDA). The authors also would like to thank the

Supercomputer CLUMEQ (Consortium Laval UQAM McGill and Eastern Quebec) for providing computing resources.

4.7 References

(1) Li, L.; Yu, Y.; Ye, G. J.; Ge, Q.; Ou, X.; Wu, H.; Feng, D.; Chen, X. H.; Zhang, Y., Black Phosphorus Field-Effect Transistors. *Nat. Nanotechnol.* **2014**, *9*, 372-377.
(2) Liu, H.; Neal, A. T.; Zhu, Z.; Luo, Z.; Xu, X.; Tománek, D.; Ye, P. D., Phosphorene: An Unexplored 2D Semiconductor with a High Hole Mobility. *ACS Nano* **2014**, *8*, 4033-4041.
(3) Koenig, S. P.; Doganov, R. A.; Schmidt, H.; Castro Neto, A. H.; Özyilmaz, B., Electric Field Effect in Ultrathin Black Phosphorus. *Appl. Phys. Lett.* **2014**, *104*, 103106.
(4) Wei, Q.; Peng, X., Superior Mechanical Flexibility of Phosphorene and Few-Layer Black Phosphorus. *Appl. Phys. Lett.* **2014**, *104*, 251915.
(5) Peng, X.; Wei, Q.; Copple, A., Strain-Engineered Direct-Indirect Band Gap Transition and Its Mechanism in Two-Dimensional Phosphorene. *Phys. Rev. B* **2014**, *90*, 085402.
(6) Ong, Z.-Y.; Cai, Y.; Zhang, G.; Zhang, Y.-W., Strong Thermal Transport Anisotropy and Strain Modulation in Single-Layer Phosphorene. *J. Phys. Chem. C* **2014**, *118*, 25272-25277.
(7) Fei, R.; Yang, L., Lattice Vibrational Modes and Raman Scattering Spectra of Strained Phosphorene. *Appl. Phys. Lett.* **2014**, *105*, 083120.
(8) Guo, H.; Lu, N.; Dai, J.; Wu, X.; Zeng, X. C., Phosphorene Nanoribbons, Phosphorus Nanotubes, and Van Der Waals Multilayers. *J. Phys. Chem. C* **2014**, *118*, 14051-14059.
(9) Wu, Q.; Shen, L.; Yang, M.; Cai, Y.; Huang, Z.; Feng, Y. P., Electronic and Transport Properties of Phosphorene Nanoribbons. *Phys. Rev. B* **2015**, *92*, 035436.
(10) Guan, L.; Chen, G.; Tao, J., Prediction of the Electronic Structure of Single-Walled Black Phosphorus Nanotubes. *Phys. Chem. Chem. Phys.* **2016**, *18*, 15177-15181.
(11) Tran, V.; Yang, L., Scaling Laws for the Band Gap and Optical Response of Phosphorene Nanoribbons. *Phys. Rev. B* **2014**, *89*, 245407.
(12) Kou, L.; Frauenheim, T.; Chen, C., Phosphorene as a Superior Gas Sensor: Selective Adsorption and Distinct *I–V* Response. *J. Phys. Chem. Lett.* **2014**, *5*, 2675-2681.
(13) Ziletti, A.; Carvalho, A.; Campbell, D. K.; Coker, D. F.; Castro Neto, A. H., Oxygen Defects in Phosphorene. *Phys. Rev. Lett.* **2015**, *114*, 046801.
(14) Kulish, V. V.; Malyi, O. I.; Persson, C.; Wu, P., Adsorption of Metal Adatoms on Single-Layer Phosphorene. *Phys. Chem. Chem. Phys.* **2015**, *17*, 992-1000.
(15) Dai, J.; Zeng, X. C., Bilayer Phosphorene: Effect of Stacking Order on Bandgap and Its Potential Applications in Thin-Film Solar Cells. *J. Phys. Chem. Lett.* **2014**, *5*, 1289-1293.
(16) Padilha, J. E.; Fazzio, A.; da Silva, A. J. R., Van Der Waals Heterostructure of Phosphorene and Graphene: Tuning the Schottky Barrier and Doping by Electrostatic Gating. *Phys. Rev. Lett.* **2015**, *114*, 066803.
(17) Liu, Q.; Zhang, X.; Abdalla, L. B.; Fazzio, A.; Zunger, A., Switching a Normal Insulator into a Topological Insulator Via Electric Field with Application to Phosphorene. *Nano Lett.* **2015**, *15*, 1222-1228.
(18) Das, S.; Demarteau, M.; Roelofs, A., Ambipolar Phosphorene Field Effect Transistor. *ACS Nano* **2014**, *8*, 11730-11738.
(19) Das, S.; Zhang, W.; Demarteau, M.; Hoffmann, A.; Dubey, M.; Roelofs, A., Tunable Transport Gap in Phosphorene. *Nano Lett.* **2014**, *14*, 5733-5739.
(20) Cho, S.-Y.; Lee, Y.; Koh, H.-J.; Jung, H.; Kim, J.-S.; Yoo, H.-W.; Kim, J.; Jung, H.-T., Superior Chemical Sensing Performance of Black Phosphorus: Comparison with MoS_2 and Graphene. *Adv. Mater.* **2016**, *28*, 7020-7028.

(21) Ray, S. J.; Kamalakar, M. V.; Chowdhury, R., *Ab Initio* Studies of Phosphorene Island Single Electron Transistor. *J. Phys.: Condens. Matter* **2016**, *28*, 195302.
(22) Abbas, A. N.; Liu, B.; Chen, L.; Ma, Y.; Cong, S.; Aroonyadet, N.; Köpf, M.; Nilges, T.; Zhou, C., Black Phosphorus Gas Sensors. *ACS Nano* **2015**, *9*, 5618-5624.
(23) Seifert, G.; Hernández, E., Theoretical Prediction of Phosphorus Nanotubes. *Chem. Phys. Lett.* **2000**, *318*, 355-360.
(24) Cabria, I.; Mintmire, J. W., Stability and Electronic Structure of Phosphorus Nanotubes. *EPL (Europhysics Letters)* **2004**, *65*, 82.
(25) Hu, T.; Hashmi, A.; Hong, J., Geometry, Electronic Structures and Optical Properties of Phosphorus Nanotubes. *Nanotechnology* **2015**, *26*, 415702.
(26) Shi, J.; Cai, K.; Liu, L.-N.; Qin, Q.-H., Self-Assembly of a Parallelogram Black Phosphorus Ribbon into a Nanotube. *Sci. Rep.* **2017**, *7*, 12951.
(27) Kresse, G.; Furthmüller, J., Efficiency of *Ab-Initio* Total Energy Calculations for Metals and Semiconductors Using a Plane-Wave Basis Set. *Comput. Mater. Sci.* **1996**, *6*, 15-50.
(28) Kresse, G.; Furthmüller, J., Efficient Iterative Schemes for *Ab Initio* Total-Energy Calculations Using a Plane-Wave Basis Set. *Phys. Rev. B* **1996**, *54*, 11169-11186.
(29) Perdew, J. P.; Burke, K.; Ernzerhof, M., Generalized Gradient Approximation Made Simple. *Phys. Rev. Lett.* **1996**, *77*, 3865-3868.
(30) Grimme, S., Semiempirical GGA-Type Density Functional Constructed with a Long-Range Dispersion Correction. *J. Comput. Chem.* **2006**, *27*, 1787-1799.
(31) Zhao, S.; Xue, J.; Kang, W., Gas Adsorption on MoS_2 Monolayer from First-Principles Calculations. *Chem. Phys. Lett.* **2014**, *595–596*, 35-42.
(32) Rongfang, C.; Bo, Z.; Cuifang, J.; Xiaodong, Z.; Zhenyi, J., Theoretical Study of the NO, NO_2, CO, SO_2, and NH_3 Adsorptions on Multi-Diameter Single-Wall MoS_2 Nanotube. *J. Phys. D: Appl. Phys.* **2016**, *49*, 045106.
(33) Yue, Q.; Shao, Z.; Chang, S.; Li, J., Adsorption of Gas Molecules on Monolayer MoS_2 and Effect of Applied Electric Field. *Nanoscale Res. Lett* **2013**, *8*, 1-7.
(34) Abbas, A. N.; Liu, B.; Chen, L.; Ma, Y.; Cong, S.; Aroonyadet, N.; Köpf, M.; Nilges, T.; Zhou, C., Black Phosphorus Gas Sensors. *ACS Nano* **2015**, *9*, 5618-5624.
(35) Cui, S.; Pu, H.; Wells, S. A.; Wen, Z.; Mao, S.; Chang, J.; Hersam, M. C.; Chen, J., Ultrahigh Sensitivity and Layer-Dependent Sensing Performance of Phosphorene-Based Gas Sensors. *Nature. Commun.* **2015**, *6*, 8632.
(36) Henkelman, G.; Arnaldsson, A.; Jónsson, H., A Fast and Robust Algorithm for Bader Decomposition of Charge Density. *Comput. Mater. Sci.* **2006**, *36*, 354-360.
(37) Sanville, E.; Kenny, S. D.; Smith, R.; Henkelman, G., Improved Grid-Based Algorithm for Bader Charge Allocation. *J. Comput. Chem.* **2007**, *28*, 899-908.
(38) Tang, W.; Sanville, E.; Henkelman, G., A Grid-Based Bader Analysis Algorithm without Lattice Bias. *J. Phys.: Condens. Matter* **2009**, *21*, 084204.
(39) Yu, M.; Trinkle, D. R., Accurate and Efficient Algorithm for Bader Charge Integration. *J. Chem. Phys.* **2011**, *134*, 064111.
(40) Yol Jeong, S., et al., Enhanced Response and Sensitivity of Self-Corrugated Graphene Sensors with Anisotropic Charge Distribution. *Sci. Rep.* **2015**, *5*, 11216.

Chapter 5 : Superior Sensing Properties of Black Phosphorus as Gas Sensors: A Case Study on the Volatile Organic Compounds

The results in Chapter 4 demonstrated the potential applications of single-walled black phosphorus (black P) nanotubes as the channel material in a gas sensor for detection of common toxic gas molecules. Recently, MoS_2 and graphene have been demonstrated experimentally to exhibit the capability to detect the volatile organic compounds (VOCs) as an effective method for the early diagnosis of lung cancer. Therefore, to widen the application range of this emerging two-dimensional nanomaterials, Chapter 5 systematically studied the candidacy of monolayer black P as the channel material for a high-performance VOCs sensor. The configurations and energetics of adsorption have been examined by first-principles calculations and it was found that VOCs generally exhibit stronger interaction with monolayer black P compared to the widely studied monolayer MoS_2. Non-equilibrium Green's function formalism was adopted to understand the anisotropic transport behaviors, followed by the analysis of the key characteristics of a VOC sensor including the resistance variation and recovery time.

- This chapter has been published in *Advanced Theory and Simulations*, appeared as: Pengfei Ou, Pengfei Song, Xinyu Liu, and Jun Song. **Superior sensing properties of black phosphorus as gas sensors: A case study on the volatile organic compounds**. *Advanced Theory and Simulations*, **2019**, *2*, 1800103.
  DOI: https://doi.org/10.1002/adts.201800103

5.1 Abstract

The unique structure and prominent properties of black phosphorus (black P) and its monolayer and multilayers in device applications has attracted significant attention to this elemental two-dimensional nanomaterial. In this study, a comprehensive evaluation of the candidacy of monolayer black P as a channel material for high-performance volatile organic compounds (VOCs) sensors is conducted combining first-principles density functional theory calculations and non-equilibrium Green's function formalism. The adsorption configurations and energetics of several typical VOCs (ethanol, propionaldehyde, acetone, toluene, and hexane) on monolayer black P have been examined and it is demonstrated that VOCs generally exhibit stronger interaction with monolayer black P than with the widely studied monolayer MoS_2, indicative of monolayer black P potentially being a more sensitive VOC sensor. Monolayer black P is shown to exhibit highly anisotropic transport behaviors, whereas the absolute modification of current-voltage responses due to VOCs is found to show a trend that is direction-independent. Moreover, the adsorption of VOCs on monolayer black P is strong enough to resist thermal disturbance, yet allows fast recovery time. The results suggest that black P is a compelling and feasible candidate for sensing application of VOCs.

5.2 Introduction

Since the discovery of the wonder material graphene,[1] new two-dimensional (2D) nanomaterials with novel electronic and optoelectronic properties continue to emerge. The 2D counterpart of black phosphorus (black P), being the most stable form amongst numerous allotropes of elemental phosphorus and introduced as "phosphorene",[2] has received great attention recently due to its great promise for use in optoelectronic devices,[3-6] memory devices,[7-8] radio frequency transistors,[9] Schottky diodes,[10-13] and energy storage/conversion systems.[14-15] Black P has a layered structure and the interaction in few-layer black P is associated with a significant charge redistribution, caused by the non-local electron-electron

correlations.[16] Within the monolayer black P that comprises puckered honeycomb structure, each phosphorus atom is bonded covalently with three adjacent phosphorus atoms, arranged in a non-planar fashion.[17-20] Atomically thin black P flakes have been successfully fabricated by methods of micromechanical cleavage using an adhesive tape from their parent bulk crystal,[17, 21] liquid-phase exfoliation,[22-23] and plasma-assisted fabrication.[24] Besides, the band gap of monolayer black P is measured to be ~1.45 eV by photoluminescence spectra.[2]

Among various applications of monolayer and/or multilayer black P, one promising area is its usage in gas/molecule sensors for environmental analysis or bioanalysis. Numerical theoretical studies have been performed to investigate the sensing properties of black P.[25-26] Kou et al.[25] studied the adsorption properties of CO, CO_2, NH_3, NO and NO_2 on monolayer black P using first-principles calculations. They demonstrated that those gas molecules, when adsorbed on monolayer, act as donors or acceptors and cause the modification of electronic properties. A larger change in, e.g., the band structure and/or charge transfer, indicates a higher sensitivity. Their results show that monolayer black P is more sensitive to NO and NO_2, indicating possible application of monolayer black P to nitrogen-based gas induction. Moreover, Kou et al.[25] showed that different gas molecules lead to distinctive current-voltage (*I-V*) responses, e.g., the adsorption of NH_3 or NO induces reduction and increase of current respectively. In another study, Suvansinpan et al.[26] performed first-principles calculations to study metal-doped monolayer black P. For the group of metal dopants (i.e., alkali (Li and Na), p-shell (Al, Pb, and Bi), 3d (Fe, Co, and Ni), 4d (Pd and Ag), and 5d (Au and Pt)) examined, it was shown that metal doping generally enhances the chemical activity of monolayer black P in sensing NO molecules.

On the experimental side, Abbas et al.[27] reported the pioneer study on the chemical sensibility of NO_2 by field-effect transistors (FETs) based on multilayer black P. They showed that the black P sensors exhibit enhanced conduction and high sensitivity when exposed to NO_2

down to 5 ppb, and further when the multilayer black P exposed to NO_2 concentrations of 5, 10, 20, and 40 ppb, the relative conduction changes in FETs followed the Langmuir isotherm for molecules adsorbed on the surface. The systematic enhancement in conductance with the increase in NO_2 concentration indicated that black P was doped with holes and the NO_2 molecules withdraw electrons from black P. It was confirmed that the charge transfer between black P and NO_2 is the dominant sensing mechanism. Compared with other 2D nanomaterials, such as MoS_2,[28-29] the sensitivity of multilayer black P was found to be significantly higher.[27] For instance, the conductance change in a 55 nm multilayer black P exposed to 5 ppb NO_2 was 2.9%, whereas the relative change for an 18 nm thick MoS_2 to 1200 ppb NO_2 was only approximately 1.0%. Cui et al.[30] investigated NO_2 sensing properties of multilayer black P as its thickness varies and proposed that a thickness of 4.8 nm led to the maximum response of the devices. Recently, Cho et al.[31] accurately compared various aspects of the NO_2 sensing performance (i.e., adsorption behavior, selectivity, response/recovery time, and mole response factor) of chemically exfoliated black P, MoS_2, and graphene with similar flake size distribution (on average ~400 nm). The electrical sensing measurements showed that the sensitivity (molar response factor) and response of black P can be up to 20 times higher and 40 times faster than those of MoS_2 and graphene when working at 0.1-100 ppm levels.

In addition to NO_2 detection, multilayer black P has also been shown to be a promising material for methanol and hydrogen sensors. Mayorga-Martinez et al.[32] demonstrated that black P is capable of detecting methanol vapor with electrochemical impedance spectroscopy. The impedance phase that measured at a constant frequency is used for selective quantification of methanol. The low detection limit (LOD) of 28 ppm in this black P vapor sensor is substantially below the approved exposure limit of 200 ppm. This vapor sensing system displayed a high selectivity to methanol at a constant frequency of 1 kHz, a good stability over a 20-day period, as well as a long-term response of about 90% of its initial response for 1140

ppm methanol vapor. Lee et al.[33] recently functionalized exfoliated multilayer black P flakes with Pt nanoparticles and showed that a significant electrical response to H_2 can be achieved by the Pt-functionalized black P sensors with a drain-source current decreased from 2.46 to 1.17 μA under the voltage of +10 meV. They also showed that when the sensor was exposed to a low concentration (4%) H_2 gas, the I_{on}/I_{off} and μ_{eff} ratio increased by 115% and 15.6%. Sensing of H_2 by black P-based sensors have also been studied by Cho et al.,[34] which showed that noble metal (i.e., Au and Pt) incorporated black P enables detection of low concentration of H_2 with high response amplitude. In particular, the as-synthesized Pt/ black P sensor exhibited selective response and highly sensitive to approximately 1% concentration H_2 gas with a resistance variation of ~500% in the channel, showing that heteroatom doping process is an effective way to modify the intrinsic properties and tune the H_2 sensing properties of black P. However, the mechanism underlying this Pt-incorporation induced highly selective H_2 gas sensing is yet to be clarified.

In the present study, we will limit our discussion of black P in its application to the sensing of volatile organic compounds (VOCs) as a case study. VOCs, are defined as organic compounds with relatively high volatility or vapor pressure, many of which can be highly neurotoxic and/or cause long-term health concerns. The analysis of VOCs in exhaled air is a newly developed methodology for early-stage screening and diagnosing the lung cancer, which is significant for enabling effective treatment and improving the survival rates of patients.[35-36] Various methods have been developed to detect the existence of VOCs, which includes gas chromatography-mass spectrometry,[37] flow-tube mass spectrometry,[38] surface acoustic wave sensors,[39] quartz crystal microbalance[40] and chemiresistors.[36] Among various methods, the chemiresistor is particularly interesting due to its power-efficiency, cost-effectiveness, rapidness, reversibility and highly sensitivity. The detection of target VOCs in a chemiresistor is dependent on the change in electrical resistance of channel material when it interacts with

analytes. Therefore, developing a highly efficient channel material is essential to the realization of a high-performance chemiresistor. Monolayer black P is considered as a promising candidate of the channel material for field-effect transistors due to its extraordinary properties. It has been shown to exhibit higher molecular adsorption energies than other 2D nanomaterials (such as MoS_2 and graphene),[25, 31] and it possesses larger inherent surface-to-volume ratio due to its puckered lattice configuration.[41] Monolayer black P also exhibits less out-of-plane electrical conductance compared to other 2D nanomaterials, therefore able to induce a much more sensitive response to target analytes near the phosphorus surface.[27] Additionally, Kou et al. [25] demonstrated that black P is a superior material for gas sensors due to its adsorption sensitive surface and distinctive *I-V* characteristics along armchair and zigzag directions. Given the extraordinary electronic properties of monolayer black P, it is highly desirable to explore and establish the trends and rules of VOCs adsorption on monolayer black P and distinguish the characteristics of the molecular influences on the transport behaviors, which can be used as the effective biomarkers for diagnosing lung cancer.

In this regard, we provide the first theoretical study on the investigation of chemical sensing properties of monolayer black P with five different VOC analytes, specifically, ethanol (C_2H_5OH), propionaldehyde (C_2H_5CHO), acetone ($(CH_3)_2CO$), toluene ($C_6H_5CH_3$), and hexane (C_6H_{14}). These VOCs selected herein are representative examples which individually belongs to the VOC categories of alcohols, aldehydes, ketones, aromatic compounds, and hydrocarbons that could be the potential biomarkers for diagnosing the lung cancer.[36] Employing first-principles density functional theory (DFT) calculations, preferential adsorption sites of VOCs on monolayer black P are identified and the corresponding adsorption energies are obtained. Our results demonstrate that VOCs generally exhibit stronger interaction with monolayer black P than that with the widely studied monolayer MoS_2, indicative of monolayer black P potentially being a more sensitive VOC sensor. The adsorption energetics

of VOCs on monolayer black P are shown to be tunable via strain engineering. The *I-V* characteristics of monolayer black P with and without VOC adsorption are calculated using the non-equilibrium Green's function (NEGF) formalism, demonstrating highly anisotropic transport behaviors, yet the absolute modification of *I-V* responses due to VOCs are found to show a trend that is direction-independent. Moreover, the simulated recovery time are well within the detectable range for most of the VOCs molecules, which indicates good reusability. Our findings suggest that monolayer black P can be a compelling candidate material, combining high sensitivity and fast recovery time for VOC sensors.

5.3 Computational method

5.3.1 First-principles DFT calculations

First-principles DFT calculations were employed for relaxing the structures of VOC/ black P systems and computing the energetics and electronic properties. The calculations were performed using the Vienna *ab-initio* simulation package (VASP)[42] with exchange-correlation interaction treated in the generalized gradient approximation (Perdew-Burke-Ernzerhof functional).[43] The long-range van der Waals interactions were considered and modeled by the DFT-D2 method of Grimme.[44] A cut-off energy of 500 eV was used for the plane wave basis set, and the gamma-only and 4 × 4 × 1 *k*-meshes were employed for the self-consistent relaxation and non-self-consistent calculations respectively. In the calculations, the system comprises a 5 × 7 supercell of monolayer black P with one VOC adsorbed. Additional scaling studies were performed to confirm that this system size is sufficient to eliminate the intermolecular interaction. The in-plane lattice parameters of the monolayer black P were optimized to be $a = 4.57$ Å and $b = 3.31$ Å along armchair and zigzag directions respectively (Figure 5.1), which are in great agreement with the values reported in the previous studies.[45-46] A vacuum slab of 20 Å in thickness was added in the out-of-plane direction to eliminate interactions between periodic images. The structural relaxation was regarded a convergence

when the magnitude of the Hellmann-Feynman force fell below 0.01 eV $Å^{-1}$ for all atoms, and the energy convergence criterion for the electronic wave function was set to be 10^{-6} eV.

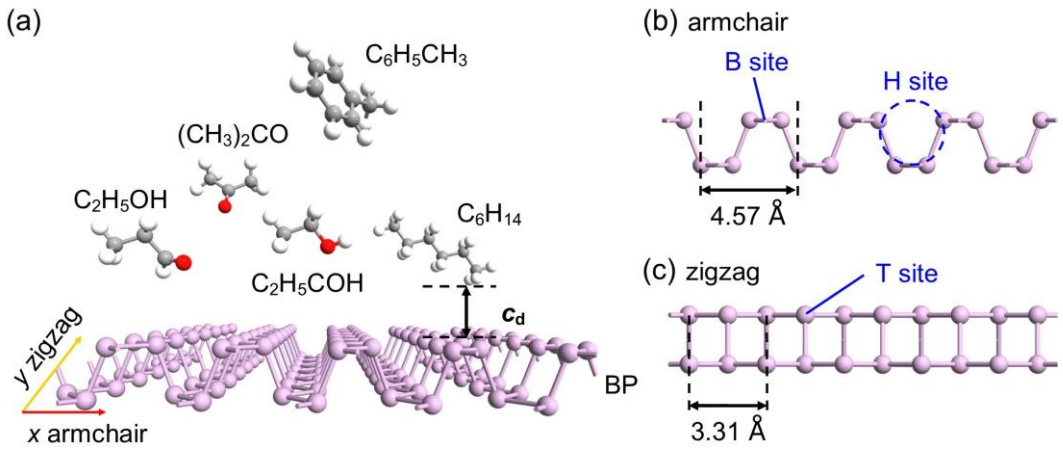

Figure 5.1 (a) Illustrations of typical VOCs adsorbed on the monolayer black P. Side projection views along the two featured directions: (b) armchair and (c) zigzag directions of the atomic structure of monolayer black P, with the three types of potential sites for VOC adsorption, namely, the B-site on top of a P–P bond, H-site above the center of a hexagon, and T-site on top of a P atom indicated.

To identify the possible configurations for VOCs adsorption on the monolayer black P, three potential adsorption locations (see Figure 5.1): i.e., on top of (i) a P−P bond (B-site), (ii) the center of a hexagon (H-site), and (iii) a P atom (T-site), were considered.[22] As a VOC molecule was introduced, its center of mass was positioned at one of these sites and different orientations of the molecule were evaluated. For instance, for $(CH_3)_2CO$, the molecular axis can be oriented parallel or perpendicular to the monolayer black P with either the C or O atom pointing towards the monolayer black P. The adsorption strength of a VOC on the monolayer black P can be quantitatively assessed via the adsorption energy E_{ad}, defined as

$$E_{ad} = E(\text{VOC/black P}) - E(\text{VOC}) - E(\text{black P}) \tag{5.1}$$

where E(VOC/black P) represents the total energy of the monolayer black P with an adsorbed VOC, while E(VOC) and E(black P) respectively denote the energies of the corresponding isolated VOC and pristine monolayer black P. A negative value of E_{ad} indicates that the adsorption is exothermic. Furthermore, to examine the effect of strain on the VOCs adsorption

on the monolayer black P, biaxial strains within the lateral plane varying from −5% to 5% with an interval of 1% were applied. The strain was applied through scaling the in-plane lattice parameters of monolayer black P, for which the details can be found in our previous studies.[47-48]

5.3.2 Transport property calculations

In order to further quantitatively assess the potential of monolayer black P as a VOC sensor, the transport properties of monolayer black P prior to and post to VOC adsorption were carried out using the NEGF technique within the Keldysh formalism as implemented in TranSIESTA package.[49] Geometry optimization has been achieved when the maximum difference between the output and input on each element of the Density Matrix is small than 10^{-4}. The energy cut-off for the real-space mesh was set to 150 Ry. The electron wave function was expanded using a double-ζ polarized (DZP) basis set. Monkhorst-Pack *k*-point grids of 1 × 2 × 50 and 1 × 2 × 1 were employed for electrodes and transport calculations respectively. The current through the atomic scale system is calculated from the Landauer-Büttiker formula,[50]

$$I(V_b) = G_0 \int_{\mu_L}^{\mu_R} T(E, V_b)[f(E-\mu_L) - f(E-\mu_R)]\mathrm{d}E \tag{5.2}$$

where V_b is the bias voltage, μ_L and μ_R are the two electrochemical potentials of left and right leads respectively, $T(E,V_b)$ is the transmission coefficient at energy E and bias voltage V_b, $f(E)$ is the Fermi-Dirac distribution function, and $G_0 = 2e^2/h$ is the quantum conductance. As seen from the above equation, the current is the integral of the transmission coefficient over the bias window.

5.4 Results and discussion

For the five VOCs considered, the adsorption sites along with the associated adsorption energies and the equilibrium positions (i.e., distances) of the molecule above the monolayer

black P are given in Table 5.1. The O-based VOCs generally exhibit smaller adsorption energies than hydrocarbon molecules lacking oxygen groups, namely, $C_6H_5CH_3$ and C_6H_{14}, due to fewer total number of atoms in the oxygen-functionalized VOCs. As seen in Table 5.1, C_2H_5OH and C_2H_5CHO prefer adsorption at the B-site and H-site with adsorption energies of −244 meV and −350 meV respectively, whereas $(CH_3)_2CO$, $C_6H_5CH_3$, and C_6H_{14} prefer T-sites with adsorption energies of −328, −499 and −370 meV respectively. These energetically preferable adsorption configurations for different VOCs are noted in Table 5.1. It is worthy to note that for all the VOCs considered, the adsorption energy is sufficiently larger to resist thermal disturbance at room temperature, i.e., the magnitude of E_{ad} being much beyond k_BT (k_B is the Boltzmann constant).[51-52] As noted from Table 5.1, the distance of a VOC molecule from monolayer black P ranges from 2.42 to 2.94 Å, similar to those for VOC adsorption on monolayer MoS_2 previously reported by Tian et al.[53] It is also interesting to see that the most energetically preferable adsorption configuration is the site where VOC is at the shortest distance from monolayer black P, suggesting that the distance be a direct indication of the interaction strength between a VOC and monolayer black P.

Table 5.1 Calculated values of the adsorption energy (E_{ad}, in meV; bold numbers indicate energetically preferable sites) and distance (c_d, in Å) of the closest atom in VOCs above the monolayer black P for VOCs adsorbed at different adsorption sites. The charge transfers ($\Delta\rho$, in electron) from monolayer black P to the VOCs on energetically preferable site. The calculated adsorption energies of VOCs on bilayer black P, along with available adsorption energies of VOCs on monolayer MoS_2 in literature, are also included for comparison.

	B-site		H-site		T-site		Bilayer black P	$\Delta\rho$	MoS_2	MoS_2
	E_{ad}	c_d	E_{ad}	c_d	E_{ad}	c_d	E_{ad}		E_{ad} [a)]	E_{ad} [b)]
C_2H_5OH	**−244**	**2.80**	−239	2.94	−241	2.86	−256	0.01	−210	−220
C_2H_5CHO	−214	2.59	**−350**	**2.44**	−211	2.60	−362	0.05	−210	−220
$(CH_3)_2CO$	−320	2.76	−247	2.77	**−328**	**2.56**	−338	0.04	−140	−160
$C_6H_5CH_3$	−432	2.47	−417	2.53	**−499**	**2.42**	−508	0.04		
C_6H_{14}	−360	2.58	−341	2.69	**−370**	**2.53**	−383	0.02		

[a)] DFT-D3 calculations;[53] [b)] vdW-DF2 calculations[53]

Fundamentally, the sensitivity of a channel material is dictated by the intercorrelated quantities of adsorption density or coverage, and interaction strength between the analyte and channel material, i.e., the adsorption energy.[54] Larger adsorption energy would lead to more VOCs molecule adsorption on the channel material and consequently enhanced sensitivity. In a previous study, Kim et al.[55] demonstrated that MoS_2 sensors exhibit high sensitivity to VOCs, specifically, down to a concentration of 1 ppm for C_2H_5CHO and $(CH_3)_2CO$ and about 10 ppm for C_2H_5OH, $C_6H_5CH_3$, and C_6H_{14}. As seen in Table 5.1, adsorption of VOCs on monolayer black P show notably larger adsorption energies than those on MoS_2 (from either DFT-D3 and vdW-DF2 calculations).[53] This indicates stronger analyte-channel interaction and suggests that monolayer black P potentially may exhibit higher sensitivity to VOCs than MoS_2.

In addition, monolayer black P was theoretically predicted to hold up almost 30% critical strain,[56] signaling the potential of tuning its chemical and physical properties by strain engineering.[57] Therefore, we examine the influence of strain on the adsorption energetics of VOCs on monolayer black P. The effect of strain is demonstrated in Figure 5.2 in the presentative cases of C_2H_5CHO and $C_6H_5CH_3$ adsorption. We note that the application of ±5% biaxial strain can tune the adsorption energies of C_2H_5CHO and $C_6H_5CH_3$ in the ranges of (−385, −332) and (−467, −551) meV, with compressive strain enhancing the (magnitude of) adsorption energy while tensile strain doing the opposite. The results imply that compression may be used as a means to magnify the sensibility of monolayer black P, e.g., for weakly binding VOC molecules, while tension can help facilitate the removal of VOCs. Moreover, it is important to mention that those adsorption characteristics reported above are well retained as black P goes from monolayer to bilayer or even few layers, except for that the adsorption energy is further enhanced, as demonstrated in Table 5.1, indicative of robust performance in spite of possible black P thickness variation.

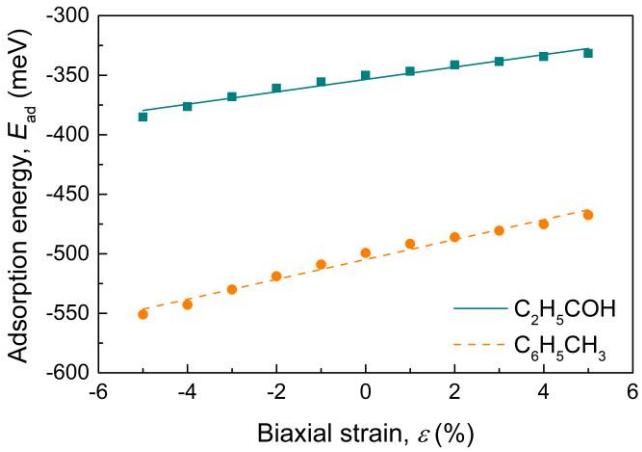

Figure 5.2 The adsorption energy under the application of biaxial strain for C_2H_5CHO and $C_6H_5CH_3$ adsorbed on the monolayer black P. The solid and dashed lines are fitted lines to guide the eyes.

To further elucidate the role of charge transfer between VOCs molecules and monolayer black P, we provide the iso-surface plot of charge density difference for these systems. In particular, we employed the Bader charge analysis[58-61] to examine the charge density difference and thus to determine the charge transfer value and direction. The charge density difference

$$\Delta\rho(r) = \rho_{\text{VOC/black P}}(r) - \rho_{\text{VOC}}(r) - \rho_{\text{black P}}(r) \tag{5.3}$$

is calculated from the spatial charge density distributions of the combined system ($\rho_{\text{VOC/black P}}$), isolated VOC ($\rho_{\text{VOC}}$) and monolayer black P ($\rho_{\text{black P}}$). Figure 5.3 shows the charge density differences for the favorable geometries, where the charge densities of pristine monolayer black P and the isolated VOCs are separately calculated. We find that the VOCs act as charge acceptors, taking charge between 0.01 and 0.05 electrons from monolayer black P. Strong charge redistribution is observed for the cases of C_2H_5OH, C_2H_5CHO, and $(CH_3)_2CO$, as seen in Figure 5.3a-c, which can be attributed to the strong electronegativity of oxygen atom in those VOC molecules. On the other hand, there is significantly less charge redistribution for $C_6H_5CH_3$ and C_6H_{14} (see Figure 5.3d and e). Comparing the charge transfer and redistribution behaviors with those of VOCs on monolayer MoS_2,[53] C_2H_5OH acts as charge acceptor while

C_2H_5CHO and $(CH_3)_2CO$ act as charge donors, when adsorbed on MoS_2. Furthermore, there is generally larger degree of charge transfer and redistribution for VOCs on monolayer black P than on monolayer MoS_2, consistent with the higher adsorption energy level.[53]

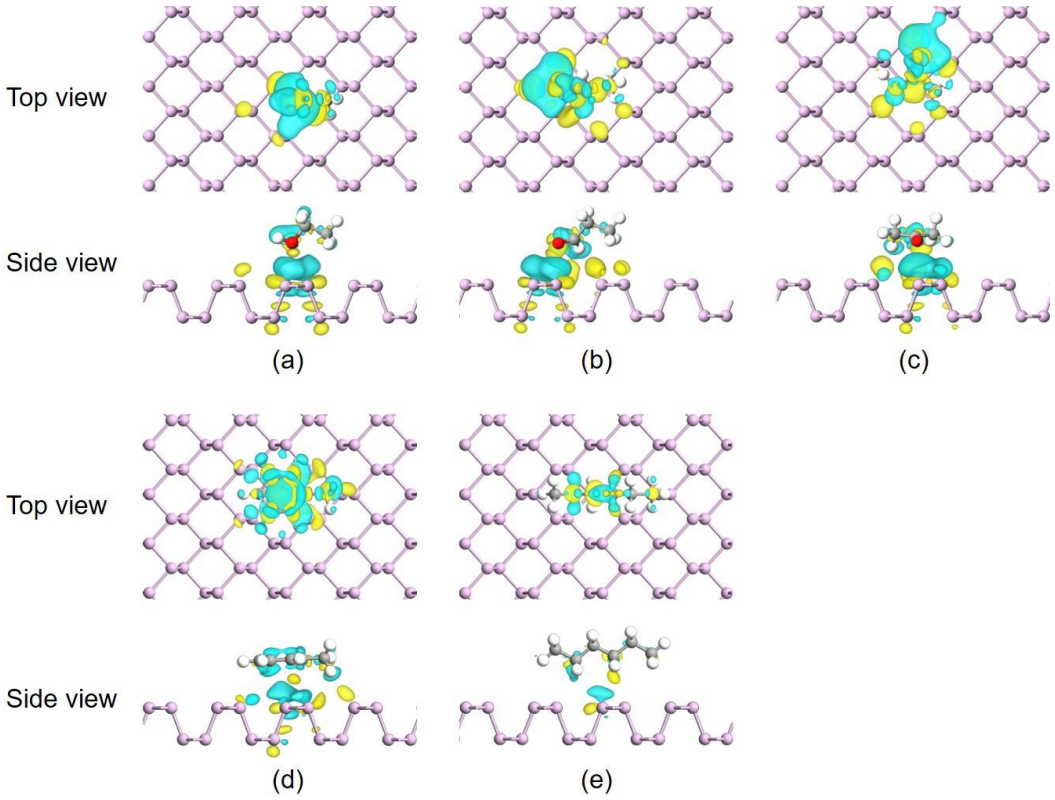

Figure 5.3 Top and side views of the charge density difference contour plots for (a) C_2H_5OH, (b) C_2H_5CHO, (c) $(CH_3)_2CO$, (d) $C_6H_5CH_3$, and (e) C_6H_{14} adsorbed on monolayer black P (only a 4 × 4 supercell is shown for readability). The white, brown, red, and purple spheres represent hydrogen, carbon, oxygen, and phosphorus atoms, respectively. Yellow and blue colors correspond to charge accumulation and depletion respectively. For the contour plots, the iso-surface value is 0.002 e $Å^{-3}$.

To clarify the effects of VOCs adsorption on the electronic structures, the total density of states (DOS) of monolayer black P post VOC adsorption and projected DOS from various VOCs are calculated and presented in Figure 5.4. Our calculations show that the pristine monolayer black P exhibits a direct band gap of 0.9 eV, in agreement with previous reported values of 0.91 eV and 0.80 eV from first-principles studies by Wang et al.[62] and Kulish et al.[63] respectively, and the experimentally measured transport band gap of 1.0-1.5 eV.[64] We can see that overall the adsorption of VOCs hardly modifies the band gap, exerting rather minor

influence on the valence and conduction bands. The adsorbed VOCs molecules only contribute deeply in the valence band within the range from −1.5 eV to −4.0 eV, producing no noticeable modifications of the DOS near the Fermi level and thus have no relevant influence on the electronic properties. This is consistent with the small adsorption energies of VOCs.

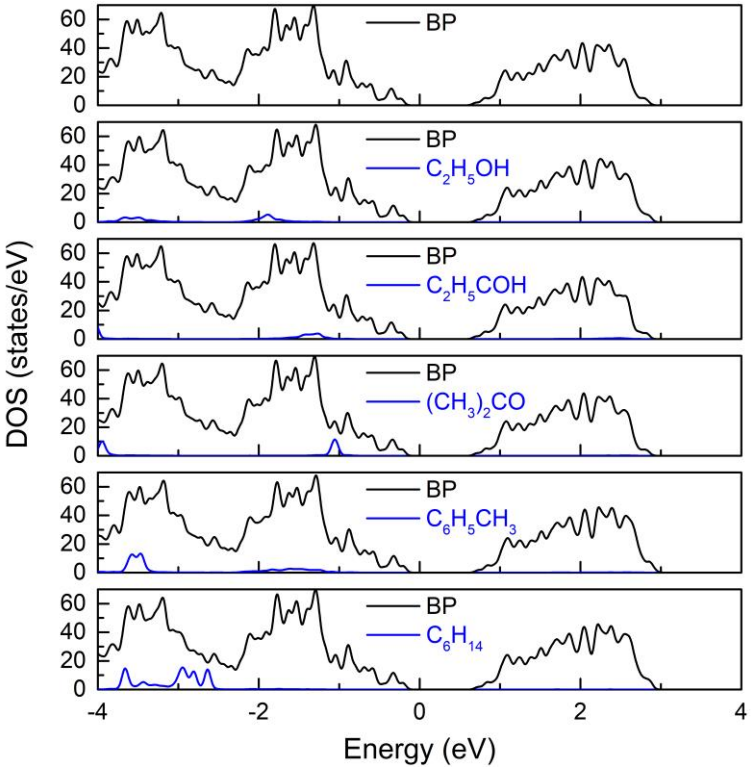

Figure 5.4 Calculated density of states (DOS) plot of pristine monolayer black P (top) in comparison with the projected DOSs of monolayer black P (black) and the VOCs (blue) post adsorption. The zero-energy point corresponds to the Fermi energy.

Although the electronic properties of monolayer black P are not much affected by the adsorption of VOCs, the charge transfer induced by the adsorption is expected to affect the resistance of the material system, which can be experimentally measured and serve as a marker for VOCs sensors. To quantitatively estimate the sensitivity of monolayer black P as a VOC sensor, the *I-V* characteristics through the material with and without VOC adsorption in the scattering region between two semi-infinite electrodes are studied using the NEGF technique.[49] As shown in Figure 5.5a,b, two semi-infinite electrodes (armchair: 9.14 × 9.96 $Å^2$, zigzag: 9.96 × 9.14 $Å^2$) of monolayer black P connect to a central scattering region

(armchair: 36.56 × 9.96 $Å^2$, zigzag: 39.84 × 9.14 $Å^2$), being built from the preferential VOC adsorption configurations (see Figure 5.3) previously obtained from DFT calculations. The corresponding *I-V* characteristics of monolayer black P with and without VOC adsorption, along the armchair and zigzag directions, are shown in Figure 5.5c and d, respectively. With a bias voltage applied, the Fermi level of the left electrode shifts upward with respect to that of the right electrode. The current starts to flow only after the valence band maximum (VBM) of the left electrode reaches the conduction band (CBM) of the right electrode. As a result, there is no current passing through the center scattering region when the bias voltage is smaller than ~0.9 V, the band gap of monolayer black P. As the bias voltage further increases, the currents increase monotonically with the voltage. Comparing Figure 5.5c and d, we note highly anisotropic *I-V* responses along the two directions, with decreased current at the scale of μA along the armchair direction after monolayer black P exposed to VOC analytes while increased current at the scale of nA along the zigzag direction. The anisotropic transport properties of monolayer black P originate from its anisotropic electronic band structures, which exhibit much more significant dispersions along the armchair direction, namely the Γ-Y direction in the reciprocal space.[25] Nonetheless, if only the absolute value (in current change) is considered, a similar trend can be observed regardless of the direction, with C_2H_5CHO causing the largest change in current, followed by C_2H_5OH, $C_6H_5CH_3$, C_6H_{14}, and $(CH_3)_2CO$, at a certain applied bias voltage. After the determination of *I-V* characteristics of monolayer black P, we further calculate the response of the VOC sensor in terms of the resistance variation. Figure 5.6a presents the normalized response ($\Delta R/R_b$) of the monolayer black P sensor for the five VOCs at bias voltage of 2 V. Here, R_b and ΔR respectively represent the baseline resistance of the sensor and the change in resistance of the sensor after exposure to VOC analytes. The monolayer black P channel shows similar response behaviors with five VOCs, with the largest increment in resistance of approximately 19% for C_2H_5CHO. The reduction of current or

increase of resistance after the VOCs adsorption which can be directly measured in experiment.[55]

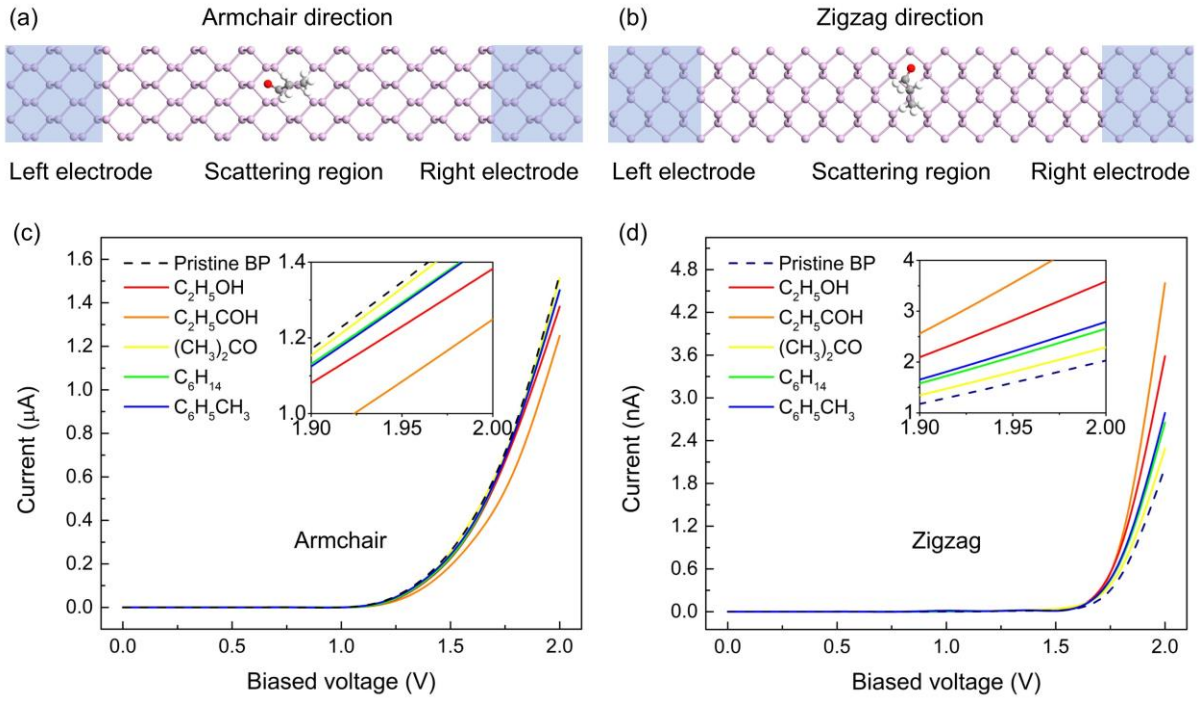

Figure 5.5 Illustrations of the two-probe systems where semi-infinite left and right electrodes of monolayer black P (blue shaded region) are in contact with the central scattering region with one VOC analyte along a) armchair and b) zigzag direction respectively. Calculated current-voltage (*I*-*V*) characteristics of monolayer black P before (black dashed line) and after (color solid lines) the exposure of VOCs analytes along c) armchair and d) zigzag direction respectively.

Besides the sensitivity, another important aspect to assess the performance of a gas sensor is its reusability, which can be typically achieved by heating. Theoretically, the recovery time is predicted by the following equation,[65]

$$\tau = \nu^{-1} \exp\left(\frac{|E_{ad}|}{k_B T}\right) \tag{5.4}$$

where ν denotes the attempt frequency of bond breaking, and thus small $|E_{ad}|$ indicates a fast desorption of VOCs molecules. Calculated from eqn. 5.4, the recovery times (we assume ν = 1THz and T = 300K) for different VOCs are shown in Figure 5.6. We see that C_2H_5CHO, C_2H_6CO and C_6H_{14} show μs scale recovery times while C_2H_6CO exhibits a ms scale recovery

time. Those τ values are well within the detectable range[31] and indicate very fast recovery.[66-68] One exception is the case of C_2H_5OH, which shows very small recovery time (at 300K), i.e., $\tau = 12.34$ ns, and would be challenging to detect at room temperature. However, μs or ms scale recovery time may be achieved for C_2H_5OH via strain engineering (to enhance its adsorption energy, as mentioned earlier) or increasing the temperature (e.g., 6.59 μs at 500K). Therefore, overall the above demonstrates that monolayer black P promise a good combination of high sensitivity and fast recovery as VOC sensors.

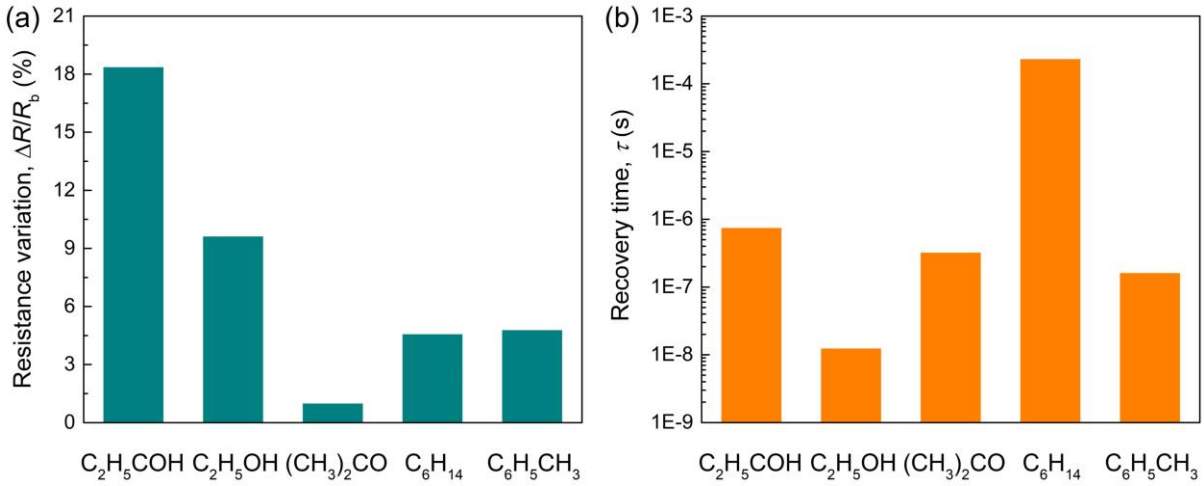

Figure 5.6 (a) The normalized resistance variation under the bias voltage of 2 V, and (b) recovery time of the monolayer black P sensor exposed to various VOCs.

5.5 Conclusions

In conclusion, we have studied the adsorption of VOCs on monolayer black P using first-principles calculations and examined its potential for application in VOC sensors. The energetically preferable adsorption sites for VOCs on monolayer black P have been identified and the corresponding adsorption energetics have been determined. VOCs were found to generally exhibit stronger interaction with monolayer black P than with the widely studied monolayer MoS_2, indicative of monolayer black P potentially being a more sensitive VOC sensor. The adsorption energetics of VOCs on monolayer black P can be engineered by elastic strain, with compressive (tensile) strain increasing (decreasing) the adsorption energy.

Furthermore, the adsorption characteristics of VOCs on monolayer black P are well retained in the event of thickness variation, *albeit* enhanced adsorption energies for bilayer and few-layer black P. VOCs molecules were found to act as charge acceptors and draw charge from monolayer black P, yet have little influence on the electronic properties of monolayer black P. Monolayer black P exhibits highly anisotropic transport properties, nonetheless, the absolute modification of *I-V* responses due to VOCs shows a direction-independent trend. Moreover, the recovery time of VOCs sensor is found to be within the detectable range and indicative of a short recovery time for next detection. Our findings suggest that monolayer black P be a compelling candidate material to achieve high sensitivity and good reusability for VOC sensors.

The present study demonstrated the capability of computational modeling as an effective means in the design and exploration of black P -based sensors. However, it is important to recognize that there remain limitations and challenges to be overcome. Taking VOC sensing as an example, realistically there will be co-existence of multiple VOCs. This necessitates the evaluation of the competitive resistance variation and mutual interference between VOCs, and in certain cases, the exact VOC adsorption sequence and possible reconstruction of VOC clusters, in order to obtain a more accurate assessment of VOC sensing and selectivity of black P. Meanwhile, monolayer and multilayer black P can be susceptible to oxygen and water in ambient environment, rendering a serious stability concern for black P -based sensors and making protective functionalization and/or processing treatments a necessity. Consequently, the impact of these treatments on sensing properties and performance of monolayer and multilayer black P need to be assessed. Moreover, abundant lattice defects and heteroatoms are often expected from the fabrication of black P, which not only may modify the properties of black P but also affect its interaction with VOCs. The above challenges, along with many others not mentioned here, require dedicated research studies and development of

new computational tools.

5.6 Acknowledgements

This research was supported by the NSERC Discovery grant (grant # RGPIN-2017-05187) and McGill Engineering Doctoral Award (MEDA). The authors also would like to acknowledge the Supercomputer Consortium Laval UQAM McGill and Eastern Quebec for providing computing resources.

5.7 References

(1) Novoselov, K. S.; Geim, A. K.; Morozov, S. V.; Jiang, D.; Zhang, Y.; Dubonos, S. V.; Grigorieva, I. V.; Firsov, A. A., Electric Field Effect in Atomically Thin Carbon Films. *Science* **2004**, *306*, 666-669.
(2) Liu, H.; Neal, A. T.; Zhu, Z.; Luo, Z.; Xu, X.; Tománek, D.; Ye, P. D., Phosphorene: An Unexplored 2D Semiconductor with a High Hole Mobility. *ACS Nano* **2014**, *8*, 4033-4041.
(3) Buscema, M.; Groenendijk, D. J.; Steele, G. A.; van der Zant, H. S. J.; Castellanos-Gomez, A., Photovoltaic Effect in Few-Layer Black Phosphorus PN Junctions Defined by Local Electrostatic Gating. *Nat. Commun.* **2014**, *5*, 4651.
(4) Engel, M.; Steiner, M.; Avouris, P., Black Phosphorus Photodetector for Multispectral, High-Resolution Imaging. *Nano Lett.* **2014**, *14*, 6414-6417.
(5) Hong, T.; Chamlagain, B.; Lin, W.; Chuang, H.-J.; Pan, M.; Zhou, Z.; Xu, Y.-Q., Polarized Photocurrent Response in Black Phosphorus Field-Effect Transistors. *Nanoscale* **2014**, *6*, 8978-8983.
(6) Guo, Q.; Pospischil, A.; Bhuiyan, M.; Jiang, H.; Tian, H.; Farmer, D.; Deng, B.; Li, C.; Han, S.-J.; Wang, H., Black Phosphorus Mid-Infrared Photodetectors with High Gain. *Nano Lett.* **2016**, *16*, 4648-4655.
(7) Zhang, X., et al., Black Phosphorus Quantum Dots. *Angew. Chem. Int. Ed.* **2015**, *54*, 3653-3657.
(8) Li, D.; Wang, X.; Zhang, Q.; Zou, L.; Xu, X.; Zhang, Z., Nonvolatile Floating-Gate Memories Based on Stacked Black Phosphorus–Boron Nitride–MoS_2 Heterostructures. *Adv. Funct. Mater.* **2015**, *25*, 7360-7365.
(9) Wang, H.; Wang, X.; Xia, F.; Wang, L.; Jiang, H.; Xia, Q.; Chin, M. L.; Dubey, M.; Han, S.-j., Black Phosphorus Radio-Frequency Transistors. *Nano Lett.* **2014**, *14*, 6424-6429.
(10) Deng, Y.; Luo, Z.; Conrad, N. J.; Liu, H.; Gong, Y.; Najmaei, S.; Ajayan, P. M.; Lou, J.; Xu, X.; Ye, P. D., Black Phosphorus–Monolayer MoS_2 Van Der Waals Heterojunction P–N Diode. *ACS Nano* **2014**, *8*, 8292-8299.
(11) Gehring, P.; Urcuyo, R.; Duong, D. L.; Burghard, M.; Kern, K., Thin-Layer Black Phosphorus/GaAs Heterojunction p-n Diodes. *Appl. Phys. Lett.* **2015**, *106*, 233110.
(12) Miao, J.; Zhang, S.; Cai, L.; Wang, C., Black Phosphorus Schottky Diodes: Channel Length Scaling and Application as Photodetectors. *Adv. Electron. Mater.* **2016**, *2*, 1500346.
(13) Jeon, P. J.; Lee, Y. T.; Lim, J. Y.; Kim, J. S.; Hwang, D. K.; Im, S., Black Phosphorus–Zinc Oxide Nanomaterial Heterojunction for p–n Diode and Junction Field-Effect Transistor. *Nano Lett.* **2016**, *16*, 1293-1298.

(14) Chen, L.; Zhou, G.; Liu, Z.; Ma, X.; Chen, J.; Zhang, Z.; Ma, X.; Li, F.; Cheng, H.-M.; Ren, W., Scalable Clean Exfoliation of High-Quality Few-Layer Black Phosphorus for a Flexible Lithium Ion Battery. *Adv. Mater.* **2016**, *28*, 510-517.
(15) Hao, C., et al., Flexible All-Solid-State Supercapacitors Based on Liquid-Exfoliated Black-Phosphorus Nanoflakes. *Adv. Mater.* **2016**, *28*, 3194-3201.
(16) Shulenburger, L.; Baczewski, A. D.; Zhu, Z.; Guan, J.; Tomanek, D., The Nature of the Interlayer Interaction in Bulk and Few-Layer Phosphorus. *Nano Lett.* **2015**, *15*, 8170-8175.
(17) Li, L.; Yu, Y.; Ye, G. J.; Ge, Q.; Ou, X.; Wu, H.; Feng, D.; Chen, X. H.; Zhang, Y., Black Phosphorus Field-Effect Transistors. *Nat. Nanotechnol.* **2014**, *9*, 372-377.
(18) Liang, L.; Wang, J.; Lin, W.; Sumpter, B. G.; Meunier, V.; Pan, M., Electronic Bandgap and Edge Reconstruction in Phosphorene Materials. *Nano Lett.* **2014**, *14*, 6400-6406.
(19) Liu, H.; Du, Y.; Deng, Y.; Peide, D. Y., Semiconducting Black Phosphorus: Synthesis, Transport Properties and Electronic Applications. *Chem. Soc. Rev.* **2015**, *44*, 2732-2743.
(20) Hultgren, R.; Gingrich, N.; Warren, B., The Atomic Distribution in Red and Black Phosphorus and the Crystal Structure of Black Phosphorus. *J. Chem. Phys.* **1935**, *3*, 351-355.
(21) Liu, H.; Neal, A. T.; Zhu, Z.; Xu, X.; Tomanek, D.; Ye, P. D.; Luo, Z., Phosphorene: An Unexplored 2D Semiconductor with a High Hole Mobility. *ACS Nano* **2014**.
(22) Yasaei, P.; Kumar, B.; Foroozan, T.; Wang, C.; Asadi, M.; Tuschel, D.; Indacochea, J. E.; Klie, R. F.; Salehi-Khojin, A., High-Quality Black Phosphorus Atomic Layers by Liquid-Phase Exfoliation. *Adv. Mater.* **2015**, *27*, 1887-1892.
(23) Brent, J. R.; Savjani, N.; Lewis, E. A.; Haigh, S. J.; Lewis, D. J.; O'Brien, P., Production of Few-Layer Phosphorene by Liquid Exfoliation of Black Phosphorus. *Chem. Commun.* **2014**, *50*, 13338-13341.
(24) Lu, W.; Nan, H.; Hong, J.; Chen, Y.; Zhu, C.; Liang, Z.; Ma, X.; Ni, Z.; Jin, C.; Zhang, Z., Plasma-Assisted Fabrication of Monolayer Phosphorene and Its Raman Characterization. *Nano Res.* **2014**, *7*, 853-859.
(25) Kou, L.; Frauenheim, T.; Chen, C., Phosphorene as a Superior Gas Sensor: Selective Adsorption and Distinct *I–V* Response. *J. Phys. Chem. Lett.* **2014**, *5*, 2675-2681.
(26) Suvansinpan, N.; Hussain, F.; Zhang, G.; Chiu, C. H.; Cai, Y.; Zhang, Y.-W., Substitutionally Doped Phosphorene: Electronic Properties and Gas Sensing. *Nanotechnology* **2016**, *27*, 065708.
(27) Abbas, A. N.; Liu, B.; Chen, L.; Ma, Y.; Cong, S.; Aroonyadet, N.; Köpf, M.; Nilges, T.; Zhou, C., Black Phosphorus Gas Sensors. *ACS Nano* **2015**, *9*, 5618-5624.
(28) He, Q.; Zeng, Z.; Yin, Z.; Li, H.; Wu, S.; Huang, X.; Zhang, H., Fabrication of Flexible Mos2 Thin-Film Transistor Arrays for Practical Gas-Sensing Applications. *Small* **2012**, *8*, 2994-2999.
(29) Late, D. J.; Huang, Y.-K.; Liu, B.; Acharya, J.; Shirodkar, S. N.; Luo, J.; Yan, A.; Charles, D.; Waghmare, U. V.; Dravid, V. P., Sensing Behavior of Atomically Thin-Layered MoS_2 Transistors. *ACS Nano* **2013**, *7*, 4879-4891.
(30) Cui, S.; Pu, H.; Wells, S. A.; Wen, Z.; Mao, S.; Chang, J.; Hersam, M. C.; Chen, J., Ultrahigh Sensitivity and Layer-Dependent Sensing Performance of Phosphorene-Based Gas Sensors. *Nat. Commun.* **2015**, *6*, 8632.
(31) Cho, S.-Y.; Lee, Y.; Koh, H.-J.; Jung, H.; Kim, J.-S.; Yoo, H.-W.; Kim, J.; Jung, H.-T., Superior Chemical Sensing Performance of Black Phosphorus: Comparison with MoS_2 and Graphene. *Adv. Mater.* **2016**, *28*, 7020-7028.
(32) Mayorga-Martinez, C. C.; Sofer, Z.; Pumera, M., Layered Black Phosphorus as a Selective Vapor Sensor. *Angew. Chem. Int. Ed.* **2015**, *54*, 14317-14320.
(33) Lee, G.; Jung, S.; Jang, S.; Kim, J., Platinum-Functionalized Black Phosphorus Hydrogen Sensors. *Appl. Phys. Lett.* **2017**, *110*, 242103.

(34) Cho, S.-Y.; Koh, H.-J.; Yoo, H.-W.; Jung, H.-T., Tunable Chemical Sensing Performance of Black Phosphorus by Controlled Functionalization with Noble Metals. *Chem. Mater.* **2017**, *29*, 7197-7205.
(35) Arya, S. K.; Bhansali, S., Lung Cancer and Its Early Detection Using Biomarker-Based Biosensors. *Chem. Rev.* **2011**, *111*, 6783-6809.
(36) Hakim, M.; Broza, Y. Y.; Barash, O.; Peled, N.; Phillips, M.; Amann, A.; Haick, H., Volatile Organic Compounds of Lung Cancer and Possible Biochemical Pathways. *Chem. Rev.* **2012**, *112*, 5949-5966.
(37) Buszewski, B.; Ulanowska, A.; Ligor, T.; Denderz, N.; Amann, A., Analysis of Exhaled Breath from Smokers, Passive Smokers and Non-Smokers by Solid-Phase Microextraction Gas Chromatography/Mass Spectrometry. *Biomed. Chromatogr.* **2009**, *23*, 551-556.
(38) Turner, C.; Španěl, P.; Smith, D., A Longitudinal Study of Ethanol and Acetaldehyde in the Exhaled Breath of Healthy Volunteers Using Selected-Ion Flow-Tube Mass Spectrometry. *Rapid Commun. Mass Spectrom.* **2006**, *20*, 61-68.
(39) Grate, J. W.; Rose-Pehrsson, S. L.; Venezky, D. L.; Klusty, M.; Wohltjen, H., Smart Sensor System for Trace Organophosphorus and Organosulfur Vapor Detection Employing a Temperature-Controlled Array of Surface Acoustic Wave Sensors, Automated Sample Preconcentration, and Pattern Recognition. *Anal. Chem.* **1993**, *65*, 1868-1881.
(40) Di Natale, C.; Macagnano, A.; Martinelli, E.; Paolesse, R.; D'Arcangelo, G.; Roscioni, C.; Finazzi-Agrò, A.; D'Amico, A., Lung Cancer Identification by the Analysis of Breath by Means of an Array of Non-Selective Gas Sensors. *Biosens. Bioelectron.* **2003**, *18*, 1209-1218.
(41) Ray, S. J.; Kamalakar, M. V.; Chowdhury, R., *Ab Initio* Studies of Phosphorene Island Single Electron Transistor. *J. Phys.: Condens. Matter* **2016**, *28*, 195302.
(42) Kresse, G.; Joubert, D., From Ultrasoft Pseudopotentials to the Projector Augmented-Wave Method. *Phys. Rev. B* **1999**, *59*, 1758-1775.
(43) Perdew, J. P.; Burke, K.; Ernzerhof, M., Generalized Gradient Approximation Made Simple. *Phys. Rev. Lett.* **1996**, *77*, 3865-3868.
(44) Grimme, S.; Antony, J.; Ehrlich, S.; Krieg, H., A Consistent and Accurate *Ab Initio* Parametrization of Density Functional Dispersion Correction (DFT-D) for the 94 Elements H-Pu. *J. Chem. Phys.* **2010**, *132*, 154104.
(45) Cai, Y.; Zhang, G.; Zhang, Y.-W., Layer-Dependent Band Alignment and Work Function of Few-Layer Phosphorene. *Sci. Rep.* **2014**, *4*, 6677.
(46) Qiao, J.; Kong, X.; Hu, Z.-X.; Yang, F.; Ji, W., High-Mobility Transport Anisotropy and Linear Dichroism in Few-Layer Black Phosphorus. *Nat. Commun.* **2014**, *5*, 4475.
(47) Li, B.; Ou, P.; Wei, Y.; Zhang, X.; Song, J., Polycyclic Aromatic Hydrocarbons Adsorption onto Graphene: A DFT and AIMD Study. *Materials* **2018**, *11*, 726.
(48) Ouyang, B.; Song, J., Strain Engineering of Magnetic States of Vacancy-Decorated Hexagonal Boron Nitride. *Appl. Phys. Lett.* **2013**, *103*, 102401.
(49) Brandbyge, M.; Mozos, J.-L.; Ordejón, P.; Taylor, J.; Stokbro, K., Density-Functional Method for Nonequilibrium Electron Transport. *Phys. Rev. B* **2002**, *65*, 165401.
(50) Xue, Y.; Datta, S.; Hong, S.; Reifenberger, R.; Henderson, J. I.; Kubiak, C. P., Negative Differential Resistance in the Scanning-Tunneling Spectroscopy of Organic Molecules. *Phys. Rev. B* **1999**, *59*, R7852-R7855.
(51) Wang, Q. H.; Kalantar-Zadeh, K.; Kis, A.; Coleman, J. N.; Strano, M. S., Electronics and Optoelectronics of Two-Dimensional Transition Metal Dichalcogenides. *Nat. Nanotechnol.* **2012**, *7*, 699-712.
(52) Lebègue, S.; Björkman, T.; Klintenberg, M.; Nieminen, R. M.; Eriksson, O., Two-Dimensional Materials from Data Filtering and *Ab Initio* Calculations. *Phys. Rev. X* **2013**, *3*, 031002.

(53) Tian, X.-Q.; Liu, L.; Wang, X.-R.; Wei, Y.-D.; Gu, J.; Du, Y.; Yakobson, B. I., Engineering of the Interactions of Volatile Organic Compounds with MoS_2. *J. Mater. Chem. C* **2017**, *5*, 1463-1470.
(54) Pu, H.; Rhim, S.; Gajdardziksa-Josifovska, M.; Hirschmugl, C.; Weinert, M.; Chen, J., A Statistical Thermodynamics Model for Monolayer Gas Adsorption on Graphene-Based Materials: Implications for Gas Sensing Applications. *RSC Adv.* **2014**, *4*, 47481-47487.
(55) Kim, J.-S.; Yoo, H.-W.; Choi, H. O.; Jung, H.-T., Tunable Volatile Organic Compounds Sensor by Using Thiolated Ligand Conjugation on MoS_2. *Nano Lett.* **2014**, *14*, 5941-5947.
(56) Wei, Q.; Peng, X., Superior Mechanical Flexibility of Phosphorene and Few-Layer Black Phosphorus. *Appl. Phys. Lett.* **2014**, *104*, 251915.
(57) Sa, B.; Li, Y.-L.; Qi, J.; Ahuja, R.; Sun, Z., Strain Engineering for Phosphorene: The Potential Application as a Photocatalyst. *J. Phys. Chem. C* **2014**, *118*, 26560-26568.
(58) Henkelman, G.; Arnaldsson, A.; Jónsson, H., A Fast and Robust Algorithm for Bader Decomposition of Charge Density. *Comput. Mater. Sci.* **2006**, *36*, 354-360.
(59) Sanville, E.; Kenny, S. D.; Smith, R.; Henkelman, G., Improved Grid-Based Algorithm for Bader Charge Allocation. *J. Comput. Chem.* **2007**, *28*, 899-908.
(60) Tang, W.; Sanville, E.; Henkelman, G., A Grid-Based Bader Analysis Algorithm without Lattice Bias. *J. Phys.: Condens. Matter* **2009**, *21*, 084204.
(61) Yu, M.; Trinkle, D. R., Accurate and Efficient Algorithm for Bader Charge Integration. *J. Chem. Phys.* **2011**, *134*, 064111.
(62) Wang, C.; Xia, Q.; Nie, Y.; Guo, G., Strain-Induced Gap Transition and Anisotropic Dirac-Like Cones in Monolayer and Bilayer Phosphorene. *J. Appl. Phys.* **2015**, *117*, 124302.
(63) Kulish, V. V.; Malyi, O. I.; Persson, C.; Wu, P., Adsorption of Metal Adatoms on Single-Layer Phosphorene. *Phys. Chem. Chem. Phys.* **2015**, *17*, 992-1000.
(64) Churchill, H. O. H.; Jarillo-Herrero, P., Two-Dimensional Crystals: Phosphorus Joins the Family. *Nat. Nanotechnol.* **2014**, *9*, 330-331.
(65) Babar, V.; Sharma, S.; Schwingenschlögl, U., Highly Sensitive Sensing of NO and NO_2 Gases by Monolayer C_3N. *Adv. Theory Simul.* **2018**, *1*, 1700008.
(66) Kong, J.; Franklin, N. R.; Zhou, C.; Chapline, M. G.; Peng, S.; Cho, K.; Dai, H., Nanotube Molecular Wires as Chemical Sensors. *Science* **2000**, *287*, 622-625.
(67) Cho, S.-Y.; Yoo, H.-W.; Kim, J. Y.; Jung, W.-B.; Jin, M. L.; Kim, J.-S.; Jeon, H.-J.; Jung, H.-T., High-Resolution P-Type Metal Oxide Semiconductor Nanowire Array as an Ultrasensitive Sensor for Volatile Organic Compounds. *Nano Lett.* **2016**, *16*, 4508-4515.
(68) Liu, D.; Lian, X.; Mallik, A. K.; Han, W.; Wei, F.; Yuan, J.; Yu, C.; Farrell, G.; Semenova, Y.; Wu, Q. In *Detection of Volatile Organic Compounds Using an Optical Fiber Sensor Coated with a Sol-Gel Silica Layer Containing Immobilized Nile Red*, Optical Fiber Sensors Conference (OFS), **2017** 25th, IEEE: 2017; pp 1-4.

Chapter 6 : Single Molybdenum Center Supported on N-Doped Black Phosphorus as an Efficient Electrocatalyst for Nitrogen Fixation

Chapter 4 and Chapter 5 demonstrated the potential of black phosphorus as an appealing candidate in the field of gas sensing. This chapter will switch gear to examine the potential of black phosphorus in another important application of catalysis. In particular, this chapter is motivated by recent studies on single-atom catalysis in the two-dimensional nanomaterials, which are demonstrated to provide a promising, attractive, and alternative strategy for sustainable NH_3 production. Specifically, we investigated the candidacy of molybdenum-based single-atom catalysts supported on nitrogen-doped black phosphorus as the electrocatalyst for nitrogen reduction.

- This chapter has been published in *Nanoscale*, appeared as: Pengfei Ou, Xiao Zhou, Fanchao Meng, Cheng Chen, Yiqing Chen, and Jun Song. **Single molybdenum center supported on N-doped black phosphorus as an efficient electrocatalyst for nitrogen fixation**. *Nanoscale*, **2019**, *11*, 13600-13611.
  DOI: https://doi.org/10.1039/C9NR02586C

6.1 Abstract

Ammonia (NH_3) is one of the most significant industrial chemical products due to its wide applications in various fields. However, the production of NH_3 from electrochemical nitrogen (N_2) reduction reaction (NRR) at ambient conditions is one of the most important issues that remain challenging for chemists. Herein, the candidacy of a series of molybdenum (Mo)-based single-atom catalysts (SACs) supported on N-doped black phosphorus (black P) as the electrocatalyst for NRR has been evaluated by means of density functional theory (DFT) calculations. In particular, Mo_1N_3 has been found to chemically adsorb the N_2, and exhibits the highest catalytic activity toward NRR with an ultralow overpotential of 0.02 V via the associative distal mechanism, indicative of catalyzing NRR under ambient conditions. Additionally, Mo_1N_3 shows fast removal of the produced NH_3 with a free energy uphill of only 0.56 eV and good stability of NRR reaction intermediates. Moreover, the Mo-based SACs were demonstrated to be more selective to NRR over the competing hydrogen evolution reaction (HER) process. These excellent features endow Mo_1N_3 on black P as a compelling highly efficient and durable catalyst for electrochemical N_2 fixation. Our results provide a rational paradigm for catalytic nitrogen fixation by SACs in two-dimensional nanomaterials at ambient conditions.

6.2 Introduction

Ammonia (NH_3) synthesis from naturally abundant nitrogen (N_2) is of significant importance not only for producing synthetic chemical, such as dyes, fertilizers, medicaments, explosives, and resins,[1-4] but also promises new pathways towards solving the stringent energy and environmental crisis.[5-6] Conventionally, the mass production of NH_3 mainly depends on the Haber-Bosch process, i.e., a high-temperature (350-550 ºC) and high-pressure (150-350 atm) reaction, which accounts for approximately 1-2% of the energy consumption worldwide.[7] Therefore, it is highly imperative to develop alternative processes that have the potential to

overcome the limitations of the Haber-Bosch process.[7-8] Contrary to the industrial Haber-Bosch process, the electrochemical N_2 reduction reaction (NRR) occurs at ambient conditions, is able to significantly reduce the energy consumption and simplify the reactor design, representing a promising, attractive, and alternative strategy for sustainable NH_3 production.[9] Thus, searching for an electrocatalyst that can perform electrochemical nitrogen fixation with high catalytic activity and good selectivity is of paramount significance.

Recently, the single-atom catalysts (SACs) have been widely explored as promising candidates for various catalytic reactions, such as carbon dioxide (CO_2) reduction, hydrogen evolution reaction (HER), oxygen reduction reaction (ORR), carbon monoxide (CO) oxidation, as well as NRR, etc.[9-28] They offer significantly improved catalytic activities and help greatly reduce the amount of noble metals used in electrocatalysts, making them much preferable than the conventional catalysts. Previous studies have suggested that drastic modifications of electronic properties of SACs from those of bulk metals can successfully manipulate the catalytic activity and selectivity.[10-14, 19, 23, 29] Among various SACs, single molybdenum (Mo) centers within the nitrogenases (i.e., Mo−N complexes) have been extensively studied, well demonstrating the significance of Mo in the design of NRR catalysts.[30-33] In 2003, Schrock and co-workers showed catalytic reduction of N_2 to NH_3 at a single Mo center under ambient temperature and pressure in their study using Mo catalysts that contain tetradentate triamidoamine ligands.[30] Later in the work by Arashiba et al., Mo−N complexes bearing a mer-tridentate triphosphine as a ligand have been designed and found to be highly effective catalysts, achieving up to 63 equiv. of ammonia based on the Mo atom.[31] In a more recent study, Arashiba et al. further demonstrated a remarkable catalytic performance of 415 equiv. NH_3 based on the Mo atom using the Mo-iodide complexes containing a PNP-type pincer ligand.[32] In addition to the development of yield rate, Chen et al. discovered a dramatically

enhanced electrochemical NRR selectivity under ambient conditions via the Li^+ incorporation into poly(N-ethyl-benzene-1,2,4,5-tetracarboxylic diimide) (PEBCD) as a catalyst.[34]

Inspired by the success in design of molecular complexes, the searching of Mo−N complexes for electrochemical NRR also has been extended to other inorganic systems, particularly for two-dimensional (2D) nanomaterials.[9, 21-24, 35-36] Zhao et al. theoretically investigated the catalytic abilities of different single transition metal atoms supported on defective hexagonal boron nitride (h-BN) for nitrogen fixation, and found that a single Mo atom at boron monovacancy exhibits the superb catalytic activity with a low overpotential of 0.19 V.[21] Azofra et al. examined the Mo_3C_2 center in the 2D d^2-d^4 M_3C_2 transition metal carbides (MXenes) and demonstrated its ability to activate the chemisorbed N_2 and subsequently the catalytic conversion into NH_3.[35] Similarly, Mo_2C nanodots embedded in 2D carbon nanosheets as highly efficient electrochemical NRR catalyst was first developed by Cheng et al., with a high NH_3 yield rate of 11.3 μg h^{-1} $mg^{-1}_{Mo_2C}$ and Faradic efficiency of 7.8%.[37] As reported by Li et al., molybdenum nitride (MoN_2) nanosheet might generate N-vacancy to actively fill N_2 via Mo−N_3 bonding and maintain excellent performance for N_2 adsorption and activation under electrochemical conditions, especially for iron (Fe) doping.[36] More recently, Ling and co-workers computationally screened the catalytic performances of a series of single metal atoms supported on N-doped carbon by density functional theory (DFT) calculations, the authors revealed that $Mo_1N_1C_2$ can catalyze NRR through the enzymatic mechanism at ambient conditions.[22]

Recently, the 2D counterpart of black phosphorus (black P), also known as phosphorene, has been introduced as a new member of the 2D nanomaterials family. Due to its unique physical and chemical properties, black P has already emerged as a new class of catalyst for a variety of significant reactions, such as HER[38-39] and oxygen evolution reaction (OER).[40-41] Very recently, Zhang et al. demonstrated that the well-exfoliated few-layer black P can also

be implemented as a promising catalyst for electrochemical NRR with a yield of 31.37 μg h^{-1} mg^{-1}_{cat}.[28] However, it was revealed by DFT calculations that only the edge sites can actively catalyze the electrocatalysis of N_2 to NH_3, with the rest of basal plane inert. The outstanding properties of black P inspire us to ask: can the Mo−N complexes supported on black P be employed to further enhance the catalytic activity on the basal plane for nitrogen fixation at ambient conditions? To answer this question, we systematically investigate the catalytic performance of Mo-based SACs anchored on N-doped black P for NRR with the help of DFT calculations. Our calculations show that Mo_1N_3 possesses ultrahigh catalytic activity for NRR with an extremely low overpotential of 0.02 V, which ensures the efficient reduction of N_2 at ambient conditions. Surprisingly, NH_3 desorption only consumes free energy of 0.56 eV, leading to a rapid removal of produced NH_3. In addition, the coordination effect on the activity and selectivity of these Mo-based SACs are further studied, and Mo_1N_3 is confirmed to own the highest activity for NRR. Therefore, by carefully controlling Mo doping sites, black P can be implemented as a novel noble-metal-free NRR electrocatalyst with high efficiency at ambient conditions.

6.3 Computational method

6.3.1 First-principles DFT calculations

First-principles DFT calculations using Vienna *ab-initio* simulation package (VASP)[42-43] were performed with the ion-electron interactions were described by the projector-augmented wave (PAW) method.[44] The generalized gradient approximation (GGA) in the Perdew-Burke-Ernzerhof (PBE) form[45-46] and a cut-off energy of 500 eV for plane-wave basis set were adopted. Spin-polarized calculations were employed for all systems, and the convergence criterion for the residual force was set to 0.01 eV $Å^{-1}$. The vacuum space perpendicular to the black P nanosheet was set to be larger than 15 Å, which is sufficient to avoid interactions between two periodic images. The Brillouin zone was sampled with the

Monkhorst-Pack mesh with a 2 × 2 × 1 *k*-point grid.[47] The climbing-nudged elastic band method was used to locate saddle points and minimum energy paths.[48]

A 6 × 4 × 1 monolayer black P supercell containing a phosphorus single vacancy (SV) with a formation energy of 2.21 eV was used for the calculations, with the SV configuration in accordance with recent experimental characterization results using scanning tunneling microscopy/spectroscopy (STM/STS).[49] Different Mo SAC centers, in the form of $Mo_1N_iP_{3-i}$ (i = 0, 1, 2, 3), anchored at the SV, were then created and examined. Here, i denotes the number of nitrogen atoms introduced to substitute those phosphorus atoms immediately neighboring the SV. As will be seen in the results below, the focus is placed on the Mo_1N_3 center (i.e., i = 3) as it offers the best performance. Meanwhile, it is worth noting that we have also investigated Mo SAC centers anchored at a phosphorus divacancy (DV). Our results reveal that, based on the adsorption and cohesive energies, the Mo atom binds much stronger with SV than DV (Figure 6.7 in the Supporting Information). Therefore, in the present study, we limit our discussion to Mo SAC centers at a phosphorus SV.

6.3.2 Computational hydrogen electrode model

The calculations of Gibbs free energy change (ΔG) for each elemental step were based on the computational hydrogen electrode (CHE) model that proposed by Nørskov et al.,[50] which can be computed by the following equation,

$$\Delta G = \Delta E + \Delta E_{ZPE} - T\Delta S + eU + \Delta G_{pH} \quad (6.1)$$

where ΔE is the electronic energy difference before and after the adsorption of reaction intermediates, ΔE_{ZPE} and ΔS are the changes in zero-point energies and entropy, respectively. T is the temperature, set to be room temperature, i.e., 298.15 K in this study. e and U are the number of electrons transferred and the applied electrode potential respectively, while ΔG_{pH} is the free energy correction of pH, calculated as $\Delta G_{pH} = k_B T \times pH \times \ln 10$. In the present study,

the pH value is set as zero and thus $\Delta G_{pH} = 0$. Moreover, according to the CHE model, the overpotential (η) of the NRR process is determined as the potential-limiting step with the most positive ΔG (ΔG_{max}), as computed by:

$$\eta = U_{equilibrium} - U_{limiting} \quad (6.2)$$

where $U_{equilibrium}$ is the equilibrium potential of NRR (about –0.16 V in the present study for the reaction $N_2 + 6H^+ + 6e^- \rightarrow 2NH_3$) and $U_{limiting}$ is the applied potential required to eliminate the energy barrier of the rate-limiting step, which can be obtained by: $U_{limiting} = -\Delta G_{max}/e$. The parameter η serves as a good indicator for catalytic activity, i.e., a smaller η value indicating a faster NRR process.

6.4 Results and discussion

6.4.1 Configuration and stability of Mo_1N_3

Among the various Mo SAC centers anchored at SV, Mo_1N_3 was found to exhibit the lowest limiting potential as NRR electrocatalyst (more details can be found in Supporting Information). Thus, here we focus on Mo_1N_3 as a representative case of the model catalysts proposed in the present study. An ultimate prerequisite for a SAC to be an effective catalyst is its good stability for long-term usage, which necessitates strong binding between the anchored atom (cluster) and the substrate material to prevent easy detachment and undesirable aggregation. The binding energy of the resultant Mo_1N_3 center at SV is –5.25 eV or –0.63 eV with reference to an isolated Mo atom or the bulk Mo respectively. This suggests that the Mo_1N_3 center can be stably present at the phosphorus SV. In the meantime, the kinetics of the adsorbed Mo atom to escape SV has also been examined, showing an energy barrier of 14.6 eV for Mo to migrate from the SV site to a neighboring hollow site (see Figure 6.8 in the Supporting Information). This extremely large barrier indicates that such process is impossible to occur at room temperature. Figure 6.1a represents the fully optimized structure of Mo_1N_3 at SV. In the newly formed Mo_1N_3 moiety, the Mo−N bond length is 2.01 Å. Since the radius of

N atom is much smaller than that of the substituted P atom, the anchored Mo atom is inward from the monolayer black P surface by 0.76 Å.

6.4.2 Feasibility of Mo_1N_3 as NRR electrocatalyst

Since N_2 is an extremely stable molecule with inert triple bonds, and the first electrochemical step of NRR is always the hydrogenation of $*N_2$ into $*N_2H$ that breaks the strong N≡N triple bond, large energy consumption is thus inevitably needed. Therefore, free energy change for this step ($\Delta G_{N_2-N_2H}$) is expected to stay positive, and this usually happens to be the potential-limiting step for most of the transition metals regardless of the mechanism.[51] More importantly, despite the possibility of NRR occurring via different mechanisms, the above step always remains the first electrochemical step. Hence, the screening efficiency will be greatly improved without losing the screening accuracy by using the $\Delta G_{N_2-N_2H}$ as one of the activity descriptors. Besides, the chemisorption of N_2, which makes sufficient activation of inert N≡N triple bond and enhances the frequency of the effective collision between reactants and catalysts. Therefore, to make sure the limiting potential of the whole NRR process is close to or even smaller than the value of the best pure transition metal catalysts,[51] a general two-step strategy were suggested to be used for screening an eligible SAC electrocatalyst for NRR by Ling et al.,[24]: (1) the catalyst can facilitate the chemisorption of N_2 and hydrogenation of $*N_2$ into $*N_2H$ to warrant sufficient activation of its inert N≡N triple bond (criterion: the adsorption energy of N_2 (ΔE_{N_2}) should be more negative than −0.50 eV and the free energy barrier for hydrogenation of $*N_2$ into $*N_2H$ ($\Delta G_{N_2-N_2H}$) should be smaller than 0.50 eV); (2) the catalyst can selectively destabilize $*NH_2$ species and achieve fast removal of NH_3 (criterion: free energy barrier for hydrogenation of $*NH_2$ into $*NH_3$ ($\Delta G_{NH_2-NH_3}$) should be no more than 0.50 eV and the desorption energy of NH_3 (ΔG_{NH_3-des}) ought not to exceed 0.70 eV), to guarantee the reduction of the overpotential.

Following this screening strategy, we first computed the adsorption energies of a gas-phase N_2 molecule at Mo_1N_3 in the N-doped black P (see Figure 6.1a) by considering both side-on and end-on initial adsorption configurations (see Figure 6.1b,c). For the side-on configuration, both N atoms interact with the Mo atom, forming two Mo–N bonds (Figure 6.1b), while for the end-on structure, only one N atom binds with the Mo atom (Figure 6.1c). The calculated ΔE_{N_2} of N_2 adsorption are −0.60 and −0.93 eV in side-on and end-on configurations respectively, both larger than −0.50 eV, indicating that N_2 can be effectively captured by the Mo_1N_3 center. Moreover, respectively for the side-on and end-on configurations, Bader charge analysis[52-55] shows that the adsorbed N_2 gains 0.53 and 0.36 e from Mo_1N_3 with the corresponding N≡N bond length elongated to 1.19 and 1.14 Å compared to that of the isolated N_2 molecule (1.11 Å). Further analysis reveals that the charge clouds are localized and distributed on both the adsorbed N_2 and Mo_1N_3 center (Figure 6.9 in the Supporting Information). The above results evidence chemisorption of N_2 and indicate that the activation of the inert N≡N triple bond is possible. The calculated free energies for hydrogenation of $*N_2$ into $*N_2H$ are with 0.31 and 0.14 eV in side-on and end-on configurations, smaller than 0.50 eV. Meanwhile, the performance of Mo_1N_3 for NH_3 generation and desorption has been examined, and it was found that the hydrogenation of $*NH_2$ and desorption of produced $*NH_3$ would overcome energy barriers of 0.18 and 0.56 eV respectively, fulfilling the afore-mentioned screening requirements of $\Delta G_{NH_2-NH_3} < 0.5$ eV and $\Delta G_{NH_3-des} < 0.7$ eV. This demonstrates the ability of Mo_1N_3 of selectively destabilizing $*NH_2$ species and rapid removal of the produced NH_3.

The above analyses confirm that the Mo_1N_3-embedded black P well satisfies the criteria in the two-step screening, and thus can serve as an eligible electrocatalyst for the NRR. In addition, to further assess the candidacy of Mo_1N_3, we have also compared it with cases of larger Mo clusters (see Supporting Information for details). In general, we found that Mo_1N_3

would have superb performance compared to larger Mo clusters as the clusters exhibit weaker stabilization of *N_2H species and stronger interaction with *NH_2 species, despite sufficient activation of the N_2 molecule (Figure 6.10 in the Supporting Information).

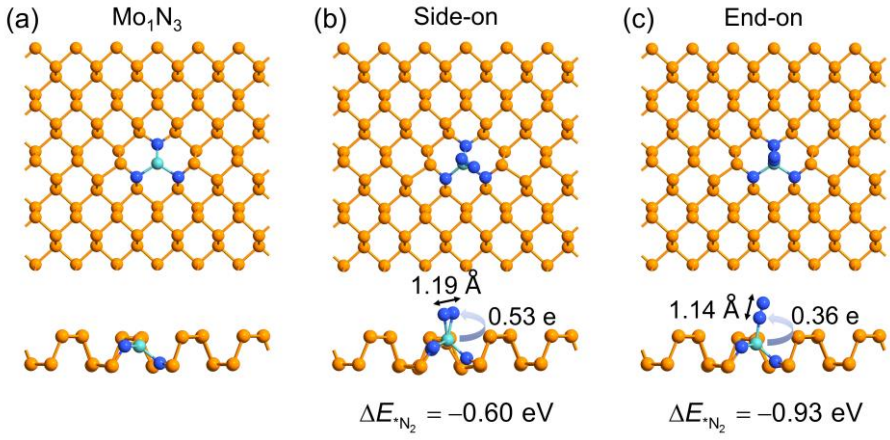

Figure 6.1 Top and side views of the structures for (a) Mo_1N_3, Mo_1N_3 with N_2 adsorption via (b) side-on and (c) end-on configurations. The N−N bond lengths and corresponding amounts of charge transfer from Mo_1N_3 to N_2 are also indicated. Blue, orange, and cyan balls represent the H, doped N, P, and Mo atoms, respectively.

6.4.3 Reaction Mechanism and Free Energy for NRR on Mo_1N_3

The NRR under electrochemical conditions is a six-electron reaction, $N_2 + 6H^+ + 6e^- \rightarrow 2NH_3$, with two potential reaction pathways, one being the dissociative pathway through which N_2 is first dissociated into two separate N atoms before being hydrogenated, and the other being the associative pathway, in which N_2 would be hydrogenated by protons simultaneously with the formation of NH_3.[51] However, the associative adsorption of N_2 is reported to be the more favorable pathway under electrochemical conditions due to the high kinetic barrier of N_2 dissociation.[56] Therefore, in the present study we focus our investigation on the reduction processes by considering the associative pathway. According to the study by Ling et al.,[22] four possible reaction mechanisms are involved in the associative pathway, labeled as enzymatic and consecutive mechanisms for N_2 adsorption via the side-on configuration, and alternating and distal mechanisms for N_2 adsorption via the end-on configuration, respectively (Figure 6.2 and Figure 6.3). For the enzymatic and alternating

mechanisms, the proton-electron pairs ($H^+ + e^-$) attack the two N atoms alternatively, whereas for the consecutive and distal mechanisms, the proton-electron pairs first attack one N atom consecutively to form a NH_3 and then act on the remaining N atom to form another NH_3.

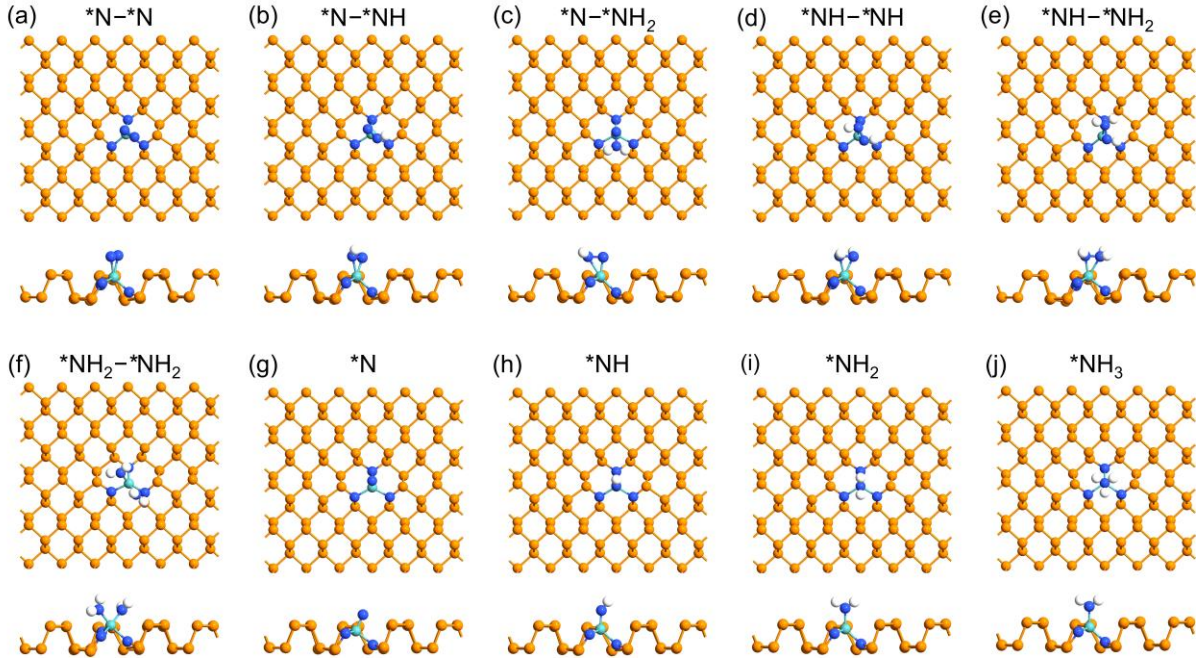

Figure 6.2 The corresponding structures of the reaction intermediates through the enzymatic and consecutive mechanisms, (a) *N−*N, (b) *N−*NH, (c) *N−*NH_2, (d)*NH−*NH, (e) *NH−*NH_2, (f) *NH_2−*NH_2, (g) *N, (h) *NH, (i) NH_2, and (j) *NH_3. White, blue, orange, and cyan balls represent H, doped N, P, and Mo atoms respectively.

For the side-on N_2 adsorption, the corresponding structures of the NRR reaction intermediates through enzymatic and consecutive mechanisms along with the free-energy diagrams are presented in Figure 6.2 and Figure 6.4a,b. From Figure 6.4a,b, N_2 adsorption via side-on configuration exhibits a negative free energy change ΔG (−0.14 eV), indicating the ability of Mo_1N_3 to effectively capture the gas-phase N_2 molecule. We can see that the first two steps of the enzymatic and consecutive routes are essentially the same, i.e., N_2 adsorption and subsequent reduction into *N−*N. However, the hydrogenation of *N−*N into *N−*NH consumes energy, with ΔG increased by 0.31 eV, being the potential-limiting step for both the enzymatic and consecutive mechanisms. Therefore, the overpotential η for the reduction of

side-on adsorbed N_2 on Mo_1N_3 becomes 0.15 V (see eqn. (6.2)) for both enzymatic and consecutive mechanisms, indicative of overall significant efficiency.

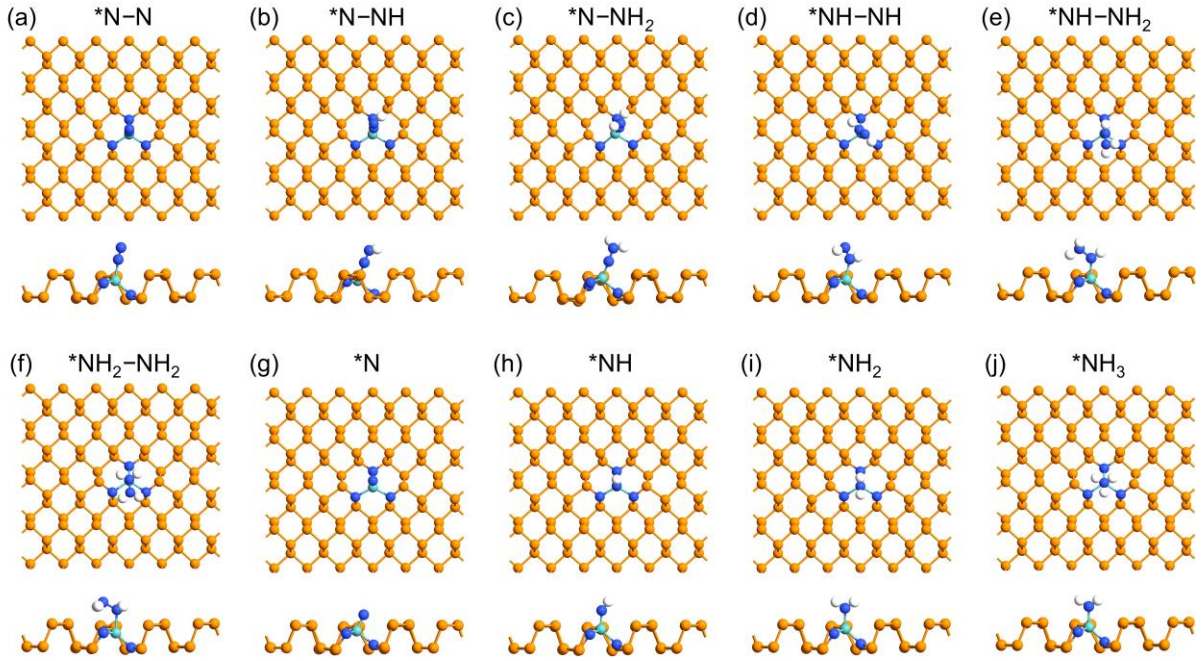

Figure 6.3 The corresponding structures of the reaction intermediates through the alternating and distal mechanisms, (a) *N−N, (b) *N−NH, (c) *N−NH_2, (d)*NH−NH, (e) *NH−NH_2, (f) *NH_2−NH_2, (g) *N, (h) *NH, (i) *NH_2, and (j) *NH_3. White, blue, orange, and cyan balls represent H, doped N, P, and Mo atoms respectively.

On the other hand, for NRR via the end-on configuration, Figure 6.4c,d and Figure 6.3 depict the free-energy diagrams and the corresponding structures of the reaction intermediates, respectively. The end-on configuration shows a more negative free energy (−0.49 eV) for N_2 adsorption than the side-on configuration, implying much stronger N_2 capture and activation. The first step is *N_2 hydrogenated by adsorbing a proton coupled with an electron transfer, and reduced into *N_2H, with the free energy slightly uphill by 0.14 eV, being smaller than that of side-on adsorbed N_2 (0.31 eV, see Figure 6.4). Examining the subsequent reaction process, we found that for the distal mechanism, the potential-limiting steps are the hydrogenation of *N into *NH and *NH_2 into *NH_3, with an extremely low limiting potentials of 0.17 and 0.18 V respectively (Figure 6.4d), which are much lower than that (greater than 0.50 V) from the best metal catalyst reported so far.[57] Such a low overpotential is an indication of superior catalytic

performance of Mo_1N_3 for NRR. On the other hand, for the alternating route, the potential-limiting step is the hydrogenation of *N−*NH into *NH−*NH with a ΔG of 0.69 eV, which is the highest value among the four possible mechanisms, as shown in Figure 6.4c. Nevertheless, despite the relatively high ΔG, the alternating mechanism exhibits a η value of 0.53 V, which is still attractive.

In the previous study by Zhang et al.,[28] the NRR processes on the basal plane and various edge sites (i.e., armchair and zigzag edges) of black P have been thoroughly examined by DFT calculations. It is found out that the electron densities are only concentrated near the zigzag and diff-zigzag edges, which is beneficial for adsorbing N_2 and boosting the NRR performance. Moreover, they have further confirmed that the zigzag and diff-zigzag edges exhibit the lowest energy barriers of 0.85 and 0.84 eV via the alternating pathway in the association mechanism, respectively, with the potential-limiting step being the protonation of N_2 to N_2H. In comparison, from our present study, the energy barrier for the potential-limiting step on the Mo_1N_3 center (~0.18 eV) is significantly lower than those of basal plane and edge sites. Therefore, Mo_1N_3 center accounts for the major contribution to the high activity of Mo-based SACs supported on N-doped black P. Based on the above results, we see that obviously, the NRR occurring on the Mo_1N_3 in N-doped black P would prefer to proceed through the distal mechanism due to the lowest overpotential (0.02 V), which is lower than the overpotential from any catalyst previously reported for 2D nanomaterials.[9, 20-24, 29, 58-59]

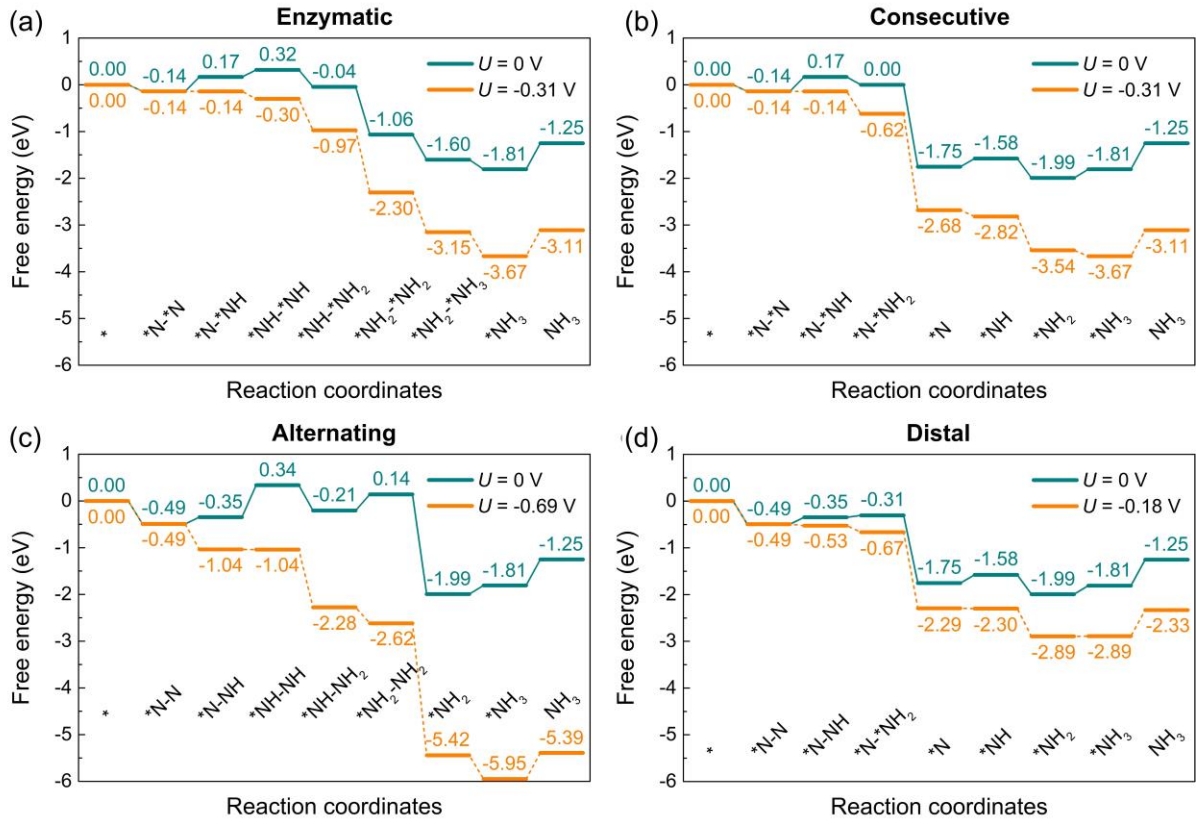

Figure 6.4 Free energy diagrams for N_2 reduction to NH_3 through (a) enzymatic, (b) consecutive, (c) alternating, and (d) distal mechanisms on Mo_1N_3 at zero and applied potentials. The green and orange curves respectively correspond to the situations of at 0 V and limiting potentials versus RHE, respectively.

Besides the N_2 electrochemical reduction process, other factors, such as desorption of the produced NH_3 and stability of reaction intermediates, may also play critical roles in determining the performance of the NRR catalyst.[24, 56-57] Generally, to efficiently catalyze NRR, the catalyst should have a relatively high surface activity to bind N_2 tightly enough to activate the inert N≡N triple bond sufficiently.[60] However, this high surface activity often also results in high binding strength between NH_3 and the catalyst and thus product poisoning of catalyst surface.[57] To this end, we examined the NH_3 desorption on Mo_1N_3, and found that, despite the high binding strength between N_2 and Mo_1N_3, the ΔG for NH_3 desorption on Mo_1N_3 is only 0.56 eV, being considerably lower than those of the recently reported candidates for highly active catalysts for NRR, e.g., V_3C_2, Nb_3C_2, and single Mo center on defective BN, which exhibit high ΔG values of 0.92, 1.16, and 0.70 eV respectively.[21, 35] This indicates a

much faster removal of the produced NH_3 from Mo_1N_3 and thus better durability of the catalyst. Meanwhile, for the stability of reaction intermediates, we considered the possibility of hydrazine (N_2H_4) production in the enzymatic and alternating mechanisms. The release of N_2H_4 is found to require energies of ~2.35 and 1.15 eV in enzymatic and alternating mechanisms respectively, which are significantly larger than that of hydrogenation of $*NH_2{-}*NH_2$ into $*NH_2{-}*NH_3$ in enzymatic mechanism (−0.54 eV) and release of first NH_3 in alternating mechanism (−2.13 eV), implying that this process would not occur at room temperature.

Moreover, to gain more insights into the excellent electrocatalytic performance of Mo_1N_3, we investigated the charge variation during the NRR process. According to previous studies, each intermediate can be divided into three moieties (as shown in Figure 6.5a), including moiety 1 (black P without Mo_1N_3), moiety 2 (Mo_1N_3 center), and moiety 3 (the adsorbed $*N_xH_y$ species).[20-22] Figure 6.5b shows the charge variations in each elementary reaction step, considering the distal mechanism as the representative. The charge variation here is defined as the charge difference of each moiety between the present step and the previous step, which is calculated using the Bader charge analysis.[52-55] The charge transfer only occurs between Mo_1N_3 and $*N_xH_y$ species in the first three steps, as the charge variation of black P moiety is close to 0. As shown in Figure 6.5b, N_2 gains 0.36 e when adsorbed on Mo_1N_3, where the charge is mainly donated by moiety 2, similar for the hydrogenation of $*N_2$ into $*N{-}NH$. However, the electrons are transfer from the adsorbed $*N_xH_y$ species to Mo_1N_3 when $*N{-}NH$ is hydrogenated to $*N{-}NH_2$. On the contrary, black P moiety will actively participate in transferring electrons between Mo_1N_3 and N_xH_y species in the subsequent four hydrogenation processes, which facilitates the formation and removal of second NH_3. Besides, N−N bond lengths in each intermediate along the pathway (Figure 6.5c) increase monotonously, indicative of the gradual activation process of N_2. Moreover, from gas phase N_2 to $*N{-}*NH_2$ (where the

N−N has not been broken), N−N bond length presents a nearly linear increase, implying that the stretching effect of adsorption is comparable to that of the hydrogenation.

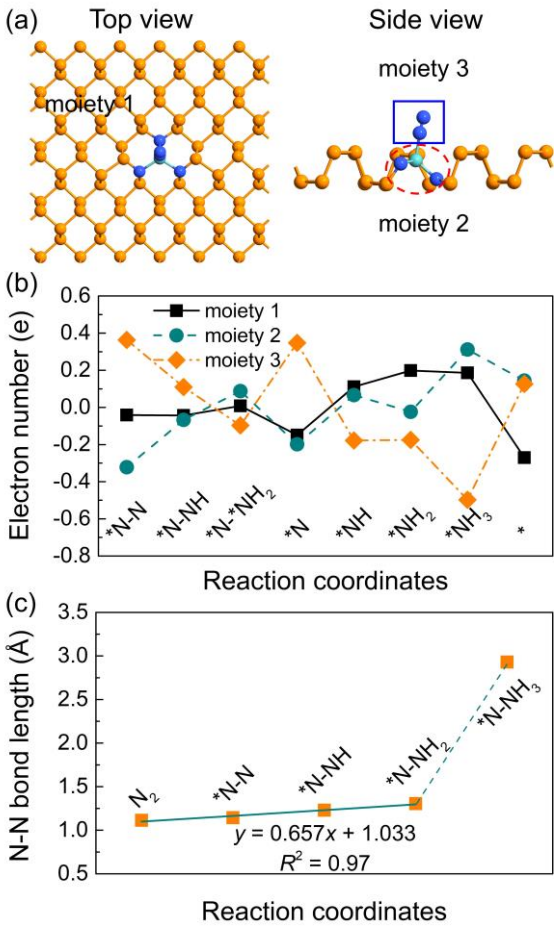

Figure 6.5 (a) Top and side views of three moieties, i.e., moiety 1 (black P without Mo_1N_3), moiety 2 (Mo_1N_3 center), and moiety 3 (the adsorbed $*N_xH_y$ species), of the *N−N intermediate. (b) charge variation of the three moieties. (c) N−N bond length at different reaction coordinates along the distal mechanism via end-on adsorption, where the bond length is observed to increase linearly before the final bond breakage.

6.4.4 Doping Effect of SACs

Our discussion above focused on the Mo_1N_3 center as a representative. Nonetheless, in practice, the Mo SAC center may assume a general form (i.e., $Mo_1N_iP_{3-i}$ (i = 0, 1, 2, or 3)), thus giving rise of varying NRR performance[30-31], [61]. Therefore, it is important to investigate the doping effect on the performance of the Mo SAC center ($Mo_1N_iP_{3-i}$) as i varies. In this regard, other types of active centers, i.e., symmetric (sym_) and asymmetric (asym_) $Mo_1N_2P_1$ and $Mo_1N_1P_2$, as well as Mo_1P_3, have been constructed (as shown in Figure 6.6a-e), with their

performance in the NRR process has been evaluated, and the corresponding free energy diagrams for N_2 reduction to NH_3 at zero and applied potentials calculated, summarized in Figure 6.11-Figure 6.15 in the Supporting Information.

Like the case of Mo_1N_3, for all those Mo SACs, the end-on adsorption of N_2 is more energetically favorable than the side-on adsorption (see Supplementary Information). However, unlike Mo_1N_3, several Mo SACs (i.e., sym_$Mo_1N_2P_1$ and $Mo_1N_1P_2$, and Mo_1P_3, see Supplementary Information) would catalyze NRR through the enzymatic mechanism other than the distal mechanism, despite the more energetically favored end-on adsorption of N_2. From the calculation results, the limiting potentials are determined to be 0.45 (Mo_1P_3), 0.33 ($Mo_1N_1P_2$, averaged from the symmetric and asymmetric configurations), 0.28 ($Mo_1N_2P_1$, averaged from the symmetric and asymmetric configurations), and 0.18 V (Mo_1N_3). We see that the limiting potential monotonously decreases with increasing number of coordinated N atoms. Moreover, it was found that, unlike Mo_1N_3 for which the hydrogenation of $*NH_2$ to $*NH_3$ is the potential-limiting step, $Mo_1N_2P_1$, $Mo_1N_1P_2$, and Mo_1P_3 all have the hydrogenation of $*N_2$ into $*N_2H$ as the potential-limiting step. Generally, the chemisorption of gas phase N_2 onto the surface of the catalysts is the prerequisite for an efficient NRR process. For transition metal (TM) based catalysts, their strong binding strength with N_2 can be ascribed to their advantageous combination of empty and occupied d orbitals. On one hand, due to the existence of lone-pair electrons of N_2, TM centers need to have empty d orbitals to accept the lone-pair electrons. On the other hand, to enhance the N−TM bonds, the TM atoms should have separate d electrons that can be donated into the anti-binding orbital and weaken the N≡N triple bond. Therefore, “acceptance-donation” of electrons is the nature of the interaction between the TM and N_2, where the combination of empty and occupied d orbitals plays a key role.62 In the case of Mo-based SACs, the electronic configuration of Mo atom is $4d^5 5s^1$, and the sp^3d^2 hybridization of these orbitals will result in six half occupied orbitals and no empty orbitals.

Therefore, the surrounding N atom act as electron acceptor due to its strong electronegativity to guarantee that Mo atom has the empty *d* orbitals to accept the lone-pair electrons from N_2. This is also evidenced by the calculations of doping effect on the NRR limiting potential, that is, the limiting potential monotonously decreases with increasing number of coordinated N atoms.

From the above results, we see that the Mo SAC group (i.e., $Mo_1N_iP_{3-i}$) generally exhibits good performance in catalyzing NRR, yet the effectiveness is much dependent on the number of coordinated N atoms, with Mo_1N_3 owning sites of the highest activity with an ultralow overpotential of 0.02 eV.

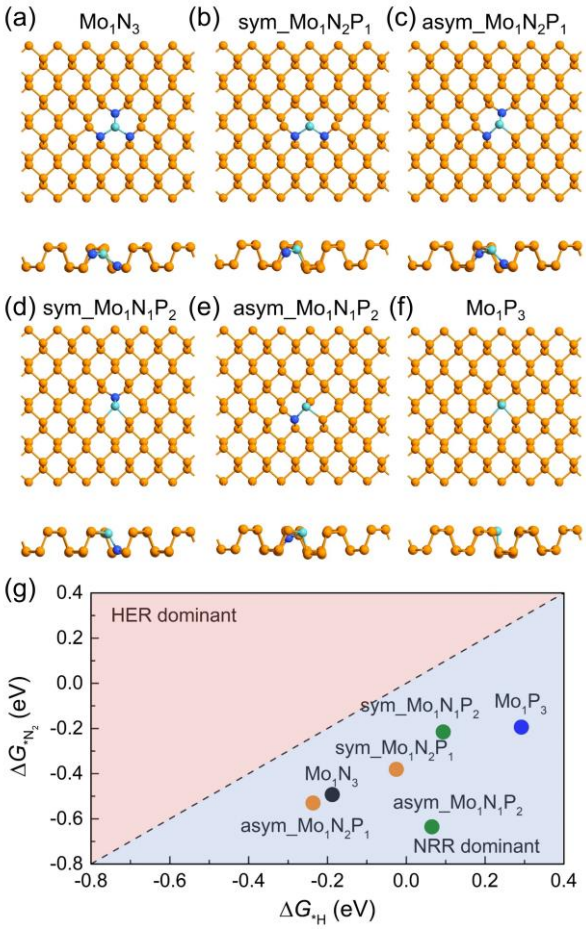

Figure 6.6 Top and side views of the optimized configurations for (a) Mo_1N_3, (b) sym_$Mo_1N_2P_1$, (c) asym_$Mo_1N_2P_1$, (d) sym_$Mo_1N_1P_2$, (e) asym_$Mo_1N_1P_2$, and (f) Mo_1P_3 SACs. (g) Calculated free energies for hydrogen (ΔG_{*H}) and N_2 adsorption (ΔG_{*N_2}) of all SACs. The red and blue shaded region in (g) respectively correspond to the HER dominant ($\Delta G_{*H} < \Delta G_{*N_2}$) and NRR dominant ($\Delta G_{*H} > \Delta G_{*N_2}$) regions at 0 V vs. RHE.

6.4.5 Competition with the Hydrogen Evolution Reaction

As we mentioned above, the free energy diagram for NRR on Mo_1N_3 demonstrated its superior electrocatalytic activity, which well surpass those of the previously reported SACs in 2D nanomaterials.[9, 20-24, 29, 58-59] As the required proton for the NRR is provided by the aqueous solution in the electrochemical environments, the H adsorption will be thermodynamically more favored than the N_2 adsorption with negative potentials.[51, 56] Therefore, the catalyst surface is easily covered by *H, and consequently such coverage would result in blockage of active sites for NRR to seriously reduce the Faradaic efficiency.[8, 63-66] Thus, in efforts to enhance the NRR selectivity, suppression of hydrogen adsorption is also an important factor to consider.[67-68] In this regard, we investigated hydrogen adsorption related to HER. Specifically, we investigated the selectivity of NRR over HER on different Mo SACs in black P by considering $*N_2$/*H selectivity. This can be quantitatively assessed by examining the free energy changes of the first reaction step for these two reactions, namely ΔG_{*N_2} and ΔG_{*H} (N_2 and H adsorption for NRR and HER, respectively), where a reaction with lower free energy is assumed to be more selective.[69] The results are illustrated in Figure 6.6g, where the catalysts in the upper left corner and lower right corner are HER and NRR dominant respectively. We can clearly see that for all the Mo SACs considered, NRR is preferred over HER. The selective electrocatalysis of N_2 to NH_3 on SACs can be largely attributed to great suppression of the HER with the synergy of geometric and electronic effects, which has been observed in previous studies on SACs in other systems, such as defective graphene[23] and $Ti_3C_2T_x$ MXene[70]. For the geometric effect, at a SAC a single metal atom exists at the active site and thus only the top site adsorption is possible on a SAC, whereas there are many metal atoms in the bulk metal surface and several adsorption sites (bridge and hollow sites) are available. On the metal surface, the *H prefers bridge and hollow sites to a top site, and *H can be destabilized on the top site. Therefore, the suppressed H adsorption is thus originated from

the availability of only the top adsorption sites on SACs, meaning that the atomic ensemble effect can play an important role in suppressing HER. While for the electronic effect, the electronic structures of SACs are quite different from those of bulk metal due to strong metal-support interaction.[17] It can lead to charge transfer between metal and support; thus an anchored metal atom usually carries some positive charge.[10, 17] Consequently the electronic structure of SAC would benefit the N_2 adsorption ability of the metal. This is also evidenced by the calculated spin-resolved density states of N_2-adsorbed Mo_1N_3, as shown in Figure 6.9 in the supporting information. It is shown that the negative charges are localized and distributed on the adsorbed N_2, while the positive charges around the anchored Mo atom.

In order to further enhance the selectivity in the design of a catalyst, other possible methods are also proposed and discussed in the previous studies.[34, 71] For instance, one method is the ion incorporation strategy, in which the Li^+ ions are incorporated into poly(N-ethyl-benzene-1,2,4,5-tetracarboxylic diimide) (PEBCD) to either hinder the Tafel or the Heyrovsky reaction, which results in a high selectivity for NRR.[34] Another possible method is to use a hydrophobic protection layer surrounding the catalyst to overcome HER-imposed bottlenecks due to its water-repelling and molecular-concentrating effects.[71] More specifically, Ling and co-workers achieved both excellent NRR selectivity of ~90% even at ambient operations by coating a superhydrophobic metal-organic framework (MOF) layer over Ag-Au platform as the NRR electrocatalyst.[71]

Further from Figure 6.6g, we note that despite the selectivity of NRR over HER for those Mo SACs, the calculated ΔG_{*H} values are within the range of ±0.3 eV (the optimal catalytic activity appears for $\Delta G_{*H} = 0$ eV in terms of HER). Given that the top-line HER catalysts (such as Pt or Pt-based catalysts) show $|\Delta G_{*H}| < 0$ eV,[57, 72-73] it is also significant to note that the current SACs candidates can also be used for other electrocatalytic reactions that require the careful control of ΔG_{*H} (e.g., catalysts for HER itself).

6.5 Conclusions

In summary, we have systematically investigated the potential of Mo-based SACs embedded in N-doped black P for electrochemical N_2 reduction into NH_3. Among those Mo-based SACs considered, Mo_1N_3 has been found to exhibit chemisorption of N_2, and an extremely low overpotential of just 0.02 V through the associative distal mechanism, indicative of catalyzing NRR under ambient conditions. In addition, Mo_1N_3 shows fast removal of the produced NH_3 with a small free energy barrier of 0.56 eV that is lower than most of reported NRR catalysts with low overpotential, and good stability of NRR reaction intermediates. Moreover, the Mo-based SACs were demonstrated to be more selective to NRR over the competing HER process. These excellent features endow Mo_1N_3 on black P as a compelling highly efficient and durable catalyst for electrochemical N_2 fixation. Our findings also further demonstrated the great potential of 2D nanomaterials, and might contribute to motivating more experimental and theoretical efforts targeting the usage of 2D nano materials in NRR electrocatalysts.

6.6 Acknowledgements

This research is supported by the NSERC Discovery grant (grant # RGPIN-2017-05187), NSERC Strategic grant (grant # STPGP 494012-16), and McGill Engineering Doctoral Award (MEDA). The authors also would like to acknowledge the Supercomputer Consortium Laval UQAM McGill and Eastern Quebec for providing computing resources.

6.7 Supporting information

6.7.1 SACs at single and double vacancies

There exist multiple other possible configurations as a Mo atom is anchored at single or double vacancies (i.e., reconstructed SV59, DV, and reconstructed DV585) in monolayer black P doped by multiple N atoms, as shown in Figure 6.7a-f. The binding energies of the

resultant Mo_1N_3 structures at SV59 are −5.96 eV and −1.34 eV with reference to atomic Mo and bulk Mo, respectively. This suggests that a single Mo atom can be stably adsorbed by three unsaturated N atoms at SV59, with even stronger bonding than that at SV. Besides, we have also examined the adsorption energies of Mo_1N_4 at DV and DV585, with the binding energies being −4.77 and −4.68 eV with reference to atomic Mo, and −0.15 and −0.05 eV with reference to bulk Mo, respectively, which again suggests strong anchoring of Mo at those defects.

To examine the relative stabilities of various types of vacancies, we have calculated the formation energies of single and double vacancies. The lowest-energy point defect is a reconstructed double vacancy (DV585) with the formation energy of 1.57 eV, which is composed of two buckled pentagons and one octagon. The reconstructed single vacancy (SV59) consisting of adjacent 9-fold and 5-fold rings exhibits the second lowest formation energy (1.77 eV). The single vacancy formed from direct removal of one P atom from the pristine black P exhibits a formation energy value of 2.21 eV. The calculated formation energies of these point defects are much lower than those in graphene.[74] Therefore, it is reasonable to expect them to form during the synthetic process. On the other hand, the formation energy of a regular DV is much higher, and as a result we do not consider it in the present study. It is worth noting that although the SV59 was theoretically predicted to be the most stable SV in black P,[75] the existence of SV has been confirmed experimentally utilizing a combination of low-temperature scanning tunneling microscopy/spectroscopy (STM/STS).[49] Consequently in the present study we put our main focus on the electrocatalytic reactions of Mo-based SACs at SV.

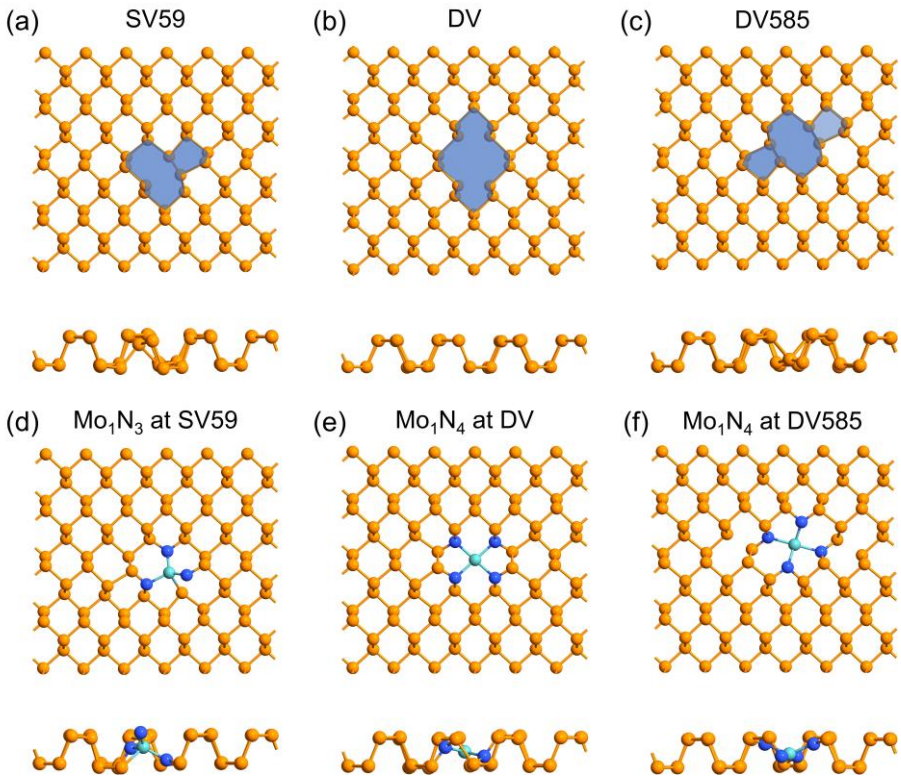

Figure 6.7 Top and side views of the optimized configurations of (a) SV59, (b) DV, and (c) DV585, as well as the Mo atom anchored at (d) SV59, (e) DV, and (f) DV585 in black P. The blue shaded areas in (a)-(c) present the defect regions. Blue, orange, and cyan balls represent doped N, P, and Mo atoms respectively.

6.7.2 Kinetics of Mo migration out of SACs

The possible migration of Mo to escape SACs has been examined, which was found to generally exhibits a large energy barrier. For instance, the energy barrier for the adsorbed Mo atom at SV to migrate to a neighboring hollow site in N-doped black P is 14.6 eV, as illustrated in Figure 6.8. Such large kinetic energy barrier effectively renders the migration of Mo at the SAC a process unlikely to occur under ambient conditions.

6.7.3 Spin-resolved density state of N_2-adsorbed Mo_1N_3

The top and side views of the spin-resolved density states of the N_2-adsorbed Mo_1N_3 via side-on and end-on adsorptions are shown in Figure 6.9a,b, respectively, clearly illustrating that the charge clouds are localized and distributed on both the adsorbed N_2 and the Mo_1N_3 center. This suggest that N_2 be in indeed activated. Noteworthy is that the spin moments of

side-on and end-on configurations are both changed to 1.00 μ_B after N_2 adsorption, and the energy differences between the spin-polarized and non-spin-polarized states are about −0.12 and −0.13 eV, respectively.

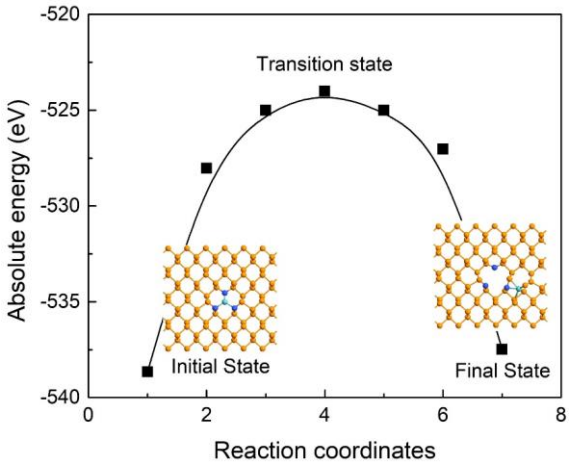

Figure 6.8 The minimum energy path (MEP) for the migration of an adsorbed Mo atom at SV in N-doped black P from the original defect binding site to a neighboring hollow site. Blue, orange, and cyan balls represent doped N, P, and Mo atoms respectively.

6.7.4 Large Mo clusters as NRR electrocatalysts

In addition to the case of Mo SACs, we also studied the possibility of larger Mo clusters supported on phosphorus SV and DV585 in black P as potential NRR electrocatalysts. Considering the similar results obtained for SV and DV585, here we take the Mo_{13} cluster at SV as a representative example. Our calculations indicate that the calculated ΔE of adsorptions for $*N_2$, $*N_2H$, and $*NH_2$ species on the immobilized Mo_{13} cluster are −1.25, −4.21, and −1.73 eV, respectively (Figure 6.10). The corresponding N≡N bond length is also elongated to 1.14 Å. These results indicate that the Mo_{13} cluster sufficiently activates the inert N_2 molecule. However, the cluster shows a weak stabilization for the $*N_2H$ species ($\Delta G_{*N_2\text{-}*N_2H} = 0.82 > 0.5$ eV), which consequently renders it unsuitable for N_2 reduction according the criteria outlined by Ling et al.[24] The above also implies that in application of Mo SACs in black P as NRR catalysts, it would be necessary to take measures to moderate or prevent Mo clustering which would have an adverse effect in the effectiveness.

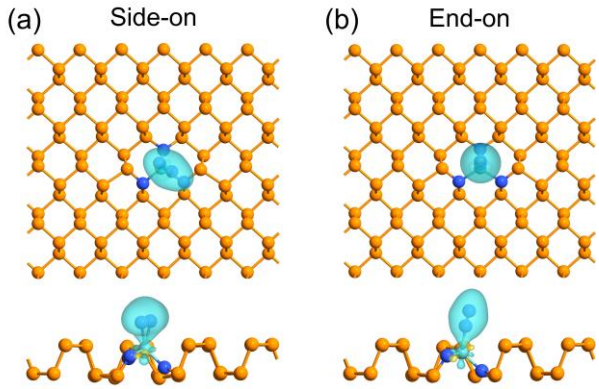

Figure 6.9 Top and side views of the optimized adsorption configurations and the spin-resolved density states of the (a) side-on and (b) end-on N_2 adsorption at Mo_1N_3 in black P. Blue, orange, and cyan balls represent doped N, P, and Mo atoms respectively. The cyan and yellow regions indicate the electron accumulation and depletion, respectively.

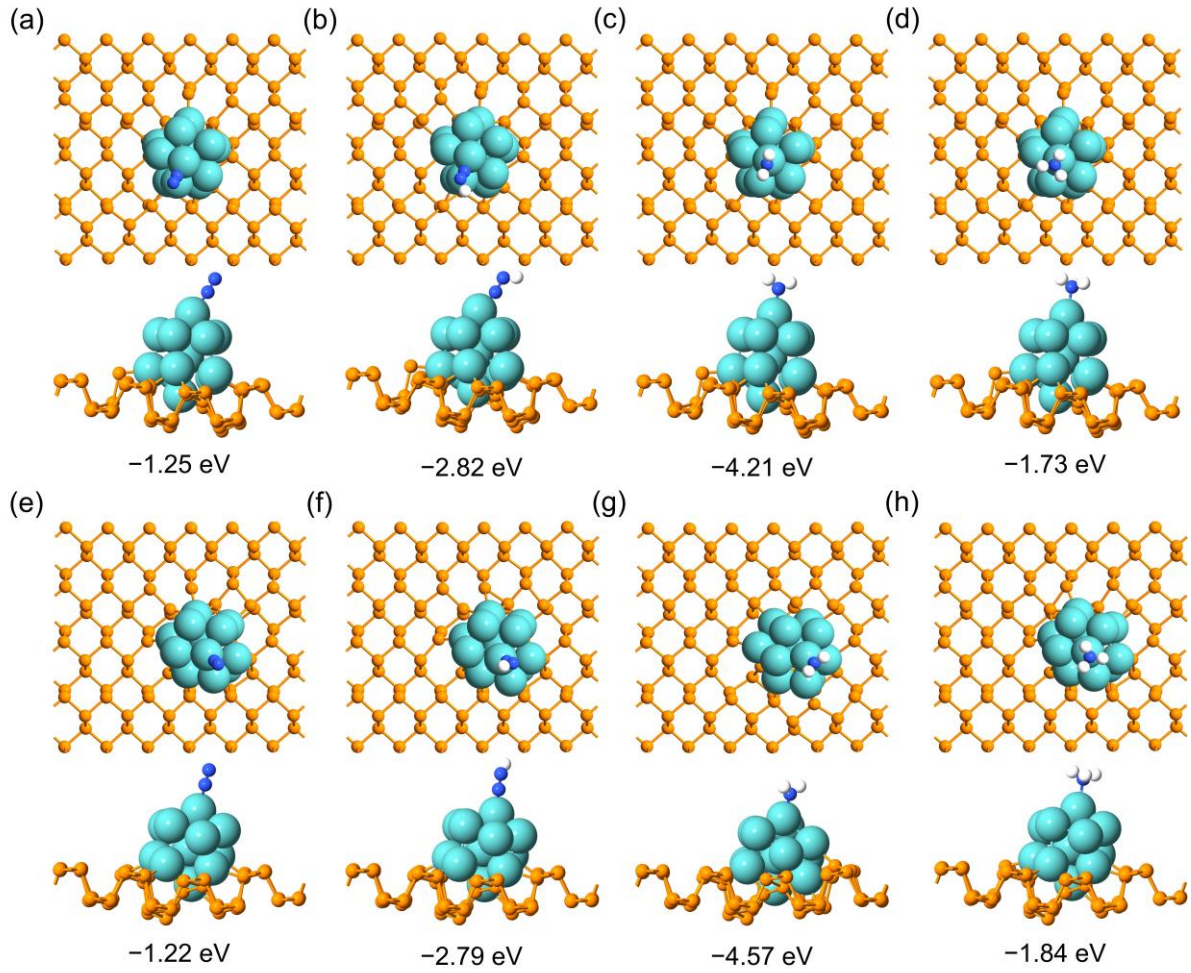

Figure 6.10 Top and side views of the optimized adsorption configurations and the corresponding adsorption energies of (a) $*N_2$, (b) $*N_2H$, (c) $*NH_2$, and (d) $*NH_3$ on Mo_{13} cluster at phosphorus SV and (e) $*N_2$, (f) $*N_2H$, (g) $*NH_2$, and (h) $*NH_3$ at phosphorus DV585 in black P. White, blue, orange, and cyan balls represent H, doped N, P, and Mo atoms respectively.

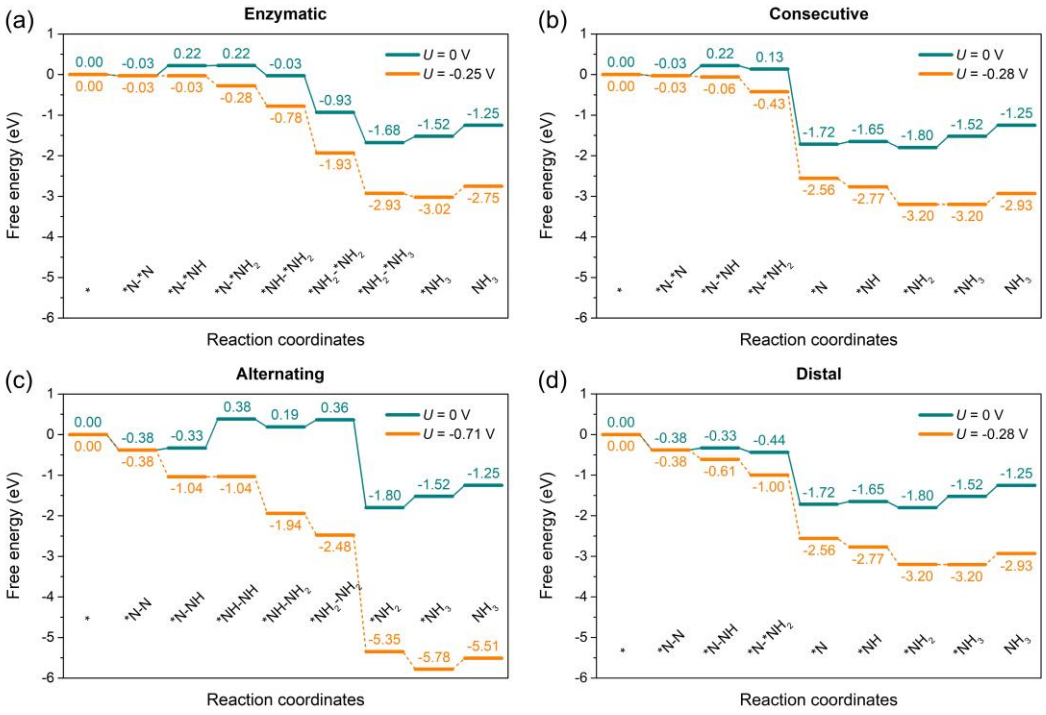

Figure 6.11 Free energy diagrams for N_2 reduction to NH_3 through (a) enzymatic, (b) consecutive, (c) alternating, and (d) distal mechanisms on sym_$Mo_1N_2P_1$ at zero and applied potentials. The green and orange curves respectively correspond to the situations of at 0 V and limiting potentials versus RHE, respectively.

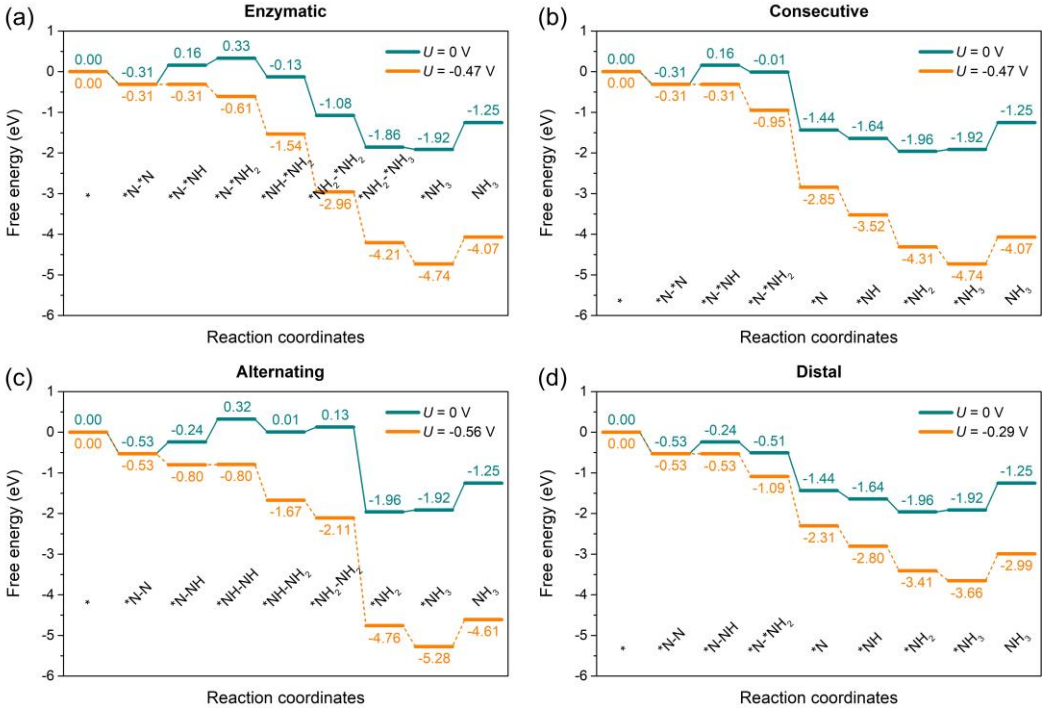

Figure 6.12 Free energy diagrams for N_2 reduction to NH_3 through (a) enzymatic, (b) consecutive, (c) alternating, and (d) distal mechanisms on asym_$Mo_1N_2P_1$ at zero and applied potentials. The green and orange curves respectively correspond to the situations of at 0 V and limiting potentials versus RHE, respectively.

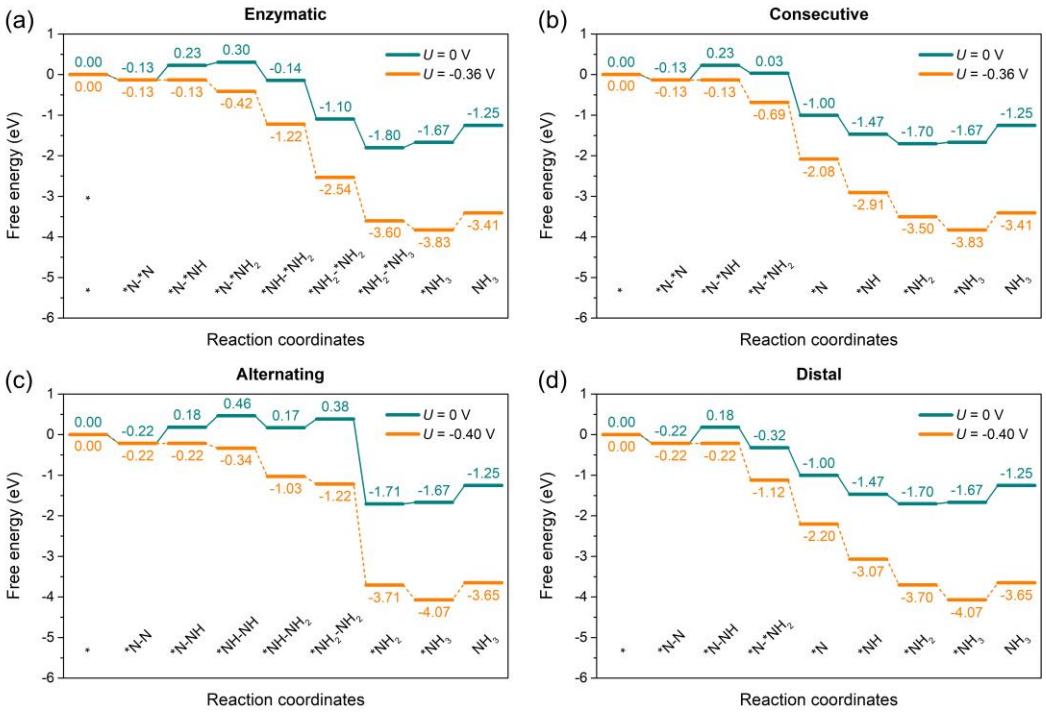

Figure 6.13 Free energy diagrams for N_2 reduction to NH_3 through (a) enzymatic, (b) consecutive, (c) alternating, and (d) distal mechanisms on sym_$Mo_1N_1P_2$ at zero and applied potentials. The green and orange curves respectively correspond to the situations of at 0 V and limiting potentials versus RHE, respectively.

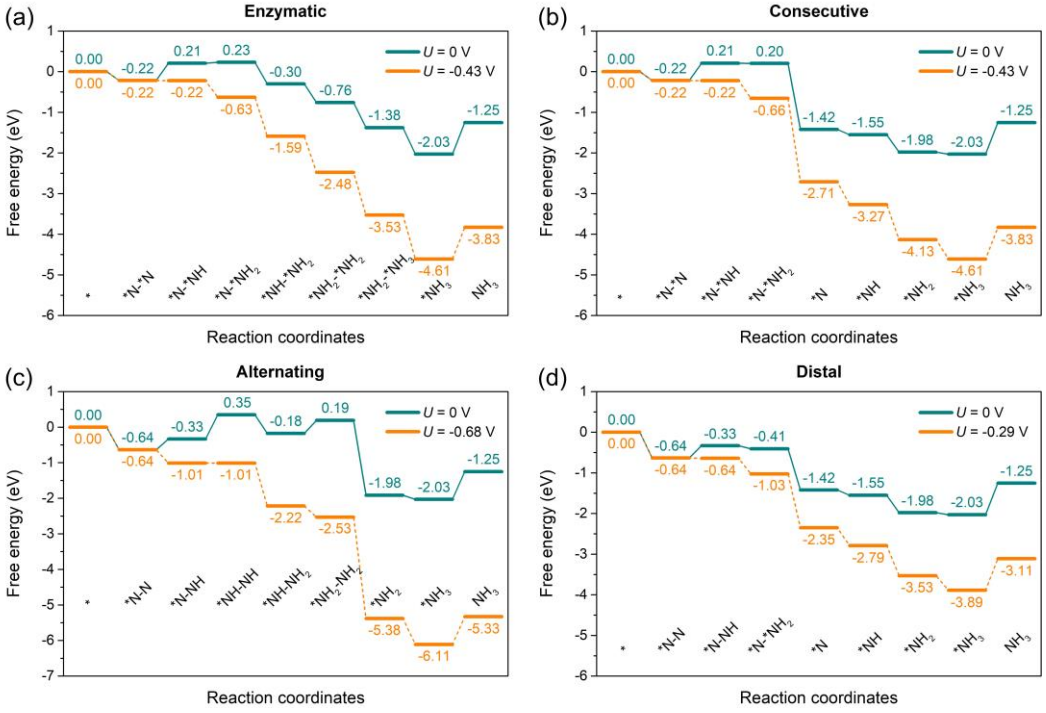

Figure 6.14 Free energy diagrams for N_2 reduction to NH_3 through (a) enzymatic, (b) consecutive, (c) alternating, and (d) distal mechanisms on asym_$Mo_1N_1P_2$ at zero and applied potentials. The green and orange curves respectively correspond to the situations of at 0 V and limiting potentials versus RHE, respectively.

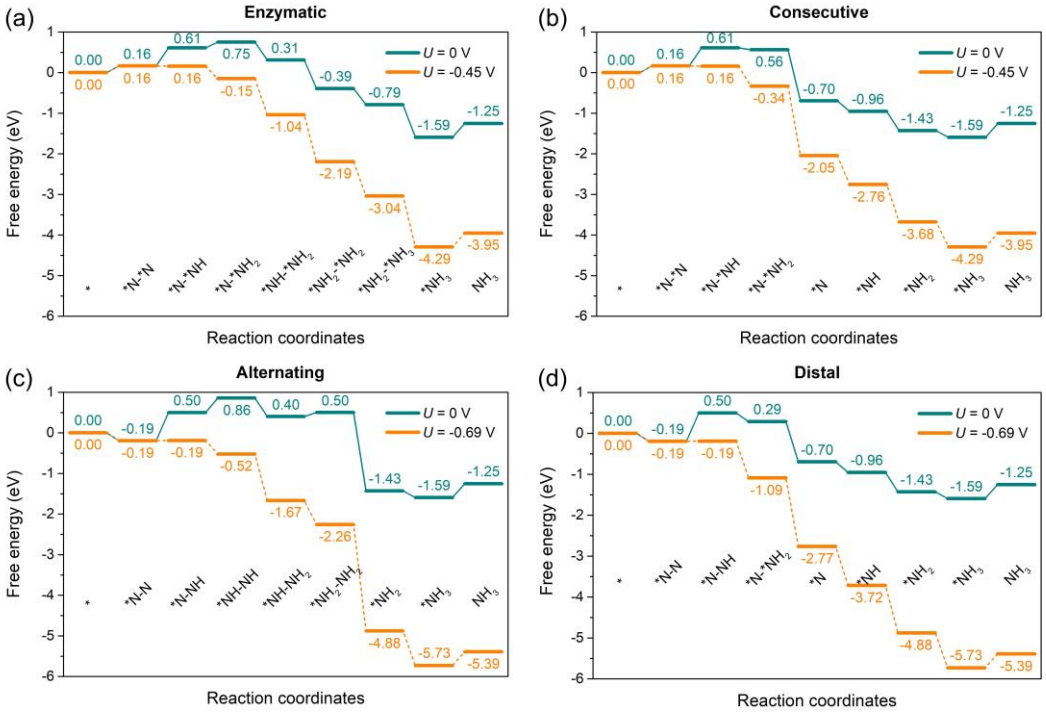

Figure 6.15 Free energy diagrams for N_2 reduction to NH_3 through (a) enzymatic, (b) consecutive, (c) alternating, and (d) distal mechanisms on Mo_1P_3 at zero and applied potentials. The green and orange curves respectively correspond to the situations of at 0 V and limiting potentials versus RHE, respectively.

6.8 References

(1) Erisman, J. W.; Sutton, M. A.; Galloway, J.; Klimont, Z.; Winiwarter, W., How a Century of Ammonia Synthesis Changed the World. *Nat. Geosci* **2008**, *1*, 636.

(2) Schlögl, R., Catalytic Synthesis of Ammonia—a "Never-Ending Story"? *Angew. Chem. Int. Ed.* **2003**, *42*, 2004-2008.

(3) Galloway, J. N.; Townsend, A. R.; Erisman, J. W.; Bekunda, M.; Cai, Z.; Freney, J. R.; Martinelli, L. A.; Seitzinger, S. P.; Sutton, M. A., Transformation of the Nitrogen Cycle: Recent Trends, Questions, and Potential Solutions. *Science* **2008**, *320*, 889-892.

(4) Canfield, D. E.; Glazer, A. N.; Falkowski, P. G., The Evolution and Future of Earth's Nitrogen Cycle. *Science* **2010**, *330*, 192-196.

(5) Chen, J. G.; Crooks, R. M.; Seefeldt, L. C.; Bren, K. L.; Bullock, R. M.; Darensbourg, M. Y.; Holland, P. L.; Hoffman, B.; Janik, M. J.; Jones, A. K., Beyond Fossil Fuel–Driven Nitrogen Transformations. *Science* **2018**, *360*, eaar6611.

(6) Chen, P., Across the Board: Ping Chen. *ChemSusChem* **2018**, *11*, 2469-2471.

(7) Van der Ham, C. J.; Koper, M. T.; Hetterscheid, D. G., Challenges in Reduction of Dinitrogen by Proton and Electron Transfer. *Chem. Soc. Rev.* **2014**, *43*, 5183-5191.

(8) Shi, M. M.; Bao, D.; Wulan, B. R.; Li, Y. H.; Zhang, Y. F.; Yan, J. M.; Jiang, Q., Au Sub-Nanoclusters on TiO_2 toward Highly Efficient and Selective Electrocatalyst for N_2 Conversion to NH_3 at Ambient Conditions. *Adv. Mater.* **2017**, *29*, 1606550.

(9) Chen, Z.; Zhao, J.; Cabrera, C. R.; Chen, Z., Computational Screening of Efficient Single-Atom Catalysts Based on Graphitic Carbon Nitride ($g\text{-}C_3N_4$) for Nitrogen Electroreduction. *Small Methods* **2018**, 1800368.

(10) Back, S.; Lim, J.; Kim, N.-Y.; Kim, Y.-H.; Jung, Y., Single-Atom Catalysts for CO_2 Electroreduction with Significant Activity and Selectivity Improvements. *Chem. Sci.* **2017**, *8*, 1090-1096.
(11) Cheng, M.-J.; Kwon, Y.; Head-Gordon, M.; Bell, A. T., Tailoring Metal-Porphyrin-Like Active Sites on Graphene to Improve the Efficiency and Selectivity of Electrochemical CO_2 Reduction. *J. Phys. Chem. C* **2015**, *119*, 21345-21352.
(12) Kornienko, N.; Zhao, Y.; Kley, C. S.; Zhu, C.; Kim, D.; Lin, S.; Chang, C. J.; Yaghi, O. M.; Yang, P., Metal–Organic Frameworks for Electrocatalytic Reduction of Carbon Dioxide. *J. Am. Chem. Soc.* **2015**, *137*, 14129-14135.
(13) Lin, S.; Diercks, C. S.; Zhang, Y.-B.; Kornienko, N.; Nichols, E. M.; Zhao, Y.; Paris, A. R.; Kim, D.; Yang, P.; Yaghi, O. M., Covalent Organic Frameworks Comprising Cobalt Porphyrins for Catalytic CO_2 Reduction in Water. *Science* **2015**, *349*, 1208-1213.
(14) Weng, Z.; Jiang, J.; Wu, Y.; Wu, Z.; Guo, X.; Materna, K. L.; Liu, W.; Batista, V. S.; Brudvig, G. W.; Wang, H., Electrochemical CO_2 Reduction to Hydrocarbons on a Heterogeneous Molecular Cu Catalyst in Aqueous Solution. *J. Am. Chem. Soc.* **2016**, *138*, 8076-8079.
(15) Qiao, B.; Wang, A.; Yang, X.; Allard, L. F.; Jiang, Z.; Cui, Y.; Liu, J.; Li, J.; Zhang, T., Single-Atom Catalysis of CO Oxidation Using Pt_1/FeO_x. *Nat. Chem.* **2011**, *3*, 634.
(16) Qiu, H. J.; Ito, Y.; Cong, W.; Tan, Y.; Liu, P.; Hirata, A.; Fujita, T.; Tang, Z.; Chen, M., Nanoporous Graphene with Single-Atom Nickel Dopants: An Efficient and Stable Catalyst for Electrochemical Hydrogen Production. *Angew. Chem. Int. Ed.* **2015**, *54*, 14031-14035.
(17) Yang, X.-F.; Wang, A.; Qiao, B.; Li, J.; Liu, J.; Zhang, T., Single-Atom Catalysts: A New Frontier in Heterogeneous Catalysis. *Acc. Chem. Res.* **2013**, *46*, 1740-1748.
(18) Yang, S.; Kim, J.; Tak, Y. J.; Soon, A.; Lee, H., Single-Atom Catalyst of Platinum Supported on Titanium Nitride for Selective Electrochemical Reactions. *Angew. Chem. Int. Ed.* **2016**, *55*, 2058-2062.
(19) Lee, D. H.; Lee, W. J.; Lee, W. J.; Kim, S. O.; Kim, Y.-H., Theory, Synthesis, and Oxygen Reduction Catalysis of Fe-Porphyrin-Like Carbon Nanotube. *Phys. Rev. Lett.* **2011**, *106*, 175502.
(20) Li, X.-F.; Li, Q.-K.; Cheng, J.; Liu, L.; Yan, Q.; Wu, Y.; Zhang, X.-H.; Wang, Z.-Y.; Qiu, Q.; Luo, Y., Conversion of Dinitrogen to Ammonia by FeN_3-Embedded Graphene. *J. Am. Chem. Soc.* **2016**, *138*, 8706-8709.
(21) Zhao, J.; Chen, Z., Single Mo Atom Supported on Defective Boron Nitride Monolayer as an Efficient Electrocatalyst for Nitrogen Fixation: A Computational Study. *J. Am. Chem. Soc.* **2017**, *139*, 12480-12487.
(22) Ling, C.; Bai, X.; Ouyang, Y.; Du, A.; Wang, J., Single Molybdenum Atom Anchored on N-Doped Carbon as a Promising Electrocatalyst for Nitrogen Reduction into Ammonia at Ambient Conditions. *J. Phys. Chem. C* **2018**, *122*, 16842-16847.
(23) Choi, C.; Back, S.; Kim, N.-Y.; Lim, J.; Kim, Y.-H.; Jung, Y., Suppression of Hydrogen Evolution Reaction in Electrochemical N_2 Reduction Using Single-Atom Catalysts: A Computational Guideline. *ACS Catal.* **2018**, *8*, 7517-7525.
(24) Ling, C.; Ouyang, Y.; Li, Q.; Bai, X.; Mao, X.; Du, A.; Wang, J., A General Two-Step Strategy–Based High-Throughput Screening of Single Atom Catalysts for Nitrogen Fixation. *Small Methods* **2018**, 1800376.
(25) Li, S.; Tuo, P.; Xie, J.; Zhang, X.; Xu, J.; Bao, J.; Pan, B.; Xie, Y., Ultrathin Mxene Nanosheets with Rich Fluorine Termination Groups Realizing Efficient Electrocatalytic Hydrogen Evolution. *Nano Energy* **2018**, *47*, 512-518.
(26) Xie, J.; Xie, Y., Transition Metal Nitrides for Electrocatalytic Energy Conversion: Opportunities and Challenges. *Chem.: Eur. J* **2016**, *22*, 3588-3598.

(27) Xu, K.; Chen, P.; Li, X.; Tong, Y.; Ding, H.; Wu, X.; Chu, W.; Peng, Z.; Wu, C.; Xie, Y., Metallic Nickel Nitride Nanosheets Realizing Enhanced Electrochemical Water Oxidation. *J. Am. Chem. Soc.* **2015**, *137*, 4119-25.
(28) Zhang, L.; Ding, L. X.; Chen, G. F.; Yang, X.; Wang, H., Ammonia Synthesis under Ambient Conditions: Selective Electroreduction of Dinitrogen to Ammonia on Black Phosphorus Nanosheets. *Angew. Chem. Int. Ed.* **2019**, *58*, 2612-2616.
(29) Li, X.; Zhong, W.; Cui, P.; Li, J.; Jiang, J., Design of Efficient Catalysts with Double Transition Metal Atoms on C_2N Layer. *J. Phys. Chem. Lett.* **2016**, *7*, 1750-1755.
(30) Yandulov, D. V.; Schrock, R. R., Catalytic Reduction of Dinitrogen to Ammonia at a Single Molybdenum Center. *Science* **2003**, *301*, 76-78.
(31) Arashiba, K.; Kinoshita, E.; Kuriyama, S.; Eizawa, A.; Nakajima, K.; Tanaka, H.; Yoshizawa, K.; Nishibayashi, Y., Catalytic Reduction of Dinitrogen to Ammonia by Use of Molybdenum–Nitride Complexes Bearing a Tridentate Triphosphine as Catalysts. *J. Am. Chem. Soc.* **2015**, *137*, 5666-5669.
(32) Arashiba, K.; Eizawa, A.; Tanaka, H.; Nakajima, K.; Yoshizawa, K.; Nishibayashi, Y., Catalytic Nitrogen Fixation Via Direct Cleavage of Nitrogen–Nitrogen Triple Bond of Molecular Dinitrogen under Ambient Reaction Conditions. *Bull. Chem. Soc. Jpn.* **2017**, *90*, 1111-1118.
(33) Eizawa, A.; Arashiba, K.; Tanaka, H.; Kuriyama, S.; Matsuo, Y.; Nakajima, K.; Yoshizawa, K.; Nishibayashi, Y., Remarkable Catalytic Activity of Dinitrogen-Bridged Dimolybdenum Complexes Bearing NHC-Based PCP-Pincer Ligands toward Nitrogen Fixation. *Nat. Commun.* **2017**, *8*, 14874.
(34) Chen, G. F.; Cao, X.; Wu, S.; Zeng, X.; Ding, L. X.; Zhu, M.; Wang, H., Ammonia Electrosynthesis with High Selectivity under Ambient Conditions Via a Li^+ Incorporation Strategy. *J. Am. Chem. Soc.* **2017**, *139*, 9771-9774.
(35) Azofra, L. M.; Li, N.; MacFarlane, D. R.; Sun, C., Promising Prospects for 2D d^2–d^4 M_3C_2 Transition Metal Carbides (MXenes) in N_2 Capture and Conversion into Ammonia. *Energy Environ. Sci.* **2016**, *9*, 2545-2549.
(36) Li, Q.; He, L.; Sun, C.; Zhang, X., Computational Study of MoN_2 Monolayer as Electrochemical Catalysts for Nitrogen Reduction. *J. Phys. Chem. C* **2017**, *121*, 27563-27568.
(37) Cheng, H.; Ding, L. X.; Chen, G. F.; Zhang, L.; Xue, J.; Wang, H., Molybdenum Carbide Nanodots Enable Efficient Electrocatalytic Nitrogen Fixation under Ambient Conditions. *Adv. Mater.* **2018**, *30*, e1803694.
(38) Zhu, M.; Kim, S.; Mao, L.; Fujitsuka, M.; Zhang, J.; Wang, X.; Majima, T., Metal-Free Photocatalyst for H_2 Evolution in Visible to Near-Infrared Region: Black Phosphorus/Graphitic Carbon Nitride. *J. Am. Chem. Soc.* **2017**, *139*, 13234-13242.
(39) Zhu, M.; Osakada, Y.; Kim, S.; Fujitsuka, M.; Majima, T., Black Phosphorus: A Promising Two Dimensional Visible and near-Infrared-Activated Photocatalyst for Hydrogen Evolution. *Appl. Catal. B* **2017**, *217*, 285-292.
(40) Jiang, Q.; Xu, L.; Chen, N.; Zhang, H.; Dai, L.; Wang, S., Facile Synthesis of Black Phosphorus: An Efficient Electrocatalyst for the Oxygen Evolving Reaction. *Angew. Chem. Int. Ed.* **2016**, *55*, 13849-13853.
(41) Ren, X.; Zhou, J.; Qi, X.; Liu, Y.; Huang, Z.; Li, Z.; Ge, Y.; Dhanabalan, S. C.; Ponraj, J. S.; Wang, S., Few-Layer Black Phosphorus Nanosheets as Electrocatalysts for Highly Efficient Oxygen Evolution Reaction. *Adv. Energy Mater.* **2017**, *7*, 1700396.
(42) Kresse, G.; Furthmüller, J., Efficient Iterative Schemes for *Ab Initio* Total-Energy Calculations Using a Plane-Wave Basis Set. *Phys. Rev. B* **1996**, *54*, 11169.
(43) Kresse, G.; Joubert, D., From Ultrasoft Pseudopotentials to the Projector Augmented-Wave Method. *Phys. Rev. B* **1999**, *59*, 1758.
(44) Blöchl, P. E., Projector Augmented-Wave Method. *Phys. Rev. B* **1994**, *50*, 17953.

(45) Perdew, J. P.; Chevary, J. A.; Vosko, S. H.; Jackson, K. A.; Pederson, M. R.; Singh, D. J.; Fiolhais, C., Atoms, Molecules, Solids, and Surfaces: Applications of the Generalized Gradient Approximation for Exchange and Correlation. *Phys. Rev. B* **1992**, *46*, 6671.
(46) Perdew, J. P.; Wang, Y., Accurate and Simple Analytic Representation of the Electron-Gas Correlation Energy. *Phys. Rev. B* **1992**, *45*, 13244.
(47) Monkhorst, H. J.; Pack, J. D., Special Points for Brillouin-Zone Integrations. *Phys. Rev. B* **1976**, *13*, 5188.
(48) Henkelman, G.; Uberuaga, B. P.; Jónsson, H., A Climbing Image Nudged Elastic Band Method for Finding Saddle Points and Minimum Energy Paths. *J. Chem. Phys.* **2000**, *113*, 9901-9904.
(49) Guo, Y.; Robertson, J., Vacancy and Doping States in Monolayer and Bulk Black Phosphorus. *Sci. Rep.* **2015**, *5*, 14165.
(50) Peterson, A. A.; Abild-Pedersen, F.; Studt, F.; Rossmeisl, J.; Nørskov, J. K., How Copper Catalyzes the Electroreduction of Carbon Dioxide into Hydrocarbon Fuels. *Energy Environ. Sci.* **2010**, *3*, 1311-1315.
(51) Skulason, E.; Bligaard, T.; Gudmundsdóttir, S.; Studt, F.; Rossmeisl, J.; Abild-Pedersen, F.; Vegge, T.; Jónsson, H.; Nørskov, J. K., A Theoretical Evaluation of Possible Transition Metal Electro-Catalysts for N_2 Reduction. *Phys. Chem. Chem. Phys.* **2012**, *14*, 1235-1245.
(52) Henkelman, G.; Arnaldsson, A.; Jónsson, H., A Fast and Robust Algorithm for Bader Decomposition of Charge Density. *Comput. Mater. Sci.* **2006**, *36*, 354-360.
(53) Sanville, E.; Kenny, S. D.; Smith, R.; Henkelman, G., Improved Grid-Based Algorithm for Bader Charge Allocation. *J. Comput. Chem.* **2007**, *28*, 899-908.
(54) Tang, W.; Sanville, E.; Henkelman, G., A Grid-Based Bader Analysis Algorithm without Lattice Bias. *J. Phys.: Condens. Matter* **2009**, *21*, 084204.
(55) Yu, M.; Trinkle, D. R., Accurate and Efficient Algorithm for Bader Charge Integration. *J. Chem. Phys.* **2011**, *134*, 064111.
(56) Montoya, J. H.; Tsai, C.; Vojvodic, A.; Nørskov, J. K., The Challenge of Electrochemical Ammonia Synthesis: A New Perspective on the Role of Nitrogen Scaling Relations. *ChemSusChem* **2015**, *8*, 2180-2186.
(57) Seh, Z. W.; Kibsgaard, J.; Dickens, C. F.; Chorkendorff, I.; Nørskov, J. K.; Jaramillo, T. F., Combining Theory and Experiment in Electrocatalysis: Insights into Materials Design. *Science* **2017**, *355*, eaad4998.
(58) Ji, S.; Wang, Z.; Zhao, J.-X., Boron-Interstitial Doped C_2N Layer as a Metal-Free Electrocatalyst for N_2 Fixation: A Computational Study. *J. Mater. Chem. A* **2019**, *7*, 2392-2399.
(59) Ling, C.; Niu, X.; Li, Q.; Du, A.; Wang, J., Metal-Free Single Atom Catalyst for N_2 Fixation Driven by Visible Light. *J. Am. Chem. Soc.* **2018**, *140*, 14161-14168.
(60) Skulason, E.; Bligaard, T.; Gudmundsdóttir, S.; Studt, F.; Rossmeisl, J.; Abild-Pedersen, F.; Vegge, T.; Jónsson, H.; Nørskov, J. K., A Theoretical Evaluation of Possible Transition Metal Electro-Catalysts for N_2 Reduction. *Phys. Chem. Chem. Phys.* **2012**, *14*, 1235-1245.
(61) Kuriyama, S.; Arashiba, K.; Nakajima, K.; Tanaka, H.; Kamaru, N.; Yoshizawa, K.; Nishibayashi, Y., Catalytic Formation of Ammonia from Molecular Dinitrogen by Use of Dinitrogen-Bridged Dimolybdenum–Dinitrogen Complexes Bearing PNP-Pincer Ligands: Remarkable Effect of Substituent at PNP-Pincer Ligand. *J. Am. Chem. Soc.* **2014**, *136*, 9719-9731.
(62) Légaré, M.-A.; Bélanger-Chabot, G.; Dewhurst, R. D.; Welz, E.; Krummenacher, I.; Engels, B.; Braunschweig, H., Nitrogen Fixation and Reduction at Boron. *Science* **2018**, *359*, 896-900.
(63) Lan, R.; Irvine, J. T.; Tao, S., Synthesis of Ammonia Directly from Air and Water at Ambient Temperature and Pressure. *Sci. Rep.* **2013**, *3*, 1145.

(64) Licht, S.; Cui, B.; Wang, B.; Li, F.-F.; Lau, J.; Liu, S., Ammonia Synthesis by N_2 and Steam Electrolysis in Molten Hydroxide Suspensions of Nanoscale Fe_2O_3. *Science* **2014**, *345*, 637-640.
(65) Kordali, V.; Kyriacou, G.; Lambrou, C., Electrochemical Synthesis of Ammonia at Atmospheric Pressure and Low Temperature in a Solid Polymer Electrolyte Cell. *Chem. Commun.* **2000**, 1673-1674.
(66) Bao, D.; Zhang, Q.; Meng, F. L.; Zhong, H. X.; Shi, M. M.; Zhang, Y.; Yan, J. M.; Jiang, Q.; Zhang, X. B., Electrochemical Reduction of N_2 under Ambient Conditions for Artificial N_2 Fixation and Renewable Energy Storage Using N_2/NH_3 Cycle. *Adv. Mater.* **2017**, *29*, 1604799.
(67) Zhang, L.; Sharada, S. M.; Singh, A. R.; Rohr, B. A.; Su, Y.; Qiao, L.; Nørskov, J. K., A Theoretical Study of the Effect of a Non-Aqueous Proton Donor on Electrochemical Ammonia Synthesis. *Phys. Chem. Chem. Phys.* **2018**, *20*, 4982-4989.
(68) Singh, A. R.; Rohr, B. A.; Schwalbe, J. A.; Cargnello, M.; Chan, K.; Jaramillo, T. F.; Chorkendorff, I.; Nørskov, J. K., Electrochemical Ammonia Synthesis—the Selectivity Challenge. *ACS Catal.* **2016**, *7*, 706-709.
(69) Chen, Z.; Zhang, X.; Lu, G., Overpotential for CO_2 Electroreduction Lowered on Strained Penta-Twinned Cu Nanowires. *Chem. Sci.* **2015**, *6*, 6829-6835.
(70) Luo, Y.; Chen, G.-F.; Ding, L.; Chen, X.; Ding, L.-X.; Wang, H., Efficient Electrocatalytic N_2 Fixation with MXene under Ambient Conditions. *Joule* **2019**, *3*, 279-289.
(71) Lee, H. K.; Koh, C. S. L.; Lee, Y. H.; Liu, C.; Phang, I. Y.; Han, X.; Tsung, C.-K.; Ling, X. Y., Favoring the Unfavored: Selective Electrochemical Nitrogen Fixation Using a Reticular Chemistry Approach. *Sci. Adv.* **2018**, *4*, eaar3208.
(72) Greeley, J.; Jaramillo, T. F.; Bonde, J.; Chorkendorff, I.; Nørskov, J. K., Computational High-Throughput Screening of Electrocatalytic Materials for Hydrogen Evolution. In *Materials for Sustainable Energy: A Collection of Peer-Reviewed Research and Review Articles from Nature Publishing Group*, World Scientific: **2011**; pp 280-284.
(73) Nørskov, J. K.; Bligaard, T.; Logadottir, A.; Kitchin, J.; Chen, J. G.; Pandelov, S.; Stimming, U., Trends in the Exchange Current for Hydrogen Evolution. *J. Electrochem. Soc.* **2005**, *152*, J23-J26.
(74) Banhart, F.; Kotakoski, J.; Krasheninnikov, A. V., Structural Defects in Graphene. *ACS Nano* **2010**, *5*, 26-41.
(75) Li, X.-B.; Guo, P.; Cao, T.-F.; Liu, H.; Lau, W.-M.; Liu, L.-M., Structures, Stabilities, and Electronic Properties of Defects in Monolayer Black Phosphorus. *Sci. Rep.* **2015**, *5*, 10848.

Chapter 7 : Electrical Metal Contacts to Monolayer Blue Phosphorus: Electronic and Chemical Properties

In addition to the theoretical studies in Chapters 4-6 regarding the black phosphorus, Chapter 7 focuses on blue phosphorus, examining the nature of common transition metal contacts to monolayer blue phosphorus and demonstrated that metal substrates would substantially alter the electronic and chemical properties of monolayer blue phosphorus in the heterojunction. In this chapter, the Fermi level pinning was observed when monolayer blue phosphorus forms n- or p-type Schottky contact with transition metals, and the intrinsic reasons for this phenomenon were clarified by comparing various interfacial properties. Using hydrogen evolution reaction as an illustration, the substrate coupling was found to significantly enhance the binding strength of hydrogen and render blue phosphorus a more optimal HER catalyst.

- This chapter is to be submitted, appeared as: Pengfei Ou, Guoqiang Lan, Yiqing Chen, Xiao Zhou, Cheng Chen, Fanchao Meng, and Jun Song. **Electrical metal contacts to monolayer blue phosphorus: electronic and chemical properties**.

7.1 Abstract

The contact nature when monolayer blue phosphorus (blue P) contacts with three transition metal electrodes (i.e., Pd, Ir, and Pt) was unraveled by the density functional theory calculations. Specifically, n-type Schottky contact with an electron Schottky barrier height (SBH) of 0.49 eV is observed between monolayer blue P and Pt(111), in contrast, p-type Schottky contacts with hole SBHs of 0.52 and 0.57 eV are formed for Ir(111) and Pt(111), respectively. The Fermi level is pinned partially at metal-blue P interfaces due to two interfacial behaviors: one being the modification of metal work function caused by interface dipole formation ascribed to a redistribution of charges, and the other being the production of gas states that dominated by P *p*-orbitals nature since the intralayer P−P bonding is weakened by the interfacial metal-P interactions. Using hydrogen evolution reaction (HER) as an illustration, it is further illustrated that the incorporation of metal substrates would significantly alter the chemical properties of adsorbed overlayer of monolayer blue P. The binding strength of hydrogen can be enhanced by as much as 0.9 eV, which resulted from two parts: one is the charge transfer from metal substrate to monolayer blue P rendering a stronger H−P coupling; the other being a strong interfacial interaction after the hydrogen adsorption. The free energy change of hydrogen adsorption onto Ir(111)-blue P is as low as 0.16 eV which is comparable to the most efficient catalyst of Pt for HER. These findings would provide theoretical guidance to future design of electronic devices based on blue P, as well as to explore its potential in novel HER catalysts.

7.2 Introduction

Among the numerous members in the two-dimensional (2D) family, the 2D counterpart of black phosphorus (black P) has attracted tremendous research interest due to its astonishing physical and chemical properties.[1-2] Black P is the most thermodynamically stable among other phosphorus allotropes, which exhibits a thickness-dependent direct band gap changing

from 0.91 eV for monolayer to 0.28 eV for five-layers,[3] and an anisotropic mobility as high as 1,000 $cm^2 V^{-1} s^{-1}$ realized by using multilayers black P field-effect transistors (FETs).[2] Additionally, monolayer black P also has been demonstrated to possess other appealing characteristics, for instance, thickness-dependent on/off ratio[1], strong in-plane anisotropy,[4] and excellent photocatalytic performance for hydrogen evolution reaction (HER).[1, 5]

Phosphorus is known to display fascinating structural diversity and be stable in a large family of structures.[6-8] Particularly, it was found recently that, aided by the dislocation of certain constituent P atoms, the puckered structure of black P can be transformed into a buckled structure of higher symmetry, resulting in another 2D phosphorus allotrope nominated as blue phosphorus (blue P).[9-10] Blue P was suggested to have the layered honeycomb structure and share similar thermodynamic stability with black P with only a few meV higher in cohesive energy.[9-10] In addition, the band gap of blue P is also thickness-dependent and can be tuned from 2.0 eV for monolayer to 1.2 eV in the bulk crystal,[9] which renders it great promise for FET device applications. Besides, Aierken et al. observed that the blue P is more thermodynamically stable than black P over 135 K by considering the finite temperature effects.[11] Recently, following the theoretical predictions, monolayer blue P has been successfully synthesized by molecular beam epitaxial growth on Au(111) by using black P as precursor[12] and quasi-free-standing growth on Au(111) surface functionalized by tellurium.[13] Therefore, the realization of high-quality and large-scale growth of monolayer blue P enables the future design of electronic and optoelectronic devices based on this emerging 2D nanomaterial. In addition, we also expect it can be a potential candidate as a HER catalyst as it shares similar structure, electronic and chemical properties of black P. However, the application of blue P for catalyzing HER has been scarcely reported theoretically or experimentally. In this regard, a more comprehensive knowledge of substrate effects on the

electronic and chemical properties of monolayer blue P is urgently required and make substantial contribution to accelerate the development towards its applications.

In the present study, we provide a systematically and comprehensively investigation of the commensurate interfaces between monolayer blue P and chosen metal substrates (Pd, Ir, and Pt) based on density function theory (DFT) calculations. These metal surfaces offers minimal lattice mismatch with blue P and cover a considerable range of work functions, and thus might also serve as potential contact materials or growth substrates for blue P. It is confirmed that the Schottky contact is formed in all situations, and the relation between Schottky barrier height (SBH) and metal work function (WF) depicts a picture of partial Fermi level pinning (FLP).[14] Using hydrogen evolution reaction (HER) as an illustration, it is further illustrated that the incorporation of metal substrates would significantly alter the chemical properties of adsorbed monolayer blue P. The binding strength of hydrogen can be enhanced by as much as 0.9 eV, partially owing to the charge transfer from metal substrate to monolayer blue P rendering a stronger H−P coupling; and partially to a strong interfacial interaction after the hydrogen adsorption. The free energy change of hydrogen adsorption onto blue P/Ir(111) is only 0.16 eV, which is comparable to the most efficient transition metal catalyst of Pt for HER.

7.3 Computational method

First-principles DFT calculations[15] were performed using the Vienna *ab-initio* simulation package (VASP) with the projector-augmented wave (PAW) pseudopotentials[16] and the Ceperley-Alder local density approximation (LDA)[17], with the exchange-correlation functional parametrized by Perdew and Zunger. The metal-blue P system is illustrated in Figure 7.1, consisting of a monolayer blue P placed on a metal substrate that contains a slab of 6 atomic layers. A vacuum layer of more than 15 Å in thickness was introduced along the direction perpendicular to the blue P nanosheet to ensure the periodic images were decoupled,

and the energy cut-off was chosen as 400 eV. The metal substrate was taken to conform to the lattice of blue P. The bottommost layer of metal atoms was fixed with respect to their bulk positions, meanwhile all the other atoms were allowed to relax. The structural relaxation was considered to be converged when the force on any given atom fell under 0.01 eV $Å^{-1}$, and the electronic optimization stopped when the total energy difference between the neighboring optimization loop was smaller than 10^{-6} eV. A 6 × 6 × 1 and 8 × 8 × 1 *k*-point meshes were used for structural and electronic optimization, respectively. It is worth noting that the bulk metal lattice constants were prior determined from separate sets of calculations. For the heaviest element, Pt, the spin-orbit coupling effect was also examined and our results indicated that it has only negligible effect on the energy.

7.4 Results and discussion

7.4.1 Geometry and Stability

The planar lattice constant of monolayer blue P is 3.22 Å optimized by LDA, which agrees reasonably with the value of 3.28 Å from experimental measurement.[12] The metal-blue P contact comprises a monolayer blue P interfacing with three different transition metal substrates (the work functions of Pd, Ir, and Pt varies from 5.69, 5.74, to 5.96 eV, respectively) exhibiting the (111) surface, which is the favored orientation with the minimum surface energy. These choices are made to minimize lattice mismatch, i.e., to ensure that a 2 × 2 unit cell of the metal substrate match closely with the $(\sqrt{3} \times \sqrt{3})R30°$ unit cell of blue P (Figure 7.1). The maximum and minimum compressive strains between the monolayer blue P and these transition metals are 4.1% and 3.0% for Ir(111) and Pt(111), respectively. As previously mentioned, the metal lattice was taken to conform to that of blue P, to capture details of the electronic behaviors at the examined interface in a consistent and comparative way. The most stable geometry of metal-blue P contacts are determined from different initial configurations, which are created by in-plane rotation and displacement between metal substrate and blue P.

Examining the contact geometry after relaxation, we found that for all the systems, the metal layer that near the interface stays planar, whereas the bottom layer of blue P undergoes substantially large distortion resulted from a strong interaction between the P and underlying metal atoms. The values of the equilibrium metal-blue P separation (d_z^0 in Figure 7.1) are listed in Table 7.1. Despite different d_z^0 values, the relative in-plane positions between blue P and the underlying substrate stay the same for all three metal substrates considered. In particular, as depicted in Figure 7.1a, the top three P atoms in the supercell sit above the top sites, fcc and hcp hollows, on the other hand, the bottom three P atoms sit directly above the triangular centers constructed by top, fcc, and hcp sites, respectively.

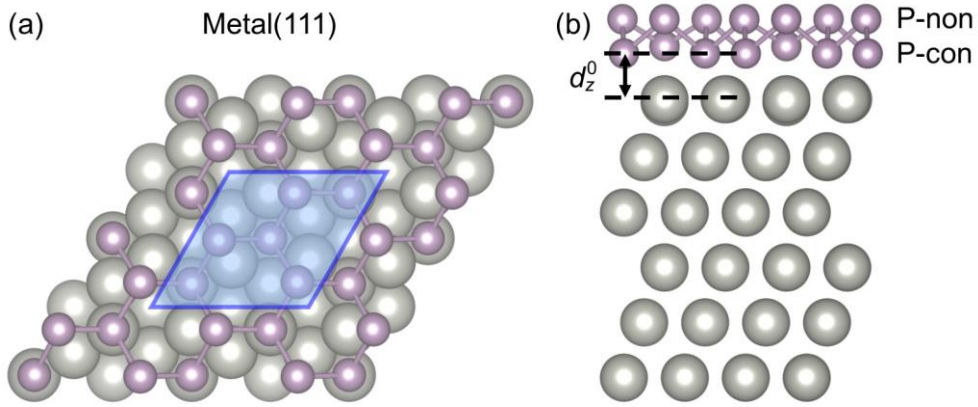

Figure 7.1 (a) Top and (b) side perspectives of monolayer blue P adsorbed on the (111) surface of metal substrates. The blue-colored region indicates the unit cell in the calculation. "P-con" and "P-non" indicate P atoms directly and not directly contact with metal substrates, respectively. Purple and grey spheres represent P and metal (Pd, Ir, and Pt) atoms, respectively.

To estimate the structural stability of the metal-blue P contacts, the binding strength is evaluated in terms of the binding energy per P atom, which is defined as

$$E_b = (E_{metal} + E_{blue\ P} - E_{metal\text{-}blue\ P})/n \quad (7.1)$$

where E_{metal} and $E_{blue\ P}$ denote the energies of isolated metal substrate and free-standing blue P, $E_{metal\text{-}blue\ P}$ the total energy of metal-blue P contact, and n denote the number of phosphorus atoms in direct contact with the metal substrate, respectively. The calculated binding energies are summarized in Table 7.1, ranging from 0.84 to 1.68 eV. The positive binding energies

indicate that the metal-blue P contacts are thermodynamically stable. As shown in Table 7.1, blue P is found to be chemically adsorbed on the metal surfaces studied herein as the binding energies are larger than 0.5 eV. It is worth to note that these *d*-electron metals interact much stronger with blue P compared to black P and MoS_2.[18-20]

Table 7.1 Metrics characterizing structures and energetics for the free-standing blue P and metal-blue P systems. Here, WF_{metal} indicates the work function of metals, ε denotes the lattice mismatch between metal and blue P, d_z^0 and d_z^H are the equilibrium metal-blue P separations without and with H adsorption respectively, d_{H-P} is length of H−P bond, θ is the angle between the H−P bond and the planar surface of blue P, and E_b is the metal-blue P binding energy per P atom. Also listed are the values of conduction band minimum (CBM) and valence band maximum (VBM) of blue P in metal-blue P, the free energy of H adsorption (ΔG_{*H}) on the basal plane of a free-standing blue P or metal-blue P systems.

	WF_{metal} (eV)	ε (%)	d_z^0 (Å)	d_z^H (Å)	E_b (eV)	CBM* (eV)	VBM* (eV)	ΔG_{*H} (eV)	d_{H-P} (Å)	θ (°)
Pristine blue P								1.07	1.52	43.1
Pd(111)-blue P	5.69	3.4	1.91	1.72	1.68	0.49	0.50	0.40	1.45	87.4
Ir(111)-blue P	5.76	4.1	1.80	1.72	0.84	0.67	0.52	0.16	1.46	52.5
Pt(111)-blue P	5.96	3.0	1.83	1.66	1.32	0.58	0.57	0.39	1.46	54.0

*The band edges of monolayer blue P are −4.46 and −6.32 eV with respect to the vacuum level, and the CBM/VBM of metal-blue P junctions are determined by the projecting the main P *p*-orbital states and treating the minor P *p*-orbital states as gap states.

7.4.2 Electronic properties

The contact nature (e.g., Schottky vs. ohmic, and p-type vs. n-type) is one of the key properties that affects the transport behavior and device performance of the metal-semiconductor junction (MSJ). To further elucidate the nature of these metal-blue P contacts, the band structures of three different metal-blue P interfaces are predicted and illustrated in Figure 7.2, and the formation of Schottky contact is confirmed in all metal-blue P junctions by the deduced band edges of blue P. Strictly speaking, the terminology band is only suitable for homogeneous crystals, whereas for heterogeneous MSJs with hybridization of orbitals, the CBM and VBM on the semiconductor side can be recognized by neglecting the spilled hybridization states as gap states.[19] As indicated in the projected band structures in Figure 7.2,

the conduction band minimum (CBM) and valence band maximum (VBM) of blue P are determined by the main P *p*-orbitals states (the evident red dots) at K and Γ point, respectively. When contacting with metal surfaces, the conduction bands of monolayer blue P are preserved well, however the valence bands are severely hybridized with the *d*-orbitals of transition metals. Electron or hole SBH ($\Phi_V^{e/h}$) can be determined from the energy difference between the Fermi energy of MSJ and the CBM or VBM of the contacted blue P, respectively. As shown in Figure 7.2, those bands of blue P with small weights crossing the Fermi level is a result of band hybridization at metal-blue P junction. These bands can be considered as a portion of interfacial gap states and would not alter the SBH. Consequently, the projected main P *p*-orbital states are used to determine the CBM/VBM and bang gap of blue P. The band gap of blue P becomes 0.99, 1.19, and 1.15 eV in the metal-blue P junctions when contacts with Pd(111), Ir(111), and Pt(111) substrates, respectively, substantially smaller than that of free-standing monolayer blue P (1.86 eV) due to the energy bands broadening perturbed by the inclusion of metal substrates. Additionally, the extension of the states of blue P at the band edges to the band gap region induces a metallic character in blue P. Pd-blue P contact forms an n-type Schottky barrier with electron SBH of 0.49 eV, in contrast, Ir- and Pt-P contacts render p-type Schottky barriers with hole SBHs of 0.52 and 0.57, respectively. By adsorbing the blue P directly onto the metal substrates leads to the Fermi level being pinned within the band gap of blue P, which is ascribed to high work functions of these chosen metals. To quantitively describe the degree of FLP, we adopted the pinning factor *S* with the definition of

$$S = d\Phi_V^{e/h}/dWF_{metal} \tag{7.2}$$

where $\Phi_V^{e/h}$ is the vertical SBH in n-type or p-type metal-blue P contacts, and WF_{metal} is the work function of isolated metal substrates. Derived from the Schottky-Mote rule, *S* varies from $S = 1$ for an unpinned Fermi level and $S = 0$ for a completely pinned Fermi level.[21-22] Realistically, *S* is usually small for MSJs due to a strong FLP effect. As shown in Figure 7.3,

the calculated pinning factor is $S = 0.29$ for monolayer blue P, which is similar to the calculated values of $S = 0.28$ for monolayer black P[23] and $S = 0.27$ for monolayer MoS_2,[24-25] but higher than the experiments measured for monolayer MoS_2.[26] This pinning factor indicates that the metal-blue P interface would be strongly impacted by FLP effect.

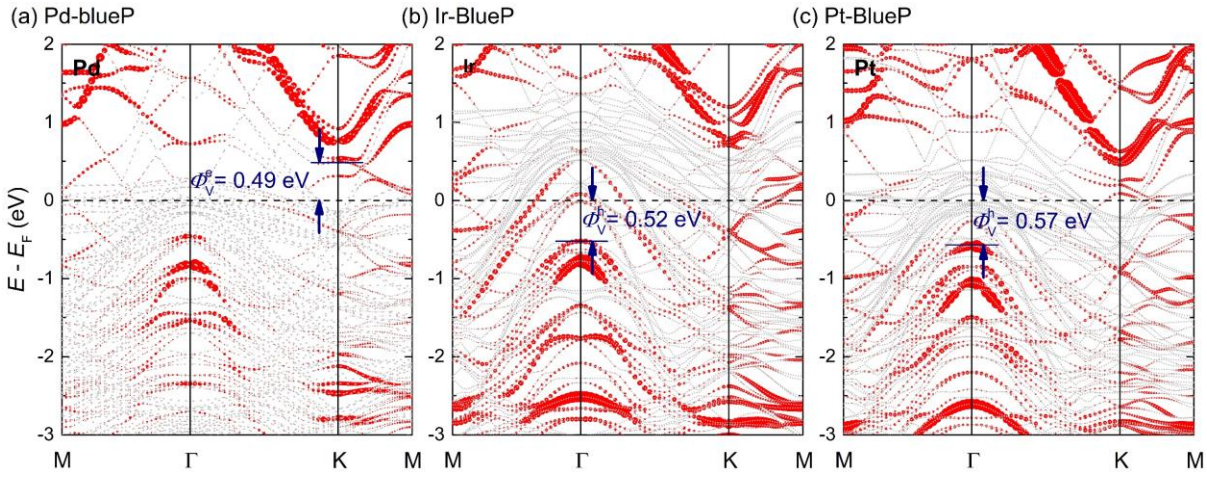

Figure 7.2 Band structures of monolayer blue P adsorbed on (a) Pd(111), (b) Ir(111), and (c) Pt(111) surfaces, respectively. The Fermi level is adjusted to 0 eV in all the three figures and is marked by the black dashed lines. The red dots indicate to the *p*-orbitals projection of the monolayer blue P, and the blue numbers denote the values of vertical SBHs.

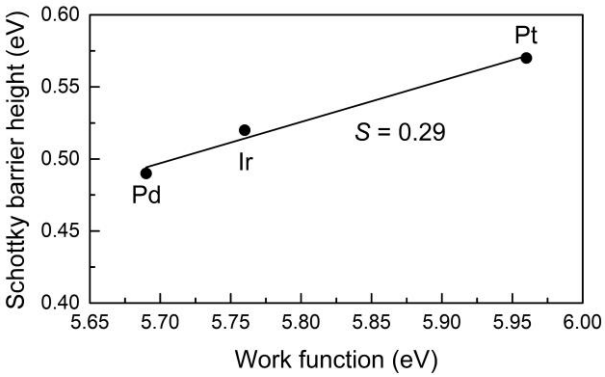

Figure 7.3 Variation in Schottky barrier heights for the monolayer blue P with work functions of Pd(111), Ir(111), and Pt(111), *S* is the pinning factor derived from the Schottky-Mote rule.

To provide a fundamental understanding of the charge transfer at the metal-blue P contacts, the charge density differences is defined to visualize the charge redistribution at the interface,

$$\Delta\rho = \rho_{\text{metal-blue P}} - \rho_{\text{metal}} - \rho_{\text{blue P}} \tag{7.3}$$

where $\rho_{\text{metal-blue P}}$, ρ_{metal}, and $\rho_{\text{blue P}}$ denote the plane-averaged charge densities of the metal-blue P interfaces, isolated metal substrates and monolayer blue P, respectively. Therefore, the charge redistribution is calculated along the vertical direction perpendicular to the interface. Zooming into the characteristics at interface region of Figure 7.4, the major difference that distinguishes metal-blue P contact from metal-graphene contact is the existence of a charge accumulation area (red colored region), which agrees well with the fact that blue P is more chemically reactive than graphene. On the other hand, both metal-blue P, metal-MoS_2,[18-19] and metal-graphene[27] contacts share the common feature of a charge depletion region (blue colored region). Generally speaking, both the charge accumulation and depletion contribute to the interfacial charge redistribution, which results in a polarization of electron wave functions, i.e., the formation of interface electric dipole. Therefore, the interface band alignment is modified by the interface electric dipole formation.[28] However, charge redistribution is much reduced to an order of magnitude smaller *y*-axis values at Pd-blue P interface when the interfacial distance increases to 4.5 Å (Figure 7.4d), compared to that of equilibrium distance. The increased distance weakens the interaction and decrease the interface electric dipole between metals and blue P, therefore reduces the FLP phenomenon at metal-blue P interfaces.

Another notable interface behavior, i.e., a strong metal-blue P hybridization is also uncovered by the charge accumulation area, which is further substantiated by analyzing the partial density of states (PDOS), as illustrated in Figure 7.5. Obviously, the direct hybridization of orbitals should be observed at the interface region of metal-blue P contact. The interlayer distances in the vertical direction between bottom P atoms in blue P and the metal atoms on surface (1.80~1.91 Å) are much smaller than that of van der Waals separation (for instance, 3.34 Å in graphite), which maximize the spatial overlapping at the interface region. Besides, the lone pairs of P atoms also constitute to the strong interaction between blue P and metals. According to the Valence Shell Electron Pair Repulsion Theory (VSEPR), each P atom in blue

P forms valence bonds with three nearest neighbors, therefore each P atom possess a lone pair that are not shared with other P atoms. The lone pairs exhibit relatively high chemical reactivity and have tendency to react with the metal atoms on the surface, rendering a stronger interaction between blue P and metals. Furthermore, a detailed analysis of PDOS discloses that the gaps states are dominated by the *d*-orbitals character of metals and primarily contribute to the lower part of the band gap when blue P contacts with Pd and Ir, compared to the upper part when contact with Ir.

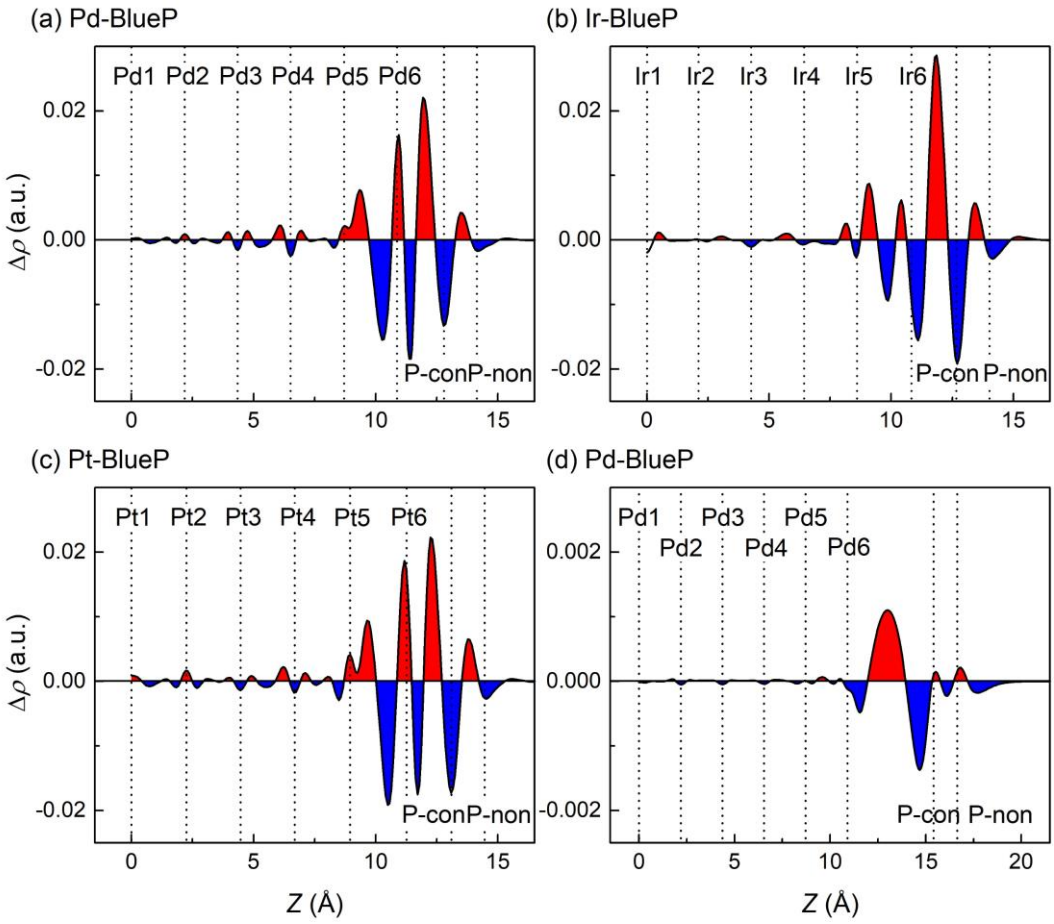

Figure 7.4 Plane-averaged charge density difference along the vertical direction perpendicular to the (a) Pd-blue P, (b) Ir-blue P, and (c) Pt-blue P interfaces at the equilibrium distance, as well as (d) Pd-blue P system at a distance of 4.5 Å. Red and blue colored regions indicate the charge accumulation and depletion regions, respectively.

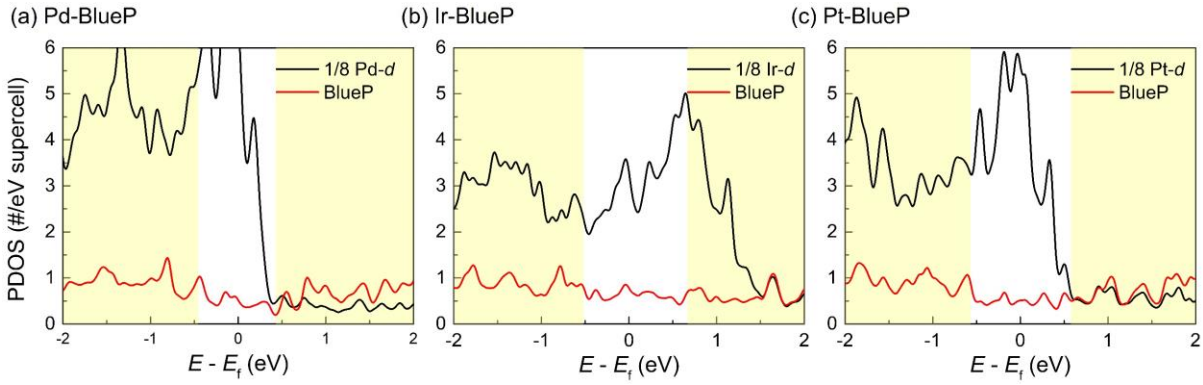

Figure 7.5 PDOSs of blue P (red line) and metal (black line) in the metal-blue P contacts for (a) Pd(111), (b) Ir(111), and (c) Pt(111), respectively. Yellow colored areas represent the band edges of conduction band and valence band, derived by the projected main P *p*-orbital states in the band structures, as shown in Figure 7.2. "1/8 Pd-*d*" in (a), for example, means that the PDOS of *d*-orbital for Pd atoms is reduced to 1/8 for a better comparison with PDOS of blue P.

In a general sense, the modification of metal WFs can be weakened by increasing separation between metal contacts and blue P, and meanwhile the interface hybridization is mitigated, which results in less gap states and therefore FL unpinning. To quantitatively analyze the CBM and VBM of blue P in the metal-blue P contacts, their exact locations are determined by the Schottky-Mott rule as follows:

$$\mathrm{VBM_{ideal}} = -\left(E_g/2 - (\mathrm{WF_{metal}} - \mathrm{WF_{blue\ P}})\right) \tag{7.4}$$

$$\mathrm{CBM_{ideal}} = E_g + \mathrm{VBM_{ideal}} \tag{7.5}$$

where E_g, $\mathrm{WF_{metal}}$, and $\mathrm{WF_{blue\ P}}$ represent for the band gap of monolayer blue P, the WFs of isolated metals and isolated blue P, respectively. As shown in Figure 7.6a-c, red and blue bars depict the dependence of CBM and VBM as a function of interfacial separation distance together with the black numbers indicate their exact locations, and the orange dashed lines and numbers indicating the ideal locations of VBM and CBM calculated from eqns. (7.4) and (7.5). At an interface separation of 6.0 Å, the exact locations of CBM and VBM for all metal-blue P contacts almost ideally match the ideal locations predicted from the Schottky-Mott rule, which reflects that SBHs are exclusively determined by the WF difference between isolated metals and blue P. Therefore, an insertion of buffer layer (for example, hexagonal boron nitride)

between metals and blue P is advised to be a promising approach for the FL unpinning. It suggests an insertion of appropriate buffering materials between metals and monolayer blue P would be a promising technique for unpinning the FLs.

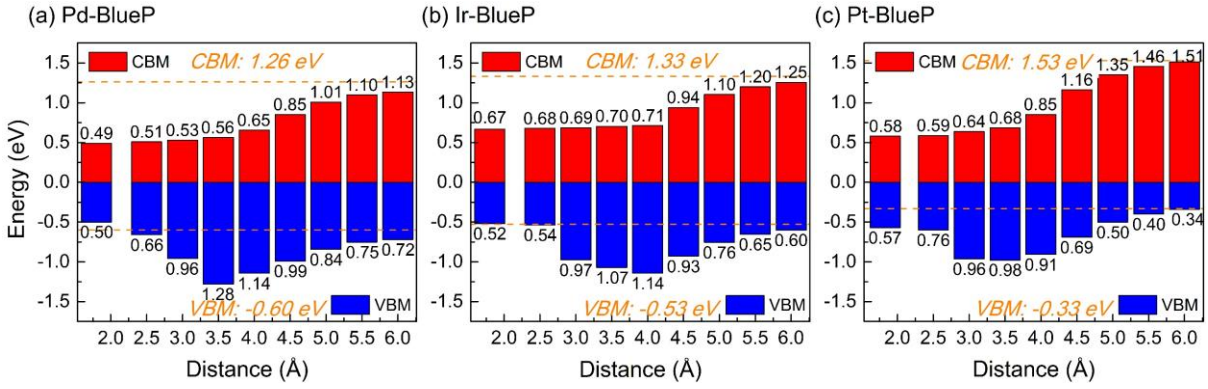

Figure 7.6 The evolution of exact locations of CBM and VBM of monolayer blue P with the interface separation in (a) Pd-blue P, (b) Ir-blue P, and (c) Pt-blue P contacts, respectively. The leftmost color bar indicates to the case of at equilibrium interface separation, and the horizontal orange dashed line corresponds to the ideal locations of CBM and VBM determined from the conventional Schottky-Mott rule.

7.4.3 Chemical properties: hydrogen binding

Aside from the modifications on the electronic properties, the strong interaction between the monolayer blue P and metal substrates is also expected to alter the chemical properties of monolayer blue P. HER is fundamentally significant in a wide range of electrochemical reactions of technological importance, which is therefore selected as an example to exploit the potential of tuning the chemical reactivity on the surface of blue P through substrate coupling. Tremendous efforts have been made to searching for alternative catalysts within the category of 2D nanomaterials (e.g., carbon nitride (g-C_3N_4), MoS_2, and black P) that are of low cost and earth abundant to replace Pt, which being the currently most efficient HER catalyst.[5, 29-33] Recently, blue P quantum dots have been predicted the possibility to function as HER catalyst, and large sizes possess higher reducing capabilities and are expected to give better photocatalytic performance.[34] Similar to other 2D nanomaterials, only the edge sites of the monolayer blue P was revealed to be chemically reactive, whereas a

large area of basal plane remains inert. It is expected that large-area growth of blue P sheets can be realized on the metal substrates mentioned above owing to the small lattice mismatch, which has also been confirmed by recent experiments.[12-13] Therefore, it is intriguing to sufficiently activate the basal plane of blue P by using the substrate coupling, since the lattice mismatch will possibly alter the catalytic performance and overall reactivity of blue P .

The most stable geometries of H adsorption on the surfaces of pristine monolayer blue P and overlayer on the metal substrates are determined by examining all the possible initial configurations with symmetry considerations. The computational hydrogen electrode (CHE) model suggested by Nørskov and co-workers[35] was chosen to establish the free energy profile of HER on the metal-blue P systems, in which the free energy of a pair of proton and electron $G(H^+ + e^-)$ is equal to that of 1/2 hydrogen molecule ($0.5G(H_2)$) under standard reaction conditions (i.e., pH = 0, 298.15 K, 1 atm) and with zero external potential. In this model, the ΔG is determined by the equation: $\Delta G = \Delta E + \Delta ZPE - T\Delta S$, where ΔE represent for the electronic energy difference directly obtained from DFT calculations, ΔZPE for the change in zero-point energy, T for the temperature ($T = 298.15K$), and ΔS for the entropy change. The contributions of zero-point energies and entropies of the HER species were estimated from the vibrational frequencies, where only considered the vibrational modes for adsorbates and neglected the contributions of metal substrates and blue P. We used the data in NIST database to calculate the vibrational frequency and entropy of molecule in its gas phase.[36] As show in Figure 7.7, the upper row illustrates the top and side views of the most stable geometries when one H adsorbed on the surfaces. According to the Sabatier principle,[37] the free energy change when one H adsorbed on the surface (ΔG_{*H}) should be near zero in order to achieve the maximum reaction rate. As shown in Table 7.1, the calculated ΔG_{*H} are 0.40, 0.16, and 0.39 eV for blue P on Pd(111), Ir(111), and Pt(111) substrates respectively, compared to the value of 1.07 eV on the planar surface of pristine monolayer blue P. It is significant to note that, the

ΔG_{*H} of Ir(111)-blue P systems is as low as the value of Pt (~0.1 eV).[38] In addition to the Gibbs free energy of H adsorption, the geometrical variations are also observed between the considered systems, as measured by the angle (θ) between the H−P bond and the planar surface of blue P. We can see in Table 7.1 and Figure 7.7, θ are 52.5º and 54.0º for Ir(111)-blue P and Pt(111)-blue P systems, respectively, which are not far away from the 43.1º on a free-standing blue P. In a stark contrast, the H atom prefers to adsorb on the top of P atoms in Pd(111)-blue P system with a θ of 87.4º. These results collectively reflect that either the free energy or the geometry of H adsorption can be adjusted with a proper choice of metal electrode. In turn, such a tunability would remarkably affect the HER efficiency on the basal plane of adsorbed blue P.

Furthermore, to further unravel the inner reason of enhanced H adsorption due to the substrate coupling, the charge density difference between H and the pristine blue P and metal-blue P surfaces have been calculated by $\Delta\rho = \rho_{\text{H/metal-blue P}} - \rho_{\text{H}} - \rho_{\text{metal-blue P}}$. As shown in Figure 7.7, the lower row demonstrates the side views of the contour images of charge density difference. Obviously, more charge is participated in the formation of H−P covalent bond on Pd(111), Ir(111), and Pt(111) substrates, which is consistent with the enhanced adsorption energy and shortened bond lengths, as shown in Table 7.1. Apart from the charge redistribution between the blue P and adsorbed H atom, the effect of H adsorption on the coupling between the blue P and metal substrates was also examined. The parameter of d_z^{H} is thus introduced to quantify such an effect, which is defined as the average separation between the lower layer of blue P and the topmost layer of metal substrates. With the presence of H, d_z^{H} is reduced by 0.19 Å, 0.08 Å, and 0.16 Å for Pd, Ir, and Pt respectively, if compared to original value of separation without H adsorption. Overall, the enhanced H adsorption originates from two aspects: (1) more charge is transferred from metal substrates to blue P in the formation of a stronger H−P covalent bonding; (2) the adsorbed H atom is acting as a “nail” to fasten the metal substrates and blue P together, and thus results in a strong metal-blue P interface.

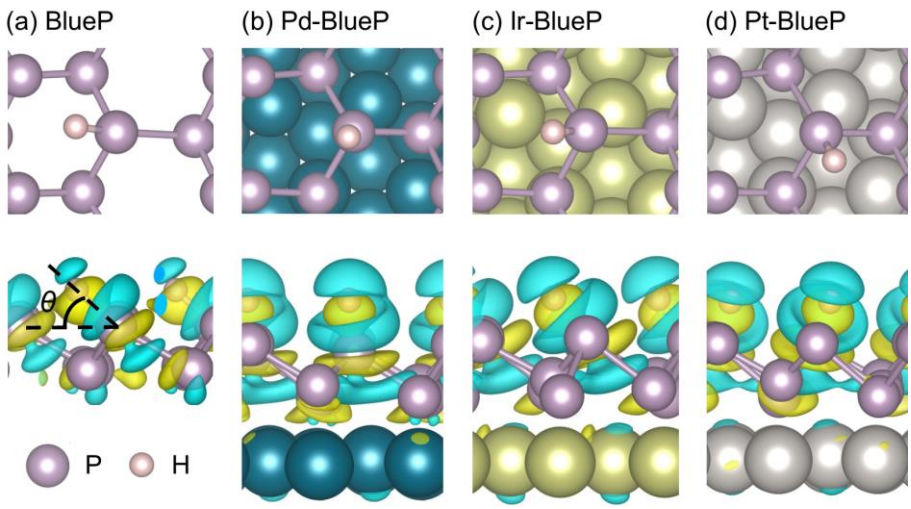

Figure 7.7 Top views of the most stable adsorption geometries (upper row) and side views of the contour images of charge density difference (lower row) when one H atom adsorbed on (a) a free-standing blue P, (b) Pd-blue P, (c) Ir-blue P, and (d) Pt-blue P systems. θ refers to the angle between the H−P bond and the planar surface of blue P. The yellow and blue colors indicate the charge accumulation and depletion, respectively. The iso-surface value of the contour plot is set to 0.002 e Bohr^{-3}.

7.5 Conclusions

To summarize, a DFT study was performed systematically on monolayer blue P when contacts with three different metals of Pd, Ir, and Pt. It is found that the Schottky barrier contacts are formed for each of metal substrates, and the relation between SBHs and metal work functions depicts a picture of partial Fermi-level pinning. The calculated CBM and VBM at metal-blue P interfaces severely deviate from the predictions from Schottky-Mott rule, due to a notable band realignment ascribed to the interface dipole formation. Besides, the interface dipole formation also results in a remarkable interface charge redistribution since the adsorbed blue P would significantly modify the metal work functions. Further, the substrate coupling effect is demonstrated to have substantial effect on tuning the free energy of H adsorption on blue P overlayer. By examining the charge density redistribution, we found that the enhanced H adsorption originates from two facts, one being more charge involving in the bond formation which gives a stronger H−P covalent bond, the other being the adsorbed H atom acting as a "nail" to pin the metals and blue P which results in a strong metal-blue P interface. These

instrumental findings might provide guidance in future design of electronic and optoelectronic devices based on this promising 2D nanomaterial and exploit its potential in catalyzing the hydrogen evolution reaction and related overall water splitting.

7.6 Acknowledgements

The authors thank the NSERC Discovery grant (grant # RGPIN-2017-05187), NSERC Strategic grant (grant # STPGP 494012-16), and McGill Engineering Doctoral Award (MEDA) for financial support. The authors also would like to acknowledge the Supercomputer Consortium Laval UQAM McGill and Eastern Quebec for the computational support.

7.7 References

(1) Liu, H.; Neal, A. T.; Zhu, Z.; Luo, Z.; Xu, X.; Tománek, D.; Ye, P. D., Phosphorene: An Unexplored 2D Semiconductor with a High Hole Mobility. *ACS Nano* **2014**, *8*, 4033-4041.
(2) Li, L.; Yu, Y.; Ye, G. J.; Ge, Q.; Ou, X.; Wu, H.; Feng, D.; Chen, X. H.; Zhang, Y., Black Phosphorus Field-Effect Transistors. *Nat. Nanotechnol.* **2014**, *9*, 372-377.
(3) Qiao, J.; Kong, X.; Hu, Z.-X.; Yang, F.; Ji, W., High-Mobility Transport Anisotropy and Linear Dichroism in Few-Layer Black Phosphorus. *Nat. Commun.* **2014**, *5*, 4475.
(4) Xia, F.; Wang, H.; Jia, Y., Rediscovering Black Phosphorus as an Anisotropic Layered Material for Optoelectronics and Electronics. *Nat. Commun.* **2014**, *5*, 4458.
(5) Zhu, X.; Zhang, T.; Sun, Z.; Chen, H.; Guan, J.; Chen, X.; Ji, H.; Du, P.; Yang, S., Black Phosphorus Revisited: A Missing Metal-Free Elemental Photocatalyst for Visible Light Hydrogen Evolution. *Adv. Mater.* **2017**, *29*, 1605776.
(6) Bachhuber, F.; von Appen, J.; Dronskowski, R.; Schmidt, P.; Nilges, T.; Pfitzner, A.; Weihrich, R., The Extended Stability Range of Phosphorus Allotropes. *Angew. Chem. Int. Ed.* **2014**, *53*, 11629-11633.
(7) Wu, M.; Fu, H.; Zhou, L.; Yao, K.; Zeng, X. C., Nine New Phosphorene Polymorphs with Non-Honeycomb Structures: A Much Extended Family. *Nano Lett.* **2015**, *15*, 3557-3562.
(8) Liu, J.; Guo, Y.; Zhang, S.; Wang, Q.; Kawazoe, Y.; Jena, P., New Phosphorene Allotropes Containing Ridges with 2- and 4-Coordination. *J. Phys. Chem. C* **2015**, *119*, 24674-24680.
(9) Zhu, Z.; Tománek, D., Semiconducting Layered Blue Phosphorus: A Computational Study. *Phys. Rev. Lett.* **2014**, *112*, 176802.
(10) Guan, J.; Zhu, Z.; Tománek, D., Phase Coexistence and Metal-Insulator Transition in Few-Layer Phosphorene: A Computational Study. *Phys. Rev. Lett.* **2014**, *113*, 046804.
(11) Aierken, Y.; Çakır, D.; Sevik, C.; Peeters, F. M., Thermal Properties of Black and Blue Phosphorenes from a First-Principles Quasiharmonic Approach. *Phys. Rev. B* **2015**, *92*, 081408.
(12) Zhang, J. L., et al., Epitaxial Growth of Single Layer Blue Phosphorus: A New Phase of Two-Dimensional Phosphorus. *Nano Lett.* **2016**, *16*, 4903-8.
(13) Pan, Y., et al., Schottky Barriers in Bilayer Phosphorene Transistors. *ACS Appl. Mater. Interfaces* **2017**, *9*, 12694-12705.
(14) Kurtin, S.; McGill, T.; Mead, C., Fundamental Transition in the Electronic Nature of Solids. *Phys. Rev. Lett.* **1969**, *22*, 1433.

(15) Kresse, G.; Furthmüller, J., Efficiency of *Ab-Initio* Total Energy Calculations for Metals and Semiconductors Using a Plane-Wave Basis Set. *Comput. Mater. Sci.* **1996**, *6*, 15-50.
(16) Blöchl, P. E., Projector Augmented-Wave Method. *Phys. Rev. B* **1994**, *50*, 17953.
(17) Ceperley, D. M.; Alder, B., Ground State of the Electron Gas by a Stochastic Method. *Phys. Rev. Lett.* **1980**, *45*, 566.
(18) Chen, W.; Santos, E. J. G.; Zhu, W.; Kaxiras, E.; Zhang, Z., Tuning the Electronic and Chemical Properties of Monolayer MoS_2 Adsorbed on Transition Metal Substrates. *Nano Lett.* **2013**, *13*, 509-514.
(19) Gong, C.; Colombo, L.; Wallace, R. M.; Cho, K., The Unusual Mechanism of Partial Fermi Level Pinning at Metal–MoS_2 Interfaces. *Nano Lett.* **2014**, *14*, 1714-1720.
(20) Pan, Y., et al., Interfacial Properties of Monolayer $MoSe_2$–Metal Contacts. *J. Phys. Chem. C* **2016**, *120*, 13063-13070.
(21) Liu, Y.; Stradins, P.; Wei, S.-H., Van Der Waals Metal-Semiconductor Junction: Weak Fermi Level Pinning Enables Effective Tuning of Schottky Barrier. *Sci. Adv.* **2016**, *2*.
(22) Kim, C.; Moon, I.; Lee, D.; Choi, M. S.; Ahmed, F.; Nam, S.; Cho, Y.; Shin, H.-J.; Park, S.; Yoo, W. J., Fermi Level Pinning at Electrical Metal Contacts of Monolayer Molybdenum Dichalcogenides. *ACS Nano* **2017**, *11*, 1588-1596.
(23) Pan, Y., et al., Monolayer Phosphorene–Metal Contacts. *Chem. Mater.* **2016**, *28*, 2100-2109.
(24) Zhong, H.; Quhe, R.; Wang, Y.; Ni, Z.; Ye, M.; Song, Z.; Pan, Y.; Yang, J.; Yang, L.; Lei, M., Interfacial Properties of Monolayer and Bilayer MoS_2 Contacts with Metals: Beyond the Energy Band Calculations. *Sci. Rep.* **2016**, *6*, 21786.
(25) Guo, Y.; Liu, D.; Robertson, J., 3D Behavior of Schottky Barriers of 2D Transition-Metal Dichalcogenides. *ACS Appl. Mater. Interfaces* **2015**, *7*, 25709-25715.
(26) Das, S.; Chen, H.-Y.; Penumatcha, A. V.; Appenzeller, J., High Performance Multilayer MoS_2 Transistors with Scandium Contacts. *Nano Lett.* **2012**, *13*, 100-105.
(27) Gong, C.; Lee, G.; Shan, B.; Vogel, E. M.; Wallace, R. M.; Cho, K., First-Principles Study of Metal–Graphene Interfaces. *J. Appl. Phys.* **2010**, *108*, 123711.
(28) Tung, R. T., Formation of an Electric Dipole at Metal-Semiconductor Interfaces. *Phys. Rev. B* **2001**, *64*, 205310.
(29) Voiry, D.; Salehi, M.; Silva, R.; Fujita, T.; Chen, M.; Asefa, T.; Shenoy, V. B.; Eda, G.; Chhowalla, M., Conducting MoS_2 Nanosheets as Catalysts for Hydrogen Evolution Reaction. *Nano Lett.* **2013**, *13*, 6222-6227.
(30) Li, G.; Zhang, D.; Qiao, Q.; Yu, Y.; Peterson, D.; Zafar, A.; Kumar, R.; Curtarolo, S.; Hunte, F.; Shannon, S., All the Catalytic Active Sites of MoS_2 for Hydrogen Evolution. *J. Am. Chem. Soc.* **2016**, *138*, 16632-16638.
(31) Zhu, J.; Wang, Z.-C.; Dai, H.; Wang, Q.; Yang, R.; Yu, H.; Liao, M.; Zhang, J.; Chen, W.; Wei, Z., Boundary Activated Hydrogen Evolution Reaction on Monolayer MoS_2. *Nat. Commun.* **2019**, *10*, 1348.
(32) He, R.; Hua, J.; Zhang, A.; Wang, C.; Peng, J.; Chen, W.; Zeng, J., Molybdenum Disulfide–Black Phosphorus Hybrid Nanosheets as a Superior Catalyst for Electrochemical Hydrogen Evolution. *Nano Lett.* **2017**, *17*, 4311-4316.
(33) Zhu, M.; Osakada, Y.; Kim, S.; Fujitsuka, M.; Majima, T., Black Phosphorus: A Promising Two Dimensional Visible and near-Infrared-Activated Photocatalyst for Hydrogen Evolution. *Appl. Catal. B* **2017**, *217*, 285-292.
(34) Zhou, S.; Liu, N.; Zhao, J., Phosphorus Quantum Dots as Visible-Light Photocatalyst for Water Splitting. *Comput. Mater. Sci.* **2017**, *130*, 56-63.

(35) Nørskov, J. K.; Rossmeisl, J.; Logadottir, A.; Lindqvist, L.; Kitchin, J. R.; Bligaard, T.; Jonsson, H., Origin of the Overpotential for Oxygen Reduction at a Fuel-Cell Cathode. *J. Phys. Chem. B* **2004**, *108*, 17886-17892.
(36) Ling, C.; Bai, X.; Ouyang, Y.; Du, A.; Wang, J., Single Molybdenum Atom Anchored on N-Doped Carbon as a Promising Electrocatalyst for Nitrogen Reduction into Ammonia at Ambient Conditions. *J. Phys. Chem. C* **2018**, *122*, 16842-16847.
(37) Rothenberg, G., Catalysis: Concepts and Green Applications. Wiley-VCH: 2008; p 65.
(38) Chao, T.; Luo, X.; Chen, W.; Jiang, B.; Ge, J.; Lin, Y.; Wu, G.; Wang, X.; Hu, Y.; Zhuang, Z., Atomically Dispersed Copper–Platinum Dual Sites Alloyed with Palladium Nanorings Catalyze the Hydrogen Evolution Reaction. *Angew. Chem. Int. Ed.* **2017**, *56*, 16047-16051.

Chapter 8 : Conclusions

8.1 Major conclusions and implications

The theoretical studies in this thesis were focused on discovering the electronic and chemical applications of monolayer black/blue P, specifically into two categories of potential fields, gas sensing and chemical catalysis, and providing theoretical guidance into the materials design of black/blue P toward high-performance chemiresistors and photocatalysts. The major conclusions are summarized below, followed by a discussion of their implications.

8.1.1 Prediction of superior chemical sensing performance of single-walled black P nanotube (SW-PNT) as an efficient gas sensor: Compared with monolayer black P

The capability of single-walled black phosphorus nanotube (SW-PNT) of sensing the common toxic gas molecules (NH_3, CO, NO, NO_2, and SO_2) was examined by using first-principles calculations. SW-PNTs exhibits the strongest interaction with NO_2 molecule, which is almost three time higher than that on its monolayer. By analyzing the charge density differences, NH_3 is acting as electron donor when adsorbed on SW-PNTs, whereas the remaining acting as electron acceptors. In contrast to the results on monolayer black P, the SW-PNTs are generally more sensitive towards sensing these gas molecules, particularly for NO_2. Furthermore, a comparative study of the curvature effect indicates that the adsorption capability of NO_2 on the outer surface is decreasing with the increasing diameter of SW-PNTs. **Implication:** The present study indicates that the adsorption capability and sensitivity can be enhanced on SW-PNTs in the detection of gas molecules, particularly for NO_2, rendering it a more sensitive gas sensor than other two-dimensional (2D) nanomaterials, including MoS_2 and graphene. In the near future, SW-PNTs are anticipated to be one of the most promising nanomaterial that guide the research field of gas sensing.

8.1.2 Prediction of efficient volatile organic compounds (VOCs) sensors based on field-effect transistors by using monolayer black P as the potential channel material

The VOC-sensing performance of monolayer black P was studied by using first-principles calculations. First, the energetically preferable adsorption sites for VOCs on monolayer black P have been identified and the corresponding adsorption energetics have been determined. VOCs were found to generally exhibit stronger interaction with black P than with the widely studied monolayer MoS_2, indicative of black P potentially being a more sensitive VOC sensor. Furthermore, the adsorption characteristics of VOCs on monolayer black P are well retained in the event of thickness variation, although enhanced adsorption energies for bilayer and multilayer black P were also observed. Monolayer black P exhibits highly anisotropic transport properties; Nonetheless, the absolute modification of *I-V* responses due to VOCs implies a direction-independent trend. Moreover, the recovery time of VOCs sensors is found to be within the detectable range and indicative of a short recovery time for next detection. **Implication:** Our findings suggest that monolayer black P be a compelling candidate material to achieve high sensitivity and good reusability for VOC sensors.

8.1.3 Design of high-performance electrocatalysts for N_2 conversion to NH_3 by constructing the molybdenum-based single-atom catalyst (SAC) in N-doped black P

The potential of Mo-based SACs embedded in nitrogen-doped black P was studied for electrochemical N_2 reduction reaction (NRR) into NH_3. Among the Mo-based SACs considered, Mo_1N_3 has been found to exhibit chemisorption of N_2, and an extremely low overpotential of just 0.02 V through the associative distal mechanism, indicative of catalyzing NRR under ambient conditions. In addition, Mo_1N_3 shows fast removal of the produced NH_3 with a small free energy barrier of 0.56 eV, which is lower than most of reported NRR catalysts with low overpotential, and offers good stability of NRR reaction intermediates. Moreover, the Mo-based SACs were demonstrated to be more selective to NRR over the competing HER

process. **Implication:** The excellent features endow Mo_1N_3 on 2D black P as a compelling highly efficient and durable catalyst for electrochemical N_2 fixation. The great potential of 2D nanomaterials was demonstrated and may contribute to motivating more experimental and theoretical efforts targeting the usage of 2D nanomaterials in NRR electrocatalysts.

8.1.4 Determination of contact nature for transition metal/blue P heterojunctions and effective tuning of hydrogen adsorption by substrate coupling

This study found that the Schottky barrier contacts are formed for each of the metal substrates, and the relation between SBHs and metal work functions creates an image of partial Fermi-level pinning. The calculated CBM and VBM at metal-blue P interfaces severely deviate from the predictions of the Schottky-Motte rule, due to a notable band realignment ascribed to the interface dipole formation. The interface dipole formation also results in a remarkable interface charge redistribution, since the adsorbed blue P would significantly modify the metal work functions. Further, the substrate coupling effect is demonstrated to have substantial effect on tuning the free energy of H adsorption on a blue P overlayer. By examining the charge density redistribution, the study found that the enhanced H adsorption originates from two facts, the first being that more charge involved in the bond formation yields a stronger H−P covalent bond, and second being that the adsorbed H atom acting as a “nail” to pin the metals and blue P results in a strong metal-blue P interface. **Implication:** These findings may provide guidance in the future design of electronic and optoelectronic devices based on this promising 2D nanomaterial, and exploit its potential in catalyzing the hydrogen evolution reaction and related overall water splitting.

8.2 Contribution to the original knowledge

The contribution to the original knowledge is reflected in the following aspects:

1. For the first time, the single-walled black P nanotubes (SW-PNT) were theoretically predicted to be a compelling candidate towards sensing the common toxic gas molecules with comparable or even better sensitivity than monolayer black P;
2. The curvature and strain effects on the adsorption characteristics of SW-PNTs were examined for the first time, providing significant implications in the design of high-performance gas sensing devices;
3. The electronic and transport characteristics of VOCs adsorbed on the monolayer black phosphorus were first clarified, demonstrating strong potential in the application of VOCs chemiresistors;
4. The Mo-based SACs were first designed in the nitrogen-doped black P to enable its application as an efficient electrochemical NRR catalyst, which exhibit ultralow overpotential and good selectivity, as well as fast removal of produced ammonia;
5. For the first time, the Schottky barrier height and pinning factor of blue P when forming electrical contacts with transition metals were determined theoretically;
6. Monolayer blue P and substrate coupling were first explored to tune the catalytic activity for hydrogen production and related water splitting processes.

8.3 Future work

Various uncharted areas remained in the engineering and discovery of a 2D allotropes of elemental phosphorus. Among them, some intriguing yet unresolved tasks that are worth pursuing in future studies are introduced below:

8.3.1 Proposing new theoretical framework for simulations of gas sensor

Chapters 4 and 5 delivered theoretical studies on the ideal scenario for a gas sensor, yet, in reality there would be co-existence between multiple VOCs. This necessitates the evaluation of the competitive resistance variation and mutual interference between VOCs, and in certain cases, the exact VOC adsorption sequence and possible reconstruction of VOC

clusters, in order to obtain a more accurate assessment of VOC sensing and selectivity of black/blue P. Moreover, further defect engineering and surface functionalization such as incorporation of nanoparticles,[1-2] exposure of edge sites,[3] and ligand conjugations[4-5] may hold the possibility of modifying the properties of black/blue P and affecting its interaction with VOCs. The above challenges, along with many others not mentioned in this thesis, require additional research efforts and further development of new computational frameworks.

8.3.2 Breaking linear scaling relations and other methods of suppressing HER

Previously, a linear scaling relations was suggested between the adsorption energies of intermediates and overpotential for the transition metals NRR catalysts, which limits the achievement of high activity and selectivity for N_2 reduction to NH_3.[6] The NRR activity volcano of various single-atom catalysts via the capture of different transition metal atoms in 2D black/blue P is significant for the computational screening of an optimal NRR catalyst. If the linear scaling relations are confirmed to exist in 2D black/blue P, enhanced performance must be fulfilled by systematically departing from the scaling relations. Initially, to conceive a system that already sits at the top of the volcano plot for NRR activity would be the most compelling approach. Other advanced methods that have been suggested to break the linear scaling relations for CO_2 reduction might also be feasible, such as functionalization or tethering of surfaces with molecular frameworks or co-adsorbed molecules.[7] Furthermore, other methods of suppressing HER (which is the major competing reaction to NRR under electrochemical environment) are also viable in developing a highly selective and efficient NRR catalyst. Overall, dedicated research studies will be required to confirm whether these methods can be realized and to what extent they can enhance the performance of NRR catalysts.

8.3.3 Schottky barrier engineering and reduction of Fermi level pinning

As demonstrated in Chapter 7, the formation of large Schottky barrier height (SBH) at the metal-semiconductor junction (MSJ), results in the absence of a correlation between SBHs

and metal WFs. Therefore, the SBH is inaccessible for tuning by using conventional metals, which obstructs the formation of ohmic contact and limits the development of black/blue P in FETs. In this regard, FLP has sparked great interest as the subject of future experimental and theoretical studies.[8-13] Some effective methods of reducing FLP at MSJ have been proposed, such as atomic passivation,[8] insertion of ultrathin material,[10-11] replacement of traditional 3D metals with 2D metals,[12] and thermal annealing.[13] These methods of tuning SBHs at MSJ based on black/blue P, and the possibility of ohmic contact formation are worth looking into, due to the benefits they offer in the advancement of electronic and optoelectronic devices.

8.4 References

(1) Cho, S.-Y.; Koh, H.-J.; Yoo, H.-W.; Jung, H.-T., Tunable Chemical Sensing Performance of Black Phosphorus by Controlled Functionalization with Noble Metals. *Chem. Mater.* **2017**, *29*, 7197-7205.

(2) Cho, S.-Y.; Koh, H.-J.; Yoo, H.-W.; Kim, J.-S.; Jung, H.-T., Tunable Volatile-Organic-Compound Sensor by Using Au Nanoparticle Incorporation on MoS_2. *ACS Sens.* **2017**, *2*, 183-189.

(3) Cho, S.-Y.; Kim, S. J.; Lee, Y.; Kim, J.-S.; Jung, W.-B.; Yoo, H.-W.; Kim, J.; Jung, H.-T., Highly Enhanced Gas Adsorption Properties in Vertically Aligned MoS_2 Layers. *ACS Nano* **2015**, *9*, 9314-9321.

(4) Kim, J.-S.; Yoo, H.-W.; Choi, H. O.; Jung, H.-T., Tunable Volatile Organic Compounds Sensor by Using Thiolated Ligand Conjugation on MoS_2. *Nano Lett.* **2014**, *14*, 5941-5947.

(5) Sim, D. M.; Kim, M.; Yim, S.; Choi, M.-J.; Choi, J.; Yoo, S.; Jung, Y. S., Controlled Doping of Vacancy-Containing Few-Layer MoS_2 Via Highly Stable Thiol-Based Molecular Chemisorption. *ACS Nano* **2015**, *9*, 12115-12123.

(6) Montoya, J. H.; Tsai, C.; Vojvodic, A.; Nørskov, J. K., The Challenge of Electrochemical Ammonia Synthesis: A New Perspective on the Role of Nitrogen Scaling Relations. *ChemSusChem* **2015**, *8*, 2180-2186.

(7) Peterson, A. A.; Nørskov, J. K., Activity Descriptors for CO_2 Electroreduction to Methane on Transition-Metal Catalysts. *J. Phys. Chem. Lett.* **2012**, *3*, 251-258.

(8) Min, K.-A.; Park, J.; Wallace, R. M.; Cho, K.; Hong, S., Reduction of Fermi Level Pinning at Au–MoS_2 Interfaces by Atomic Passivation on Au Surface. *2D Mater.* **2016**, *4*, 015019.

(9) Liu, Y.; Stradins, P.; Wei, S. H., Air Passivation of Chalcogen Vacancies in Two-Dimensional Semiconductors. *Angew. Chem.* **2016**, *128*, 977-980.

(10) Nishimura, T.; Kita, K.; Toriumi, A., A Significant Shift of Schottky Barrier Heights at Strongly Pinned Metal/Germanium Interface by Inserting an Ultra-Thin Insulating Film. *Appl. Phys. Express* **2008**, *1*, 051406.

(11) Tsui, B.-Y.; Kao, M.-H., Mechanism of Schottky Barrier Height Modulation by Thin Dielectric Insertion on n-Type Germanium. *Appl. Phys. Lett.* **2013**, *103*, 032104.

(12) Liu, Y. Y.; Stradins, P.; Wei, S. H., Van Der Waals Metal-Semiconductor Junction: Weak Fermi Level Pinning Enables Effective Tuning of Schottky Barrier. *Sci Adv* **2016**, *2*, e1600069.

(13) Ling, Z.-P.; Sakar, S.; Mathew, S.; Zhu, J.-T.; Gopinadhan, K.; Venkatesan, T.; Ang, K.-W., Black Phosphorus Transistors with near Band Edge Contact Schottky Barrier. *Sci. Rep.* **2015**, *5*, 18000.